

**The Neoproterozoic-Paleoproterozoic Evolution of the
Fuping Complex in the Central Segment of the North
China Craton**

July 2017

Li TANG

**The Neoproterozoic-Paleoproterozoic Evolution of the
Fuping Complex in the Central Segment of the North
China Craton**

A Dissertation Submitted to
the Graduate School of Life and Environmental Sciences,
the University of Tsukuba
in Partial Fulfillment of the Requirements
for the Degree of Doctor of Philosophy in Science
(Doctoral Program in Earth Evolution Sciences)

Li TANG

Contents

Contents	i
Abstract.....	iv
List of Figures	vi
List of Tables.....	xvi
Chapter 1: General introduction.....	1
1.1 Research background and controversies.....	1
1.2 Research objectives.....	5
Chapter 2: Regional geology.....	7
2.1 North China Craton.....	7
2.2 Trans-North China Orogen.....	9
2.3 Fuping Complex.....	9
Chapter 3: Neoproterozoic evolution of the Fuping Complex	12
3.1 Introduction.....	12
3.2 Sample description.....	13
3.2.1 Hornblendites	13
3.2.2 Pyroxene hornblendites.....	13
3.2.3 TTG gneisses.....	15
3.3 Analytical results.....	15
3.3.1 Mineral chemistry	15
3.3.2 Whole rock geochemistry	20
3.3.3 Zircon U-Pb geochronology.....	22
3.3.4 Zircon Lu-Hf isotopes	23
3.3.5 Zircon O isotopes	24
3.4 Discussion	25
3.4.1 Neoproterozoic arc magmatism.....	25
3.4.2 Magma sources and evolution.....	27
3.4.3 Tectonic implications	29

3.5 Conclusions	31
Chapter 4: Paleoproterozoic (2.1-2.0 Ga) magmatism in the Fuping Complex	33
4.1 Introduction.....	33
4.2 Sample description.....	35
4.3 Analytical results	37
4.3.1 Major and trace elements	37
4.3.2 Zircon U-Pb geochronology.....	40
4.3.3 Zircon Lu-Hf isotopes	45
4.4 Discussion	47
4.4.1 Petrogenesis	47
4.4.2 Formation of the Wanzi supracrustal rocks	48
4.4.3 Tectonic implications	49
4.5 Conclusions	54
Chapter 5: Paleoproterozoic sedimentation in the Fuping and Zanhuang Complexes	55
5.1 Introduction.....	55
5.2 Sample description.....	57
5.3 Analytical results	59
5.3.1 Major and trace elements	59
5.3.2 Zircon U-Pb geochronology.....	62
5.3.3 C-O isotopes.....	66
5.4 Discussion	66
5.4.1 Effects of diagenesis and metamorphism.....	66
5.4.2 Nature of protolith.....	68
5.4.3 Provenance and depositional age	69
5.4.4 Tectonic implication.....	71
5.5 Conclusions	75
Chapter 6: Paleoproterozoic (1.96-1.80 Ga) metamorphism in the Fuping Complex	77
6.1 Introduction.....	77
6.2 Samples and petrography	79
6.2.1 15FP-02.....	80

6.2.2 15FP-03.....	81
6.2.3 15FP-06.....	81
6.3 Analytical results.....	85
6.3.1 Mineral chemistry	85
6.3.2 Pseudosection modelling.....	87
6.3.3 Geothermobarometry	93
6.3.4 Zircon U-Pb geochronology.....	94
6.4 Discussion	97
6.4.1 Metamorphic evolution of the mafic granulites	97
6.4.2 Age and tectonic setting of protolith.....	100
6.4.3 Metamorphic ages and implications for the evolution of the TNCO ..	102
6.5 Conclusions	104
Chapter 7: Discussion and Conclusions	106
7.1 Late Neoproterozoic microblock amalgamation of the NCC	106
7.2 Paleoproterozoic rift and subduction processes along the TNCO	111
7.3 Paleoproterozoic final collision along the TNCO.....	112
Acknowledgements	114
References	116
Appendix I: Methodology.....	149
I.1 Field investigation	149
I.2 Petrology and EMPA	150
I.3 Pseudosection modelling	150
I.4 Whole rock geochemistry	150
I.5 Zircon U-Pb geochronology and Hf-O isotopes	151
I.6 C-O isotopes	153
Appendix II: Analytical data	154
Appendix III: Curriculum Vitae	249

Abstract

As one of the major ancient cratonic nuclei in eastern Eurasia, the North China Craton (NCC) preserves a complex history of crustal evolution, cratonization and stabilization. The Trans-North China Orogen (TNCO) is considered as the collisional suture between the Western and Eastern Blocks of the NCC. The Fuping Complex incorporates important basement units in the central segment of the TNCO, and is dominantly composed of TTG gneiss, gneissic granite, meta-sedimentary rock (paragneiss, schist, marble and calc-silicate rock), hornblendite, pyroxene hornblendite, mafic granulite, amphibolite and garnet amphibolite. This thesis presents the results from an integrated study including field investigation, petrology, mineral chemistry, whole rock geochemistry, P - T pseudosection modelling, zircon U-Pb geochronology, zircon Hf-O isotopes and C-O isotopes, in conjunction with previous data, to gain further insights into the Late Neoproterozoic tectonic evolution of the Fuping Complex and the TNCO.

The late Neoproterozoic arc magmatism recorded by the Yangmuqiao mafic-ultramafic intrusion and the Fuping TTG gneiss is probably related to the subduction-collision process of the Ordos and the Qianhuai microblocks along the zone of ocean closure represented by the Wutai greenstone belt.

The geochemical data suggest that the 2.1–2.0 Ga granitic rocks and amphibolites from the Fuping Complex formed in subduction-related arc setting. Based on the widespread 2.1–2.0 Ga magmatism as recorded in different rock types within the TNCO, this study proposes a tectonic model where it is envisaged simultaneous subduction and continental rifting process between several micro-blocks (or complexes). During 2.1–2.0 Ga, the Wutai Complex and the Fuping Complex were separated by the Longquanguan ocean. The double-sided subduction of the Longquanguan oceanic lithosphere resulted in distinct arc magmatism. Continental rift setting developed in the Hengshan, Huai'an and Zanhuang Complexes coevally.

The salient lithological, geochemical and isotopic features imply that the

protoliths of the meta-carbonates from the Wanzi Group (Fuping Complex) and Central Zanhuang Domain (Zanhuang Complex) were formed in a proximal and shallow marine environment. The Wanzi Group was deposited in a forearc basin during 1.95–1.93 Ga and the Central Zanhuang Domain was formed in a back-arc basin during 2.03–1.90 Ga. The geochemical imprints and biospheres of the oceanic basin in the Fuping area were possibly affected by the Lomagundi or Jatulian Event, resulting in the positive excursion of $\delta^{13}\text{C}$ values in the dolomite-calcite marbles. However, the back-arc basin in the Zanhuang area was formed after the 2.1–2.0 Ga rifting event, thus it was generated after the Jatulian Event, thus preserving normal $\delta^{13}\text{C}$ values of marine carbonates.

Mafic granulites are exposed as boudins within TTG gneisses, and record peak metamorphic P – T conditions of 8.2–9.2 kbar, 870–882 °C (15FP-02), 9.6–11.3 kbar, 855–870 °C (15FP-03) and 9.7–10.5 kbar, 880–900 °C (15FP-06), respectively. Data from LA-ICP-MS zircon U–Pb dating show that the mafic dyke protoliths of the granulite were emplaced at ~2327 Ma. The metamorphic zircons show two groups of ages at 1.96–1.90 Ga (peak at 1.93–1.92 Ga) and 1.90–1.80 Ga (peak at 1.86–1.83 Ga), consistent with the two metamorphic events widely reported from different segments of the Trans-North China Orogen. The 1.93–1.92 Ga ages are considered to date the peak granulite-facies metamorphism, whereas the 1.86–1.83 Ga ages are correlated with the retrograde event. Thus, the collisional assembly of the major crustal blocks in the North China Craton might have occurred during 1.93 to 1.90 Ga, marking the final cratonization of the North China Craton.

Keywords: Neoproterozoic; Magmatism; Metamorphism; Fuping Complex; North China Craton

List of Figures

Fig. 1-1 Tectonic map of China showing the major cratons and younger orogens (Zhao et al., 2001a).	1
Fig. 1-2 Updated subdivision of the North China Craton (modified after Zhai and Santosh, 2011; Zhao and Zhai, 2013) showing the major microblocks, granite-greenstone belts and Neoproterozoic basement rocks. Abbreviations: GGB, granite-greenstone belt; JL, Jiaoliao Block; QH, Qianhuai Block; OR, Ordos Block; JN, Jining Block; XCH, Xuchang Block; XH, Xuhuai Block; ALS, Alashan Block. ..	3
Fig. 1-3 Tectonic subdivision of the North China Craton (modified after Zhao et al., 2005). Abbreviations of metamorphic complexes: CD, Chengde; NH, Northern Hebei; XH, Xuanhua; HA, Huai'an; HS, Hengshan; WT, Wutai; FP, Fuping; LL, Lüliang; ZH, Zanhuang; ZT, Zhongtiao; DF, Dengfeng; TH, Taihua; WB, Western Block; EB, Eastern Block.	5
Fig. 2-1 Geological map of the Fuping Complex (after Zhao et al., 2002a).	10
Fig. 3-1 (a) Geological sketch map of the Hengshan-Wutai-Fuping Complexes. (b) Geological map of the Fuping Complex within the Trans-North China Orogen (modified after Cheng et al., 2004), showing major lithological units, their relationships and sampling locations.	14
Fig. 3-2 Representative field photographs of the Yangmuqiao mafic-ultramafic intrusion and the Fuping TTG gneiss.	15
Fig. 3-3 Representative photomicrographs of the rock samples from the Yangmuqiao mafic-ultramafic intrusion and the Fuping TTG gneiss. (a) Hornblende (FP-24). (b) Pyroxene hornblende (FP-28). (c) Pyroxene hornblende (FP-28), chromites occur as mineral inclusions in hornblende. (d) TTG gneiss (FP-7). Mineral abbreviations: Hbl, hornblende; Pl, plagioclase; Cpx, clinopyroxene, Chr, chromite; Chl, chlorite; Bt, biotite; Qtz, quartz.	16
Fig. 3-4 Classification diagram of hornblende in the rock samples from the Yangmuqiao mafic-ultramafic intrusion (after Leake et al., 1997).	17
Fig. 3-5 Plots of clinopyroxene compositions in pyroxene hornblende from the	

Yangmuqiao mafic-ultramafic intrusion. (a) The fields of the Alaskan-type mafic–ultramafic intrusions are from [Himmelberg and Loney \(1995\)](#). (b) Al₂O₃ versus SiO₂ diagram, the fields of the Alaskan-type complexes are from [Pettigrew and Hattori \(2006\)](#).18

Fig. 3-6 Plots of chromite compositions in the pyroxene hornblendite from the Yangmuqiao mafic-ultramafic intrusion. (a) Al₂O₃ versus TiO₂ diagram, Alaskan-type field after Alaska complex ([Himmelberg et al., 1986](#); [Himmelberg and Loney 1995](#)); Ocean island basalt (OIB), mid-ocean ridge basalt (MORB), and island-arc fields after [Kamenetsky et al. \(2001\)](#). (b) Fe²⁺/(Mg+Fe²⁺) versus Cr# diagram, the fields of Alaskan-type complexes are after [Barnes and Roeder \(2001\)](#)..19

Fig. 3-7 Chondrite-normalized REE patterns (a, c) and primitive mantle-normalized trace elements multi-element variation diagram (b, d) for the rock samples from the Fuping TTG gneisses (a, b) and Yangmuqiao mafic-ultramafic intrusion (c, d). The normalization values are from [Sun and McDonough \(1989\)](#).21

Fig. 3-8 Primitive mantle-normalized PGE patterns of the Yangmuqiao mafic-ultramafic intrusion. The primitive mantle values are from [Barnes and Maier \(1999\)](#).22

Fig. 3-9 Cathodoluminescence (CL) images of representative zircons in Fuping TTG gneiss (FP-7) and pyroxene hornblendite (FP-29-1). Yellow circles for U–Pb analysis and red circles for Lu–Hf analysis, ages in Ma and ε_{Hf}(t) values are also shown.23

Fig. 3-10 Zircon U–Pb concordia plots for the Fuping TTG gneiss (FP-7) and the pyroxene hornblendite (FP-29-1).23

Fig. 3-11 ε_{Hf}(t) versus ²⁰⁷Pb/²⁰⁶Pb age diagram of zircons from the Fuping TTG gneiss (FP-7) and the pyroxene hornblendite (FP-29-1).24

Fig. 3-12 Histograms of zircon δ¹⁸O values (a, b), relationship of zircon U–Pb ages and δ¹⁸O values (c) of zircons from the Fuping TTG gneiss (FP-7) and the pyroxene hornblendite (FP-29-1).25

Fig. 3-13 (a) Archean tectonic framework of the North China Craton showing the distribution of ancient nuclei, microblocks and greenstone belts (after [Zhai and](#)

Santosh, 2011). The major microblocks are the Jiaoliao Block (JL), Qianhuai Block (QH), Ordos Block (OR), Jining Block (JN), Xuchang Block (XCH), Xuhuai Block (XH) and Alashan Block (ALS). GB: Greenstone belt. (b) Proposed tectonic model showing the late Neoproterozoic subduction-related arc magmatism in the Fuping area.28

Fig. 4-1 (a) Geological sketch map of the Hengshan-Wutai-Fuping Complexes. (b) Geological map of the Fuping Complex within the Trans-North China Orogen (modified after Cheng et al., 2004), showing major lithological units, their relationships and sampling locations.34

Fig. 4-2 Representative field photographs of the different rock types in the Fuping Complex. (a) Relationship between gneissic granite (FP-1-1) and amphibolite (FP-1-2); (b) gneissic syenogranite (FP-3); (c) epidote-biotite schist (FP-8) of the Wanzi supracrustal assemblage; (d) mica schist (FP-18) of the Wanzi supracrustal assemblage; (e) BIF and amphibolite (FP-9-2); (f) amphibolite in association with marble (FP-15).35

Fig. 4-3 Photomicrographs of major rock types from the Fuping Complex. (a) Gneissic granite (FP-1-1); (b) gneissic syenogranite (FP-3); (c) amphibolite (FP-1-2), associated with leucite and gneissic granite; (d) amphibolite (FP-9-2) associated with BIF; (e) amphibolite (FP-15) occurring in association with marble; (f) mica schist (FP-18).36

Fig. 4-4 Plots of SiO₂ versus K₂O (a) and SiO₂ versus K₂O+Na₂O-CaO (b) for the granitic rock samples, reference lines after Frost et al. (2001); (c) log-ratio discriminant function major element tectonic plot of Verma et al. (2006) for the basic rocks. $DF1 = -4.6761\ln(TiO_2/SiO_2) + 2.5330\ln(Al_2O_3/SiO_2) - 0.3884\ln(Fe_2O_3/SiO_2) + 3.9688\ln(FeO/SiO_2) + 0.8980\ln(MnO/SiO_2) - 0.5832\ln(MgO/SiO_2) - 0.2896\ln(CaO/SiO_2) - 0.2704\ln(Na_2O/SiO_2) + 1.080\ln(K_2O/SiO_2) + 0.1845\ln(P_2O_5/SiO_2) + 1.5445$. $DF2 = 0.6751\ln(TiO_2/SiO_2) + 4.5895\ln(Al_2O_3/SiO_2) + 2.0897\ln(Fe_2O_3/SiO_2) + 0.8514\ln(FeO/SiO_2) - 0.4334\ln(MnO/SiO_2) + 1.4832\ln(MgO/SiO_2) - 2.3627\ln(CaO/SiO_2) - 1.6558\ln(Na_2O/SiO_2) + 0.6757\ln(K_2O/SiO_2) + 0.4130\ln(P_2O_5/SiO_2) + 13.1639$; (d) Ti-Zr discrimination diagram (Pearce, 1996), WPB: within-plate basalt, VAB: volcanic arc basalt.37

Fig. 4-5 Zr/TiO ₂ versus Nb/Y classification diagram (Pearce, 1996) for the rock samples from the Fuping Complex.	38
Fig. 4-6 Triangular diagrams showing compositions of amphibolites. (a) Plots of La/10-Y/15-Nb/8, 1A: calc-alkali basalt; 1C: volcanic-arc tholeiite; 1B: overlapped field of 1A and 1C; 2A:continental basalt; 2B: back-arc basin basalt; 3A: alkalic basalt from intercontinental rift; 3B: enriched E-type MORB; 3C: weakly enriched E-type MORB; 3D: N-type MORB (Cabani sand Lecolle, 1989).(b) Th-Hf-Ta diagram (after Wood, 1980), A: N-MORB, B: E-MORB and within plate tholeiite, C: within plate alkalic basalt, D1: calc-alkaline basalt (Hf/Th<3), D2: island arc tholeiite (Hf/Th>3).	39
Fig. 4-7 Chondrite-normalized REE patterns (a, c) and primitive mantle-normalized trace elements multi-element variation diagram (b, d) for the granitic rocks and amphibolites from the Fuping Complex. The normalization values are from Sun and McDonough (1989).	40
Fig. 4-8 Representative CL images (a, c) of zircons and concordia plots (b, d) of the gneissic granite (FP-1-1) and gneissic syenogranite (FP-3). Scale bars are 100 μm.	41
Fig. 4-9 Representative CL images (a, c) of zircons and concordia plots (b, d) of the amphibolites (FP-9-2 and FP-17). Scale bars are 50 μm.	42
Fig. 4-10 Representative CL images (a, c) of zircons and concordia plots (b, d) of the epidote-biotite schist (FP-8) and mica schist (FP-18). Scale bars are 100 μm.	44
Fig. 4-11 Chondrite-normalized REE patterns of zircons in samples FP-1-1 (a), FP-3 (b), FP-9-2 (c), FP-17 (d), FP-8 (e) and FP-18 (f).	45
Fig. 4-12 ε _{Hf} (t) versus ²⁰⁷ Pb/ ²⁰⁶ Pb age diagram of zircons in various rock types from the Fuping Complex.	47
Fig. 4-13 Compiled zircon U-Pb ages. (A) Fuping, Wutai and Hengshan TTG gneisses (Data source: Guan et al., 2002; Zhao et al., 2002a, 2007, 2011; Kr öner et al., 2005b; Wilde et al., 2004, 2005; Lu et al., 2014b), (B) 2.1-2.0 Ga meta-granitic and meta-basaltic rocks in the TNCO (Data source from Table 4-6), (C) 2.1-2.0 Ga meta-granitic and meta-basaltic rocks from this study.	50
Fig. 4-14 Zircon U-Pb ages of 2.1-2.0 Ga granitic and meta-basaltic rocks within the	

TNCO (after [Zhao and Zhai, 2013](#)). Abbreviations: CD, Chengde; NH, Northern Hebei; XH, Xuanhua; HA, Huai'an; HS, Hengshan; WT, Wutai; FP, Fuping; LL, Lüliang; ZH, Zanhuang; ZT, Zhongtiao; DF, Dengfeng; TH, Taihua. HA, Huai'an. .51

Fig. 4-15 (A) Lithotectonic map of the Wutai-Fuping area (after [Trap et al., 2012](#)). (B) Proposed tectonic model showing the amalgamation of different complexes in the central domain of the TNCO during 2.1-2.0 Ga. (C) Model for tectonic evolution of the middle part of the TNCO during 2.1-2.0 Ga. Abbreviations: HS, Hengshan; WT, Wutai; FP, Fuping; ZH, Zanhuang; LL, Lüliang; HA, Huai'an.53

Fig. 5-1 Geological map of the Fuping Complex and the adjacent Wutai Complex (modified after [Zhao et al., 2000a](#)), showing major lithological units and sample locations.56

Fig. 5-2 Geological map of the Zanhuang Complex (modified after [Trap et al., 2009](#)), showing major lithological units and sample locations.57

Fig. 5-3 Representative field photographs of marbles and calc-silicates. (a) Dolomite-calcite marble (15FP-13-1) from the Fuping Complex; (b) Calc-silicate (15FP-07-2) from the Fuping Complex; (c) White dolomite-calcite marble (ZH-9) from the Zanhuang Complex; (d) Pinkish dolomite-calcite marble (ZH-10) intercalated with quartzite and mica-schist from the Zanhuang Complex.58

Fig. 5-4 Representative photomicrographs of marbles and calc-silicates. (a) Calc-silicate (15FP-07-2) from the Fuping Complex, showing mineral assemblage of calcite, dolomite, diopside and muscovite; (b) Calc-silicate (15FP-14-3) from the Fuping Complex, showing mineral assemblage of calcite, dolomite and olivine; (c) Dolomite-calcite marble (ZH-15-4) from the Zanhuang Complex, showing mineral assemblage of calcite, dolomite, muscovite and phlogopite; (d) Dolomite marble (ZH-19-1) from the Zanhuang Complex. Mineral abbreviations: Cal, calcite; Dol, dolomite; Di, diopside; Ol, olivine; Ms, muscovite; Phl, phlogopite.59

Fig. 5-5 Post-Archean Australian Shales (PAAS) normalized rare earth element patterns. (a) Calc-silicates and dolomite-calcite marbles from the Fuping Complex. (b) Dolomite-calcite marbles and dolomite marbles from the Zanhuang Complex. The normalization values of PAAS are from [McLennan \(1989\)](#).60

Fig. 5-6 Cathodoluminescence (CL) images of representative zircons in sample 15FP-07-2 (a), 15FP-08-2 (b), 15FP-13-1 (c) and ZH-9 (d), showing analytical positions, spot numbers and $^{207}\text{Pb}/^{206}\text{Pb}$ ages. Scale bars are in 50 μm	61
Fig. 5-7 Zircon U-Pb concordia plots and relative probability diagrams of $^{207}\text{Pb}/^{206}\text{Pb}$ ages for samples 15FP-07-2 (a-b) and 15FP-08-2 (c-d).	63
Fig. 5-8 Zircon U-Pb concordia plots and relative probability diagrams of $^{207}\text{Pb}/^{206}\text{Pb}$ ages for samples 15FP-13-1 (a-b) and ZH-9 (c-d).	64
Fig. 5-9 Scatter diagrams of $\delta^{13}\text{C}$ versus $\delta^{18}\text{O}$ values. LPMC: field of late Paleoproterozoic (2.0-1.8 Ga) marine carbonates (Veizer et al., 1992, Shield and Veizer, 2002).	65
Fig. 5-10 Cross plots of geochemical results and $\delta^{13}\text{C}$ values. (a) Mn versus $\delta^{13}\text{C}$ values, (b) Sr versus $\delta^{13}\text{C}$ values, (c) Mn/Sr ratios versus $\delta^{13}\text{C}$ values, (d) Mg/Ca ratios versus $\delta^{13}\text{C}$ values, (e) Ca/Sr ratios versus $\delta^{13}\text{C}$ values, (f) Fe/Sr ratios versus $\delta^{13}\text{C}$ values.	68
Fig. 5-11 Cross plots of geochemical results and $\delta^{18}\text{O}$ values. (a) Mn versus $\delta^{18}\text{O}$ values, (b) Sr versus $\delta^{18}\text{O}$ values, (c) Mn/Sr ratios versus $\delta^{18}\text{O}$ values, (d) Mg/Ca ratios versus $\delta^{18}\text{O}$ values, (e) Ca/Sr ratios versus $\delta^{18}\text{O}$ values, (f) Fe/Sr ratios versus $\delta^{18}\text{O}$ values.	68
Fig. 5-12 Zircon U-Pb age spectra of detrital zircons from the Fuping Complex and Zhanhuang Complex. (a) All available detrital zircon U-Pb ages of Wanzi Group in the Fuping Complex, data from Xia et al. (2006); Ren et al. (2013); Tang et al. (2015a) and this study. (b) Detrital zircon U-Pb age results (15FP-07-2, 15FP-08-2 and 15FP-13-1) of Fuping Complex in this study. (c) Available detrital zircon U-Pb ages of Gaotaohe Group in the Zhanhuang Complex, data from Liu et al. (2012a). (d) Detrital zircon U-Pb age results (ZH-9) of Central Zhanhuang Domain in this study. .	72
Fig. 5-13 $\delta^{13}\text{C}$ variation of meta-carbonate rocks through Paleoproterozoic, showing the $\delta^{13}\text{C}$ values through the globe (Karhu and Holland, 1996; Melezhik et al., 1999), Liaohu Group in the NCC (Tang et al., 2008) and this study.	74
Fig. 6-1 Geological map of the Fuping Complex and the adjacent Wutai Complex (modified after Zhao et al., 2000a).	79

Fig. 6-2 Field photographs of mafic granulite from the Fuping Complex. (a) Mafic granulite sample 15FP-02 occurs as enclave in the TTG gneiss. (b) Sample 15FP-02, showing mineral assemblage of garnet + clinopyroxene + orthopyroxene + plagioclase + quartz. (c) Sample 15FP-03, showing mafic granulite occurs as boudin and enclave in the migmatized TTG gneiss. (d) Sample 15FP-06, showing “white eye” texture in which coarse grained garnets are surrounded by plagioclase + amphibole/pyroxene coronas.80

Fig. 6-3 Representative photomicrographs of mafic granulites (15FP-02 and 15FP-03) from the Fuping Complex. (a) Sample 15FP-02, showing peak mineral assemblage of garnet + quartz + magnetite and plagioclase + amphibole + magnetite symplectite between garnet and quartz (plane polarized light). (b) Sample 15FP-02, showing peak mineral assemblage of garnet + clinopyroxene + orthopyroxene + plagioclase + quartz + K-feldspar (plane polarized light). (c) Sample 15FP-02, orthopyroxene + plagioclase symplectite around porphyroblastic garnet (plane polarized light). The red line is the location of the compositional profile shown in Fig. 6-5a. (d) Sample 15FP-02, showing peak mineral assemblage of garnet + amphibole + quartz + ilmenite and thin rim of quartz moat occurs around porphyroblastic garnet (plane polarized light). (e) Sample 15FP-03, the garnet porphyroblast contains few inclusions of quartz, clinopyroxene and ilmenite, biotite occur as fine-grained mineral in the matrix (plane polarized light). (f) Sample 15FP-03, showing peak mineral assemblage of garnet + amphibole + quartz + K-feldspar and amphibole + plagioclase symplectite around garnet (plane polarized light). (g) Sample 15FP-03, showing equilibrium peak mineral assemblage of garnet + clinopyroxene + plagioclase + quartz, and amphibole + plagioclase symplectite between garnet and quartz. The red line is the location of the compositional profile shown in Fig. 6-5b (plane polarized light). (h) Sample 15FP-03, plagioclase + clinopyroxene pseudomorph after porphyroblastic garnet (crossed polarized light). Scale bars are in 500 μm.82

Fig. 6-4 Representative photomicrographs of mafic granulites (15FP-06) from the Fuping Complex. (a) Peak mineral assemblage of garnet + clinopyroxene + plagioclase + quartz + ilmenite (plane polarized light). (b) Amphibole + plagioclase

corona around garnet (plane polarized light). (c) Plagioclase + clinopyroxene + orthopyroxene + amphibole symplectite between garnet and quartz, the red line is the location of the compositional profile shown in Fig. 6-5c (plane polarized light). (d) Quartz + K-feldspar + plagioclase moat occurs around porphyroblastic garnet (plane polarized light). (d) Quartz + K-feldspar + plagioclase moat occurs around porphyroblastic garnet (cross polarized light). Scale bars are in 500 μm83

Fig. 6-5 Compositional zoning profiles of the porphyroblastic garnets, showing the approximate boundaries of the core and rim of the grains.84

Fig. 6-6 Compositional diagrams of principal minerals in mafic granulites from the Fuping Complex. (a) Classification diagram of amphibole after [Leake et al. \(1997\)](#). (b) Al versus $\text{Mg}/(\text{Mg}+\text{Fe}^{2+})$ plot for clinopyroxene. (c) Al versus $\text{Mg}/(\text{Mg}+\text{Fe}^{2+})$ plot for orthopyroxene. (d) Ternary $X_{\text{An}}-X_{\text{Ab}}-X_{\text{Or}}$ diagram for plagioclase. PG, prograde stage; PK, peak stage; RG, retrograde stage.86

Fig. 6-7 Pseudosections for mafic granulite sample 15FP-02 calculated in the system NCKFMASHTO. (a) $P-M_{\text{H}_2\text{O}}$ diagram at 850 $^{\circ}\text{C}$. (b) $P-T$ pseudosection calculated at the adjusted H_2O content of 0.20 mol.%, the stable field for the peak phase assemblage is shown in blue color. (c) $P-M_{\text{H}_2\text{O}}$ diagram at 760 $^{\circ}\text{C}$. (d) $P-T$ pseudosection calculated at the adjusted H_2O content of 2.00 mol.%, the stable field for the retrograde phase assemblage is shown in yellow color. Mineral abbreviations: g, garnet; cpx, clinopyroxene; opx, orthopyroxene; hb, amphibole; pl, plagioclase; q, quartz; ksp, K-feldspar; bi, biotite; ilm, ilmenite; mt, magnetite; ru, rutile; liq, liquid. PK, peak stage; RG, retrograde stage.89

Fig. 6-8 Pseudosections for mafic granulite sample 15FP-03 calculated in the system NCKFMASHTO. (a) $T-M_{\text{H}_2\text{O}}$ diagram at 11 kbar. (b) $P-T$ pseudosection calculated at the adjusted H_2O content of 1.00 mol.%, the stable field for the peak phase assemblage is shown in blue color. (c) $P-M_{\text{H}_2\text{O}}$ diagram at 780 $^{\circ}\text{C}$. (d) $P-T$ pseudosection calculated at the adjusted H_2O content of 3.50 mol.%, the stable field for the retrograde phase assemblage is shown in yellow color. The pseudosections are contoured with compositional isopleths of garnet ($z_g = \text{Ca}/(\text{Ca} + \text{Mg} + \text{Fe}^{2+})$). Abbreviations are the same with Fig. 6-7.91

Fig. 6-9 Pseudosections for mafic granulite sample 15FP-06 calculated in the system NCKFMASHTO. (a) $T-M_{H_2O}$ diagram at 10 kbar. (b) $P-T$ pseudosection calculated at the adjusted H_2O content of 1.50 mol.%, the stable field for the peak phase assemblage is shown in blue color. (c) $P-M_{H_2O}$ diagram at 800 °C. (d) $P-T$ pseudosection calculated at the adjusted H_2O content of 2.00 mol.%, the field for the retrograde phase assemblage is shown in yellow color. The pseudosection is contoured with compositional isopleths of garnet ($z_g = Ca/(Ca + Mg + Fe^{2+})$). Abbreviations are the same with Fig. 6-7.92

Fig. 6-10 Representative CL images (a) of zircons and concordia plots (b) of the mafic granulite sample 15FP-02.95

Fig. 6-11 Representative CL images (a) of zircons and concordia plots (b) of the mafic granulite sample 15FP-03.96

Fig. 6-12 Representative CL images (a) of zircons and concordia plots (b) of the mafic granulite sample 15FP-06.96

Fig. 6-13 Metamorphic P-T paths of high- and medium-pressure granulites from the TNCO. The P-T paths are shown: 1, Fuping Complex (Zhao et al., 2000a); 2, Fuping Complex (Liu, 1996); 3, Hengshan Complex (Zhao et al., 2000b); 4-5, Hengshan Complex (Zhao et al., 2001b); 6, Hengshan Complex (Guo et al., 1999); 7, Hengshan Complex (O'Brien et al., 2005); 8-9, Xuanhua-Huai'an (Guo et al., 2002); 10, Xuanhua-Huai'an (Zhai et al., 1992); 11, Xuanhua-Chicheng (Zhang et al., 2016b); 12, Chengde Complex (Zhang et al., 2006); 13, sample 15FP-02; 14, sample 15FP-03; 15, sample 15FP-06. P-T grid is after O'Brien and Rötzler (2003).99

Fig. 6-14 Metamorphic ages of various rock types within the TNCO (after Zhao and Zhai, 2013). Abbreviations: CD, Chengde; NH, Northern Hebei; XH, Xuanhua; HA, Huai'an; HS, Hengshan; WT, Wutai; FP, Fuping; LL, Lüliang; ZH, Zanhuang; ZT, Zhongtiao; DF, Dengfeng; TH, Taihua.101

Fig. 6-15 Metamorphic zircon U-Pb age spectra and relative probability plots of various rock types within the TNCO. Data from references are shown in Fig. 6-14.103

Fig. 7-1 Chondrite-normalized REE diagrams and primitive mantle-normalized trace element spider diagrams for meta-basalts from the Yanlingguan GGB (a-b, data

source: Polat et al., 2006; Wang et al., 2013b), the Western Shandong GGB (c-d, data source: Peng et al., 2013a), the Wutai GGB (e-f, data source: Wang et al., 2004, 2014a; Polat et al., 2005) and the Dengfeng GGB (g-h, data source: Diwu et al., 2011; Deng et al., 2016).107

Fig. 7-2 Chondrite-normalized REE diagrams and primitive mantle-normalized trace element spider diagrams for meta-basalts from the Zunhua GGB (a-b, data source: Guo et al., 2013), the Dongwufenzi GGB (c-d, data source: Liu et al., 2014c), the Hongtoushan-Qingyuan-Helong GGB (e-f, data source: Guo et al., 2015b, 2016; Peng et al., 2015) and the Yixian-Fuxin GGB (g-h, data source: Wang et al., 2011, 2015).....108

Fig. 7-3 (a) Nb/Yb vs. Th/Yb diagram (Pearce, 2008). (b) La/10-Y/15-Nb/8 triangular diagram, 1A: calc-alkali basalt; 1C: volcanic-arc tholeiite; 1B: overlapped field of 1A and 1C; 2A: continental basalt; 2B: back-arc basin basalt; 3A: alkalic basalt from intercontinental rift; 3B: enriched E-type MORB; 3C: weakly enriched E-type MORB; 3D: N-type MORB (Cabanis and Lecolle, 1989). Data sources are same with those in Figs. 7-1 and 7-2. 109

Fig. 7-4 Age distribution of granitoid rocks, meta-basalts, BIFs and sulfide ores from representative GGB of the NCC. Data sources are shown in Table 7-1. 110

List of Tables

Table 3-1 Details of samples from the Fuping TTG gneiss and Yangmuqiao mafic-ultramafic intrusion.	154
Table 3-2 EMPA data of hornblende.	154
Table 3-3 EMPA data of clinopyroxene.	159
Table 3-4 EMPA data of biotite and titanite.	164
Table 3-5 Whole-rock major, trace and platinum-group elements (PGE) data.	166
Table 3-6 Zircon U-Pb analytical data.	170
Table 3-7 LA-MC-ICP-MS Lu-Hf isotopic data.	174
Table 3-8 Zircon oxygen isotopic data.	175
Table 4-1 Details of samples from the Fuping Complex used for this study.	176
Table 4-2 Major, trace and rare earth element concentrations of the whole-rock samples from the Fuping Complex.	178
Table 4-3 Zircon U-Pb analytical data.	181
Table 4-4 Rare earth element concentrations for zircons of the rock samples from the Fuping Complex.	190
Table 4-5 LA-MC-ICP-MS Lu-Hf isotope data on zircons from the rock samples of the Fuping Complex.	200
Table 4-6 Compilation of 2.1-2.0 Ga age data from the TNCO.	202
Table 5-1 Details of samples from the Fuping Complex and Zanhuang Complex. ..	204
Table 5-2 Major and trace element compositions for samples from the Fuping Complex and Zanhuang Complex.	206
Table 5-3 Zircon U-Pb analytical data.	209
Table 5-4 Carbon and Oxygen isotopic compositions for samples in this study.	214
Table 6-1 Bulk rock compositions (wt.%) of mafic granulites from the Fuping Complex.	215
Table 6-2. EPMA data of garnet.	215
Table 6-3 EMPA data of amphibole.	225
Table 6-4 EMPA data of plagioclase.	228

Table 6-5 EMPA data of clinopyroxene.	231
Table 6-6 EMPA data of ilmenite and magnetite.	234
Table 6-7 EMPA data of K-feldspar and biotite.	235
Table 6-8 Calculated P–T conditions for the peak mineral assemblage.	237
Table 6-9 Zircon U-Pb analytical data.	238
Table 7-1 Compilation of age data from representative GGBs of the NCC.	243

Chapter 1: General introduction

1.1 Research background and controversies

The NCC is one of the major ancient cratonic nuclei in eastern Eurasia which is bordered by the Qinling-Dabie orogenic belt to the south-west, Central Asian Orogenic Belt to the north and Sulu orogen to the east (Fig. 1-1) (Zhao et al., 2001a). The NCC records the early Precambrian crustal growth history and the formation of the Columbia supercontinent during Paleoproterozoic, thus attracting wide attention (e.g. Zhao et al., 2001a; 2005, 2012; Zhai et al., 2005; Wan et al., 2006, 2012; Wang, 2009; Zhang et al., 2009, 2012; Zhai and Santosh, 2011; Zhai, 2011, 2014; Tsunogae et al., 2011; Geng et al., 2012; Liu et al., 2012a, 2016; Trap et al., 2012; Zhao and Zhai, 2013; Nutman et al., 2014; Wei et al., 2014; Santosh et al., 2015, 2016; Du et al., 2016; Zhang et al., 2016a).

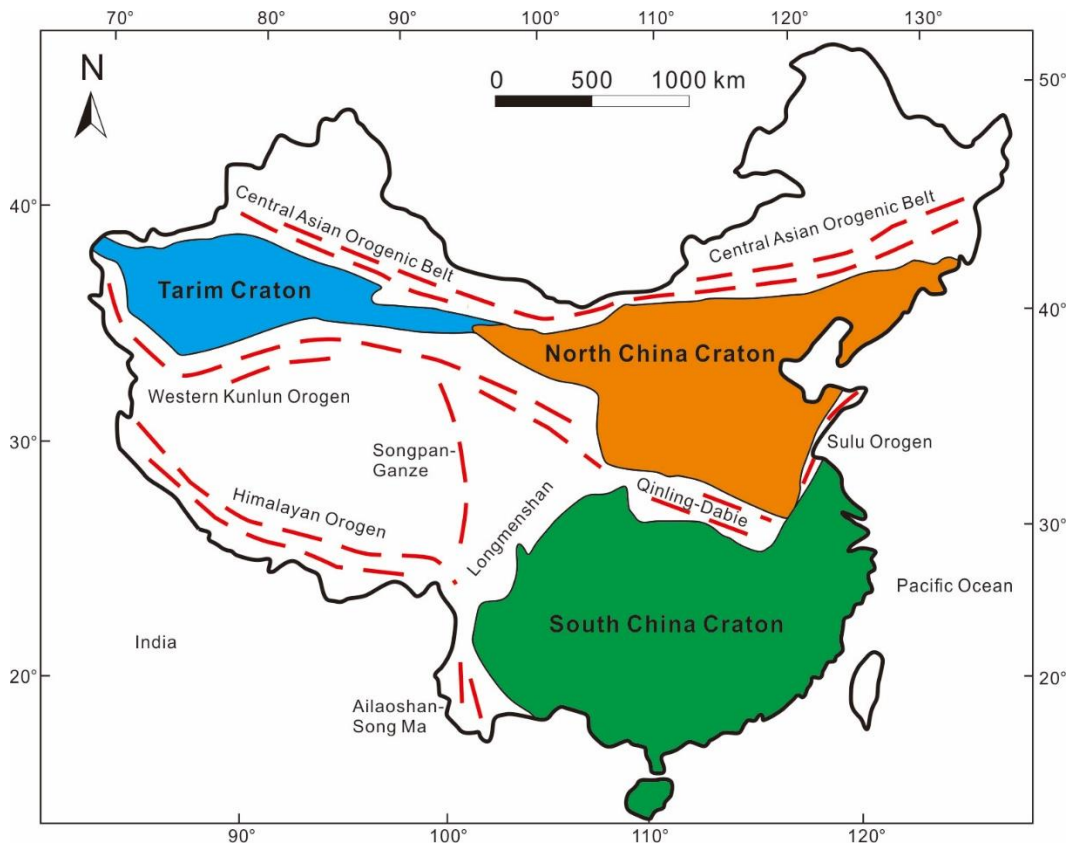


Fig. 1-1 Tectonic map of China showing the major cratons and younger orogens (Zhao et al., 2001a).

Two diverse models have been proposed for the tectonic framework of the NCC: (i) the Neoproterozoic micro-block amalgamation model (e.g. [Zhai and Santosh, 2011](#); [Santosh et al., 2016](#); [Yang et al., 2016](#)), and ii) the Paleoproterozoic continent–continent collision model (e.g. [Zhao et al., 2001a, 2005, 2012](#); [Trap et al., 2012](#)).

In the first model, the NCC is considered to be amalgamated by seven microblocks represented by a number of small Archean nuclei along several granite-greenstone belts. [Wu et al. \(1998\)](#) proposed that the NCC comprises five microblocks including the Jiaoliao, Qianhuai, Jinji, Yuwan and Mongshan Blocks, among which the Jiaoliao and Qianhuai Blocks assembled at ~2.5 Ga. [Zhang et al. \(1998\)](#) suggested that the NCC can be divided into fifteen microblocks/terranes. [Zhai et al. \(2000\)](#) divided the NCC into six microblocks (Alashan, Jining, Fuping, Jiaoliao, Xuchang and Qianhuai Blocks) which were amalgamated together at the late Neoproterozoic. In recent studies, an alternate model was proposed that the Archean tectonic framework of the NCC was built through the amalgamation of seven microblocks, named the Jiaoliao Block (JL), Qianhuai Block (QH), Ordos Block (OR), Jining Block (JN), Xuchang Block (XCH), Xuhuai Block (XH) and Alashan Block (ALS) ([Zhai and Santosh, 2011](#); [Yang et al., 2016](#); [Santosh et al., 2016](#); [Tang et al., 2016a](#)). These microblocks were welded by 2.6–2.75 Ga and ~2.5 Ga along zones of ocean closure now represented by Neoproterozoic granite-greenstone belts (Fig. 1-2). Eight representative granite-greenstone belts have been recognized which carry remnants of oceanic crust and the vestiges of arc-continent collision, such as Yanlingguan, Western Shandong, Wutai, Dengfeng, Zunhua, Dongwufenzi, Hongtoushan-Qingyuan-Helong and Yixian-Fuxin granite-greenstone belts ([Tang et al., 2017a](#), and references therein).

In the second model, Paleoproterozoic continent-continent collisional belts have been identified that subdivide the NCC into two or three major crustal blocks (e.g. [Zhao et al., 2001a, 2005, 2012](#); [Kusky and Li, 2003](#); [Zhang et al., 2006](#); [Kusky et al., 2007](#); [Zhai and Peng, 2007](#)). [Zhao et al. \(2001a, 2005\)](#) identified three Paleoproterozoic orogenic belts (Trans-North China Orogen, Jiao-Liao-Ji Belt and Khondalite Belt), of which the Trans-North China Orogen (TNCO) divides the NCC

into the Western and Eastern blocks (Fig. 1-3), the Jiao-Liao-Ji Belt further subdivides the Eastern Block into the Langrim Block in the south and the Longgang Block (or Yanliao Block; Santosh, 2010) in the north, the Khondalite Belt (or Inner Mongolia Suture Zone; Santosh, 2010) further subdivides the Western Block into the Ordos Block and the Yinshan Block (Fig. 1-3). Zhai and Peng (2007) also proposed three Paleoproterozoic tectonic belts termed as the Jinyu, Fengzhen and Liaoji orogenic belts in the western, central and eastern parts of the NCC, respectively, which are partly coincident with the TNCO, Khondalite Belt and Jiao-Liao-Ji Belt. Kusky and Li (2003) suggested an alternative Central Orogenic Belt marking the collisional boundary between the Western and Eastern Blocks. Kusky et al. (2007) proposed that the NCC was incorporated into the Columbia (Nuna) supercontinent during 1.85-1.92 Ga along the Inner Mongolia–Northern Hebei Orogen at the northern margin of the craton.

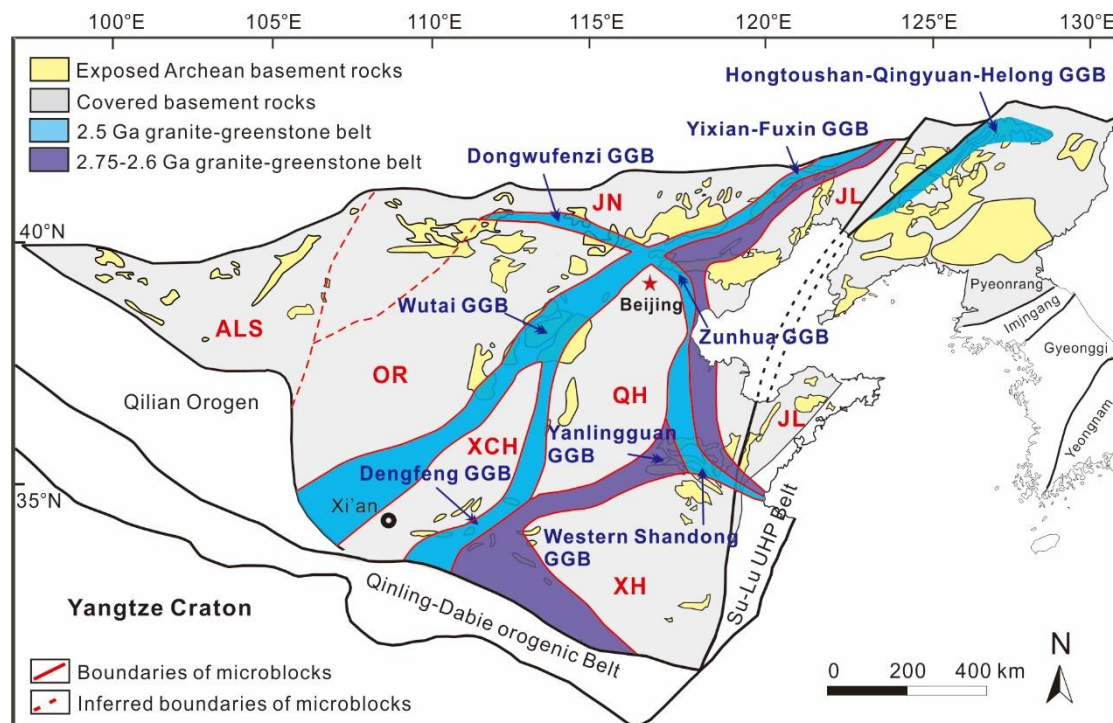


Fig. 1-2 Updated subdivision of the North China Craton (modified after Zhai and Santosh, 2011; Zhao and Zhai, 2013) showing the major microblocks, granite-greenstone belts and Neoproterozoic basement rocks. Abbreviations: GGB, granite-greenstone belt; JL, Jiaoliao Block; QH, Qianhuai Block; OR, Ordos Block; JN, Jining Block; XCH, Xuchang Block; XH, Xuhuai Block; ALS, Alashan Block.

The NCC experienced a complex tectonic evolution history during the Neoproterozoic-Paleoproterozoic. Especially the tectonic models and processes for the formation of the NCC along the TNCO are hotly debated. 1) The TNCO represents a long-lived magmatic arc developed during the east-ward subduction beneath the Eastern Block during 2.56-1.88 Ga (Zhao et al., 2001a, 2005, 2012; Zhang et al., 2007, 2009, 2012); 2) The TNCO was formed by two stages of Paleoproterozoic west-ward subduction-collision events at ~2.1 Ga and 1.9-1.8 Ga, and there existed a Fuping micro-Block between the Western and Eastern Blocks (Faure et al., 2007; Trap et al., 2007, 2008, 2012); 3) The Central Orogenic Belt, which is equivalent to the TNCO, was formed by Neoproterozoic (~2.5 Ga) or 2.3-2.2 Ga assembly of the NCC through continent-arc-continent collision (Kusky and Li, 2003; Li and Kusky, 2007); 4) The tectonic evolution of the TNCO is characterized by subduction-accretion processes and the development of arc-backarc basin systems through multiple subduction process during Neoproterozoic-Paleoproterozoic and collision at ca. 1.85 Ga (Wang, 2009; Wang et al., 2010a); 5) The TNCO was formed simultaneously with the Inner Mongolia Suture Zone through double-side subduction process with an oblique east-to south-ward subduction of the Yinshan Block and a west-ward subduction of the Yanliao Block (Eastern Block) during Paleoproterozoic, and the collision between the Western and Eastern Blocks occurred at 2.0-1.9 Ga (Santosh, 2010; Zhang et al., 2016a; Tang et al., 2017b). The controversies and debates in the above models mainly surround the following five aspects: 1) the age of the final collision along the TNCO (2.5 Ga, 2.3 Ga, 2.0-1.9 Ga, or 1.9-1.8 Ga?); 2) the polarity of subduction along the TNCO is west-ward or east-ward; 3) the ocean between the Western and Eastern Blocks is a unified ocean, several oceans or an ocean-back arc basin system; 4) does the Fuping micro-Block exist? 5) the Paleoproterozoic evolution history along the TNCO remain unclear.

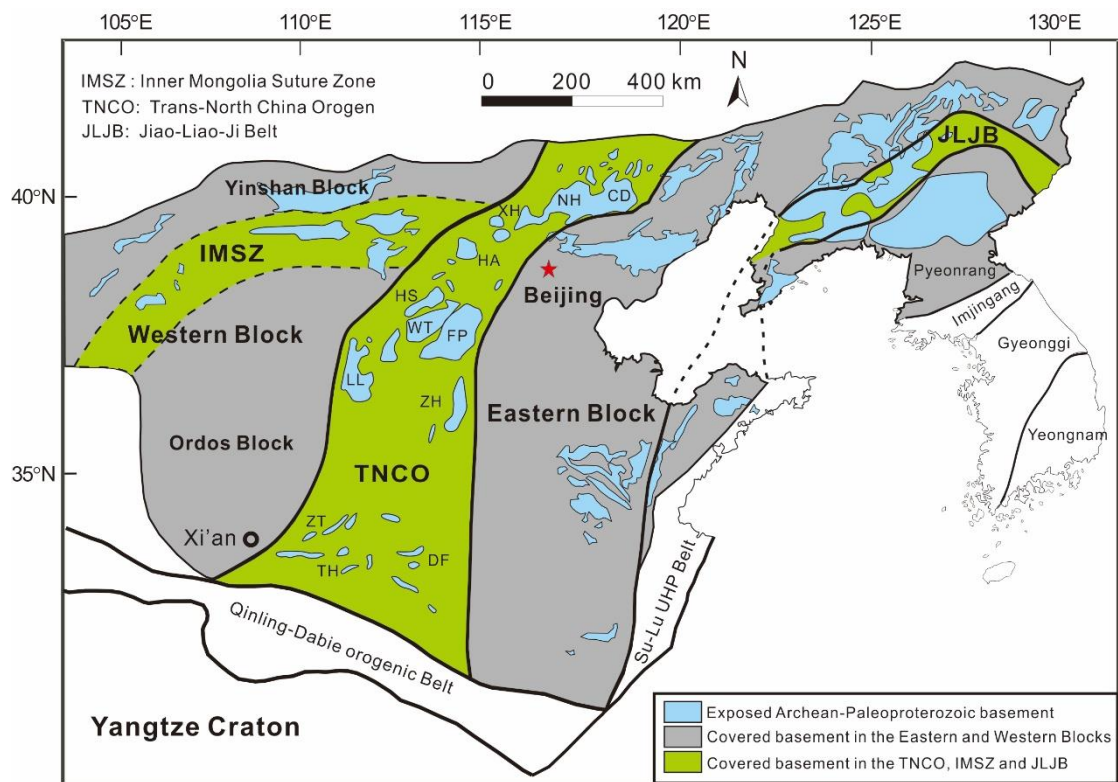


Fig. 1-3 Tectonic subdivision of the North China Craton (modified after Zhao et al., 2005). Abbreviations of metamorphic complexes: CD, Chengde; NH, Northern Hebei; XH, Xuanhua; HA, Huai'an; HS, Hengshan; WT, Wutai; FP, Fuping; LL, Lüliang; ZH, Zanhuang; ZT, Zhongtiao; DF, Dengfeng; TH, Taihua; WB, Western Block; EB, Eastern Block.

1.2 Research objectives

In order to address the existing controversies and debates, in this study, the Fuping Complex was chosen as the research area. The Fuping Complex is a typical basement terrane in the central segment of the TNCO, and it incorporates various rock types. Multidisciplinary investigations were carried including field studies, petrology, mineral chemistry, whole rock geochemistry, P-T pseudosection modelling, zircon U-Pb geochronology, zircon Hf-O isotopes and C-O isotopes on different rock types from the Fuping Complex, with several research objectives as summarized below:

1. Based on mineral chemistry and whole rock geochemistry, to study the genesis and tectonic setting of the granitoid rocks, amphibolites, hornblendites and pyroxene hornblendites.
2. Based on LA-ICP-MS zircon U-Pb geochronological study and CL imaging,

to date the magmatic, metamorphic and detrital zircon ages of the granitoid rocks, amphibolites, hornblendites, pyroxene hornblendites, paragneisses, schists, calc-silicate rocks and mafic granulites.

3. Based on zircon Lu-Hf and oxygen isotopic study, to discuss the magma sources and evolution.

4. Based on whole rock geochemistry and calcite C-O isotopic study, to reveal the depositional environment of the calc-silicate rocks and marbles.

5. Based on petrology and metamorphic P-T estimation (conventional study and pseudosection modelling), to identify different metamorphic stages and constrain the corresponding P-T conditions.

6. Based on comparison of geochemical, geochronological and metamorphic results of the present study with available data from the TNCO, to propose a comprehensive tectonic model for the formation and evolution of the Fuping Complex and the TNCO.

Chapter 2: Regional geology

2.1 North China Craton

The NCC occupies over 300,000 square kilometers, and is mainly composed of Archean to Paleoproterozoic metamorphic basement and Mesoproterozoic to Cenozoic cover sequences (e.g. Zhai and Santosh, 2011; Zhao et al., 2001a, 2005, 2012; Zhao and Zhai, 2013; Nutman et al., 2014; Zhai, 2014). Archean basement rocks are widely distributed in many areas of the NCC (Fig. 1-2), including Eoarchean (3.85–3.6 Ga, Liu et al., 1992; Nutman et al., 2011), Paleo-Mesoarchean (3.6–2.8 Ga, Jahn et al., 2008) and Neoarchean (2.8–2.5 Ga, Wan et al., 2012) trondhjemitic–tonalitic–granodioritic (TTG) gneisses, amphibolites, paragneisses, quartzites, banded iron formations (BIF) and leptynites. Up to date, the Eoarchean (3.85–3.6 Ga) and Paleo-Mesoarchean (3.6–2.8 Ga) rocks have only been reported in the Eastern Hebei and Anshan areas in the Eastern Block of the NCC (e.g. Liu et al., 1992; Jahn et al., 2008; Nutman et al., 2011). Neoarchean rocks make up more than 85% of Precambrian basements of the NCC, implying the major crustal growth of the NCC has occurred during Neoarchean (Geng et al., 2012). Base on zircon U-Pb geochronology, Lu-Hf isotope, and whole rock Nd isotope results, the Neoarchean rocks within the NCC show two age groups at 2.8–2.7 Ga and 2.6–2.5 Ga, of which the older age group is considered as the result of juvenile crustal growth and the younger one represents the period of reworking event (Wu et al., 2005; Geng et al., 2012).

The Eastern Block includes the Archean basements (high-grade rocks and low-grade granites-greenstones) and the Paleoproterozoic Jiao-Liao-Ji Belt. The block is mainly covered by Neoarchean rocks such as TTG gneisses, supracrustal rocks, greenstones, charnockites and syenogranites, and minor Eoarchean to Mesoarchean rocks exposed in the Anshan and Eastern Hebei areas (Liu et al., 1992; Jahn et al., 2008). The late Neoarchean (2.55–2.50 Ga) TTG gneisses make up more than 80% of the basement of the Eastern Block, and are considered to have derived

from the partial melting of 2.7–2.8 Ga juvenile mafic crust (Wu et al., 2005; Peng et al., 2012b). The Neoproterozoic supracrustal rocks are composed of meta-sedimentary and bimodal volcanic rocks metamorphosed from greenschist- to granulite-facies, and the latter contain ultramafic rocks with komatiitic affinity (Polat et al., 2006; Wang et al., 2013b). Furthermore, the supracrustal rocks also contain Algoma-type banded iron formations (BIF, Zhang et al., 2016c). The Neoproterozoic metamorphic rocks in the Eastern Block have experienced the ~2.5 Ga regional metamorphism which is featured by anticlockwise P–T paths involving isobaric cooling (Zhao et al., 1999; Nutman et al., 2011). The Jiao-Liao-Ji Belt comprises mainly of the Liaoji granites, alkaline syenites and rapakivi granites and greenschist- to lower amphibolite-facies meta-sedimentary and volcanic rocks (Li et al., 2004, 2006; Li and Zhao, 2007). Available geochronological data show that most meta-sedimentary and volcanic rocks and gneissic granites in the Jiao-Liao-Ji Belt have been formed during 2.2–2.0 Ga and metamorphosed at ~1.9 Ga, whereas the rapakivi granites and alkaline syenites were crystallized at ~1.86 Ga (Luo et al., 2004; Lu et al., 2006).

The Western Block includes the Ordos Block in the south, the Yinshan Block in the north and the Inner Mongolia Suture Zone (Fig. 1-3). The Yinshan Block is dominantly composed of Neoproterozoic TTG gneisses and minor supracrustal rocks which have experienced ~2.5 Ga greenschist- to granulite-facies metamorphism (Jian et al., 2012). The Ordos Block is entirely covered by Mesozoic to Cenozoic sedimentary rocks, but available drill holes and aeromagnetic data suggest the existence of granulite facies basement beneath the overlying Ordos Basin (Wu et al., 1986). He et al. (2016) reported peak metamorphic conditions of 7–9 kbar and 775–825 °C for three cordierite-bearing metapelites from deep drill cores in the Ordos Block which underwent granulite-facies metamorphism involving clockwise P–T path during 1930–1940 Ma. The Inner Mongolia Suture Zone (also called the Khondalite Belt) is a nearly east-west trending orogenic belt between the Ordos Block and Yinshan Block. The Inner Mongolia Suture Zone is represented by high-pressure (HP) pelitic granulites and ultra-high temperature (UHT) Mg-Al granulites, formed during the continent-continent collision between the Yinshan and Ordos Block at ca.

1.95-1.92 Ga (e.g. Zhao et al., 2005; Santosh et al., 2007a, 2007b, 2008, 2012).

2.2 Trans-North China Orogen

The TNCO is a nearly north-south trending orogen across the central part of the NCC (Fig. 1-3). This Paleoproterozoic collisional orogen incorporates several fragments of basement terranes which include Chengde, Northern Hebei, Xuanhua, Huai'an, Hengshan, Wutai, Fuping, Lüliang, Zanhuang, Zhongtiao, Dengfeng and Taihua Complexes from the north to south (Fig. 1-3). The basement rocks comprise Neoarchean to Paleoproterozoic tonalite-trondhjemite-granodiorite (TTG) gneisses, meta-supracrustal rocks, syn- to post-tectonic granitoids, mafic dykes, and ultramafic to mafic rocks (Wang et al., 1996; Wei et al., 2014). Geochemical data suggest that the TTG gneisses formed in continental magmatic arc-, island arc- or back-arc basin environments (Sun et al., 1992; Liu et al., 2004, 2005). The low-grade supracrustal successions in the Lüliang, Wutai, Zanhuang and Zhongtiao Complexes have been regarded as foreland basins (Trap et al., 2007; Liu et al., 2014a, 2014b). The ultramafic to mafic rocks (e.g. Jingangku Formation of the Wutai Complex) have been interpreted as the fragments of ancient oceanic crust (Wang et al., 1996). The occurrence of linear structural belts (Trap et al., 2007; Zhang et al., 2007, 2012), high pressure granulites and retrograde eclogites in the Hengshan, Huai'an, Xuanhua and Chengde Complexes (Guo et al., 2002, 2005), the clockwise metamorphic P-T paths involving near isothermal decompression (Zhao et al., 1999, 2000b, 2001b; Xiao et al., 2011) and widespread metamorphic ages in the range of 1.95-1.80 Ga (Zhao et al., 2012 and references there in) constrain the TNCO as the collisional suture between the Eastern and Western Blocks.

2.3 Fuping Complex

The Fuping Complex (FPC) comprises four major rock units: Fuping TTG gneisses, Longquanguan augen gneisses, Wanzi supracrustals and Nanying gneissic granites (Fig. 2-1).

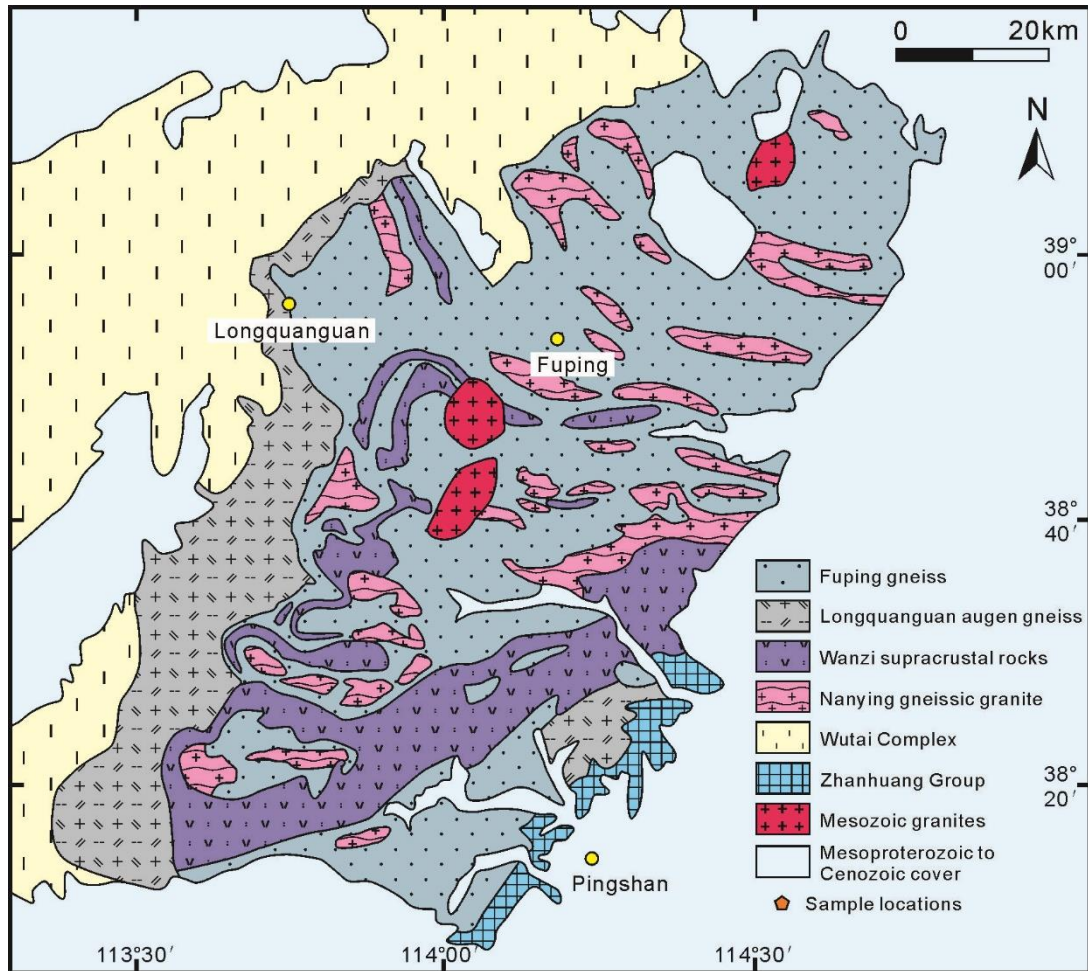


Fig. 2-1 Geological map of the Fuping Complex (modified after Zhao et al., 2002a).

The TTG gneisses make up >60% of the exposure of the complex and are mainly composed of medium-grained tonalitic, trondhjemitic, granodioritic and dioritic gneisses, which carry enclaves of mafic granulites and amphibolites (Zhao et al., 2000a, 2007). Zircon U-Pb age data reveal that the protoliths of the Fuping TTG gneisses were emplaced during 2.48-2.52 Ga (Guan et al., 2002; Zhao et al., 2002a; Tang et al., 2016a). The Fuping TTG gneisses were proposed to have derived from the partial melting of mantle-derived basaltic rocks based on petrological and geochemical evidences (Wang et al., 1991). The Longquanguan augen gneisses are emplaced along the Longquanguan ductile shear zone in the western part of the FPC and with crystallization at ~2.54 Ga based on SHRIMP U-Pb zircon data (Wilde et al., 1997). The Longquanguan augen gneisses include supracrustal units of the Maheqing Formation, which experienced polyphase deformation and are represented by leptynite, leptite, minor amphibolite, marble and calc-silicate (Cheng et al., 2004).

The Longquanguan augen gneisses show tectonic contact with the Fuping gneisses and the Wanzi supracrustal assemblage (Zhao et al., 2002a). The Wanzi supracrustal assemblage forms a 100 km long and 15 km wide NE–SW-trending extensively folded belt in the southern part and swings northward to the central part of the complex (Zhao et al., 2002a). The Wanzi supracrustal assemblages are metamorphosed to amphibolite facies and represented by felsic- and pelitic-gneisses, pelitic schists, calc-silicates, marbles, amphibolites and minor pelitic granulites (Xia et al., 2006; Ren et al., 2013). The Nanying gneissic granites occur as younger intrusions (2.10-2.02 Ga) only within the Fuping TTG gneisses, and are mainly composed of fine- to medium-grained, weakly-foliated and gneissic monzogranite, granodiorite and granite. The Nanying gneissic granites are clearly intrusive into the Fuping TTG gneisses with consistent foliation, implying that they experienced the same deformational event (Zhao et al., 2002a).

Chapter 3: Neoproterozoic evolution of the Fuping Complex

3.1 Introduction

The late Neoproterozoic is an important period of continental growth to build the modern earth (e.g. Puchtel et al., 1999; Polat et al., 2005; Zhai et al., 2005; Shan et al., 2015). The subduction-accretion related island-arc magmatism in ancient terranes provides crucial insights into the horizontal growth of the continental crust (e.g. Windley and Garde, 2009; Samuel et al., 2014; Spencer et al., 2015).

The NCC experienced a complex evolutionary history of multi-stage crustal growth during the early Precambrian (Zhai, 2014; Wang and Liu, 2012), and the ca. 2.5 Ga tectonothermal event is widely preserved in various rock types in different parts of the craton (e.g. Kröner et al., 2005a; Wilde et al., 2005; Geng et al., 2006, 2012; Diwu et al., 2011; Liu et al., 2012b; Wan et al., 2012; Wang et al., 2015). The Fuping-Wutai-Hengshan Complexes constitute important part of the Neoproterozoic-Paleoproterozoic basement of the NCC, with major imprints of late Neoproterozoic magmatism (Wilde et al., 1997, 2005; Guan et al., 2002; Zhao et al., 2002a; Kröner et al., 2005a; Han et al., 2012). However, the tectonic models related to the late Neoproterozoic magmatism in these complexes remain debated and various views have been proposed as follows. (1) Zhai and Santosh (2011) emphasized a microblock model involving the amalgamation of seven ancient microblocks with closure of the intervening oceans represented by granite-greenstone belts. Among these, the Wutai greenstone belt represents the suture between the Ordos (OR) and the Qianhuai (QH) Blocks. (2) The Fuping-Wutai-Hengshan Complexes were once part of the long-lived continental magmatic arc developed by eastward subduction of an ancient ocean during 2.56-1.88 Ga (Kröner et al., 2005b; Zhao et al., 2005, 2007; Zhang et al., 2009, 2012). (3) The collision of the Western and Eastern Blocks in the NCC occurred along the Central Orogenic belt (Trans-North China Orogen; TNCO) to form a coherent craton at ~2.5 Ga (Kusky and Li, 2003; Polat et al., 2005). (4)

An arc-back arc basin systems existed in the TNCO with multiple stages of rift and subduction process during 2.56-2.47 Ga (Wang, 2009; Wang et al., 2004).

One of the key issues surrounding the various models above relate to the tectonic setting of the late Neoproterozoic magmatic rocks in the Fuping-Wutai-Hengshan Complexes. This study provides systematic petrology, mineral chemistry, whole rock major, trace and platinum-group element geochemistry, zircon U-Pb geochronology and Hf-O isotopes from the Yangmuqiao mafic-ultramafic intrusion and the coeval TTG gneiss in the Fuping Complex. This study also discusses petrogenesis, and proposes late Neoproterozoic subduction-accretion related arc magmatism in this region.

3.2 Sample description

3.2.1 Hornblendites

Two hornblende samples were collected from the Yangmuqiao mafic-ultramafic intrusion (FP-24, FP-25-2) (Fig. 3-1, 3-2, Table 3-1). Sample FP-24 is coarse grained and dark greenish, and is mainly composed of hornblende (90-95%), plagioclase (2-3%) and biotite (2-3%) (Fig. 3-3a). The hornblende crystals are mainly coarse grained (1-5 mm) with a minor population of medium grained (50-200 μm) ones. The coarse grained hornblendes are subhedral to euhedral, dark brown to light green with strong pleochroism. The medium grained hornblendes are anhedral and occur as matrix assemblage. The plagioclase laths are anhedral, medium to fine grained and occur as inclusions in the hornblende or in the matrix between the coarse grained hornblende. The biotite laths are euhedral and occur as poikilitic crystals.

Sample FP-25 is from an intrusive contact with biotite gneiss and is a medium grained, greenish hornblende (Fig. 3-2c). The dominant mineral is hornblende (~95%) which occurs as subhedral to euhedral crystals with grain size in the range of 100-300 μm and shows weak orientation. Few hornblende grains contain rare plagioclase inclusions.

3.2.2 Pyroxene hornblendites

Two pyroxene hornblende samples were collected from the Yangmuqiao

mafic-ultramafic intrusion (FP-28 and FP-29-1). The rocks are massive and dark colored with no visible deformation. They display clear cumulate texture (Fig. 3-3b, 3-3c), with the cumulate crystals composed of hornblende and pyroxene. Three types of hornblende (75-85 %) are recognized in the pyroxene hornblendites, 1) as euhedral phenocrystic minerals, 2) as medium to fine grained inclusions in the hornblende, 3) as medium to fine grained, subhedral to anhedral hornblende in the matrix. Minor chlorite (1-3 %) occurs as alteration products of these hornblendes. The pyroxenes (10-20 %) occur as euhedral grains, or inclusions in hornblende crystals (Fig. 3-3b). Chromites are common as accessory minerals and mainly occur as inclusions in hornblende (Fig. 3-3c). Minor biotite (1-2 %) occurs as inclusion in the hornblende.

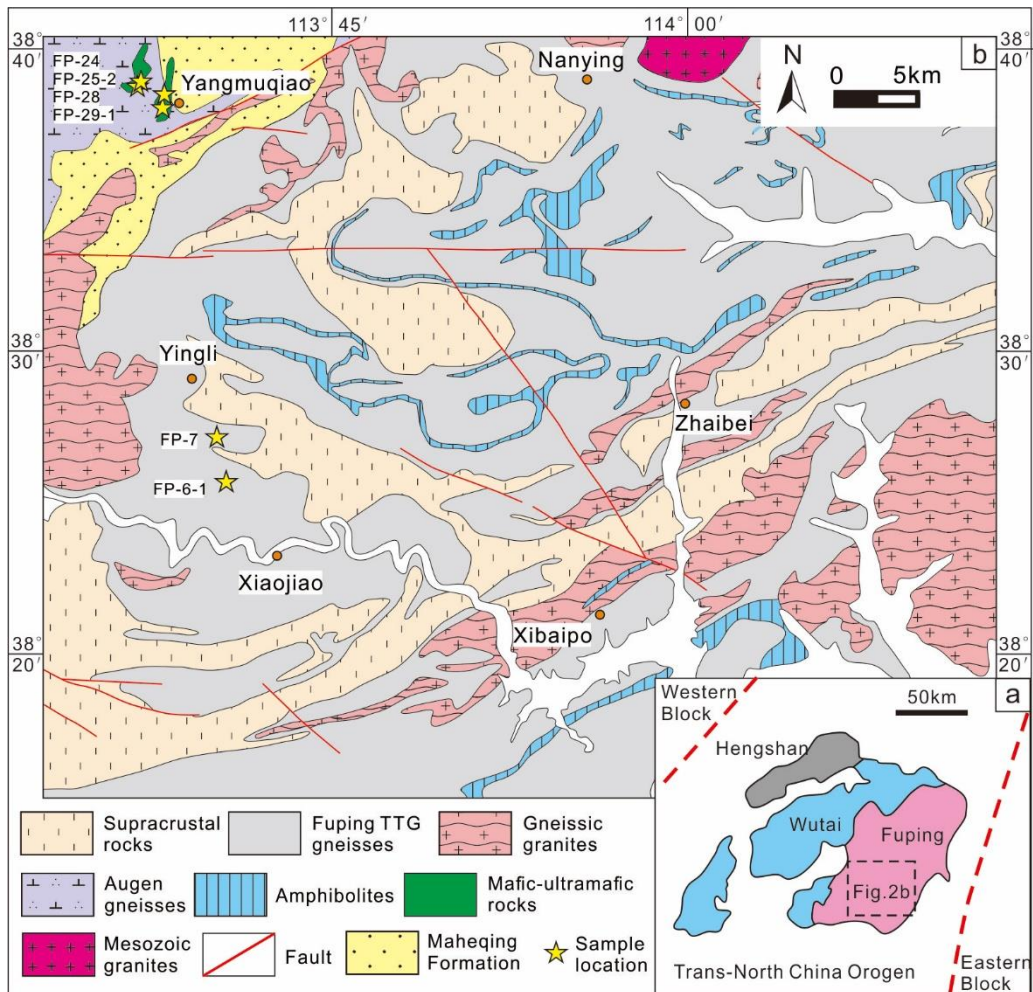


Fig. 3-1 (a) Geological sketch map of the Hengshan-Wutai-Fuping Complexes. (b) Geological map of the Fuping Complex within the Trans-North China Orogen (modified after Cheng et al., 2004), showing major lithological units, their relationships and sampling locations.

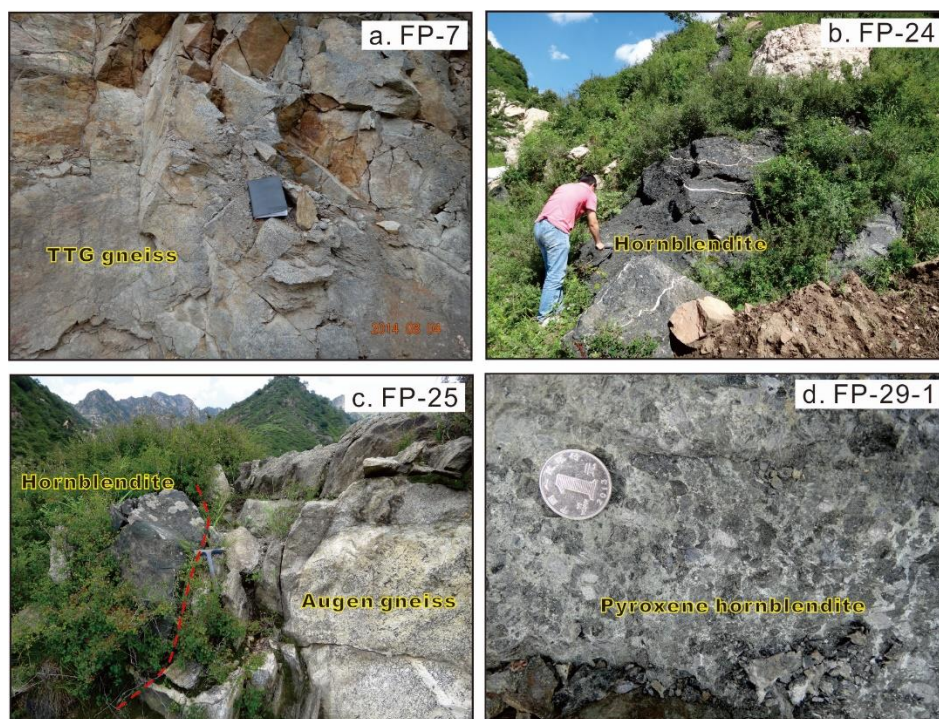


Fig. 3-2 Representative field photographs of the Yangmuqiao mafic-ultramafic intrusion and the Fuping TTG gneiss.

3.2.3 TTG gneisses

Samples FP-6-1 and FP-7 are hornblende and biotite-bearing TTG gneisses, and are gray colored and medium grained (Fig. 3-2a). The hornblende biotite gneisses are dominated by plagioclase (50-60 %), quartz (15-20 %), biotite (10-15 %), K-feldspar (5-10 %), hornblende (2-5 %), and minor accessory minerals (magnetite, zircon and apatite). The rocks show granoblastic and “triple junction” textures, with biotite defining foliation (Fig. 3-3d).

3.3 Analytical results

3.3.1 Mineral chemistry

3.3.1.1 Hornblende

Hornblendes in the hornblendites and pyroxene hornblendite are all magnesio-hornblende and actinolite in composition (Fig. 3-4). The primary hornblendes in the hornblendites (FP-24 and FP-25) are mainly magnesio-hornblende and the secondary ones are actinolites, showing minor variations of SiO_2 (47.4-52.8

wt.%), FeO (9.8-10.9 wt.%), MgO (14.9-16.5 wt.%), CaO (11.6-12.5 wt.%), and relatively wide variation of Al₂O₃ (3.7-8.5 wt.%). The three types of hornblende in the pyroxene hornblendite display different compositions. The hornblendes occurring as inclusions and porphyritic cores display lower SiO₂ (46.2-49.8 wt.%) and MgO (14.0-15.7 wt.%) contents, higher Al₂O₃ (6.9-10.1 wt.%) and FeO (9.8-11.3 wt.%) contents. In contrast, the hornblendes occurring as rims and matrix show SiO₂ (50.6-55.8 wt.%), MgO (16.5-19.1 wt.%), Al₂O₃ (2.0-6.3 wt.%) and FeO (7.9-8.4 wt.%) contents (Table 3-2).

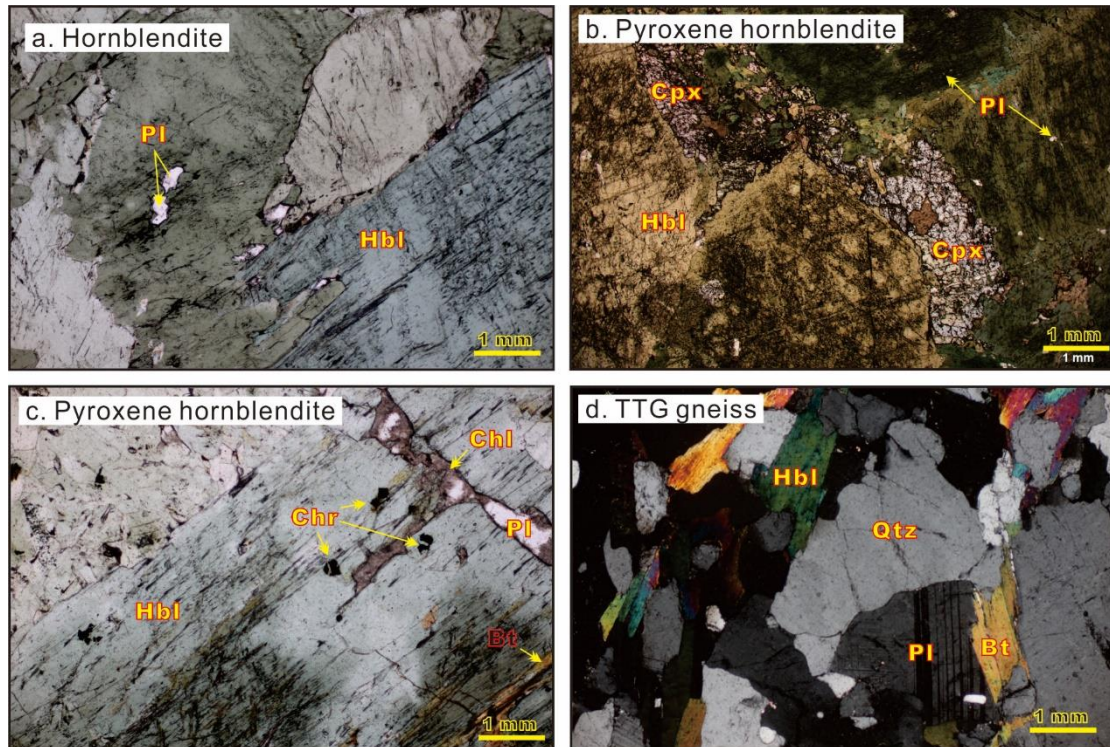


Fig. 3-3 Representative photomicrographs of the rock samples from the Yangmuqiao mafic-ultramafic intrusion and the Fuping TTG gneiss. (a) Hornblendite (FP-24). (b) Pyroxene hornblendite (FP-28). (c) Pyroxene hornblendite (FP-28), chromites occur as mineral inclusions in hornblende. (d) TTG gneiss (FP-7). Mineral abbreviations: Hbl, hornblende; Pl, plagioclase; Cpx, clinopyroxene, Chr, chromite; Chl, chlorite; Bt, biotite; Qtz, quartz.

3.3.1.2 Clinopyroxene

The clinopyroxenes in the pyroxene hornblendite are all augite and diopside in composition (Fig. 3-5a). The compositions of the clinopyroxenes are characterized by moderate MgO (11.84-14.77 wt.%) and $X_{Mg} = Mg/(Fe + Mg) = 0.69-0.82$, high CaO (23.30-24.53 wt.%), low Al₂O₃ (0.03-1.12 wt.%), TiO₂ (0.00-0.04 wt.%) and

Na₂O (0.14-0.75 wt.%) contents (Table 3-3). Almost all of the clinopyroxenes fall in the compositional field of Quetico Alaskan-type complex in the SiO₂ versus Al₂O₃ diagram (Fig. 3-5b).

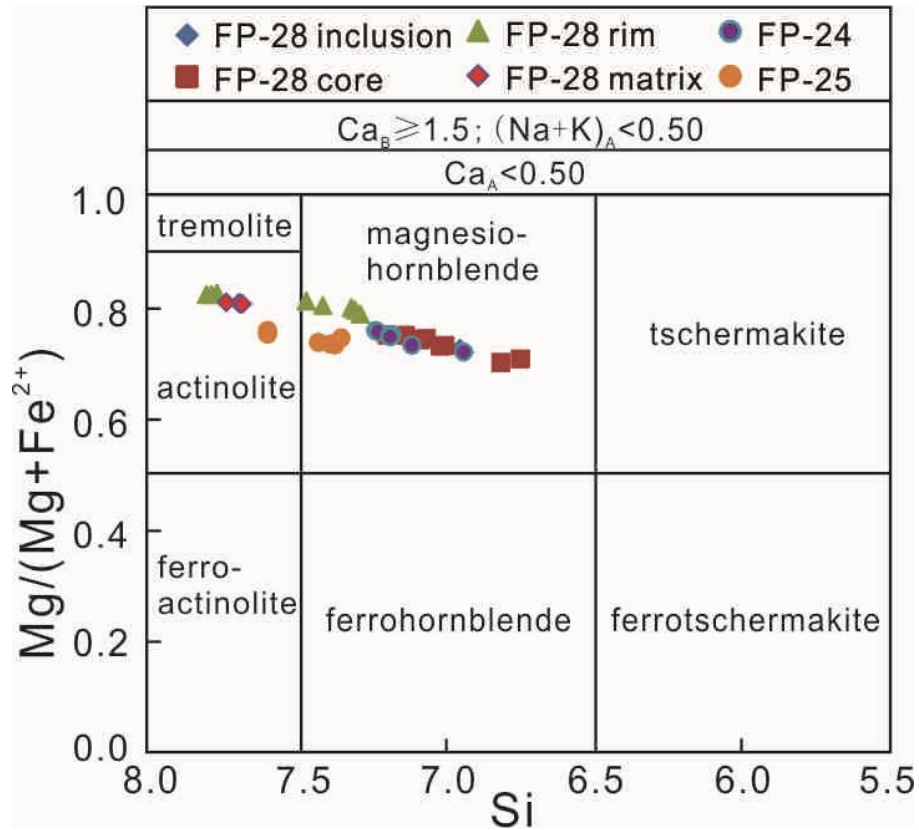


Fig. 3-4 Classification diagram of hornblende in the rock samples from the Yangmuqiao mafic-ultramafic intrusion (after Leake et al., 1997).

3.3.1.3 Chromite

The chromites show Cr₂O₃, Cr# [100*Cr/(Cr+Al)], TiO₂, Al₂O₃ and FeO contents in the range of 49.90-52.53 wt.%, 84-90, 0.12-0.25 wt.%, 3.85-6.30 wt.% and 35.85-38.71 wt.%, respectively. In the TiO₂ versus Al₂O₃ diagram, the chromites plot in the field of island arc (Fig. 3-6a). Furthermore, the chromites show affinity of Alaskan-type complex in the Cr# versus Fe²⁺/(Mg+Fe²⁺) diagram (Fig. 3-6b).

3.3.1.4 Plagioclase

Few plagioclase crystals are present in the hornblendite and pyroxene hornblendite, and they are partly altered into chlorites (Fig. 3-3c). The plagioclase in the hornblendite is of labradorite and bytownite composition with anorthite (An) numbers varying from 68 to 79, whereas the plagioclase in the pyroxene

hornblendites is bytownite with An numbers of 75-88.

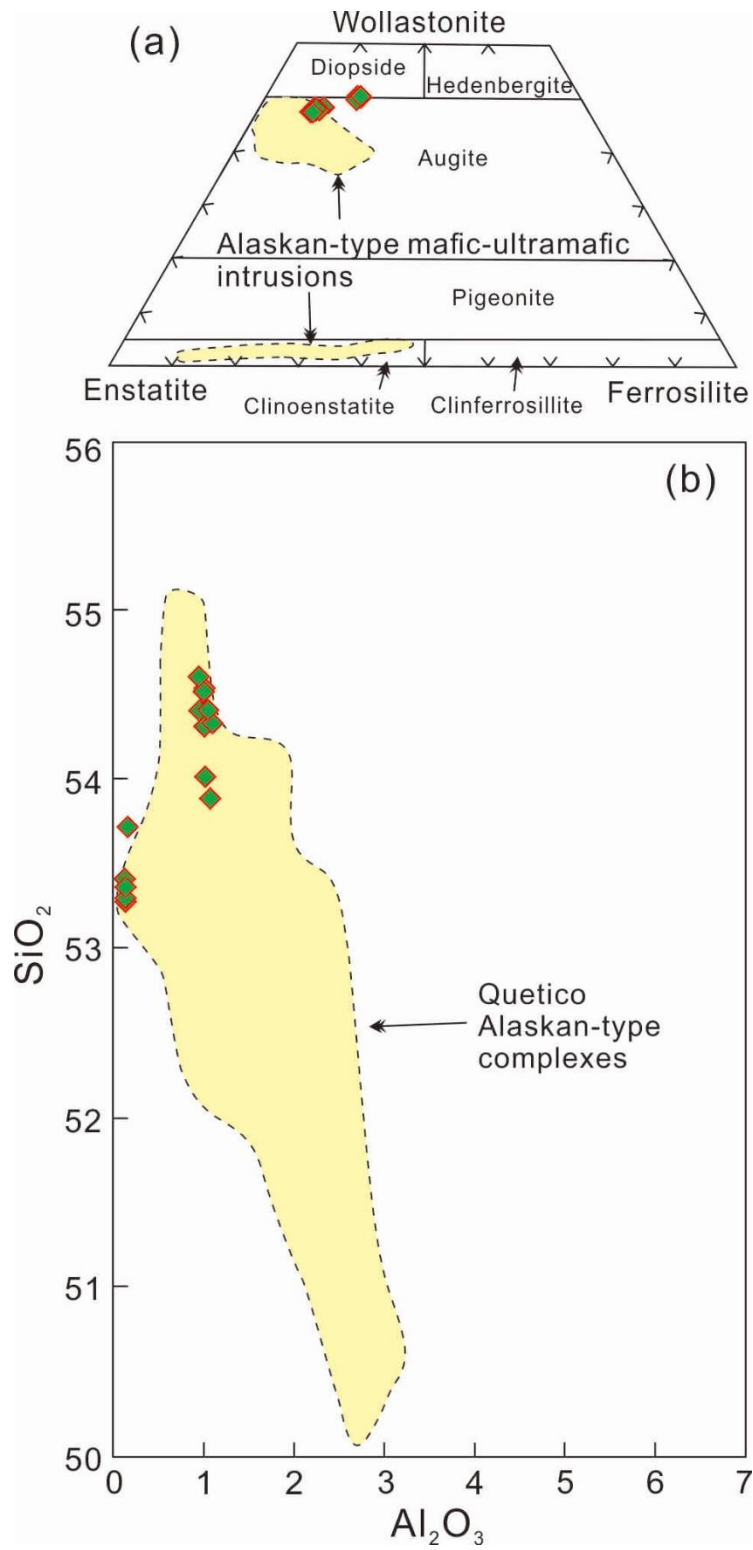


Fig. 3-5 Plots of clinopyroxene compositions in pyroxene hornblendite from the Yangmuqiao mafic-ultramafic intrusion. (a) The fields of the Alaskan-type mafic-ultramafic intrusions are from Himmelberg and Loney (1995). (b) Al₂O₃ versus SiO₂ diagram, the fields of the Alaskan-type complexes are from Pettigrew and Hattori (2006).

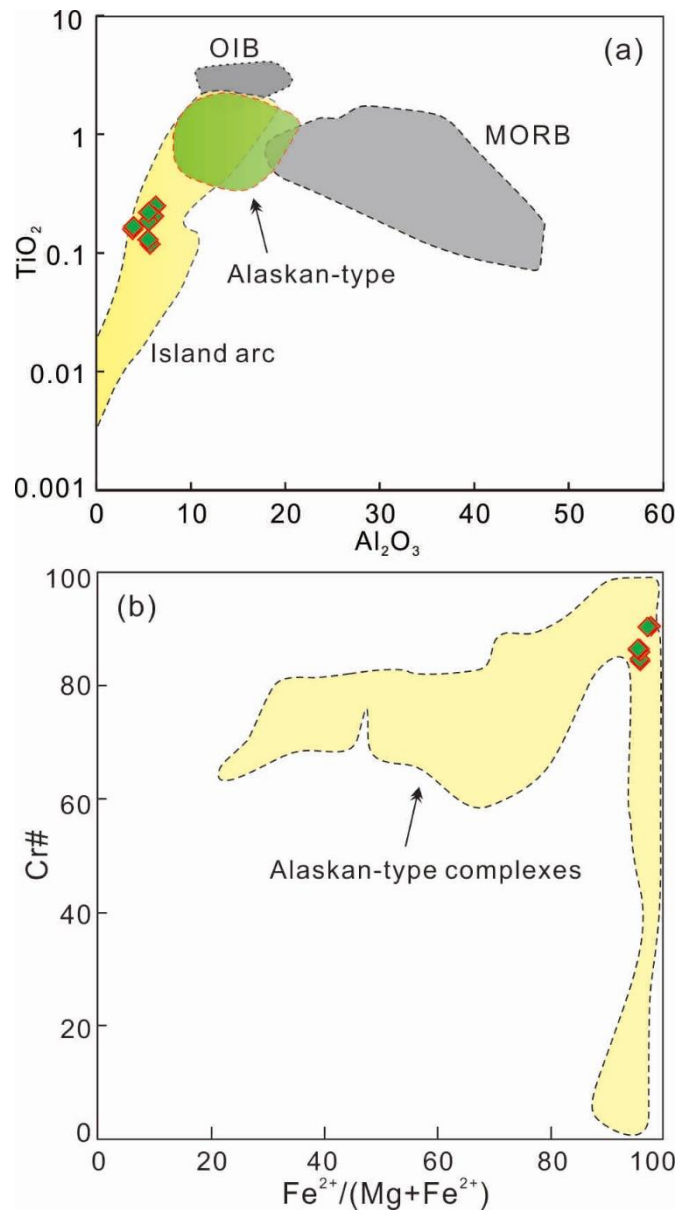


Fig. 3-6 Plots of chromite compositions in the pyroxene hornblende from the Yangmuqiao mafic-ultramafic intrusion. (a) Al₂O₃ versus TiO₂ diagram, Alaskan-type field after Alaska complex (Himmelberg et al., 1986; Himmelberg and Loney 1995); Ocean island basalt (OIB), mid-ocean ridge basalt (MORB), and island-arc fields after Kamenetsky et al. (2001). (b) Fe²⁺/(Mg+Fe²⁺) versus Cr# diagram, the fields of Alaskan-type complexes are after Barnes and Roeder (2001).

3.3.1.5 Other minerals

Biotite is present in the hornblende and pyroxene hornblende, and shows homogeneous compositions of Al₂O₃ (14.31-15.98 wt.%), MgO (16.48-16.95 wt.%) and K₂O (8.36-8.94 wt.%). Titanite also occurs in both rock types, displaying high

TiO₂ (37.12-38.45 wt.%) and CaO (27.94-28.33 wt.%) contents (Table 3-4).

3.3.2 Whole rock geochemistry

3.3.2.1 Major elements

Major element data on the TTG gneisses and mafic-ultramafic rocks are listed in Table 3-5. The TTG gneisses exhibit SiO₂ variation of 63.20-71.02 wt.%, and are calc-alkaline with K₂O contents of 1.42-2.32 wt.%, Na₂O contents of 3.96-4.84 wt.% and CaO contents of 2.96-3.57 wt.%. The high Na₂O/K₂O ratios (1.7-3.4) and Al₂O₃ concentrations (15.17-16.80 wt.%) suggest that they are typical high-Al TTG suit rocks (Barker, 1979). The TTG gneisses also show relatively high MgO contents of 1.13-2.74 wt.% and Mg# values of 49-52.

The mafic-ultramafic rocks of the Fuping Complex exhibit a limited range of variation for SiO₂ content (47.20-50.65 wt.%). The pyroxene hornblendites are characterized by high MgO (13.21-15.08 wt.%), Mg# (68-75) and moderate Al₂O₃ (7.10-7.32 wt.%), whereas the hornblendites have higher MgO (15.20-15.85 wt.%), Mg# (72-74) and relatively lower Al₂O₃ (5.66-6.81 wt.%).

3.3.2.2 Trace elements

The TTG gneisses show Σ REE concentrations of 93.47-193.65 ppm. These rocks display significant LREE-enriched patterns with (La/Yb)_N of 30.84-33.77, with weak Eu anomalies. On the primitive mantle normalized spider diagram (Fig. 3-7; Sun and McDonough, 1989), the TTG gneisses are selectively enriched in LILE (e.g. K, Rb, Ba and Pb) and LREE (e.g. La and Ce), and show depletion of HFSE (e.g. Nb, Ta and Ti) and HREE.

The pyroxene hornblendites and hornblendites display moderate Σ REE concentrations of 53.05-166.11 and strongly fractionated REE patterns ((La/Yb)_N=4.82-25.78). On the primitive mantle normalized spider diagram (Fig. 3-7d; Sun and McDonough, 1989), the mafic-ultramafic intrusions show enrichment of LILE (e.g. K and Rb) and LREE (e.g. La and Ce), remarkable depletion of HSFE (e.g. Nb, Ta, Zr and Hf) and HREE, and slight depletion of Sr. The depletion in Nb-Ta and relatively enrichment of LILE is typical of subduction related magmatism,

particularly corresponding to arc magmas (Condie, 1993).

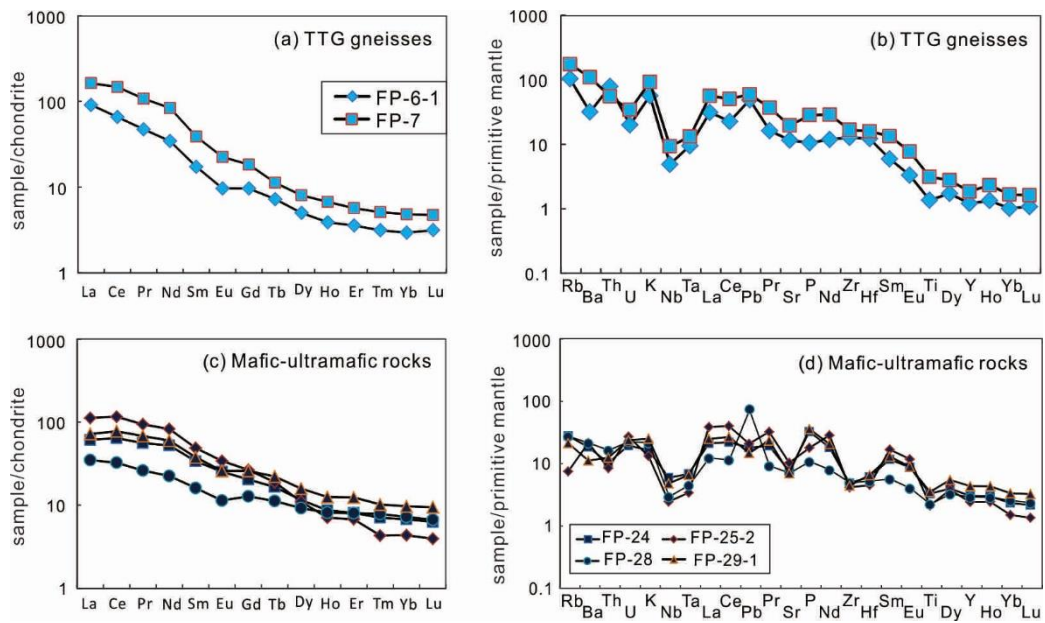


Fig. 3-7 Chondrite-normalized REE patterns (a, c) and primitive mantle-normalized trace elements multi-element variation diagram (b, d) for the rock samples from the Fuping TTG gneisses (a, b) and Yangmuqiao mafic-ultramafic intrusion (c, d). The normalization values are from Sun and McDonough (1989).

3.3.2.3 Platinum-group elements

Two hornblendites and two pyroxene hornblendites were chosen for platinum-group elements (PGE) analyses, the results of which are presented in Table 3-5. The pyroxene hornblendites are characterized by higher PGE contents with Σ PGE (7.41-10.29 ppb), Σ IPGE (1.69-2.39 ppb), 0.74-0.87 ppb Ru, 0.27-0.68 ppb Rh, 2.45-3.88 ppb Pd, 0.56-0.87 ppb Os, 0.39-0.65 ppb Ir and 3.00-3.34 ppb Pt. Pd/Ir ratios vary from 5.97-6.28 and Pd/Pt ratios range between 0.82-1.16. In comparison, the hornblendites display lower PGE contents, the Σ PGE vary from 4.66-5.29. The hornblendites are characterized by lower IPGE (Os, Ir and Ru) contents with Σ IPGE (0.56-0.72 ppb), 0.19-0.23 ppb Os, 0.12-0.23 ppb Ir and 0.25-0.26 Ru (Fig. 3-8). The Pd/Ir ratios and Pd/Pt ratios vary 6.48-15.25 and 0.54-0.90. Both the hornblendites and pyroxene hornblendites are enriched in PPGE (Rh, Pt, Pd) in the primitive mantle normalized PGE patterns (Fig. 3-8).

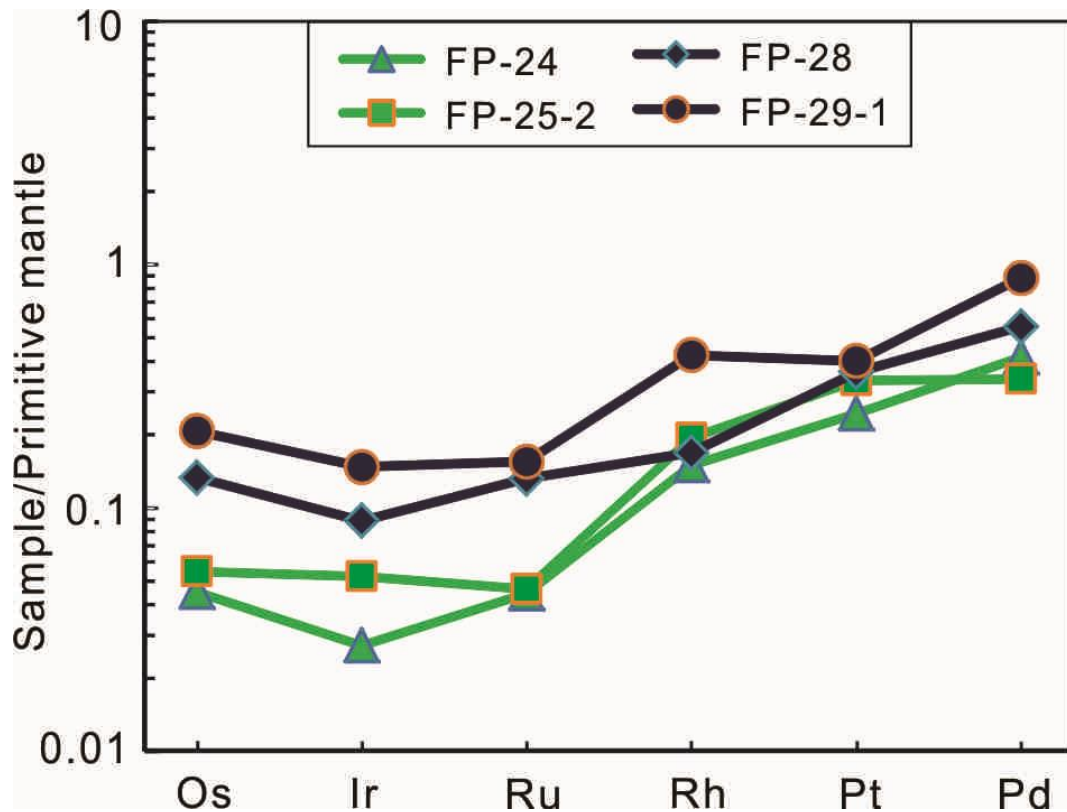


Fig. 3-8 Primitive mantle-normalized PGE patterns of the Yangmuqiao mafic-ultramafic intrusion. The primitive mantle values are from [Barnes and Maier \(1999\)](#).

3.3.3 Zircon U-Pb geochronology

Zircon U-Pb age data are presented in Table 3-6. Zircon grains from the TTG gneiss sample (FP-7) are mostly colorless, translucent, and well developed prismatic crystals. The grains are euhedral to subhedral with size range of 50-200 μm and length to width ratios of 2.5:1 to 1:1. Their CL images show clear magmatic oscillatory zoning (Fig. 3-9a). Thirty-seven analytical spots display relatively high and varied Th/U ratios of 0.34-1.45, indicating magmatic origin. All analyses are distributed along the concordia or along the Pb loss line, yielding a weighted mean $^{207}\text{Pb}/^{206}\text{Pb}$ age of 2513 ± 13 Ma (MSWD = 0.31) (Fig. 3-10a). The ca. 2.51 Ga age is taken to represent the crystallization age of the Fuping TTG gneisses.

Zircon grains from the pyroxene-bearing hornblendite sample (FP-29-1) are colorless, anhedral to subhedral, and translucent. Crystal lengths vary from 50 to 180 μm , with aspect ratios of 1.5:1 to 1:1. CL images show that most zircons have oscillatory or patchy linear zoning (Fig. 3-9b). Twenty-six analytical spots display

Th/U ratios of 0.12-0.62 (Table 3-6), indicating that they are of magmatic origin. All analyses are distributed along the concordia or along the Pb loss line, yielding a weighted mean $^{207}\text{Pb}/^{206}\text{Pb}$ age of 2514 ± 15 Ma (MSWD = 0.20) (Fig. 3-10b). The age of ca. 2.51 Ga represents the crystallization age of the mafic-ultramafic intrusion.

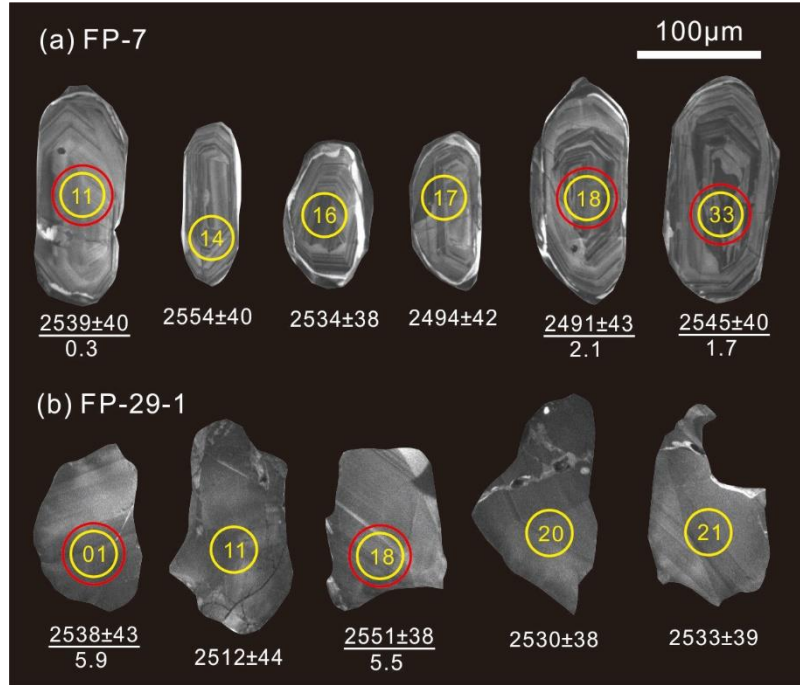


Fig. 3-9 Cathodoluminescence (CL) images of representative zircons in Fuping TTG gneiss (FP-7) and pyroxene hornblende (FP-29-1). Yellow circles for U–Pb analysis and red circles for Lu–Hf analysis, ages in Ma and $\epsilon_{\text{Hf}}(t)$ values are also shown.

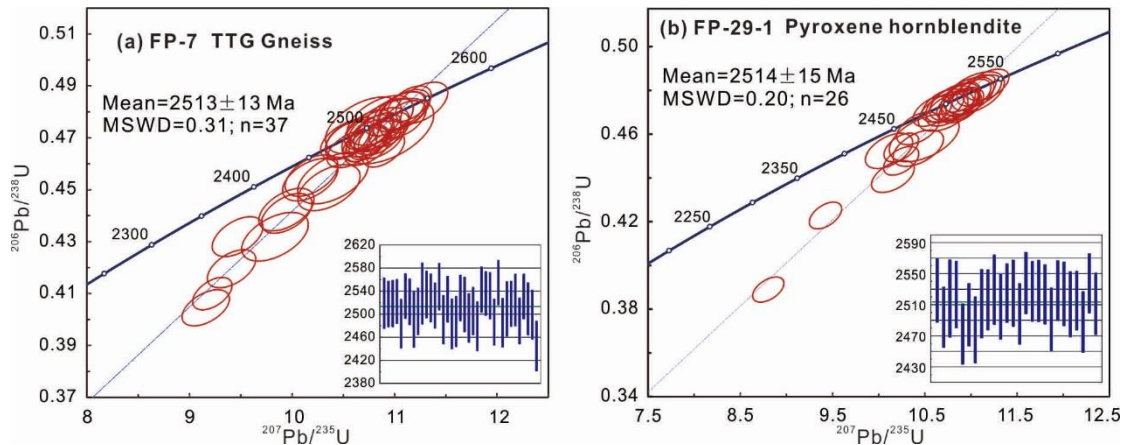


Fig. 3-10 Zircon U–Pb concordia plots for the Fuping TTG gneiss (FP-7) and the pyroxene hornblende (FP-29-1).

3.3.4 Zircon Lu–Hf isotopes

Zircon Lu–Hf isotopic results are listed in Table 3-7 and plotted in Fig. 3-11.

Totally eight spots were analysed for zircons in TTG gneiss sample FP-7. The results display $\epsilon_{\text{Hf}}(t)$ values of -1.8 to 4.9, initial $^{176}\text{Hf}/^{177}\text{Hf}$ ratios of 0.281129-0.281318, T_{DM} (2627-2888 Ma) and T_{DM}^{C} (2709-3119 Ma). Among two spots have negative $\epsilon_{\text{Hf}}(t)$ values of -1.8 to -0.1, and show homogenous initial $^{176}\text{Hf}/^{177}\text{Hf}$ ratios of 0.281129-0.281176, constant T_{DM} (2827-2888 Ma) and T_{DM}^{C} (3017-3119 Ma). The results suggest that the parental magma of the ~2.51 Ga Fuping TTG gneiss was mostly derived from Neoproterozoic juvenile material mixed with minor Mesoproterozoic crustal components.

Eight spots on zircons from the pyroxene hornblendite sample FP-29-1 show constant Hf compositions of initial $^{176}\text{Hf}/^{177}\text{Hf}$ ratios (0.281252-0.281365), positive $\epsilon_{\text{Hf}}(t)$ values (2.6 to 6.7), Neoproterozoic T_{DM} (2570-2723 Ma). The obvious positive $\epsilon_{\text{Hf}}(t)$ values suggest that the parental magma of the mafic-ultramafic rock was derived from the depleted mantle source.

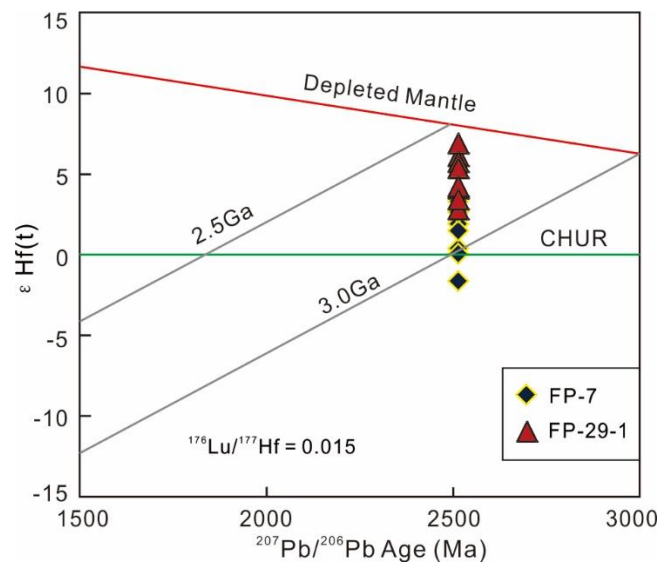


Fig. 3-11 $\epsilon_{\text{Hf}}(t)$ versus $^{207}\text{Pb}/^{206}\text{Pb}$ age diagram of zircons from the Fuping TTG gneiss (FP-7) and the pyroxene hornblendite (FP-29-1).

3.3.5 Zircon O isotopes

A total of 22 spots were analyzed for $\delta^{18}\text{O}$ on zircons from the TTG sample FP-7 and the pyroxene hornblendite sample FP-29-1 (Table 3-8, Fig. 3-12). The range of $\delta^{18}\text{O}$ values obtained are similar to those found in Archean igneous zircons worldwide (5.1‰ to 7.3‰; Valley et al., 2005). For the TTG gneiss sample (FP-7), analyses on

magmatic zircons display $\delta^{18}\text{O}$ values vary from 4.1‰ to 6.7‰, with an average of 6.1‰. Among these, 11 spots show $\delta^{18}\text{O}$ values in the range of 5.8‰ to 6.7‰. The $\delta^{18}\text{O}$ values obtained from the pyroxene hornblendite sample are in the range of 3.8‰ to 7.0‰, with an average of 6.2‰, and 9 spots display tight $\delta^{18}\text{O}$ range (6.0‰ to 7.0‰). It can be seen from Fig. 3-12c that most of the zircons in the TTG gneiss and pyroxene-bearing hornblendite samples have $\delta^{18}\text{O}$ values slightly higher than that of typical mantle derived zircons ($5.3\text{‰} \pm 0.3\text{‰}$, [Valley et al., 1998](#)), suggesting that the parental magma mostly derived from a depleted mantle source, and was mixed with minor crustal components.

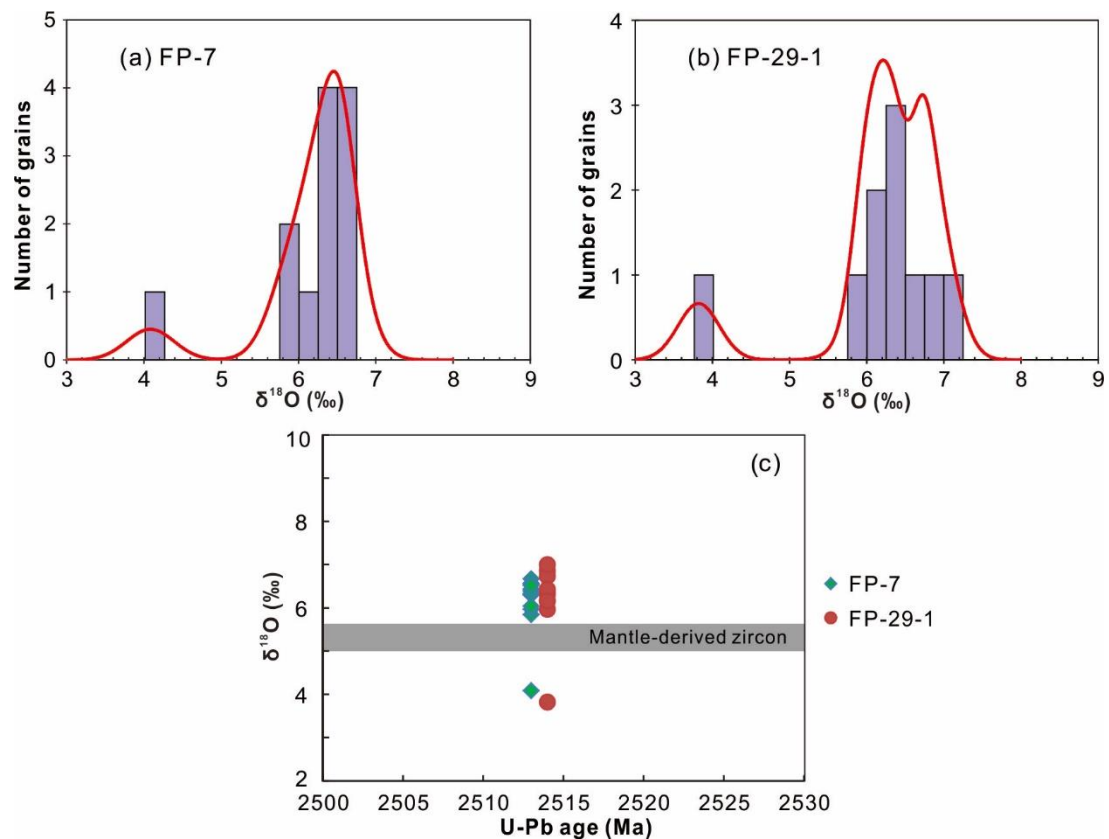


Fig. 3-12 Histograms of zircon $\delta^{18}\text{O}$ values (a, b), relationship of zircon U-Pb ages and $\delta^{18}\text{O}$ values (c) of zircons from the Fuping TTG gneiss (FP-7) and the pyroxene hornblendite (FP-29-1).

3.4 Discussion

3.4.1 Neoproterozoic arc magmatism

[Cheng et al. \(2004\)](#) presented the geological features of the Yangmuqiao mafic-ultramafic intrusion based on field mapping (Fig. 3-1b), although the

geochemical features, geochronological constraints, and petrogenesis remained unclear. The present study obtained weighted mean $^{207}\text{Pb}/^{206}\text{Pb}$ ages of 2514 ± 15 Ma (MSWD = 0.20, Th/U = 0.12-0.62) for the pyroxene hornblendite, and 2513 ± 13 Ma (MSWD = 0.31, Th/U = 0.34-1.45) for the coeval TTG gneiss. The zircon characteristics and the relatively high Th/U ratios confirm late Neoproterozoic (~2.51 Ga) magmatism in the Fuping area.

Both the mafic-ultramafic intrusion and TTG gneiss show island arc signatures based on whole rock geochemistry and mineral chemistry. All of the samples display fractionated REE patterns with elevated LREE and little or no Eu anomalies (Fig. 3-7a, 3-7c), enrichment of LILE (K, Rb and Ba) and LREE (La and Ce), and depletion of HSFRE (Nb, Ta, Zr and Hf) and HREE (Fig. 3-7b, 3-7d). Such features are commonly attributed to a hydrous magma component in subduction-related environments (e.g. [Himmelberg and Loney, 1995](#); [Berly et al., 2006](#); [Dhuime et al., 2007](#)). Clinopyroxene and chromite have been used as proxies to derive petrogenetic information and tectonic settings (e.g. [DeBari and Coleman, 1989](#); [Himmelberg and Loney, 1995](#); [Li et al., 2012](#)). The clinopyroxenes in the studied rocks are mainly composed of augite and diopside (Fig. 3-5a), and display compositions similar to those in Alaskan-type mafic-ultramafic intrusions (Fig. 3-5b). The low TiO_2 (0.00-0.05 wt.%) contents of the clinopyroxenes imply that they crystallized from the Ti poor magma, possibly derived from a depleted mantle source in subduction zone setting ([Parlak et al., 2002](#)). The chemical features of high Ca and low Al, Na and Ti contents in clinopyroxene from the pyroxene hornblendite are consistent with the characteristics of the Alaskan-type complexes ([Snoke et al., 1981](#); [Helmy and El Mahallawi, 2003](#)). Chromite commonly occurs as accessory mineral in the arc cumulate intrusions ([Himmelberg and Loney, 1995](#); [Kamenetsky et al., 2001](#); [Su et al., 2012](#)). In the Al_2O_3 versus TiO_2 diagram, the chromite from present study falls in the island arc field based on the relatively low Al_2O_3 contents (Fig. 3-6a). The chromite show high Cr# contents between 84 and 90, and plot in the Alaskan-type complexes field in the Cr# versus $\text{Mg}/(\text{Mg}+\text{Fe}^{2+})$ diagram (Fig. 3-6b). In summary, the Yangmuqiao mafic-ultramafic intrusion and the coeval TTG gneiss

from the Fuping Complex indicate formation in a subduction related arc environment.

3.4.2 Magma sources and evolution

Zircon is a refractory mineral and is an ideal tool for radiometric dating and isotopic tracing (Hoskin and Schaltegger, 2003). Zircon Hf and O isotopic compositions can be simultaneously used to gain insights on magma source and crustal evolution (Kemp et al., 2007; Li et al., 2010a; Heinonen et al., 2015). Igneous zircons derived from mantle magma display an average $\delta^{18}\text{O}$ value of $5.3\text{‰} \pm 0.3\text{‰}$ (Valley et al., 1998). Positive $\epsilon_{\text{Hf}}(t)$ values and Hf model age close to the crystallization age suggest magma derivation from a depleted mantle source (Su et al., 2011). On the other hand, zircon $\delta^{18}\text{O}$ value above 5.6‰ is considered to result from an ^{18}O -enriched supracrustal component (Kemp et al., 2007). Therefore, the more 'crustal-like' $\delta^{18}\text{O}$ values, relatively low (negative) $\epsilon_{\text{Hf}}(t)$ values, and Hf model ages which are older than formation ages, suggest that the parental magma was derived from the enriched mantle source or was contaminated by crustal components (Hawkesworth and Kemp, 2006).

The zircons from pyroxene hornblendite (FP-29-1) have $\delta^{18}\text{O}$ values in the range of 3.8‰ to 7.0‰ (average 6.2‰), positive $\epsilon_{\text{Hf}}(t)$ values (2.6 to 6.7) and Neoproterozoic T_{DM} (2570-2723 Ma), suggesting that the magma was predominantly extracted from the depleted mantle. The zircons from the TTG gneiss (FP-7) display $\delta^{18}\text{O}$ values, $\epsilon_{\text{Hf}}(t)$ values, T_{DM} and T_{DM}^{C} of 4.1‰ to 6.7‰ (average of 6.1‰), -1.8 to 4.9, 2637-2888 Ma and 2709-3119 Ma, respectively. The results suggest that the parental magma of the TTG gneiss was mainly derived from juvenile source. Regarding the relatively higher $\delta^{18}\text{O}$ values than those of mantle-derived zircon ($5.3\text{‰} \pm 0.3\text{‰}$), two spots in zircons from the TTG gneiss have negative $\epsilon_{\text{Hf}}(t)$ values and relatively older Hf model age than the crystallization age, suggesting that the parental magma of the mafic-ultramafic intrusion and TTG gneiss experienced different degree of crustal contamination and the TTG gneiss was contaminated by more crustal components. The crustal contamination is also supported from the geochemical results. Continental crust is typically characterized by low content of Ti with

depletion of Nb and Ta (Barth et al., 2000; Rudnick and Gao, 2003). The mafic-ultramafic intrusion and TTG gneiss in this study show obvious depletion of Nb, Ta and Ti in the primitive mantle normalized spider diagram (Fig. 3-7b, 3-7d). Thus, the parental magma of the Neoproterozoic magmatic suite in the Fuping area was dominantly extracted from the depleted mantle and contaminated by different degrees of crustal components. The crustal contamination process might have been controlled by the slab-derived fluids and the subduction setting (Fig. 3-13b).

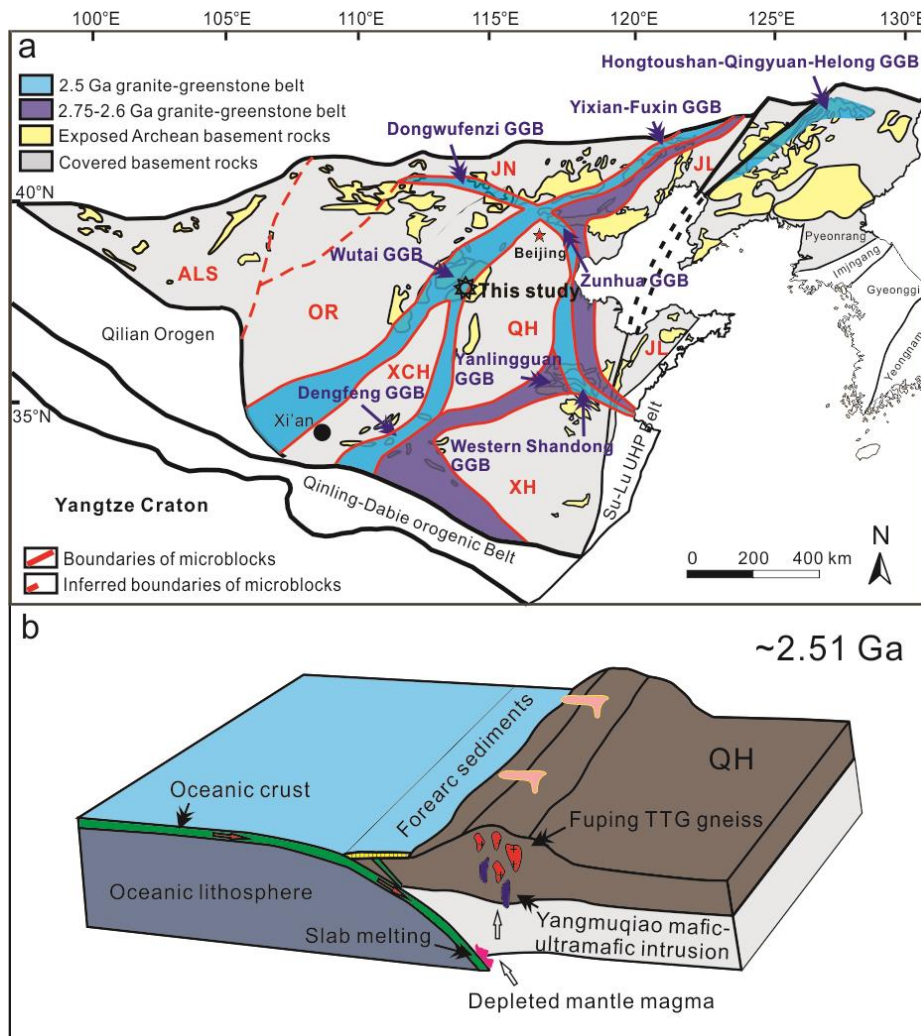


Fig. 3-13 (a) Archean tectonic framework of the North China Craton showing the distribution of ancient nuclei, microblocks and greenstone belts (after Zhai and Santosh, 2011). The major microblocks are the Jiaoliao Block (JL), Qianhuai Block (QH), Ordos Block (OR), Jining Block (JN), Xuchang Block (XCH), Xuhuai Block (XH) and Alashan Block (ALS). GB: Greenstone belt. (b) Proposed tectonic model showing the late Neoproterozoic subduction-related arc magmatism in the Fuping area.

Platinum group elements (PGEs) are immobile during low-grade metamorphism and hydrothermal alteration, thus PGEs are effective tracers for fractional crystallization of magmas (Garuti et al., 1997; Day et al., 2008; Said et al., 2011; Singh et al., 2015). The PGEs can be divided into Ir-group PGE (IPGE=Os, Ir, Ru) and Pd-group PGE (PPGE=Rh, Pt, Pd), where the IPGE are compatible and the PPGE are more incompatible during fractional crystallization (Barnes et al., 1985; Day et al., 2008). The pyroxene hornblendites have obviously higher IPGE contents than those in the hornblendites (Fig. 3-8), indicating the different compatibility of IPGE and PPGE during the fractional crystallization. The unfractionated materials should have Pd/Ir close to 1, and the Pd/Ir ratio increases with differentiation in magmatic fractionation process (Garuti et al., 1997). Thus, the magmatic fractional crystallization process is also supported by the lower Pd/Ir ratios (5.97-6.28) of the pyroxene hornblendites and the relatively higher Pd/Ir ratios (6.48-15.25) of the hornblendites.

3.4.3 Tectonic implications

Previous zircon U-Pb geochronological studies have recorded Neoproterozoic-early Paleoproterozoic magmatism from the Fuping Complex (Wilde et al., 1997; Guan et al., 2002; Zhao et al., 2002a). Zhao et al. (2002a) reported SHRIMP U-Pb ages of 2523 ± 14 Ma, 2499 ± 10 Ma, 2486 ± 8 Ma and 2510 ± 22 Ma from Fuping TTG gneisses, and 2507 ± 11 Ma from one pegmatitic dyke. Guan et al. (2002) obtained SHRIMP U-Pb ages of 2520 ± 20 Ma, 2513 ± 12 Ma and 2475 ± 8 Ma from Fuping TTG gneisses. The TTG gneiss sample in this study shows weighted mean $^{207}\text{Pb}/^{206}\text{Pb}$ age of 2513 ± 13 Ma, and combined with the previous data, the protolith crystallization time of the Fuping TTG gneisses can be inferred as 2523-2475 Ma. For the Longquanguan augen gneiss, Wilde et al. (1997) reported three SHRIMP U-Pb ages of 2543 ± 7 Ma, 2541 ± 14 Ma and 2540 ± 18 Ma, and the ca. 2.54 Ga age was interpreted as the emplacement age of the protolith. The available zircon U-Pb ages within the Fuping-Wutai-Hengshan area fall between 2550 Ma and 2475 Ma (Wilde et al., 1997, 2004, 2005; Guan et al., 2002; Zhao et al., 2002a, 2011; Kröner et

al., 2005b; Zhang et al., 2009). The 2.55-2.47 Ga magmatism has been variously interpreted as arc-related (e.g. Zhao et al., 2005, 2007) or collision-related, associated with the assembly of the Western and the Eastern Blocks of the NCC (Kusky et al., 2007).

The study area is located at the western segment of the Fuping Complex and the eastern periphery of the Wutai greenstone belt (4-13a). The Wutai greenstone belt marks the boundary between the Ordos Block (OR) and the Qianhuai Block (QH), with the greenstones and related granitoids considered to have formed in an island-arc or back-arc basin setting (Liu et al., 2004, 2006; Wang, 2009; Zhai and Santosh, 2011). The Yangmuqiao mafic-ultramafic intrusion and the Fuping TTG gneiss show clear Neoproterozoic crystallization age (ca. 2.51 Ga), and the whole-rock geochemistry and mineral chemistry suggest that these rocks were formed in an island-arc setting. This study correlates the magmatic event to the subduction-collision process of the OR and the QH microblocks with closure of the intervening ocean represented by the Wutai greenstone belt. However, the Wutai greenstone belt is traditionally considered to be restricted in the Wutai Complex, with debates surrounding the formation of the arc-related granitoid gneisses from the Wutai greenstone belt and adjacent Fuping and Hengshan Complexes (Wang, 2009; Liu et al., 2004; Wang et al., 2004, 2010a; Polat et al., 2005; Zhao et al., 2007, 2010). The Wutai granitoid gneisses were emplaced during 2560-2520 Ma, followed by the formation of intermediate to felsic volcanic rocks during 2530-2515 Ma. The granitoid gneisses in the Fuping and Hengshan Complexes were emplaced during 2520-2475 Ma (Wilde et al., 1997, 2004, 2005; Guan et al., 2002, Zhao et al., 2002a; Kröner et al., 2005a). The debates surrounding the formation of the granitoid gneisses from the Wutai-Fuping-Hengshan Complexes are mainly related to the subduction process, tectonic setting, and the time of collision (Wang, 2009, 2010; Zhao et al., 2007, 2010). However, there is a general consensus that the granitoid gneisses in the Fuping Complex were formed in an arc setting related to the eastward subduction (Wang, 2009; Zhao et al., 2007, 2010; Wang et al., 2010a; Zhang et al., 2015c). A polyphase subduction process cannot be eliminated for the polyphase emplacement of the

protoliths of the granitoid gneisses in the Wutai-Fuping-Hengshan Complexes. This study therefore proposes the possibility that the Yangmuqiao mafic-ultramafic intrusion and Fuping TTG gneiss formed at ~2.51 Ga associated with the eastward subduction and accretion between the OR and the QH microblocks along the Wutai greenstone belt which represents the suture of a paleo ocean. The Fuping TTG gneiss may represent a part of the Wutai granite-greenstone belt, and record the important crustal growth event in the late Neoproterozoic.

The late Neoproterozoic microblock amalgamation model is widely supported by several recent studies (Santosh et al., 2015; Li et al., 2016). Santosh et al. (2016) reported the discovery of dismembered suprasubduction zone ophiolite (Yishui ophiolite) from the southern periphery of the Jiaoliao microblock (Fig. 3-13a). They reported zircon U-Pb ages of 2538 ± 30 Ma from hornblende, 2538 ± 16 Ma and 2503 ± 21 Ma from granites, and 2503 ± 16 Ma and 2495 ± 10 Ma from gabbros. The suprasubduction zone ophiolite complex was correlated to the northward subduction of the Xuhuai microblock and the Jiaoliao microblock with construction of the intervening Yanlingguan greenstone belt in an active convergent margin during the Neoproterozoic. Yang et al. (2015) reported a suite of metagabbro, gneiss and amphibolite from the western margin of the northern segment of the Jiaoliao microblock. The geochemical data suggest that these rocks were formed in a subduction-related arc setting. Zircon U-Pb age data from these rocks display magmatic ages range from 2587 ± 10 Ma to 2536 ± 8 Ma and metamorphic ages of 2533-2490 Ma. The Neoproterozoic arc magmatism was suggested to be related to the subduction event along the western margin of the Jiaoliao Block (Yang et al., 2015). This study further confirms the amalgamation of the various microblocks in the North China Craton during the late Neoproterozoic (Zhai and Santosh, 2011).

3.5 Conclusions

- (1) This study reports zircon U-Pb age of 2514 ± 15 Ma for the Yangmuqiao mafic-ultramafic intrusion from the Fuping Complex. The coeval Fuping TTG gneiss display weighted mean $^{207}\text{Pb}/^{206}\text{Pb}$ ages of 2513 ± 13 Ma.

- (2) Whole rock geochemical and mineral chemical data suggest that these rocks were formed in subduction related arc setting. The rocks commonly display fractionated REE patterns with elevated LREE, enrichment of LILE (K, Rb and Ba) and LREE (La and Ce), and depletion of HSFTE (Nb, Ta, Zr and Hf) and HREE. The chemical features of the clinopyroxene and chromite in the pyroxene hornblendites show affinity with the Alaskan-type mafic-ultramafic intrusion.
- (3) The parental magma of the Neoproterozoic magmatism in the Fuping area was dominantly extracted from the depleted mantle and variably contaminated by crustal components.
- (4) The late Neoproterozoic (~2.51 Ga) arc magmatism recorded by the Yangmuqiao mafic-ultramafic intrusion and the Fuping TTG gneiss resulted from the subduction-collision process of the OR and the QH Blocks and closure of the intervening ocean represented by the Wutai greenstone belt.

Chapter 4: Paleoproterozoic (2.1-2.0 Ga) magmatism in the Fuping Complex

4.1 Introduction

In the early earth history, the stable cratons were constructed through long periods of aggregation of Precambrian micro-blocks, micro-continents or terranes that are dominantly composed of gneisses and greenstone belts (Rogers and Santosh, 2003; Zhai and Santosh, 2011). The formation of continents and cratons involves complex and multiple geodynamic processes including rifting, density-inversion, back-arc basin formation, arc-arc accretion, subduction and collision (e.g. Windley, 1993; Condie, 2000; Zhai and Santosh, 2011; Santosh et al., 2015).

As one of the major ancient cratonic nuclei in eastern Eurasia, the NCC preserves a complex history of crustal evolution, cratonization and stabilization (Zhai and Santosh, 2011; Zhai, 2014). The widespread metamorphic ages (~1.85 Ga) from the Trans-North China Orogen (TNCO), a major collisional zone that sutured the crustal blocks within the NCC, is considered to mark the final cratonization event (e.g. Kröner et al., 2005a; Wang, 2009; Trap et al., 2012; Zhao et al., 2012; Yang and Santosh, 2015), accompanied by syn-subduction to post-collisional slab break off and magmatism (Teng and Santosh, 2015). However, the tectonic evolution of the NCC prior to this collision remains debated. Zhao et al. (2012) proposed that the TNCO represents a long-lived magmatic arc developed during the eastward subduction of the Eastern Block during 2.56-1.88 Ga. Zhai and Santosh (2011) suggested that the initial cratonization of the NCC occurred at ~2.5 Ga, followed by rifting, subduction, accretion and collision events during 2.3-1.82 Ga. However, some other models assumed two stages of Paleoproterozoic west-ward subduction-collision events at ~2.1 Ga and 1.9-1.8 Ga (Faure et al., 2007; Trap et al., 2007, 2008, 2012), Neoproterozoic assembly of the NCC represented by a continent-arc-continent collision orogen (the Central Orogenic Belt) (Kusky and Li, 2003; Li and Kusky, 2007) or the closure of an arc – back arc system within the TNCO during 2.3-1.9 Ga (Wang, 2009;

Wang et al., 2010) have also been suggested. Santosh (2010) proposed a double-side subduction model with an oblique east- to south-ward subduction of the Yinshan Block and a west-ward subduction of the Yanliao Block (Eastern Block).

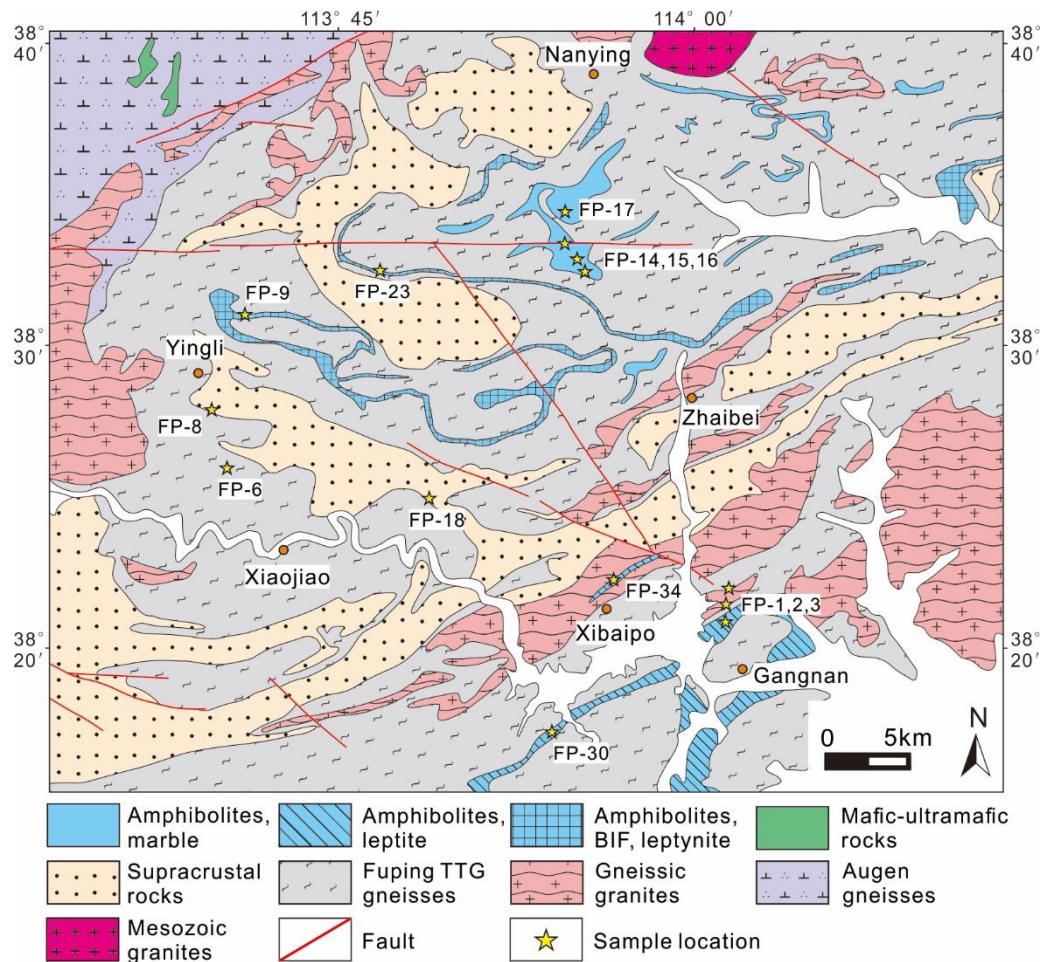


Fig. 4-1 (a) Geological sketch map of the Hengshan-Wutai-Fuping Complexes. (b) Geological map of the Fuping Complex within the Trans-North China Orogen (modified after Cheng et al., 2004), showing major lithological units, their relationships and sampling locations.

One of the key controversial issues in the debates above is whether the TNCO was in a compressional setting (e.g. Wilde et al., 2005; Zhao et al., 2005, 2012; Liu et al., 2009; Wang, 2009; Trap et al., 2012; Santosh et al., 2015) or in an extensional setting (e.g. Yang et al., 2011; Zhai and Santosh, 2011; Zhao et al., 2011; Xie et al., 2012; Zhang et al., 2011; Wei et al., 2014) during 2.0-2.1 Ga. This study thus presents new geochemical, zircon U-Pb geochronological and Lu-Hf isotope data on granitoids, amphibolites and metasedimentary rocks from the Fuping Complex in the TNCO. Combined with previous lithological, geochemical and geochronological

data, this study proposes a new model that provides insights into the understanding of the Paleoproterozoic tectonic evolution history of the TNCO.



Fig. 4-2 Representative field photographs of the different rock types in the Fuping Complex. (a) Relationship between gneissic granite (FP-1-1) and amphibolite (FP-1-2); (b) gneissic syenogranite (FP-3); (c) epidote-biotite schist (FP-8) of the Wanzi supracrustal assemblage; (d) mica schist (FP-18) of the Wanzi supracrustal assemblage; (e) BIF and amphibolite (FP-9-2); (f) amphibolite in association with marble (FP-15).

4.2 Sample description

In this study, eighteen representative samples were collected from the southern part of the FPC (Fig. 4-1). These include four gneissic granites, one gneissic syenogranite, two schists and eleven amphibolites (Table 4-1). The gneissic granites are pink colored, medium grained, weakly foliated (Fig. 4-2a) and characterized by the mineral assemblage of plagioclase + quartz + K-feldspar + biotite + rutile + magnetite (Fig. 4-3a). The gneissic syenogranite (FP-3) is medium- to coarse-grained and slightly foliated with an assemblage of K-feldspar + quartz +

plagioclase + biotite + magnetite (Fig. 4-2b, 4-3b). The two metasedimentary rock samples are epidote biotite schist (FP-8) and mica-schist (FP-18), showing well-developed foliations and lineation defined by plagioclase + quartz + biotite assemblage (Fig. 4-2c, 4-2d, 4-3f). The amphibolites are exposed as bands or boudins and show various associations including with leptite and gneissic granite (five samples, Fig. 4-2a), as thick layers with BIF (two samples, Fig. 4-2e) and as disrupted bands or blocks with metacarbonates (marble) (four samples, Fig. 4-2f). The amphibolites are fine to medium grained and in grayish green in color, with hornblende and plagioclase defining prominent lineation (Fig. 4-3, c-e).

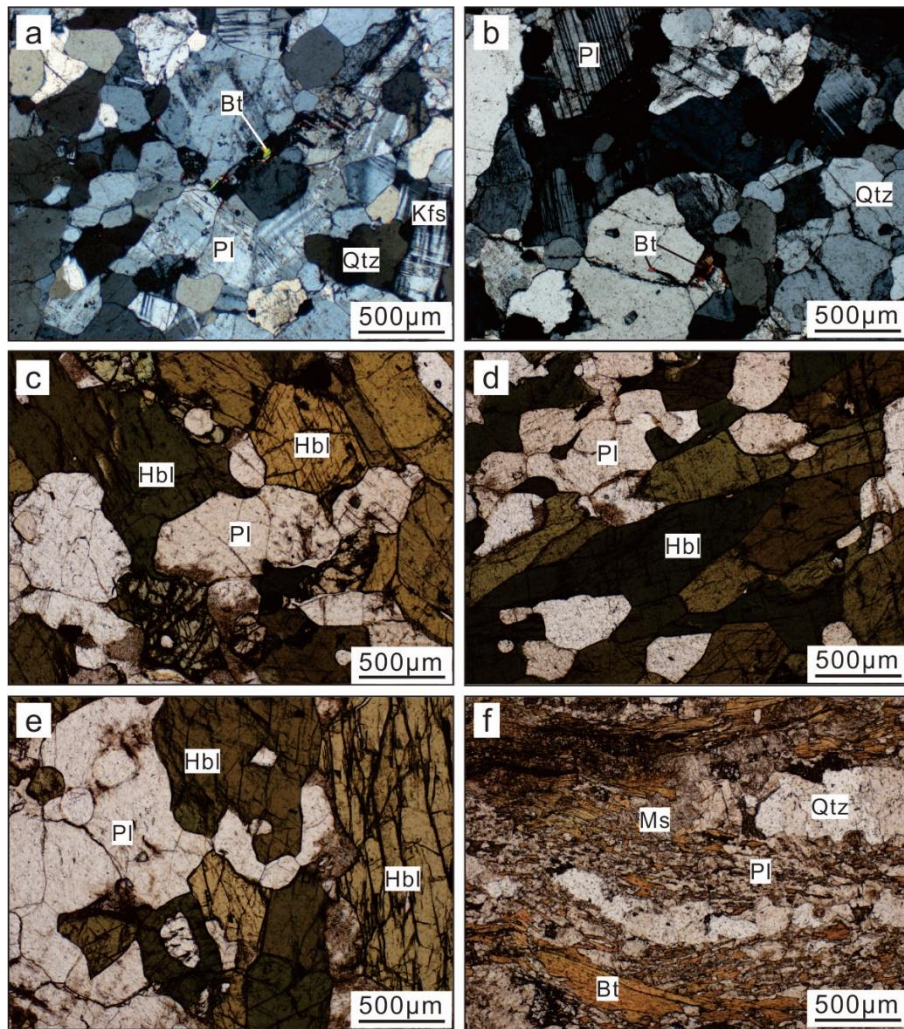


Fig. 4-3 Photomicrographs of major rock types from the Fuping Complex. (a) Gneissic granite (FP-1-1); (b) gneissic syenogranite (FP-3); (c) amphibolite (FP-1-2), associated with leptite and gneissic granite; (d) amphibolite (FP-9-2) associated with BIF; (e) amphibolite (FP-15) occurring in association with marble; (f) mica schist (FP-18).

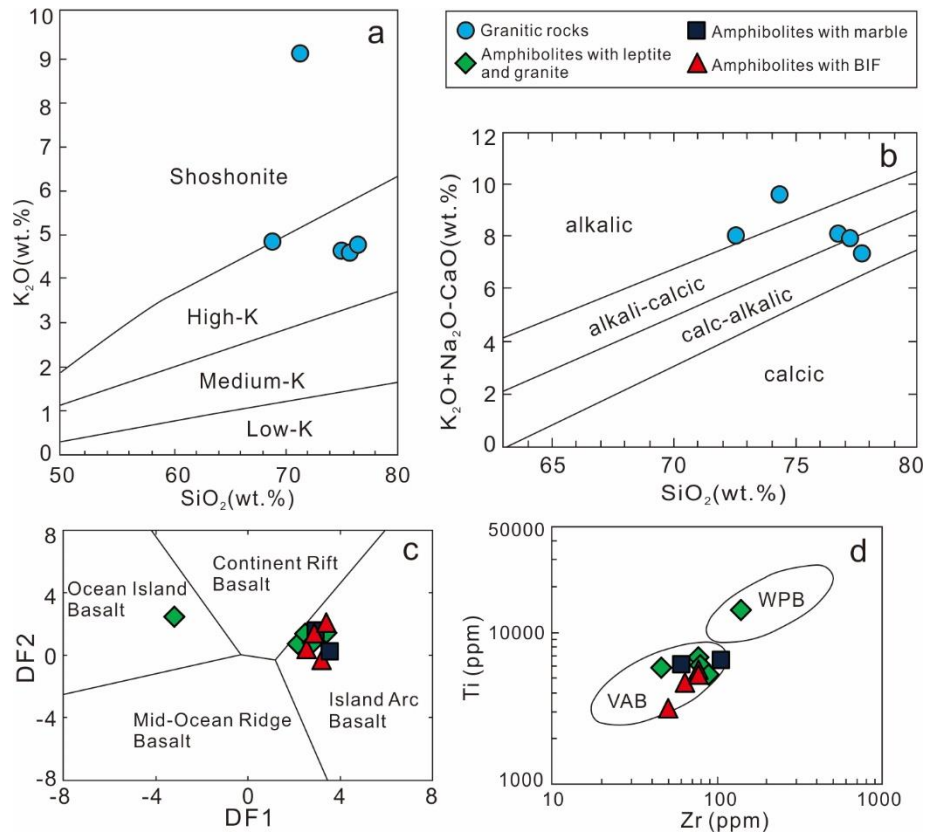


Fig. 4-4 Plots of SiO_2 versus K_2O (a) and SiO_2 versus $\text{K}_2\text{O}+\text{Na}_2\text{O}-\text{CaO}$ (b) for the granitic rock samples, reference lines after [Frost et al. \(2001\)](#); (c) log-ratio discriminant function major element tectonic plot of [Verma et al. \(2006\)](#) for the basic rocks. $\text{DF1} = -4.6761\ln(\text{TiO}_2/\text{SiO}_2) + 2.5330\ln(\text{Al}_2\text{O}_3/\text{SiO}_2) - 0.3884\ln(\text{Fe}_2\text{O}_3/\text{SiO}_2) + 3.9688\ln(\text{FeO}/\text{SiO}_2) + 0.8980\ln(\text{MnO}/\text{SiO}_2) - 0.5832\ln(\text{MgO}/\text{SiO}_2) - 0.2896\ln(\text{CaO}/\text{SiO}_2) - 0.2704\ln(\text{Na}_2\text{O}/\text{SiO}_2) + 1.080\ln(\text{K}_2\text{O}/\text{SiO}_2) + 0.1845\ln(\text{P}_2\text{O}_5/\text{SiO}_2) + 1.5445$. $\text{DF2} = 0.6751\ln(\text{TiO}_2/\text{SiO}_2) + 4.5895\ln(\text{Al}_2\text{O}_3/\text{SiO}_2) + 2.0897\ln(\text{Fe}_2\text{O}_3/\text{SiO}_2) + 0.8514\ln(\text{FeO}/\text{SiO}_2) - 0.4334\ln(\text{MnO}/\text{SiO}_2) + 1.4832\ln(\text{MgO}/\text{SiO}_2) - 2.3627\ln(\text{CaO}/\text{SiO}_2) - 1.6558\ln(\text{Na}_2\text{O}/\text{SiO}_2) + 0.6757\ln(\text{K}_2\text{O}/\text{SiO}_2) + 0.4130\ln(\text{P}_2\text{O}_5/\text{SiO}_2) + 13.1639$; (d) Ti-Zr discrimination diagram ([Pearce, 1996](#)), WPB: within-plate basalt, VAB: volcanic arc basalt.

4.3 Analytical results

4.3.1 Major and trace elements

Field and petrographic observations indicate that the amphibolites in the FPC underwent amphibolite facies metamorphism and were little altered (Fig. 4-2, 4-3). Therefore, the concentrations of the fluid-mobile elements (e.g. Na, K, Ca, Rb, Sr, Cs and Ba) may have been affected during the metamorphic event. This study prefers

to use the immobile elements (e.g. HFSEs and REEs) and transitional elements to evaluate the geochemical feature, petrogenesis and tectonic setting of the amphibolites. Whole-rock geochemical results of four gneissic granites, one gneissic syenogranite and eleven amphibolites are given in Table 4-2.

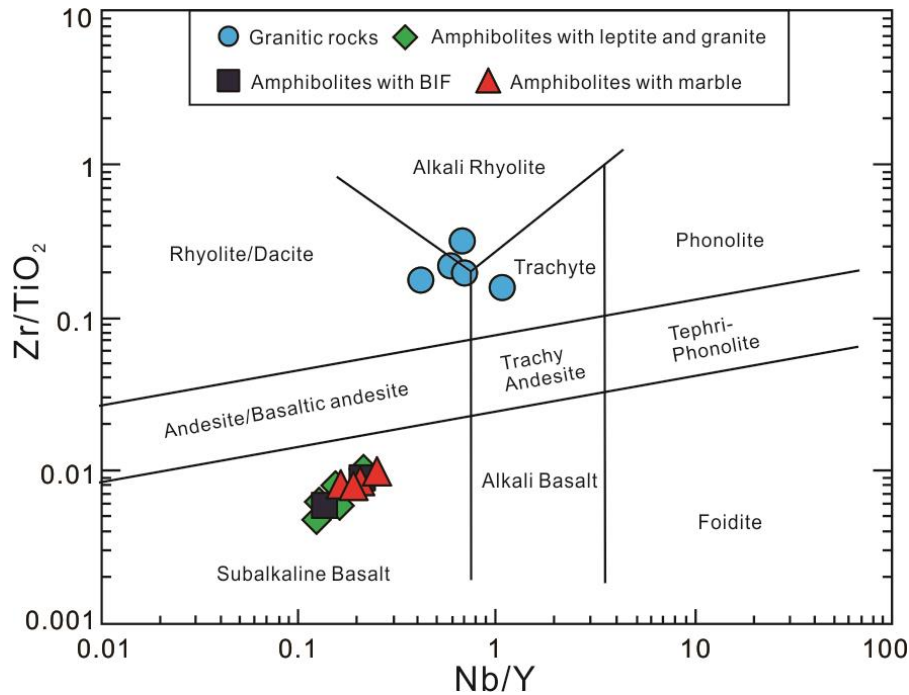


Fig. 4-5 Zr/TiO₂ versus Nb/Y classification diagram (Pearce, 1996) for the rock samples from the Fuping Complex.

4.3.1.1 Nanying gneissic granites

The four gneissic granites and one gneissic syenogranite show high silica contents with SiO₂ ranging from 72.53 to 77.67 wt.%. The rocks are enriched in K₂O (5.09-9.22 wt.%) and plot in the high-K to shoshonitic field on the SiO₂ versus K₂O plot (Fig. 4-4). They display varying Na₂O (0.64-3.60 wt.%), low CaO (0.15-0.82 wt.%), moderate Al₂O₃ (11.08-12.71 wt.%) and A/CNK (0.96-1.08). On the SiO₂ versus K₂O+Na₂O-CaO plot, most of the granitic samples fall in the alkali-calcic and alkali fields (Fig. 4-4). The granitic samples show similar compositions plotting in the fields of rhyolite, dacite and trachyte (Fig. 4-5). In the chondrite-normalized REE distribution patterns, the granitoids exhibit enriched LREE and flat HREE patterns with strong negative Eu anomalies ($\delta\text{Eu}=0.12\text{-}0.53$). In the primitive mantle-normalized trace elements multi-element variation diagram, they

show enrichment of Rb and HFSEs (e.g. Th, Ce, Zr and Hf) and depletion in Sr, Ba, Nb, P and Ti.

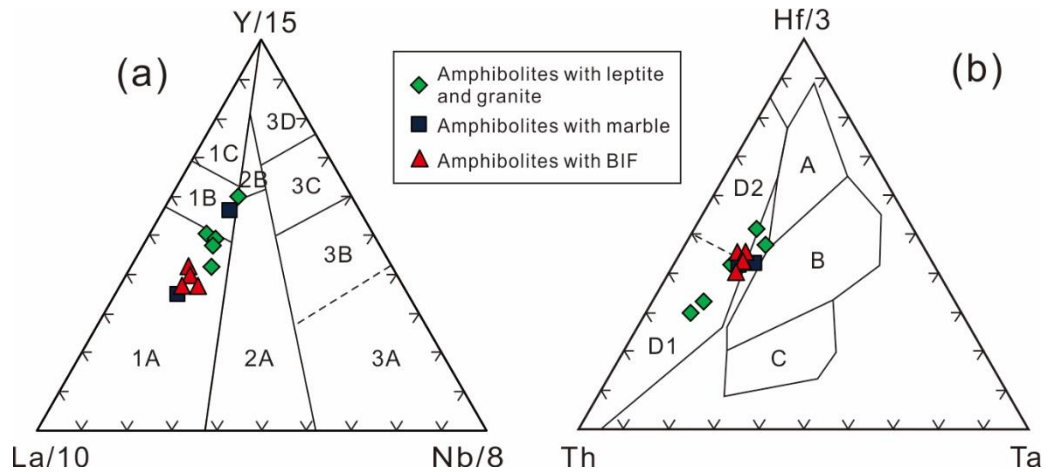


Fig. 4-6 Triangular diagrams showing compositions of amphibolites. (a) Plots of La/10-Y/15-Nb/8, 1A: calc-alkali basalt; 1C: volcanic-arc tholeiite; 1B: overlapped field of 1A and 1C; 2A:continental basalt; 2B: back-arc basin basalt; 3A: alkalic basalt from intercontinental rift; 3B: enriched E-type MORB; 3C: weakly enriched E-type MORB; 3D: N-type MORB (Cabanis and Lecolle, 1989). (b) Th-Hf-Ta diagram (after Wood, 1980), A: N-MORB, B: E-MORB and within plate tholeiite, C: within plate alkalic basalt, D1: calc-alkaline basalt ($Hf/Th < 3$), D2: island arc tholeiite ($Hf/Th > 3$).

4.3.1.2 Amphibolites

The amphibolites from the FPC display moderate SiO_2 (47.10-51.48 wt.%), varying MgO (4.47-12.06 wt.%), FeO^T (8.12-15.71 wt.%), $Mg\#$ (35.20-73.43) and TiO_2 (0.50-2.32 wt.%). All of the amphibolite samples are classified as subalkaline basalt on the Zr/TiO_2 versus Nb/Y diagram (Fig. 4-5), which is used as an immobile element proxy for the TAS diagram (e.g. Pearce, 1996). Ten amphibolites fall in the island arc basalt field and one amphibolite associated with leptonite/gneissic granite (FP-33-1) fall in the ocean island basalt field in the DF1 versus DF2 diagram (Verma et al., 2006) (Fig. 4-4c). On the Ti-Zr diagram (Pearce, 1996), nearly all sample fall in the field of volcanic arc basalt (Fig. 4-4d). On the La-Y-Nb ternary discrimination diagram (Cabanis and Lecolle, 1989), the amphibolite samples display mostly volcanic arc basalt character (Fig. 4-6a). On the Th-Hf-Ta diagram (Wood, 1980), the samples show affinity with island arc tholeiite and calc-alkaline basalt (Fig. 4-6b).

The metabasaltic rocks show varying LREE enrichment ($[La/Yb]_N=1.55-8.06$) and without discernible Eu anomalies ($\delta Eu=0.82-0.99$) (Fig. 4-7c) in the chondrite-normalized REE patterns (Sun and McDonough, 1989). In the primitive mantle-normalized trace element multi-element variation diagram (Fig. 4-7d), the metabasaltic rocks show enrichment in K, Rb, Ba, P, Ce and Sm and depletion in Nb, Ta, Zr and Hf.

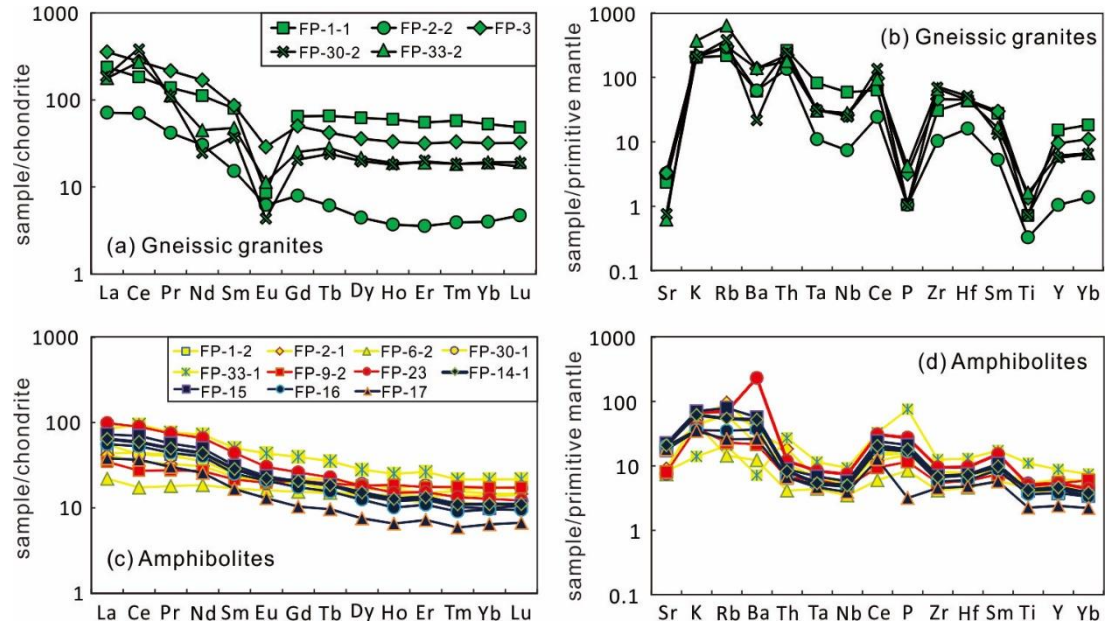


Fig. 4-7 Chondrite-normalized REE patterns (a, c) and primitive mantle-normalized trace elements multi-element variation diagram (b, d) for the granitic rocks and amphibolites from the Fuping Complex. The normalization values are from Sun and McDonough (1989).

4.3.2 Zircon U-Pb geochronology

The zircon U-Pb age data from two gneissic granites, two amphibolites and two meta-sedimentary rocks from the FPC are given in Table 4-3, and zircon REE results are given in Table 4-4.

4.3.2.1 Nanying gneissic granites

Zircon grains in sample FP-1-1 are euhedral to subhedral and show short prismatic or irregular morphology. They are light brown to colorless, and translucent. The grains range in size between 40 μm and 200 μm and show length to width ratios of 2:1 to 1:1. In CL images, most of the grains show oscillatory zoning, with few zircon grains displaying core-rim texture (Fig. 4-8a). A total of twenty-two

spots were analyzed from twenty-two zircon grains (Fig. 4-8b). Eighteen spots on the cores or oscillatory zoned domains form a coherent group and fall along a discordia line, yielding weight mean $^{207}\text{Pb}/^{206}\text{Pb}$ age of 2050 ± 21 Ma (MSWD = 0.12) with Th/U ratios of 0.38-1.25. Four spots on the rim domains define another group and yield weight mean $^{207}\text{Pb}/^{206}\text{Pb}$ age of 1891 ± 44 Ma (MSWD = 0.79), with Th/U ratios range 0.14-0.40 (three spots show Th/U ratios 0.14-0.26). The results suggest that the protolith of the gneissic granite (FP-1-1) crystallized at ca. 2050 Ma and was metamorphosed at ca. 1891 Ma. The zircon trace element results exhibit fractionated REE patterns with LREE depletion and HREE enrichment, and obvious negative Eu anomalies (Fig. 4-11a).

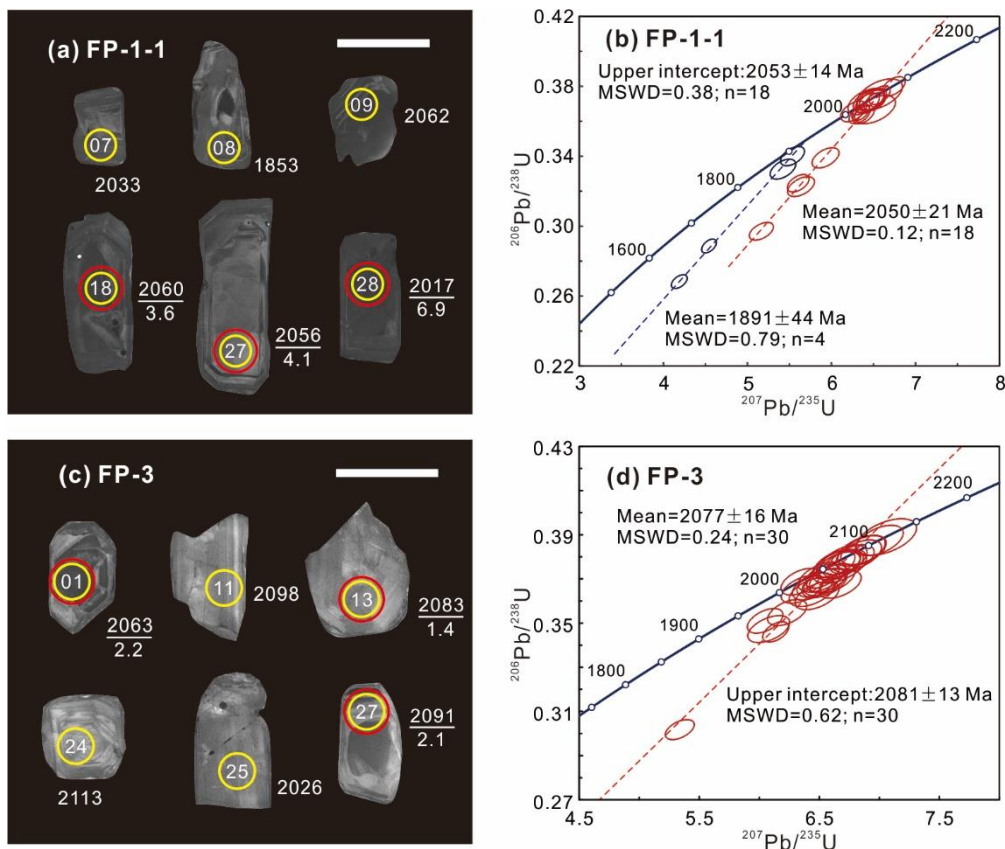


Fig. 4-8 Representative CL images (a, c) of zircons and concordia plots (b, d) of the gneissic granite (FP-1-1) and gneissic syenogranite (FP-3). Scale bars are 100 μm .

Zircon grains in sample FP-3 are translucent, and light brown to colorless. The euhedral to subhedral grains show prismatic or irregular morphology with size range of 50-250 μm and length to width ratios of 2.5:1 to 1:1. In CL images, most zircons show oscillatory zoning or heterogeneous fractured domains (Fig. 4-8c), suggesting

magmatic crystallization. A total of thirty spots were analyzed from thirty magmatic zircon grains (Fig. 4-8d). All of the spots form a coherent group yielding weighted mean $^{207}\text{Pb}/^{206}\text{Pb}$ age of $2077 \pm 16 \text{ Ma}$ (MSWD = 0.24), with Th/U ratios range from 0.27 to 0.84 (mean 0.65). The ca. 2.08 Ga is interpreted as the crystallization age of the protolith of the Nanying gneissic granite (FP-3). The zircon trace element results display fractionated REE patterns with LREE depletion and HREE enrichment, and obvious negative Eu anomalies (Fig. 4-11b).

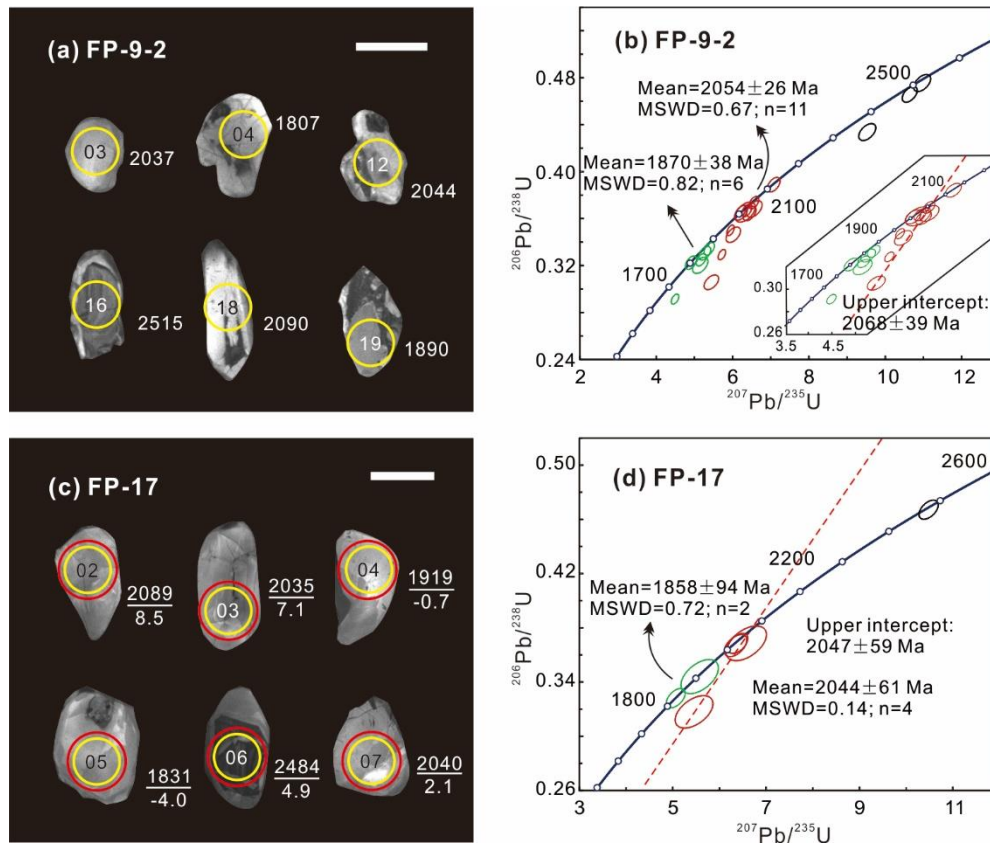


Fig. 4-9 Representative CL images (a, c) of zircons and concordia plots (b, d) of the amphibolites (FP-9-2 and FP-17). Scale bars are 50 μm .

4.3.2.2 Amphibolites

Zircon grains in sample FP-9-2 are small (20-100 μm), subhedral to anhedral with irregular or near spherical morphology. They are colorless and translucent. In CL images, most zircons are structureless, and some grains show core-rim texture with dark core and light bright rim (Fig. 4-9a). A total of twenty spots were analyzed from twenty zircon grains (Fig. 4-9b). Eleven spots on the heterogeneous fractured domains are distributed along a discordia and yield weighted mean

$^{207}\text{Pb}/^{206}\text{Pb}$ age of 2054 ± 26 Ma (MSWD = 0.67), with Th/U ratios range from 0.18 to 1.77 (mean 1.06). Six spots on the rim domains form another group near the concordia, yielding weighted mean $^{207}\text{Pb}/^{206}\text{Pb}$ age of 1870 ± 38 Ma (MSWD = 0.82), with Th/U ratios ranging from 0.09 to 0.41 (five spots show Th/U=0.09-0.26). The other analyses (spots 16, 23, 27) made on dark cores give $^{207}\text{Pb}/^{206}\text{Pb}$ age range from 2449 ± 41 Ma to 2530 ± 39 Ma and high Th/U ratios (0.37-0.91). These dark cores are interpreted to represent xenocrystic zircons and the protolith of the amphibolite (FP-9-2) is inferred to have crystallized at ca. 2054 Ma, followed by metamorphism at ca. 1870 Ma. The zircon trace element data show fractionated REE patterns with LREE depletion and HREE enrichment, and variable Eu anomalies (Fig. 4-11c).

Zircon grains in sample FP-17 are translucent and colorless. The subhedral to anhedral grains show irregular or near spherical morphology with size of 40-120 μm , and length to width ratios of 2.5:1 to 1:1. In CL images, most of the zircons are structureless, and some grains show core-rim texture with dark core and light bright rim (Fig. 4-9c). A total of seven spots were analyzed from seven zircon grains (Fig. 4-9d). Four spots on the heterogeneous fractured domains define a group that gives a weighted mean $^{207}\text{Pb}/^{206}\text{Pb}$ age of 2044 ± 61 Ma (MSWD = 0.14) with Th/U=0.25-1.70. Two spots on the structureless and rim domains display $^{207}\text{Pb}/^{206}\text{Pb}$ ages of 1919 ± 87 Ma and 1831 ± 57 Ma respectively, with weighted mean $^{207}\text{Pb}/^{206}\text{Pb}$ age of 1858 ± 94 Ma (MSWD = 0.72) and Th/U ratios of 0.02-0.35. The remaining spot (spot 6) was analyzed at core domain and shows $^{207}\text{Pb}/^{206}\text{Pb}$ age of 2484 ± 39 Ma (Th/U=1.06), which might represent a xenocrystic core. The results suggest that the protolith of the amphibolite (FP-17) crystallized at ca. 2044 Ma followed by metamorphism at 1858 Ma. The zircon trace element results exhibit fractionated REE patterns with LREE depletion and HREE enrichment, and slightly negative Eu anomalies (Fig. 4-11d).

4.3.2.3 Wanzi supracrustal assemblages

The detrital zircons in epidote biotite schist sample FP-8 are subhedral to anhedral, light brown to colorless and translucent. The grains show near spherical morphology with size of 50-200 μm , and length to width ratios of 2:1 to 1:1. They

display oscillatory zoning in CL images (Fig. 4-10a), suggesting igneous provenance. A total of thirty-two spots were analyzed from thirty-two magmatic zircon grains (Fig. 4-10b). The dominant population shows $^{207}\text{Pb}/^{206}\text{Pb}$ ages from 2433 ± 46 Ma to 2554 ± 42 Ma with peak at 2502 ± 18 Ma (Fig. 4-10b). Four spots define another population with $^{207}\text{Pb}/^{206}\text{Pb}$ ages ranging from 2013 ± 40 Ma to 2052 ± 41 Ma and peak at 2031 ± 40 Ma. One grain with a concordant age of 1955 ± 44 Ma ($\text{Th}/\text{U}=0.45$) was also obtained from this sample (Fig. 4-10a). The zircon trace element results display fractionated REE patterns with LREE depletion and HREE enrichment, and variable Eu anomalies (Fig. 4-11e).

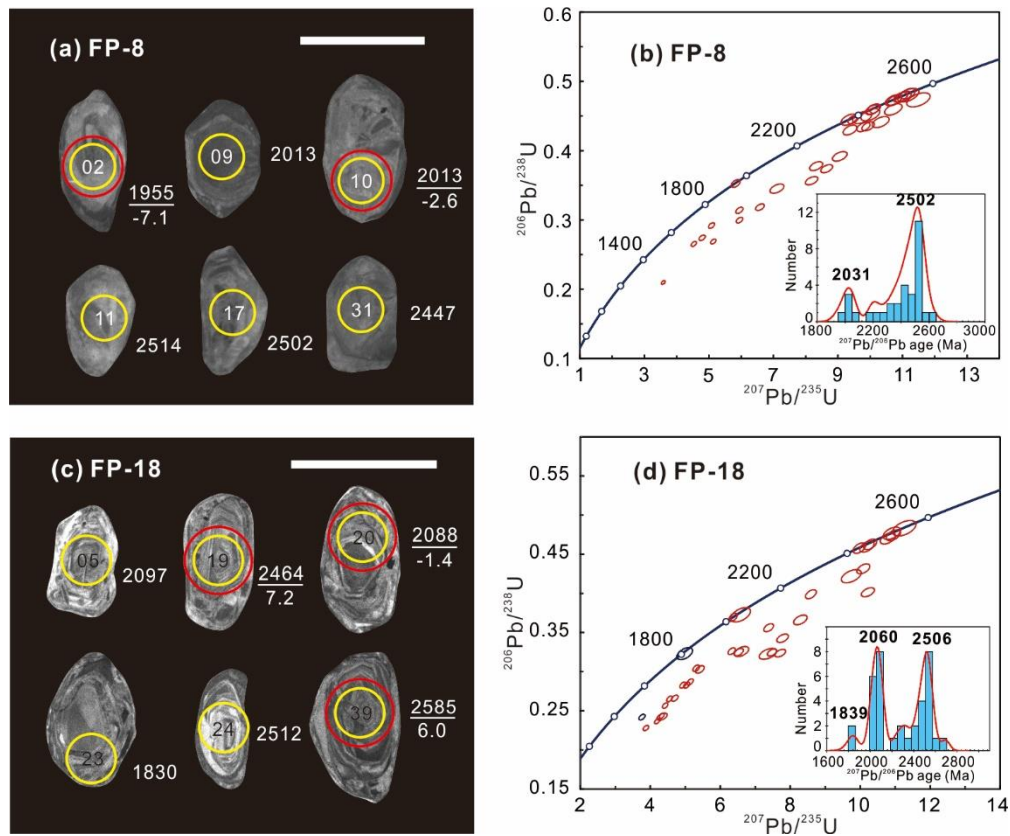


Fig. 4-10 Representative CL images (a, c) of zircons and concordia plots (b, d) of the epidote-biotite schist (FP-8) and mica schist (FP-18). Scale bars are 100 μm .

The detrital zircons in mica-schist sample FP-18 are also subhedral to anhedral and well rounded. The near spherical grains are light brown to colorless and translucent with size of 40-150 μm , and length to width ratios of 2:1 to 1:1. In CL images, most zircons showing oscillatory zoning or heterogeneous fractured domains and few zircons displaying core-rim textures (Fig. 4-10c). A total of thirty-six spots

were analyzed from thirty-six zircon grains (Fig. 4-10d). The results define two major populations with $^{207}\text{Pb}/^{206}\text{Pb}$ ages in the range of 2416 ± 38 Ma to 2585 ± 39 Ma and from 2004 ± 41 Ma to 2097 ± 39 Ma, with peaks at 2506 ± 26 Ma and 2060 ± 22 Ma, respectively. Two spots which were analyzed at the rim domains give $^{207}\text{Pb}/^{206}\text{Pb}$ ages of 1830 ± 62 Ma ($\text{Th}/\text{U}=0.05$) and 1844 ± 45 Ma ($\text{Th}/\text{U}=0.09$). The zircon trace element results exhibit fractionated REE patterns with LREE depletion and HREE enrichment, and variable Eu anomalies (Fig. 4-11f).

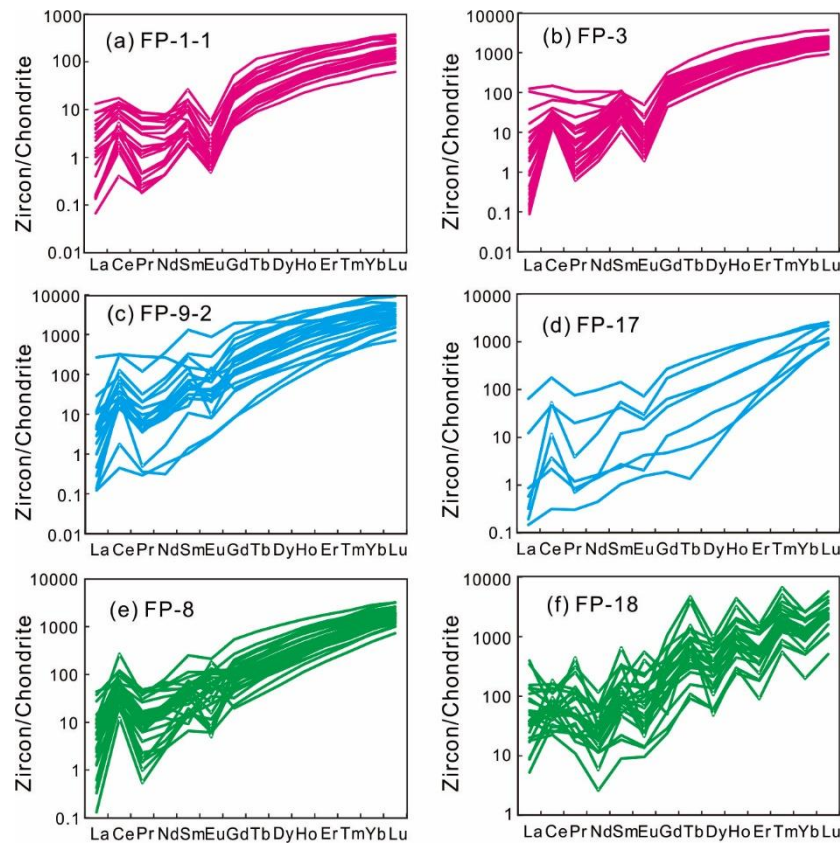


Fig. 4-11 Chondrite-normalized REE patterns of zircons in samples FP-1-1 (a), FP-3 (b), FP-9-2 (c), FP-17 (d), FP-8 (e) and FP-18 (f).

4.3.3 Zircon Lu-Hf isotopes

4.3.3.1 Nanying gneissic granites

Zircons from sample FP-1-1 show variable initial $^{176}\text{Hf}/^{177}\text{Hf}$ ratios in the range of 0.281509 to 0.281828, Their $\epsilon_{\text{Hf}}(t)$ values range from 0.3 to 6.9, with Paleoproterozoic T_{DM} (2170-2415 Ma) and Archean-Paleoproterozoic T_{DM}^{C} (2226-2639 Ma) values (Table 4-5, Fig. 4-12). The dominant positive $\epsilon_{\text{Hf}}(t)$ values

suggest that the parental magma was derived from the Archean-Paleoproterozoic juvenile components.

Zircons from sample FP-3 show a tight range of initial $^{176}\text{Hf}/^{177}\text{Hf}$ ratios vary from 0.281536 to 0.281672, $\epsilon_{\text{Hf}}(t)$ values from 0.6 to 3.0, yielding Paleoproterozoic T_{DM} (2338-2429 Ma) and Archean-Paleoproterozoic T_{DM}^{C} (2492-2637 Ma) (Table 4-5, Fig. 4-12). The dominant positive $\epsilon_{\text{Hf}}(t)$ values suggest that the parental magma was sourced from the Archean-Paleoproterozoic juvenile components.

4.3.3.2 Amphibolites

Six zircons were analyzed from sample FP-17 for Lu-Hf isotopes. The ~ 2044 Ma zircons show initial $^{176}\text{Hf}/^{177}\text{Hf}$ ratios of 0.281553-0.281778, $\epsilon_{\text{Hf}}(t)$ values of 2.1-8.5, and T_{DM}^{C} of 2124-2522 Ma. One spot with the age of 2484 Ma shows initial $^{176}\text{Hf}/^{177}\text{Hf}$ ratio of 0.281372, positive $\epsilon_{\text{Hf}}(t)$ value (4.9) and T_{DM}^{C} of 2690 Ma. Two spots were analyzed at the metamorphic rims, which display relatively lower $\epsilon_{\text{Hf}}(t)$ values from -4.0 to -0.7 and T_{DM}^{C} varying from 2552-2753 Ma (Table 4-5, Fig. 4-12). The zircon grains in sample FP-9-2 are too tiny for Lu-Hf isotopic analyses.

4.3.3.3 Wanzi supracrustal assemblages

Eight zircons were analyzed from sample FP-8 for Lu-Hf isotopes. The ~2502 Ma zircons show positive $\epsilon_{\text{Hf}}(t)$ values (3.1 to 7.9), T_{DM} of 2513-2693 Ma and T_{DM}^{C} in the range of 2520-2811 Ma. Compared to the ~2506 Ma zircons, the ~2031 Ma zircons show relatively lower $\epsilon_{\text{Hf}}(t)$ values varying from -2.6 to -1.9 and T_{DM}^{C} of 2759-2801 Ma. The remaining 1955 Ma grain shows negative $\epsilon_{\text{Hf}}(t)$ value of -7.1 and T_{DM}^{C} in the range of 3021 Ma (Table 4-5, Fig. 4-12).

Eight zircons were analyzed from sample FP-18 for Lu-Hf isotopes. Four zircons with ages of ~2502 Ma show positive $\epsilon_{\text{Hf}}(t)$ values (6.0-7.5), T_{DM} of 2466-2516 Ma, and T_{DM}^{C} of 2710-2800 Ma. Compared to the ~2506 Ma zircons, the four younger zircons 2031 Ma show relatively lower $\epsilon_{\text{Hf}}(t)$ values varying from -2.2 to -0.8, T_{DM} of 2530-2563 Ma, and T_{DM}^{C} of 2544-2640 Ma (Fig. 4-12).

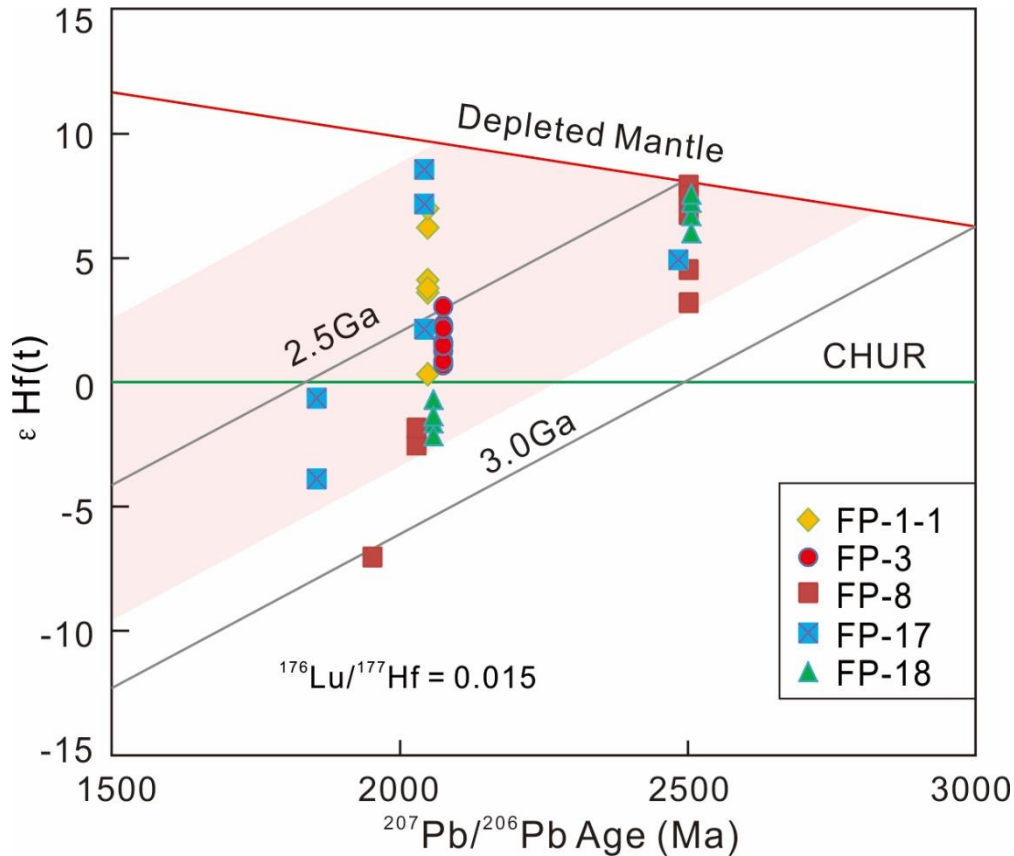


Fig. 4-12 $\epsilon_{\text{Hf}}(t)$ versus $^{207}\text{Pb}/^{206}\text{Pb}$ age diagram of zircons in various rock types from the Fuping Complex.

4.4 Discussion

4.4.1 Petrogenesis

The amphibolites of the study are all subalkaline basalts in composition. Production of mafic magmas occurs in various geodynamic settings including subduction zones, mid-ocean ridges, continental rift zones, collisional belts or hot spots (e.g. Eyuboglu et al., 2011; Manikyamba and Kerrich, 2012). In the trace element discrimination diagrams, all the meta-basaltic samples fall in the field of island arc basalt or volcanic arc basalt field, suggesting convergent margin origin. Furthermore, these subduction-related mafic suite shows LILE and LREE enrichment compared to the HFSE and HREE, negative anomaly of Nb, Ta, Zr, Hf and Ti (Nakamura and Iwamori, 2009; Pearce and Robinson, 2010). In the primitive-mantle normalized (Sun and McDonough, 1989) trace element plot, the amphibolites display enrichment of K, Rb, Ce and Sm, and negative Nb, Ta, Zr and

Hf anomalies, further attesting to subduction zone setting.

The gneissic granites and gneissic syenogranite in this study show SiO₂ in the range of 72.53-77.67 wt.% and fall in the fields of high-K to shoshonite, and calc-alkalic to alkalic granite. All of the samples display relative enrichment in LREE as compared to HREE and relatively constant HREE patterns (Fig. 4-7a). In the primitive-mantle normalized (Sun and McDonough, 1989) trace element plot (Fig. 4-7b), they show enrichment of K, Rb and Ce, and obvious negative P and Ti anomaly. In the Nb-Y diagram (Pearce et al., 1984), together with the results of Liu et al. (2005), most of the data fall in the field of volcanic arc + syn-collisional granite. The geochemical features of the granitic rocks are consistent with subduction-related arc affinity.

Han et al. (2012) suggested that the Nanying gneissic granites were derived from partial melting of 2.7 Ga crustal rocks and 2.5 Ga TTG gneisses, and that the 2.1 Ga magmatism represents only intracrustal recycling within the Fuping Complex. Ren et al. (2013) proposed that the 2.1-2.0 Ga zircons were correlated to the partial melting and migmatization. In the present study, zircons from the 2.1-2.0 Ga granitic rocks and amphibolites display positive $\epsilon_{\text{Hf}}(t)$ values varying from 0.3-8.5 and Hf crustal model ages (T_{DM}^{C}) ranging from 2124 to 2639 Ma. In contrast, the 2.1-2.0 Ga magmatic zircons in the Wanzi supracrustal assemblage show relatively lower $\epsilon_{\text{Hf}}(t)$ values (-0.8 to -2.6) and Hf crustal model ages (T_{DM}^{C}) of 2710-2801 Ma. The results indicate that the 2.1-2.0 Ga magma was sourced from the reworked 2.7-2.8 Ga crustal rocks and Neoproterozoic-Paleoproterozoic juvenile materials.

4.4.2 Formation of the Wanzi supracrustal rocks

The Wanzi supracrustal assemblage is composed of felsic- and pelitic- gneisses, pelitic-schists, calc-silicates and marbles. Previous investigators suggested that the supracrustal assemblage was deposited between 2.10 and 1.84 Ga (Xia et al., 2006). The deposition age was constrained by the youngest detrital zircon age and the metamorphic age of the metasedimentary rocks. Zircon U-Pb age results from the two schist samples show prominent age populations of 2450-2585 Ma and 2004-2097

Ma, suggesting that the Fuping TTG gneisses and Nanying gneissic granites could have served as the provenance of the Wanzi supracrustals, as also inferred in some previous studies (Xia et al., 2006). However, the youngest igneous detrital zircons from the studied samples yield a concordant age of 1955 ± 44 Ma (Th/U=0.45), and two metamorphic rims show $^{207}\text{Pb}/^{206}\text{Pb}$ ages of 1830 ± 62 Ma (Th/U=0.05) and 1844 ± 45 Ma (Th/U=0.09). These results further constrain the depositional age as 1.95-1.84 Ga for the Wanzi supracrustal assemblage. Thus, the Wanzi supracrustal assemblage was most likely deposited in an arc-related basin (fore-arc or back-arc basin), and the basin had not closed until 1.95 Ga.

4.4.3 Tectonic implications

The various rock types analyzed in this study including gneissic granite, amphibolites and schist show identical metamorphic ages varying from 1.89 to 1.83 Ga, which is in accordance with the ages of high grade metamorphism within the TNCO reported in earlier studies (Fig. 4-13; Zhao et al., 2012 and references there in). Therefore, the 1.89-1.83 Ga metamorphic event in the Fuping Complex can be correlated with the metamorphic event associated with the final collision between the Western Block and the Eastern Block along the TNCO.

The geochemical features and age data reported in this study suggest that the protoliths of the basement TTG gneisses of the Fuping-Wutai-Hengshan Complex were emplaced during 2.80-2.48 Ga (Fig. 4-13a). A major magmatic event during 2.1-2.0 Ga, has been recorded from the various complexes in the TNCO (Figs. 4-13b, 4-14). The 2.1-2.0 Ga granitic and metabasaltic suites in these complexes have been considered to have formed in subduction-related arc setting (Guan et al., 2002; Zhao et al., 2002a; Wilde et al., 2005; Liu et al., 2009; Santosh et al., 2016) or intra-plate rift setting (Yang et al., 2011; Zhao et al., 2011; Zhang et al., 2011; Peng et al., 2012b; Xie et al., 2012). Zircons in the granitic, metabasaltic, and metasedimentary samples from this study from the Fuping Complex record an important magmatic event at 2.09-2.03 Ga (Fig. 4-13a), which forms part of the widespread 2.1-2.0 Ga magmatism within the TNCO. The protolith magmas of the granitoids and metabasalts formed

in an arc or subduction related tectonic setting. Here this study proposes a tectonic model it is envisaged that subduction and continental rifting process occurred coevally among several micro-blocks (or complexes) within the TNCO during 2.1-2.0 Ga (Fig. 4-15b, c). The following tectonic processes are inferred during this period. (1) The Wutai Complex and the Fuping Complex were separated by the Longquanguan ocean, and the double subduction of the oceanic lithosphere resulted in arc magmatism. (2) Simultaneously, continental rifting developed in the Hengshan, Huai'an and Zanhuang Complexes. The proposed tectonic model is supported by the following lines of evidence.

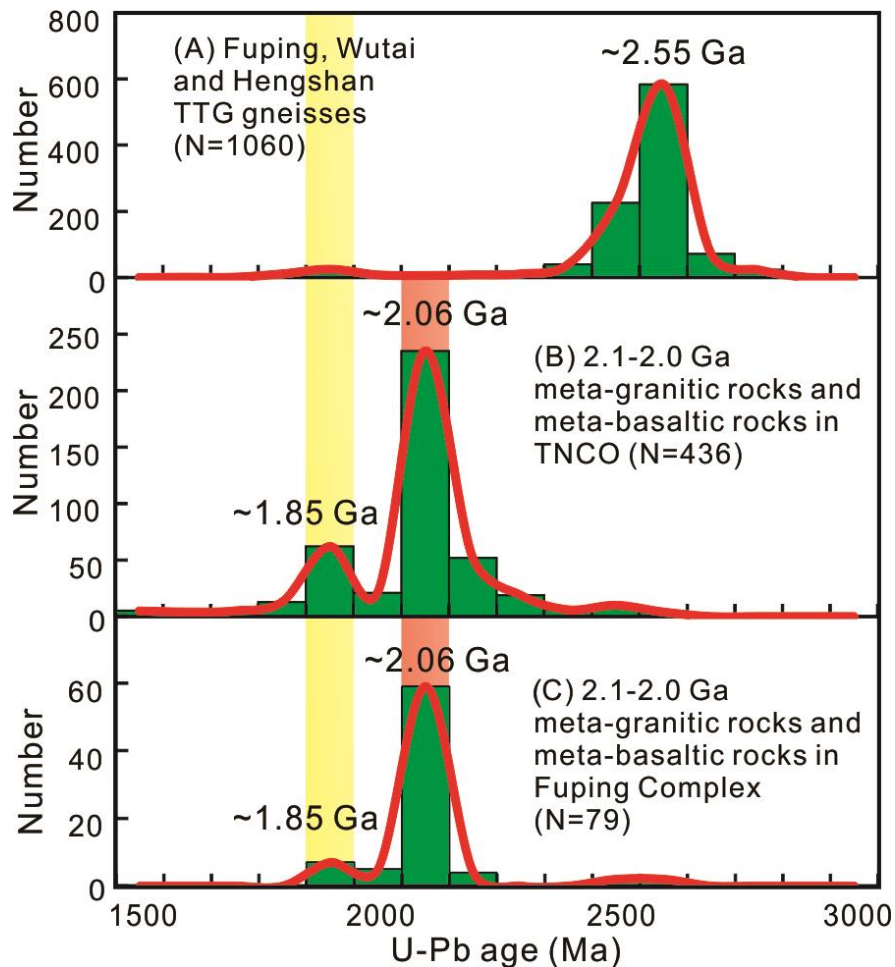


Fig. 4-13 Compiled zircon U-Pb ages. (A) Fuping, Wutai and Hengshan TTG gneisses (Data source: Guan et al., 2002; Zhao et al., 2002a, 2007, 2011; Kröner et al., 2005b; Wilde et al., 2004, 2005; Lu et al., 2014b), (B) 2.1-2.0 Ga meta-granitic and meta-basaltic rocks in the TNCO (Data source from Table 4-6), (C) 2.1-2.0 Ga meta-granitic and meta-basaltic rocks from this study.

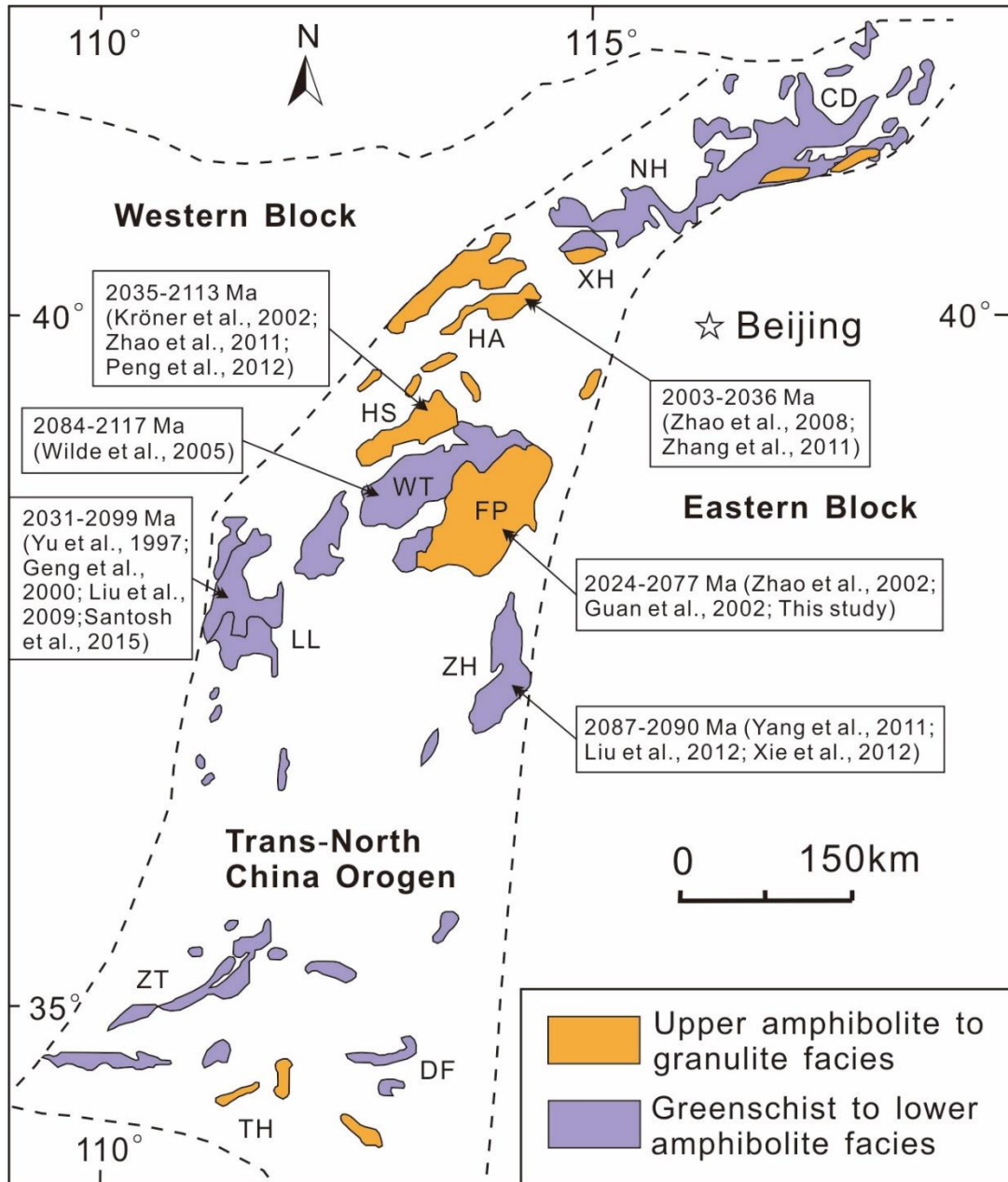


Fig. 4-14 Zircon U-Pb ages of 2.1-2.0 Ga meta-granitic and meta-basaltic rocks within the TNCO (after Zhao and Zhai, 2013). Abbreviations: CD, Chengde; NH, Northern Hebei; XH, Xuanhua; HA, Huai'an; HS, Hengshan; WT, Wutai; FP, Fuping; LL, Lüliang; ZH, Zanhuang; ZT, Zhongtiao; DF, Dengfeng; TH, Taihua.

(1) The common presence of 2.12-2.02 Ga arc magmatism in the Fuping, Wutai and Lüliang Complexes (Table 4-6, Fig. 4-14). In the Fuping Complex, Zhao et al. (2002a) reported SHRIMP U-Pb ages of 2077 ± 23 Ma and 2024 ± 21 Ma from granitic gneisses belonging to the Nanying granitoids, and suggested that these ages represent the timing of magmatism. Another granitic gneiss sample from the

Nanying granitic gneiss with SHRIMP U-Pb age of 2045 ± 64 Ma was reported by [Guan et al. \(2002\)](#). The granitoids and metabasalts in this study display ages in the tight range of 2044 ± 61 Ma to 2077 ± 16 Ma and show subduction-related arc features. In the Wutai Complex, [Wilde et al. \(2005\)](#) reported zircon SHRIMP U-Pb ages of 2117 ± 17 Ma, 2116 ± 16 Ma and 2084 ± 20 Ma from the pink phase of the Wangjiahui granite and Dawaliang granite, and interpreted that these granites were formed by the magmatic activity prior to collision. In the Lüliang Complex, the granitic, dioritic, and metabasaltic rocks show zircon U-Pb ages ranging from 2031 ± 47 Ma to 2070 ± 34 Ma ([Yu et al., 1997](#); [Geng et al., 2000](#); [Liu et al., 2009](#); [Santosh et al., 2016](#)). [Liu et al. \(2009\)](#) inferred that the granitoids in the Lüliang Complex were formed in a continental arc setting. [Santosh et al. \(2015\)](#) reported new zircon U-Pb ages of 2070 ± 34 Ma and 2053 ± 32 Ma on two meta-diorite samples and combined with geochemical features, proposed that these rocks form part of continental arc magmatism association with Paleoproterozoic convergent margin process.

(2) The occurrence of 2.09-2.00 Ga continent rift related magmatism in the Hengshan, Huai'an and Zanhuang Complexes (Table 4-6, Fig. 4-14). In the Hengshan Complex, [Zhao et al. \(2011\)](#) reported zircon U-Pb ages of 2052 ± 17 Ma to 2083 ± 15 Ma on four monzonitic granites and suggested these rocks might have formed in an extensional setting. [Peng et al. \(2012b\)](#) proposed that the 2035-2060 Ma Yixingzhai mafic dykes were emplaced in an intra-continental rifting setting. In the Huai'an Complex, [Zhang et al. \(2011\)](#) reported zircon U-Pb age of 2003 ± 24 Ma from garnet-bearing syenogranite sample, the geochemical features of which were correlated to ferro-potassic aluminous A-type granite which formed within intraplate extension or rift setting. In the Zanhuang Complex, [Yang et al. \(2011\)](#) reported 2090 ± 10 Ma ages from the Xuting granite which is characterized by compositional features of A-type granite generated within an extensional setting. [Xie et al. \(2012\)](#) reported zircon SHRIMP U-Pb ages of 2087 ± 16 Ma from a meta-basalt that shows affinity of within-plate basalt formed in an intra-continental environment.

(3) The Longquanguan thrust (LQGT) may represent the suture between the Fuping Complex and the Wutai Complex. The LGQT consists of a ~200 km long,

~2 km thick and NW-SE stretching ductile shear zone and incorporates both orthogneiss-volcanic units from the Fuping Complex and meta-pelitic rocks (Trap et al., 2012). The meta-pelitic rocks discontinuously exposed along the north-western side of the LGQT, represent the remnants of the oceanic sediments (Fig. 4-15a).

(4) The double subduction resulted in the closure of the Longquanguan ocean basin, and destruction of the oceanic crust, following soft collision between the Fuping Complex and the Wutai Complex without any high-grade metamorphism of continental crust and uplift/exhumation of high-grade metamorphic rocks. Such features are similar to typical divergent double subduction zones (e.g. Soesoo et al., 1997; Xiao et al., 2003; Zhao, 2014).

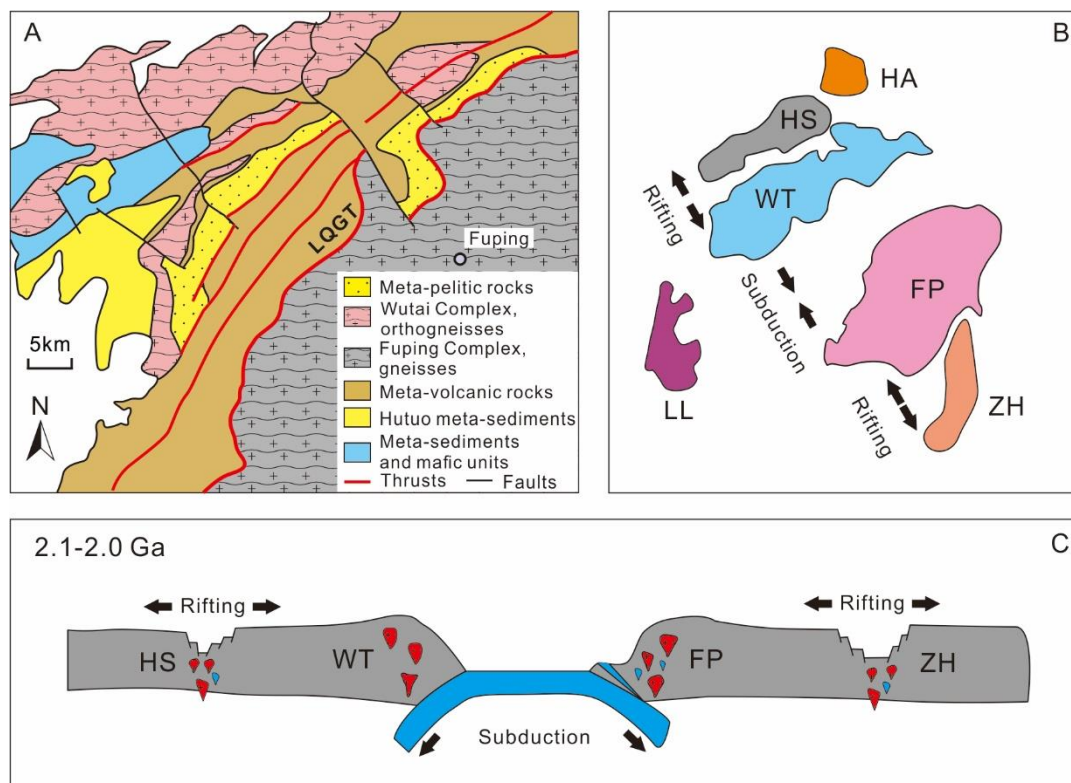


Fig. 4-15 (A) Lithotectonic map of the Wutai-Fuping area (after Trap et al., 2012). (B) Proposed tectonic model showing the amalgamation of different complexes in the central domain of the TNCO during 2.1-2.0 Ga. (C) Model for tectonic evolution of the middle part of the TNCO during 2.1-2.0 Ga. Abbreviations: HS, Hengshan; WT, Wutai; FP, Fuping; ZH, Zanhuang; LL, Lüliang; HA, Huai'an.

The Paleoproterozoic magmatism and continent building as recorded from the Fuping Complex is broadly coeval with similar features in the constituent fragments

of the Columbia supercontinent (Zhao et al., 2002b; Rogers and Santosh, 2002, 2009; Meert, 2012; Nance et al., 2014).

4.5 Conclusions

(1) This study reports widespread 2.1-2.0 Ga magmatism from a suite of granitoids, amphibolites and metasedimentary rocks in the Fuping Complex within the Trans-North China Orogen that sutures the Western and Eastern Blocks of the North China Craton. The geochemical features suggest that the protolith magmas of the amphibolites and granitic rocks were generated in an arc setting associated with the subduction of oceanic lithosphere. The 2.1-2.0 Ga magma was sourced from reworked 2.7-2.8 Ga crustal rocks and Neoproterozoic-Paleoproterozoic juvenile components.

(2) The two schist samples analyzed in this study yield prominent age populations of 2450-2585 Ma and 2004-2097 Ma, suggesting that the provenance of the Wanzi supracrustal sequences were largely sourced from the Fuping TTG gneisses and Nanying gneissic granites. The timing of deposition of the Wanzi supracrustal assemblage is constrained to be between 1.95 and 1.84 Ga.

(3) The tectonic model proposed in this study envisages simultaneous subduction and continental rifting process among several micro-blocks (or complexes) within the TNCO during 2.1-2.0 Ga. During the period of 2.1-2.0 Ga, 1) the Wutai Complex and the Fuping Complex were separated by the Longquanguan ocean, and the divergent double subduction of the oceanic lithosphere resulted in distinct arc magmatism; and 2) continental rift setting developed in the Hengshan, Huai'an and Zanhuang Complexes.

(4) The Paleoproterozoic arc magmatism in the Fuping Complex correlates with the continental building process in the crustal fragments of the Columbia supercontinent.

Chapter 5: Paleoproterozoic sedimentation in the Fuping and Zhanhuang Complexes

5.1 Introduction

Meta-carbonate rocks with geological attributes of marine sediments are important components in Precambrian orogenic belts (Veizer et al., 1989; Singh et al., 2016). Their stratigraphic features as well as isotopic and geochemical data have been used as important clues to unravel the depositional environment, and post-depositional tectonic activities (Veizer et al., 1992; Bau et al., 1999). Detrital zircon U-Pb dating can provide reliable geochronological constraints on the depositional age and provenance of impure meta-carbonate rocks (Tang et al., 2006; Tam et al., 2011). The most extensively used tracers for the depositional environment are the stable isotopes (carbon and oxygen) and trace elements, which are controlled mainly by the primary features of the marine water and biosphere (Veizer et al., 1992; Bau et al., 1999; Swart, 2015). Investigations combining detrital zircon U-Pb dating, geochemistry, C and O isotopes on meta-carbonates have been successfully applied to elucidate Precambrian tectonic processes (e.g. Tang et al., 2006; Paula-Santos et al., 2015).

The Trans-North China Orogen (TNCO) welding the Eastern and Western Blocks in the North China Craton (NCC) is one of the major Paleoproterozoic collisional orogenic belts in the NCC, and exposes accreted and metamorphosed sedimentary sequences and associated rocks which have been interpreted as remnants of ancient oceanic crust (Zhao and Zhai, 2013, and references therein). However, the origins of these rocks in terms of their depositional history in forearc/foreland basin/trench, back-arc environments remain controversial (Wu et al., 1989; Sun et al., 1992; Zhao et al., 2005, 2007, 2012; Xia et al., 2006; Faure et al., 2007; Wang, 2009; Liu et al., 2011, 2012a, 2012b, 2014; Santosh et al., 2015). Paleoproterozoic meta-carbonate rocks are well preserved in the basement terranes of the TNCO, including the Fuping Complex, Zhanhuang Complex, Lüliang Complex, Wutai

Complex and Zhongtiao Complex. Investigations on the detrital zircon record, geochemistry and stable isotopes of these rocks are critical to elucidating the depositional age and environment. This study presents zircon U-Pb geochronological, geochemical and isotopic (carbon and oxygen isotopes for calcite and dolomite) data on a suite of impure marbles and calc-silicate rocks from the Fuping and Zhanhuang Complexes which are two representative basement terranes located within the central segment of the TNCO. The objective of this study is to constrain the depositional age and environment for the meta-sedimentary sequences in the Fuping and Zhanhuang Complexes, use the results to gain insights into the Paleoproterozoic tectonic processes in the NCC.

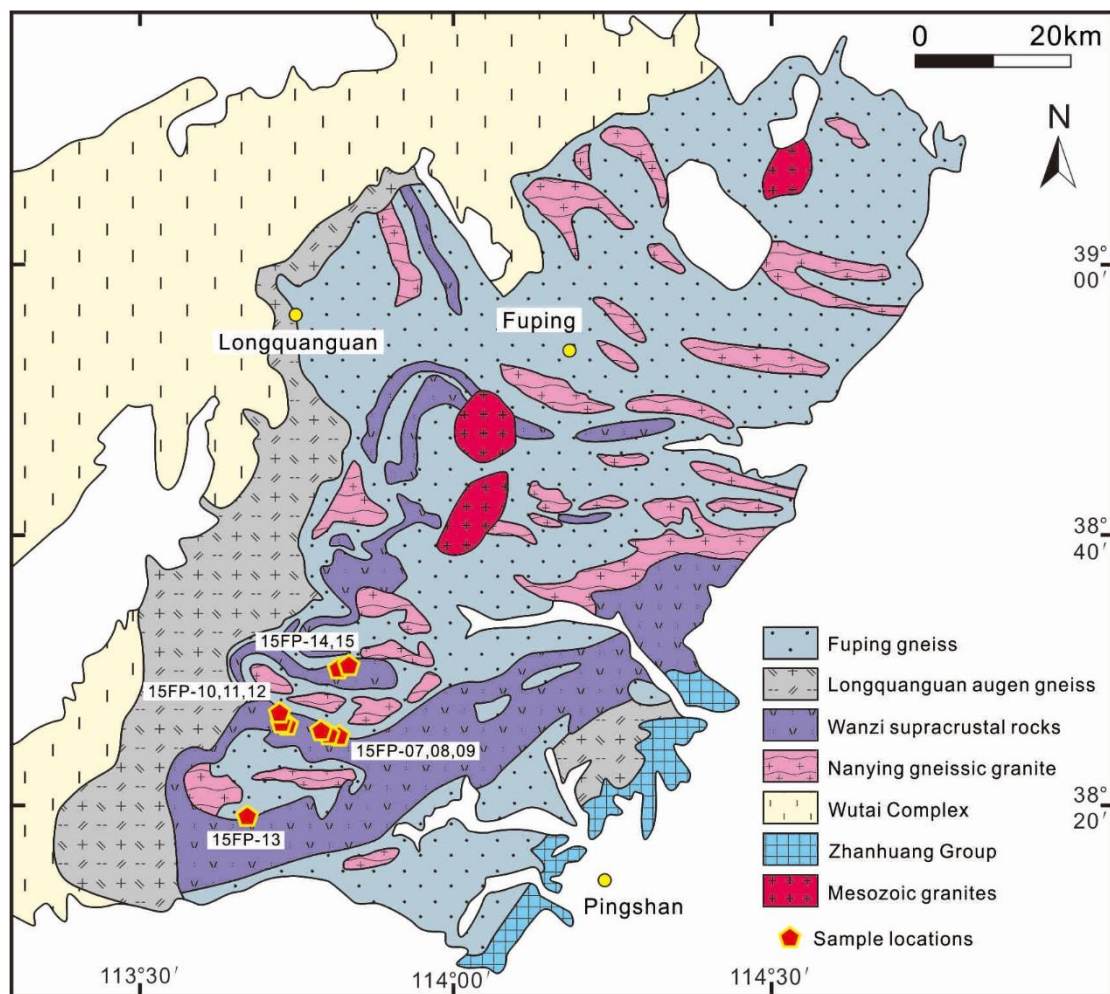


Fig. 5-1 Geological map of the Fuping Complex and the adjacent Wutai Complex (modified after Zhao et al., 2000a), showing major lithological units and sample locations.

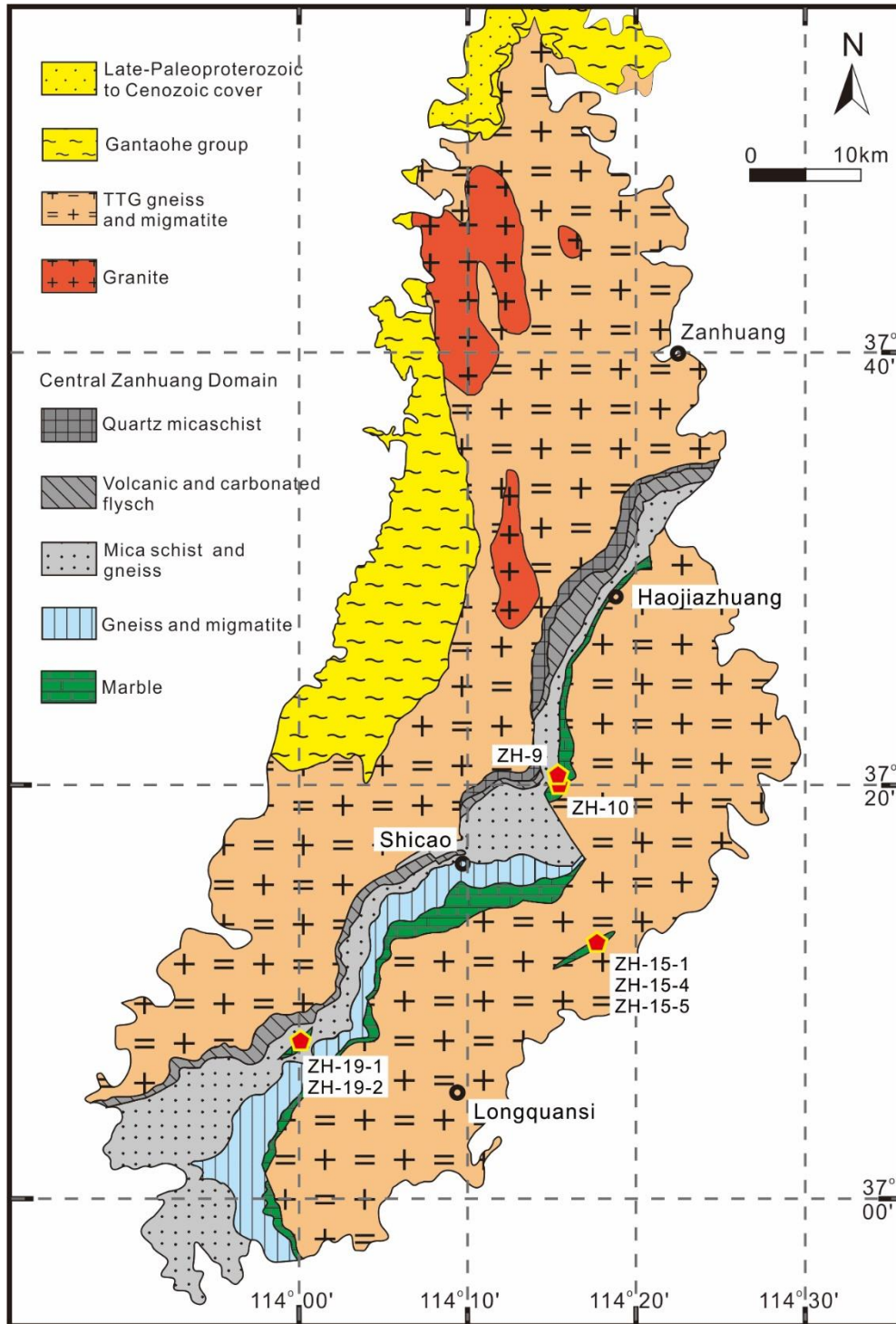


Fig. 5-2 Geological map of the Zanhuang Complex (modified after Trap et al., 2009), showing major lithological units and sample locations.

5.2 Sample description

Nine representative dolomite-calcite marbles and nine calc-silicate rocks were collected from the Wanzi Group of the Fuping Complex from road cuttings or open

cast mines (Table 5-1, Fig. 5-1). The dolomite-calcite marbles and calc-silicates occur as thick layers (>10 meter, and sometimes reaching up to hundreds of meters). The dolomite-calcite marbles are impure with minor lamellae of muscovite and or phlogopite. The calc-silicate rocks show gray color and comprise coarse- to medium-grained diopside, olivine, calcite, dolomite, muscovite and phlogopite. Five dolomite-calcite marbles and two dolomite marbles were collected from the Central Zhanhuang Domain (Table 5-1, Fig. 5-2). The marbles are exposed as thick layers (0.4-10 m) intercalated with amphibolites, mica-schists, quartzites and fine grained metavolcanics. Sample ZH-10 is a pinkish dolomite-calcite marble intercalated with mica-schist and quartzite (Fig. 5-3). The other samples show white color and are impure with minor muscovite and phlogopite (Fig. 5-4).

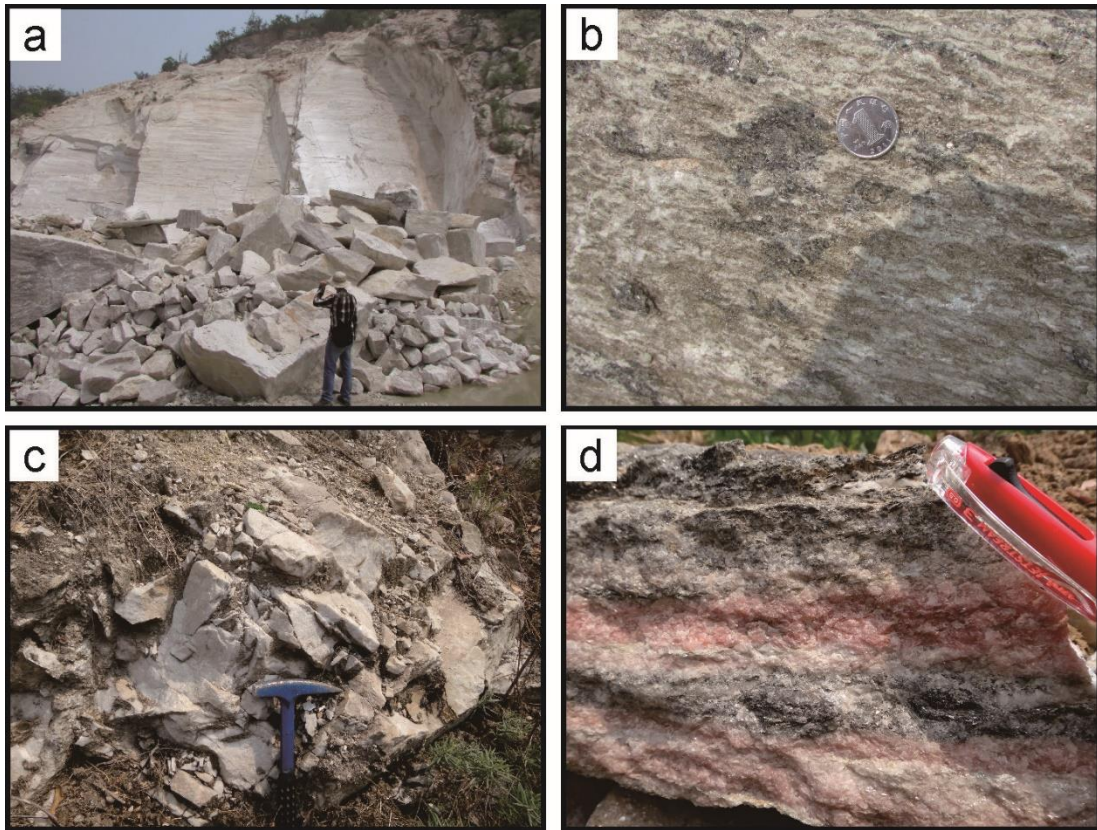


Fig. 5-3 Representative field photographs of marbles and calc-silicates. (a) Dolomite-calcite marble (15FP-13-1) from the Fuping Complex; (b) Calc-silicate (15FP-07-2) from the Fuping Complex; (c) White dolomite-calcite marble (ZH-9) from the Zhanhuang Complex; (d) Pinkish dolomite-calcite marble (ZH-10) intercalated with quartzite and mica-schist from the Zhanhuang Complex.

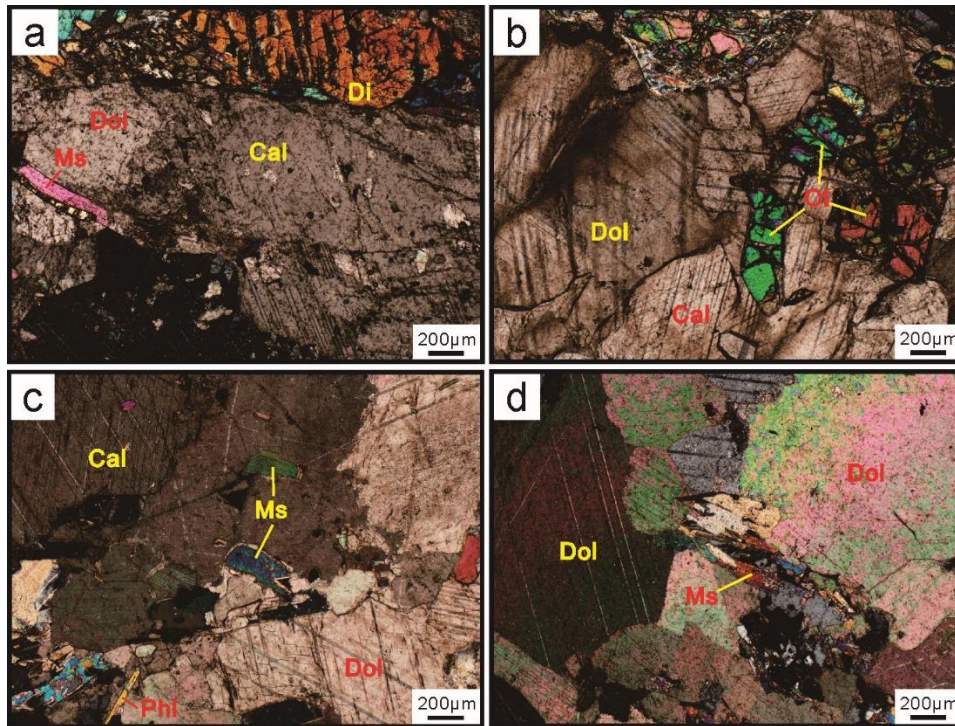


Fig. 5-4 Representative photomicrographs of marbles and calc-silicates. (a) Calc-silicate (15FP-07-2) from the Fuping Complex, showing mineral assemblage of calcite, dolomite, diopside and muscovite; (b) Calc-silicate (15FP-14-3) from the Fuping Complex, showing mineral assemblage of calcite, dolomite and olivine; (c) Dolomite-calcite marble (ZH-15-4) from the Zanhuang Complex, showing mineral assemblage of calcite, dolomite, muscovite and phlogopite; (d) Dolomite marble (ZH-19-1) from the Zanhuang Complex. Mineral abbreviations: Cal, calcite; Dol, dolomite; Di, diopside; Ol, olivine; Ms, muscovite; Phl, phlogopite.

5.3 Analytical results

5.3.1 Major and trace elements

The five dolomite-calcite marbles from Fuping Complex show constant MgO (19.95-20.75 wt.%), CaO (28.35-30.10 wt.%) and Mg/Ca values (0.58-0.62). These dolomite-calcite marbles are impure with variable SiO₂ contents (1.80-6.82 wt.%), in accordance with the petrological observations that show the occurrence of silicic minerals (phlogopite and muscovite). K₂O and Al₂O₃ concentrations are low (0.05-0.41 wt.% and 0.10-1.30 wt.%, respectively). The dolomite-calcite marbles have variable trace element components including Mn (105-229 ppm), Sr (46.7-64.8 ppm), Mn/Sr (1.82-3.82), Ca/Sr (3145-4336) and Fe/Sr (40.9-63.0) (Table 5-2). In

the shale-normalized REE distribution patterns, they show near flat patterns with positive Eu anomaly (Fig. 5-5a). The calc-silicate rocks from the Fuping Complex display relatively high SiO₂ (13.25-30.03 wt.%), Al₂O₃ (2.87-5.17 wt.%), MgO (12.21-19.02 wt.%) and CaO (23.37-32.69 wt.%) contents with Mg/Ca ratios of 0.31-0.60. Their Mn, Sr, Mn/Sr, Ca/Sr and Fe/Sr values vary from 148 ppm to 499 ppm, 80.2 ppm to 201 ppm, 1.73 to 3.24, 1084 to 2384 and 42.2 to 101.7, respectively. The shale-normalized REE distribution diagram shows nearly flat pattern and slightly positive Eu anomaly (Fig. 5-5a).

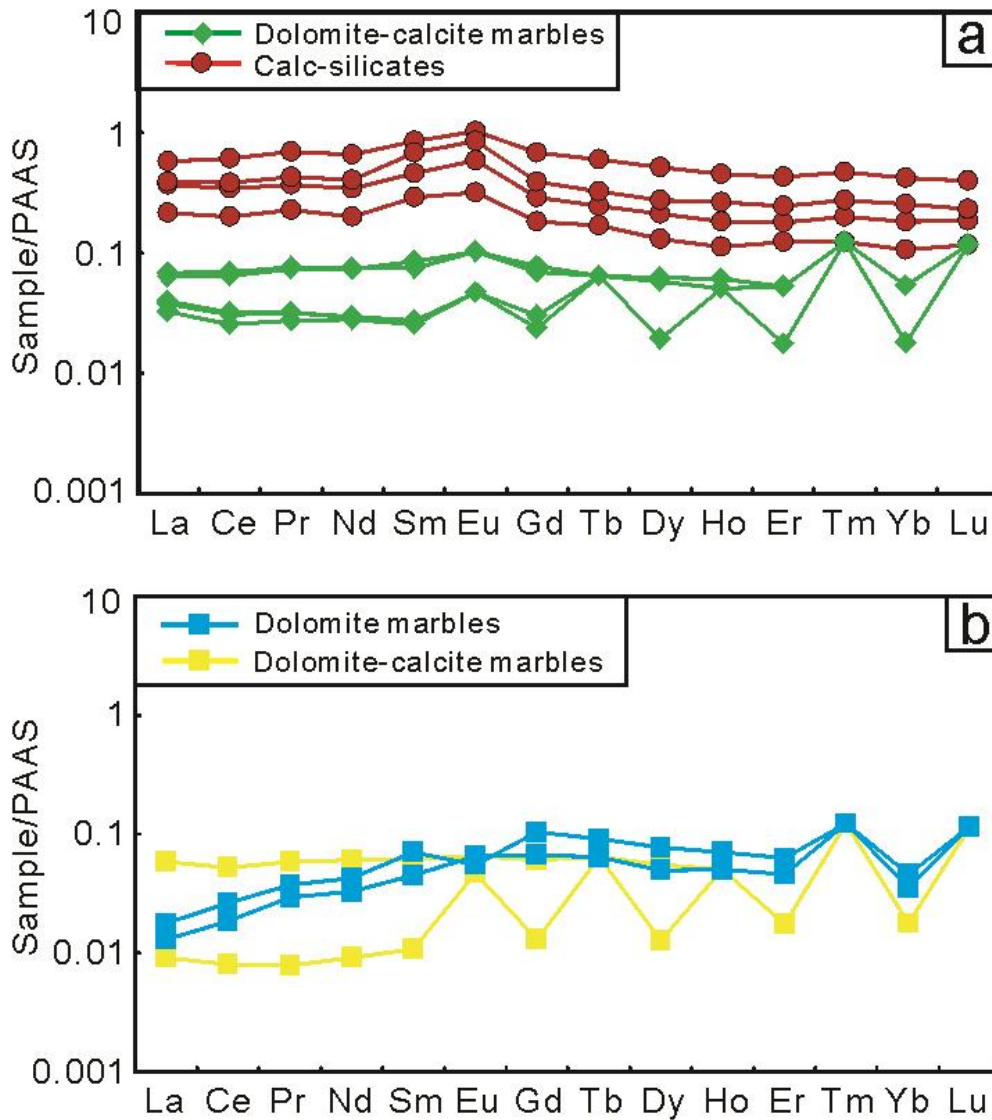


Fig. 5-5 Post-Archean Australian Shales (PAAS) normalized rare earth element patterns. (a) Calc-silicates and dolomite-calcite marbles from the Fuping Complex. (b) Dolomite-calcite marbles and dolomite marbles from the Zanzhuang Complex. The normalization values of PAAS are from McLennan (1989).

The dolomite-calcite marbles from the Zanhuang Complex have moderate MgO (21.06-21.38 wt.%) and CaO (30.11-30.26 wt.%) contents, and low SiO₂ contents (0.02-0.62 wt.%). These dolomite-calcite marbles display moderate Mn contents (125-228 ppm), Sr contents (25.7-50.8 ppm), Mn/Sr ratios (2.46-8.87), Ca/Sr ratios (4234-8410) and Fe/Sr ratios (60.6-68.7). In comparison, the dolomite marbles contain high MgO values of 45.54-46.32 wt.%, low SiO₂ and CaO contents of 0.28-0.74 wt.% and 0.34-0.44 wt.%, respectively. The rocks are also characterized by high Mn concentrations of 287-455 ppm and extremely low Sr contents of 2.25-2.74 ppm with high Mn/Sr ratios of 128-166. In the shale-normalized REE distribution patterns, all samples from the Zanhuang Complex show near flat pattern with slightly positive Eu anomaly (Fig. 5-5b).

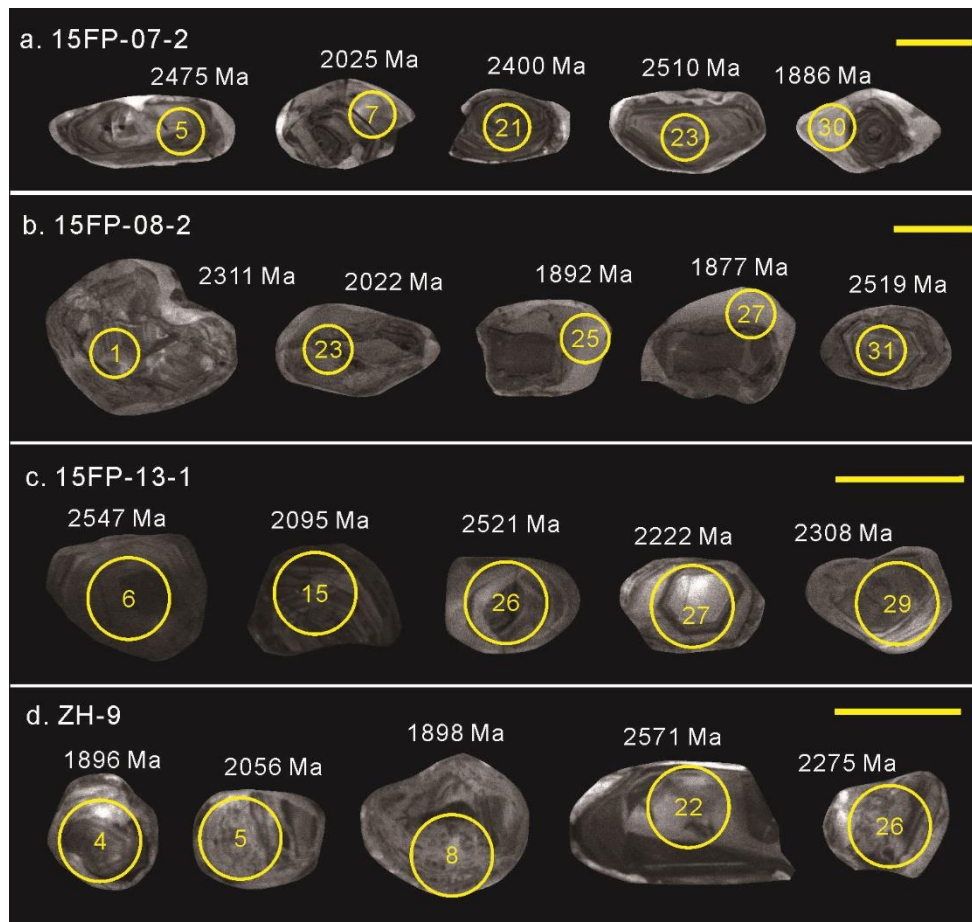


Fig. 5-6 Cathodoluminescence (CL) images of representative zircons in sample 15FP-07-2 (a), 15FP-08-2 (b), 15FP-13-1 (c) and ZH-9 (d), showing analytical positions, spot numbers and ²⁰⁷Pb/²⁰⁶Pb ages. Scale bars are in 50 μm.

5.3.2 Zircon U-Pb geochronology

Two calc-silicates (15FP-07-2 and 15FP-08-2), an impure dolomite-calcite marble (15FP-13-1) from the Fuping Complex, and an impure dolomite-calcite marble (ZH-9) from the Zanhuang Complex were chosen for zircon separation and LA-ICP-MS zircon U-Pb analyses (Table 5-3). Representative cathodoluminescence (CL) images of zircon grains are shown in Figs. 5-6 and U-Pb age data plots are displayed in Fig. 5-7 and 5-8.

5.3.2.1 Fuping Complex

Zircons from calc-silicate sample 15FP-07-2 are colorless to light brown, and transparent to translucent. Most zircon grains are rounded in shape, with lengths of 50-200 μm and length to width ratios vary from 2:1 to 1:1. Under CL images, most grains show clear core-rim texture with oscillatory zoned core surrounded by bright rim, suggesting magmatic origin for the core and metamorphic origin for the rim (Fig. 5-6a). A total of 25 spots from 25 zircons were analyzed. The results show Th contents from 45 to 390 ppm, U contents from 21 to 599 ppm and Th/U ratios vary from 0.32 to 5.48. The analyzed core domains show $^{207}\text{Pb}/^{206}\text{Pb}$ ages vary from 2515 ± 19 Ma to 2025 ± 20 Ma and can be divided into three populations. Seven zircons form the oldest population with $^{207}\text{Pb}/^{206}\text{Pb}$ ages between 2443 ± 19 Ma and 2515 ± 19 Ma, yield upper intercept age of 2490 ± 29 Ma (MSWD=1.9). Another population (n=13) displays a wide age range of ages (2170~2400 Ma) with a peak at ca. 2320 Ma, implying a complex provenance. The youngest group includes four zircons (2025~2107 Ma) and display weighted mean age of 2066 ± 66 Ma (Fig. 5-7). The metamorphic rims are too tiny to analyze, with only one spot analysed that shows an age of 1886 ± 20 Ma.

Zircons from calc-silicate rock sample 15FP-08-2 are colorless and transparent to translucent. The grains show rounded morphology with a length of 60-200 μm and aspect ratios vary from 2:1 to 1:1. Under CL images, most zircons show similar core-rim texture with oscillatory zoned core and bright rim (Fig. 5-6b). A total of 24 spots from 24 zircons were analyzed. All analyses show Th contents range from 19

to 731 ppm, U contents range from 45 to 488 ppm and Th/U ratios vary from 0.25 to 1.72 (except Th/U=0.06 of spot 20). The dominant populations show $^{207}\text{Pb}/^{206}\text{Pb}$ ages of 2457~2535 Ma (peak at 2499 Ma), 2202~2402 Ma and 2022~2081 Ma (peak at 2048 Ma). The youngest age from the core domain shows 1959 ± 20 Ma (Th/U = 0.76), representing the youngest magmatic zircon from the provenance. The metamorphic rims are tiny, and only two spots were analyzed which show $^{207}\text{Pb}/^{206}\text{Pb}$ ages of 1892 ± 21 Ma and 1877 ± 22 Ma (Fig. 5-7).

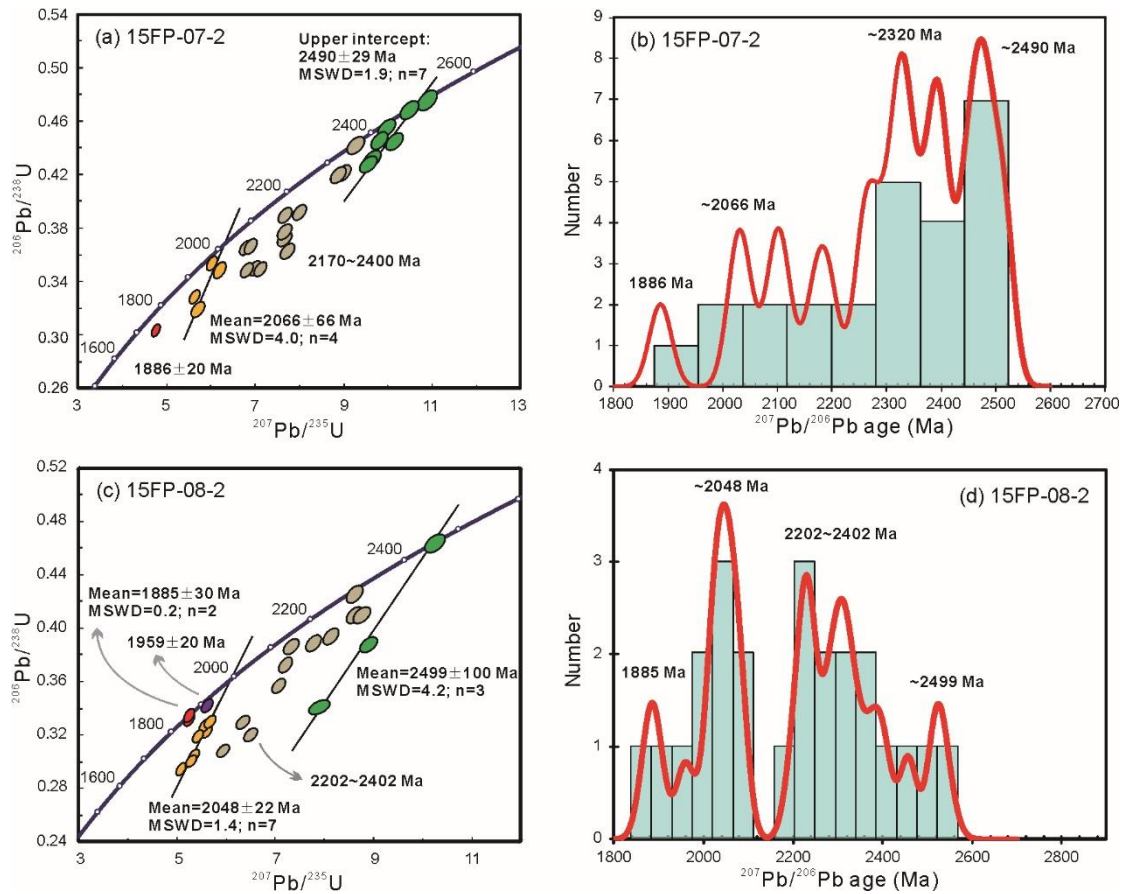


Fig. 5-7 Zircon U-Pb concordia plots and relative probability diagrams of $^{207}\text{Pb}/^{206}\text{Pb}$ ages for samples 15FP-07-2 (a-b) and 15FP-08-2 (c-d).

Zircons are rare in the impure dolomite-calcite marble sample 15FP-13-1 and small. They are colorless and transparent to translucent. The grains show rounded morphology with a length of 30-70 μm and aspect ratios vary from 2:1 to 1:1. Under CL images, zircon grains display different features in internal structure with broad compositional zoning, obvious oscillatory zoning and fractured domains (Fig. 5-6c). A total of 16 spots from 16 zircons were analyzed. The results show Th contents

vary from 110 to 707 ppm, U contents vary from 128 to 1017 ppm and Th/U ratios range from 0.32 to 1.87, suggesting magmatic origin. The most dominant population with $^{207}\text{Pb}/^{206}\text{Pb}$ ages varying from 2468 ± 19 Ma to 2547 ± 19 Ma yield a weighted mean age of 2507 ± 20 Ma (MSWD = 1.9, n=10). One zircon shows the youngest age of 2095 ± 20 Ma (Th/U=0.57), and the remaining five ages range from 2222 ± 19 Ma to 2405 ± 19 Ma (Fig. 5-8).

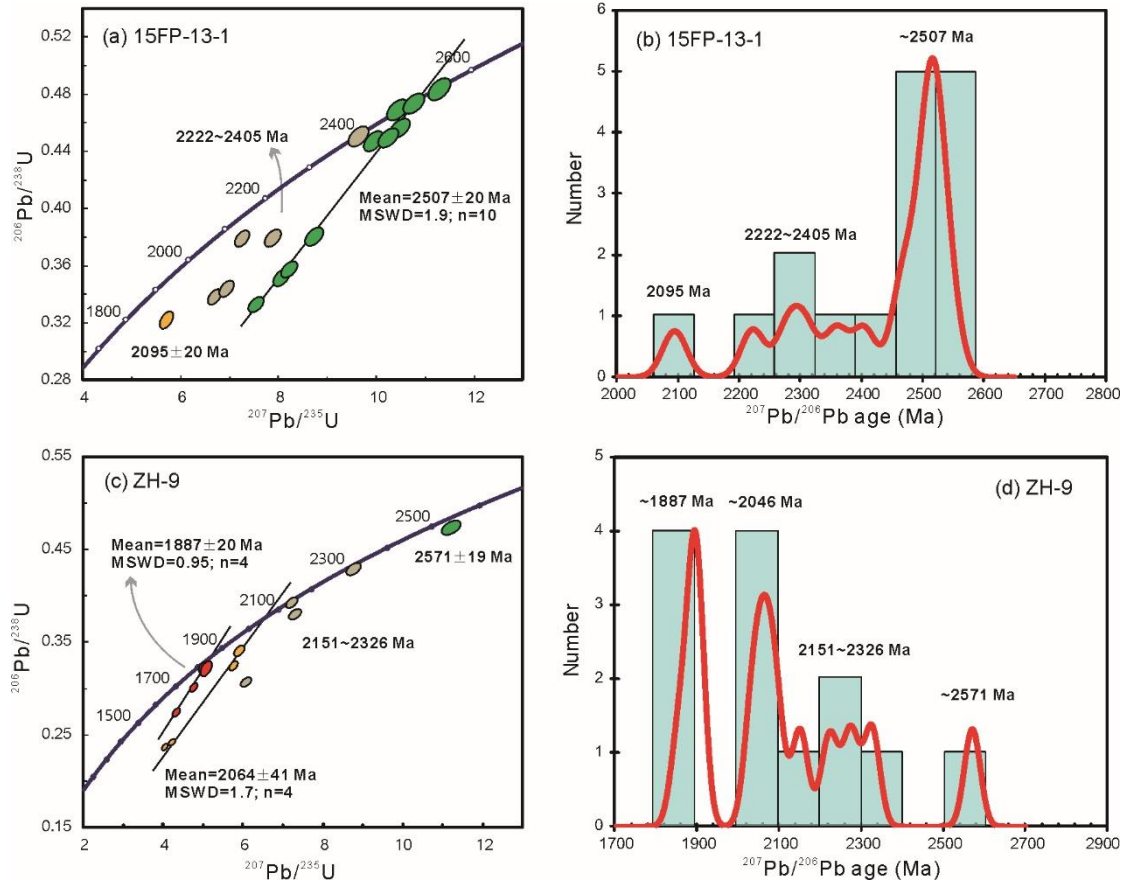


Fig. 5-8 Zircon U-Pb concordia plots and relative probability diagrams of $^{207}\text{Pb}/^{206}\text{Pb}$ ages for samples 15FP-13-1 (a-b) and ZH-9 (c-d).

5.3.2.2 Zhanhuang Complex

Zircon grains are rare and small in the impure dolomite-calcite marble sample ZH-9, and are colorless and translucent. The grains show rounded morphology with a length of 40-80 μm and aspect ratios vary from 2:1 to 1:1. In CL images, most zircon grains are fractures and show zoning, a few grains show core-rim texture (Fig. 5-6d). A total of 13 spots from 13 zircons were analyzed. The results show Th contents vary from 132 to 878 ppm, U contents vary from 268 to 2590 ppm and Th/U

ratios range from 0.14 to 0.79. Nine spots from the core domains show three age populations with one age at 2571 ± 19 Ma, one age population of 2151~2326 Ma and the third group of 2033~2094 Ma (peak at 2046 Ma) (Fig. 5-8). Four spots define the youngest age group with $^{207}\text{Pb}/^{206}\text{Pb}$ ages varying from 1857 ± 20 Ma to 1898 ± 20 Ma, yielding a weighted mean age of 1887 ± 20 Ma (MSWD = 0.95) and showing Th/U ratios vary from 0.14-0.45 (0.14-0.16 for two spots).

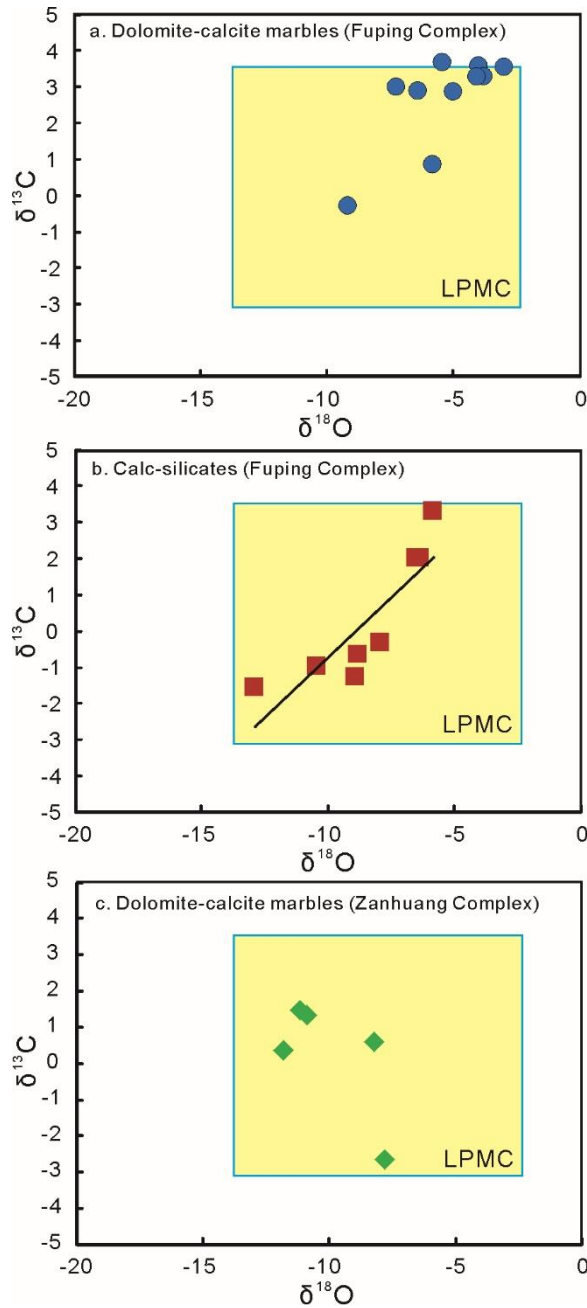


Fig. 5-9 Scatter diagrams of $\delta^{13}\text{C}$ versus $\delta^{18}\text{O}$ values. LPMC: field of late Paleoproterozoic (2.0-1.8 Ga) marine carbonates (Veizer et al., 1992, Shield and Veizer, 2002).

5.3.3 C-O isotopes

The C and O isotopic results of carbonate minerals (calcite and dolomite) are listed in Table 5-4. The dolomite-calcite marbles from the Fuping Complex have $\delta^{13}\text{C}$ values range from -0.31 ‰ to 3.65 ‰ (mean = 2.65 ‰) and $\delta^{18}\text{O}$ values vary from -9.12 ‰ to -2.96 ‰ (mean = -5.35 ‰). In contrast, the calc-silicate rock samples from the Fuping Complex show a larger variation of $\delta^{13}\text{C}$ (-1.56 ‰ to 3.30 ‰, mean = 0.31 ‰) and lower $\delta^{18}\text{O}$ (-12.89 ‰ to -5.84 ‰, mean = -8.45 ‰). Dolomite marbles from the Zhanhuang Complex show low $\delta^{13}\text{C}$ and $\delta^{18}\text{O}$ values ranging from -3.31 ‰ to -3.69 ‰ and -12.98 ‰ to -13.59 ‰, respectively. The dolomite-calcite marbles from the Zhanhuang Complex contain moderate $\delta^{13}\text{C}$ and $\delta^{18}\text{O}$ compositions of -2.68 ‰ to 1.44 ‰ (mean = 0.20 ‰) and -11.77 ‰ to -7.76 ‰ (mean = -9.93 ‰), respectively.

5.4 Discussion

5.4.1 Effects of diagenesis and metamorphism

For Precambrian meta-carbonate rocks, processes including diagenesis, fluid-rock interaction and metamorphism may affect the primary geochemical and isotopic features (Veizer et al., 1989; Melezhik and Fallick, 2003; Tang et al., 2006). Diagenetic and metamorphic processes result in the enrichment of Mn and depletion of Sr, and for rocks that have not been affected by later events, Mn/Sr ratio lower than 10 is suggested (Veizer, 1983; Guan and Wang, 2009). The dolomite marbles in this study (ZH-19-1 and ZH-19-2) show relatively high Mn contents (287-455 ppm), extremely low Sr contents (2.25-2.74 ppm) and corresponding Mn/Sr ratios are in the range of 128-166, suggesting that the two samples have been strongly affected by the later diagenetic or metamorphic processes. The remaining samples display moderate Mn and Sr contents, and Mn/Sr ratios vary from 1.73 to 8.87, suggesting limited diagenetic or metamorphic effects on the geochemical signature. Thus, the two dolomite marbles were excluded in the following discussion. The carbonates affected by diagenetic processes have convex-up type REE pattern with enrichment of MREE (Bau et al., 1999). All samples in this study display near flat patterns with

slight positive Eu anomaly, suggesting that the rocks preserve the primary geochemical features without diagenetic effects.

Diagenetic or metamorphic processes lead to the depletion of $\delta^{13}\text{C}$ and $\delta^{18}\text{O}$ values, and the two values show good correlation (Melezhik et al., 2005; Mohanty et al., 2015). In the $\delta^{13}\text{C}$ versus $\delta^{18}\text{O}$ plots (Fig. 5-9), the dolomite-calcite marbles from Fuping Complex and Zanhuang Complex show poor correlation between $\delta^{13}\text{C}$ (-2.68 ‰ to 3.65 ‰) and $\delta^{18}\text{O}$ (-12.89 ‰ to -2.96 ‰), suggesting no post-depositional effects on the isotopic compositions. The calc-silicate rocks from the Fuping Complex show positive correlation between the $\delta^{13}\text{C}$ and $\delta^{18}\text{O}$ values (Fig. 5-9b), suggesting post-depositional disturbance. The calc-silicate rocks have relatively lower $\delta^{13}\text{C}$ (-1.56 ‰ to 3.30 ‰, mean = 0.31 ‰) and $\delta^{18}\text{O}$ (-12.89 ‰ to -5.84 ‰, mean = -8.45 ‰) values in comparison with those in the dolomite-calcite marbles from the Fuping Complex, the latter showing $\delta^{13}\text{C}$ values of -0.31 ‰ to 3.65 ‰ (mean = 2.65 ‰) and $\delta^{18}\text{O}$ value of -9.12 ‰ to -2.96 ‰ (mean = -5.35 ‰). The depletion of $\delta^{13}\text{C}$ and $\delta^{18}\text{O}$ values suggests that the calc-silicate rocks were affected by the post-depositional processes. Some other elements like Fe, Ca and Mg are also sensitive to the diagenetic or metamorphic disturbance (Veizer, 1983; Veizer et al., 1989; Swart, 2015). Compared to the depletion of Sr, $\delta^{13}\text{C}$ and $\delta^{18}\text{O}$ values during post-depositional processes, the Ca/Sr and Fe/Sr ratios show regular change. In the plots of Mg/Ca, Ca/Sr and Fe/Sr ratios versus $\delta^{13}\text{C}$ and $\delta^{18}\text{O}$ values (Fig. 5-10), the results display no or poor correlations, implying limited effects of diagenesis and metamorphism. In summary, the dolomite marbles from the Zanhuang Complex are strongly disturbed and the calc-silicate rocks are weakly to moderately affected by the post-depositional processes, whereas the dolomite-calcite marbles preserve their primary geochemical features without post-depositional effects.

Previous studies on carbonate rocks show that $\delta^{13}\text{C}$ values can remain undisturbed even under diagenetic or metamorphic conditions, and that the $\delta^{18}\text{O}$ values are much easier to be disturbed (Melezhik and Fallick, 2003; Melezhik et al., 2005; Prave et al., 2009). Diagenesis always leads to the decrease of $\delta^{18}\text{O}$ values (up to reach 2‰) (Veizer et al., 1999). Thus the following discussion will mainly focus

on the carbon isotopic results from the dolomite-calcite marbles that were mostly unaffected.

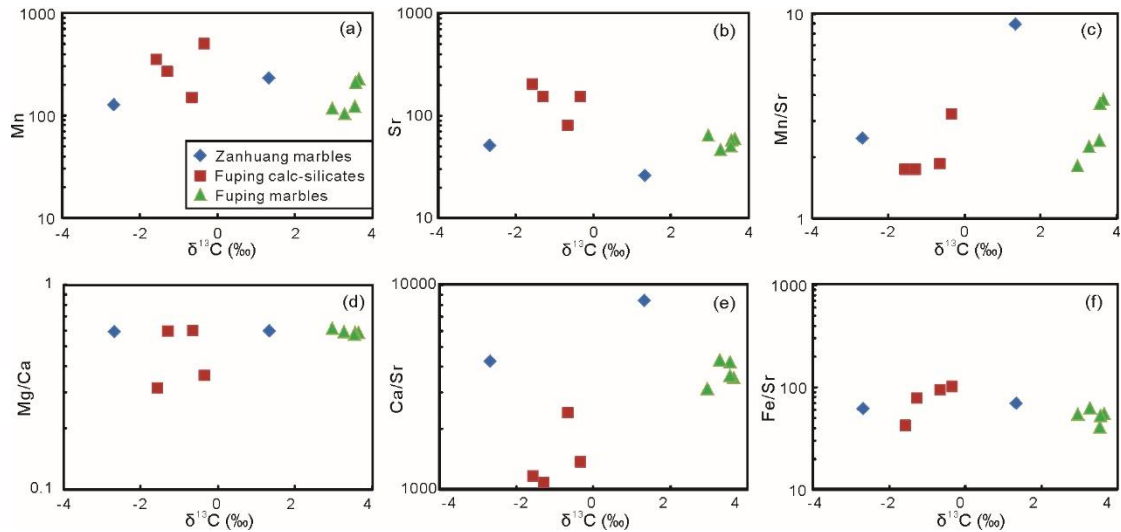


Fig. 5-10 Cross plots of geochemical results and $\delta^{13}\text{C}$ values. (a) Mn versus $\delta^{13}\text{C}$ values, (b) Sr versus $\delta^{13}\text{C}$ values, (c) Mn/Sr ratios versus $\delta^{13}\text{C}$ values, (d) Mg/Ca ratios versus $\delta^{13}\text{C}$ values, (e) Ca/Sr ratios versus $\delta^{13}\text{C}$ values, (f) Fe/Sr ratios versus $\delta^{13}\text{C}$ values.

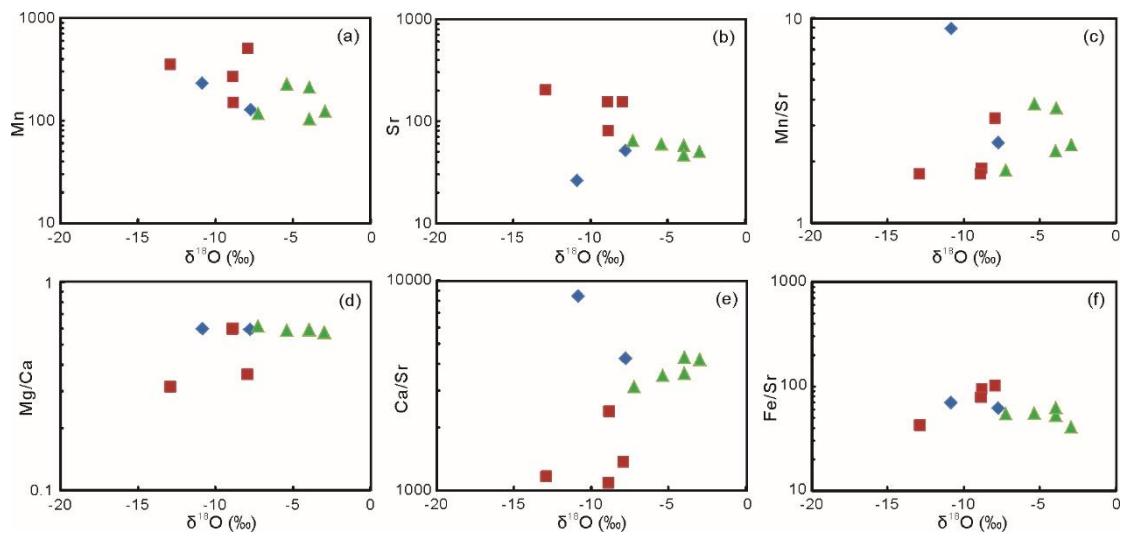


Fig. 5-11 Cross plots of geochemical results and $\delta^{18}\text{O}$ values. (a) Mn versus $\delta^{18}\text{O}$ values, (b) Sr versus $\delta^{18}\text{O}$ values, (c) Mn/Sr ratios versus $\delta^{18}\text{O}$ values, (d) Mg/Ca ratios versus $\delta^{18}\text{O}$ values, (e) Ca/Sr ratios versus $\delta^{18}\text{O}$ values, (f) Fe/Sr ratios versus $\delta^{18}\text{O}$ values.

5.4.2 Nature of protolith

The trace elements and carbon isotopes of meta-carbonate rocks can be used to trace the sedimentary environment of their protolith (Rumble et al., 2000; Tang et al., 2006; Santos et al., 2013). Shale-normalized REE patterns of sea water and marine

sediment are almostly plotted below the concentration ratio of 1 (Mohanty et al., 2015; Singh et al., 2016; Zhang et al., 2017a). In the shale-normalized REE distribution patterns, all samples from the Fuping and Zanhuang Complexes show near flat patterns below the concentration level of 1, suggesting marine depositional environment. The carbon and oxygen isotopic results show moderate variation of $\delta^{13}\text{C}$ (-2.68 ‰ to 3.65 ‰) and $\delta^{18}\text{O}$ (-12.89 ‰ to -2.96 ‰) values, and the data plot in the field of typical late Paleoproterozoic (2.0-1.8 Ga) marine carbonate (Veizer et al., 1992; Shield and Veizer, 2002). Shield and Veizer (2002) compiled available isotopic compositions of Precambrian marine carbonate, and in their compilation, late Paleoproterozoic (2.0-1.8 Ga) marine carbonates display $\delta^{13}\text{C}$ values varying from -3.0 ‰ to 3.5 ‰ and $\delta^{18}\text{O}$ values range from -13.8 ‰ to -2.4 ‰.

The dolomite-calcite marbles and calc-silicate rocks from the Wanzi Group of the Fuping Complex are associated with meta-clastic sediments like pelitic-gneisses, pelitic schists and quartzites, and their protoliths are considered to be sandstone, siltstone, carbonate and minor volcanics (Wu et al., 1989; Ren et al., 2013). The Central Zanhuang Domain also contains quartz schist, mica-schist and paragneiss unit together with the marble unit representing remnants of an oceanic basin (Trap et al., 2009). The above lithological sequence, occurrence of detrital zircons and other silicate minerals suggest the input of clastic sediments during the deposition of carbonates. This study therefore proposes that the impure marbles and calc-silicate rocks from the Fuping and Zanhuang Complexes were formed in a proximal and shallow marine environment, as indicated by their comparable trace elements, carbon and oxygen isotopic compositions, lithology and mineral assemblage.

5.4.3 Provenance and depositional age

Previous geochronological studies have focused on the different rock types from the Wanzi supracrustal rocks to constrain the depositional age of the Wanzi Group (Xia et al., 2006; Ren et al., 2013; Tang et al., 2015a). Xia et al. (2006) carried out detrital zircon study on sillimanite-bearing gneisses and suggested that the Wanzi Group was deposited during 2.10-1.84 Ga. Ren et al. (2013) reported detrital zircon

ages of a quartzite and proposed that the sedimentation time for the protolith was before 2.1-2.0 Ga and after 2.5 Ga. In a recent study, [Tang et al. \(2015a\)](#) studied two schist samples which show prominent age populations of 2450-2585 Ma and 2004-2097 Ma, the youngest igneous detrital zircon age of 1955 ± 44 Ma and metamorphic ages of 1830 ± 62 Ma and 1844 ± 45 Ma and suggested depositional age between 1.95 Ga and 1.84 Ga. In this study, the results from two calc-silicate rocks and a dolomite-calcite marble show four dominant age populations of 2.50-2.55 Ga, 2.2-2.4 Ga (peaks at 2.30-2.35 Ga), 2.0-2.1 Ga and 1.8-1.9 Ga. The age group of 2.50-2.55 Ga suggests that provenance is mainly the Fuping TTG gneiss ([Xia et al., 2006](#); [Ren et al., 2013](#); [Tang et al., 2015a](#)) with a possible minor contribution from the adjacent late Neoproterozoic TTG gneisses (e.g. Wutai, Hengshan, Zhanhuang and Lüliang Complexes, [Zhao et al., 2007](#); [Santosh et al., 2015](#), and references there in). The 2.2-2.4 Ga zircons were sourced from the granitic and mafic rocks in the Fuping, Hengshan, Lüliang, Huai'an-Xuanhua Complexes which record common arc- or rift-related magmatism at 2.37-2.10 Ga ([Liu et al., 2002](#); [Kröner et al., 2005b](#); [Zhao et al., 2008b](#); [Santosh et al., 2015](#)). The 2.30-2.35 Ga age peaks are most probably derived from the mafic dykes of the Fuping Complex ([Liu et al., 2002](#)). The 2.0-2.1 Ga age group suggests derivation from the Nanying gneissic granite ([Xia et al., 2006](#); [Tang et al., 2015a](#)) and probable source from the arc-related and rift-related rocks from the Wutai, Hengshan, Lüliang, Zhanhuang and Huai'an Complexes ([Tang et al., 2015a](#), and references there in). The youngest igneous detrital zircon shows concordant age of 1959 ± 20 Ma ($\text{Th/U} = 0.76$), and the metamorphic rims show ages range from 1892 ± 21 Ma to 1877 ± 22 Ma which are in accordance with the retrograde cooling age (1.9-1.8 Ga) after the high pressure granulite-facies metamorphism (1.93~1.92 Ga) in the Fuping Complex. Thus, the zircon data further constrain the depositional age as 1.95-1.93 Ga for the Wanzi Group.

The meta-sedimentary rocks in the Zhanhuang Complex are exposed in the western part of the Zhanhuang Complex (Gantaohu Group) and the Central Zhanhuang Domain ([Wang et al., 2003](#); [Trap et al., 2009](#); [Liu et al., 2012a](#)). [Liu et al. \(2012a\)](#) reported detrital zircon ages for a series of low grade meta-sedimentary rocks from

the Gantaohu Group, and the results show that the largest age population between 2600 Ma and 2400 Ma with a subordinate population of 3010-2600 Ma (Fig. 5-12). The depositional age was constrained to be between 2088 Ma and 1850 Ma based on the crystallization age of 2088 ± 8 Ma for the rhyolite and metamorphic ages in meta-sedimentary rocks (Liu et al., 2012a). Detrital zircon U-Pb ages have not been reported before for the meta-sedimentary rocks in the Central Zhanhuang Domain. These rocks are proposed to have been deposited during the closure of the Taihang Ocean between 1880 Ma and 1850 Ma based on structural evidence, monazite U-Th-Pb dating and amphibole Ar-Ar dating results (Trap et al., 2009). The dolomite-calcite marble (ZH-9) shows age populations of 2.20-2.35 Ga, 2.03-2.10 Ga, 1.85-1.90 Ga and a zircon grain of ~ 2.57 Ga (Fig. 5-12). The 2.20-2.35 Ga zircons show similar source with the 2.2-2.4 Ga age population of the Fuping Complex, with a possible source from the 2.37-2.10 Ga rocks in Fuping, Hengshan, Lüliang, Huai'an-Xuanhua Complexes (Kröner et al., 2005b; Zhao et al., 2008b; Santosh et al., 2015). The abundant 2.03-2.10 Ga ages are most probably derived from the 2090 ± 10 Ma Xuting granite (Yang et al., 2011; Liu et al., 2012a) and 2087 ± 16 Ma meta-basalt (Xie et al., 2012) in the Zhanhuang Complex, and minor contribution from 2.0-2.1 Ga magmatic rocks from the adjacent Complexes (Tang et al., 2015a, and references there in). One zircon with age of 2571 ± 19 Ma suggests contribution from the Neoproterozoic TTG gneisses. Four metamorphic rims display $^{207}\text{Pb}/^{206}\text{Pb}$ ages varying from 1857 ± 20 Ma to 1898 ± 20 Ma, implying the deposition before ~ 1.90 Ga. In combination with the youngest igneous detrital zircon age of 2033 ± 20 Ma and the oldest metamorphic age, it is reasonable to constrain the depositional age of the Central Zhanhuang Domain as 2.03-1.90 Ga.

5.4.4 Tectonic implication

There is a board consensus that the TNCO represents a subduction-accretion-collision belt built through the closure of oceanic basin in Paleoproterozoic (Zhao et al., 2001b, 2005, 2012; Wang, 2009; Zhang et al., 2009, 2015c; Trap et al., 2012; Santosh et al., 2016). In the central segment of the TNCO,

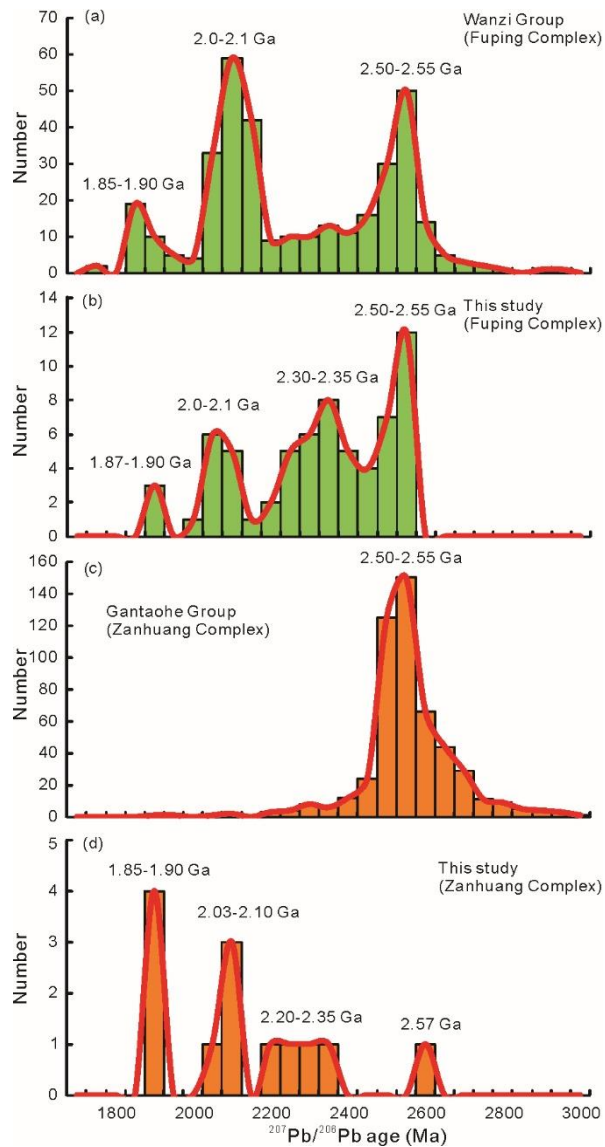


Fig. 5-12 Zircon U-Pb age spectra of detrital zircons from the Fuping Complex and Zhanhuang Complex. (a) All available detrital zircon U-Pb ages of Wanzi Group in the Fuping Complex, date from Xia et al. (2006); Ren et al. (2013); Tang et al. (2015a) and this study. (b) Detrital zircon U-Pb age results (15FP-07-2, 15FP-08-2 and 15FP-13-1) of Fuping Complex in this study. (c) Available detrital zircon U-Pb ages of Gaotaohu Group in the Zhanhuang Complex, data from Liu et al. (2012a). (d) Detrital zircon U-Pb age results (ZH-9) of Central Zhanhuang Domain in this study.

the adjacent Fuping and Zhanhuang Complexes both contain meta-sedimentary rocks (meta-clastic and meta-carbonate rocks). The meta-sedimentary rocks (Wanzi Group) in the Fuping Complex were deposited during 1.95-1.93 Ga, and the Gantaohu Group and the Central Zhanhuang Domain in the Zhanhuang Complex were deposited at

2.09-1.85 Ga and 2.03-1.90 Ga, respectively. Furthermore, the protoliths of these meta-sedimentary rocks are suggested to have formed in a proximal and shallow marine environment. However, the obviously higher $\delta^{13}\text{C}$ values of dolomite-calcite marbles in the Fuping Complex (-0.31 ‰ to 3.65 ‰, mean = 2.65 ‰) than those in the Zhanhuang Complex (-2.68 ‰ to 1.44 ‰, mean = 0.20 ‰) imply that the adjacent Fuping and Zhanhuang Complexes may not have experienced a unified depositional environment in the late Paleoproterozoic.

Tang et al. (2015a) proposed a tectonic model which envisaged subduction and continental rifting process coevally among several micro-blocks (or complexes) within the TNCO during 2.1-2.0 Ga, in which the Fuping Complex recorded subduction-related arc magmatism and the Zhanhuang Complex witnessed continental rifting process. Thus, it is reasonable to suggest that the Wanzi Group in the Fuping Complex was deposited in a forearc basin during the later period of the continuous subduction, and the protoliths of the meta-sedimentary rocks in the Zhanhuang Complex were deposited in a back-arc basin which formed after the 2.0-2.1 Ga continental rifting. Previous studies proposed that the Wanzi Group was formed in a magmatic arc or intra-arc basin (Wu et al., 1989; Sun et al., 1992; Zhao et al., 2000b; Xia et al., 2006). Based on lithostratigraphic features, provenance and depositional age, Liu et al. (2012a) proposed that the Gantaohu Group in the Zhanhuang Complex was deposited in a back-arc basin. Trap et al. (2009) proposed that the Central Zhanhuang Domain represented the remnant of an oceanic basin.

The Paleoproterozoic global positive excursion of $\delta^{13}\text{C}$ during 2.33-2.06 Ga was affected by the Lomagundi or Jatulian Event (Schidlowski et al., 1975; Karhu and Holland, 1996; Melezhik et al., 1999; Bekker et al., 2006), or the Great Oxidation Event (Anbar et al., 2007; Konhauser et al., 2009). Schidlowski et al. (1975) first reported the remarkable positive excursion of $\delta^{13}\text{C}$ (9.4 ± 2.0 ‰) in the dolomites of the Middle Precambrian Lomagundi Group (Rhodesia). The global event was genetically related to environmental changes (Karhu and Holland, 1996; Melezhik et al., 1999) or breakup of the Kenorland/Superia supercontinent (Bekker et al., 2006). Several Paleoproterozoic carbonate strata in the North China Craton show positive

excursion of $\delta^{13}\text{C}$ and were proposed to be affected by the Jatulian Event (Fig. 5-13, Chen et al., 2000; Tang et al., 2008; Song et al., 2011). Recent studies reveal that the NCC is composed of a number of Archean microblocks which were amalgamated along multiple zones of ocean closure during late Neoproterozoic (e.g., Santosh et al., 2016; Tang et al., 2016a; Yang et al., 2016). The oceanic basin in the Fuping area was formed after the rifting event (2.33-2.31 Ga) recorded by the mafic dykes (Liu et al., 2002; Wei et al., 2014). The geochemical features and biospheres of the oceanic basin in the Fuping area were possibly affected by the Jatulian Event, which is probably reflected in the positive excursion of $\delta^{13}\text{C}$ values in dolomite-calcite marbles. However, the back-arc basin in the Zhanhuang area was formed after the 2.1-2.0 Ga rifting event, thus it was formed after the Jatulian Event and it preserved the original $\delta^{13}\text{C}$ values (-2.68 ‰ to 1.44 ‰, mean = 0.20 ‰) of marine carbonates.

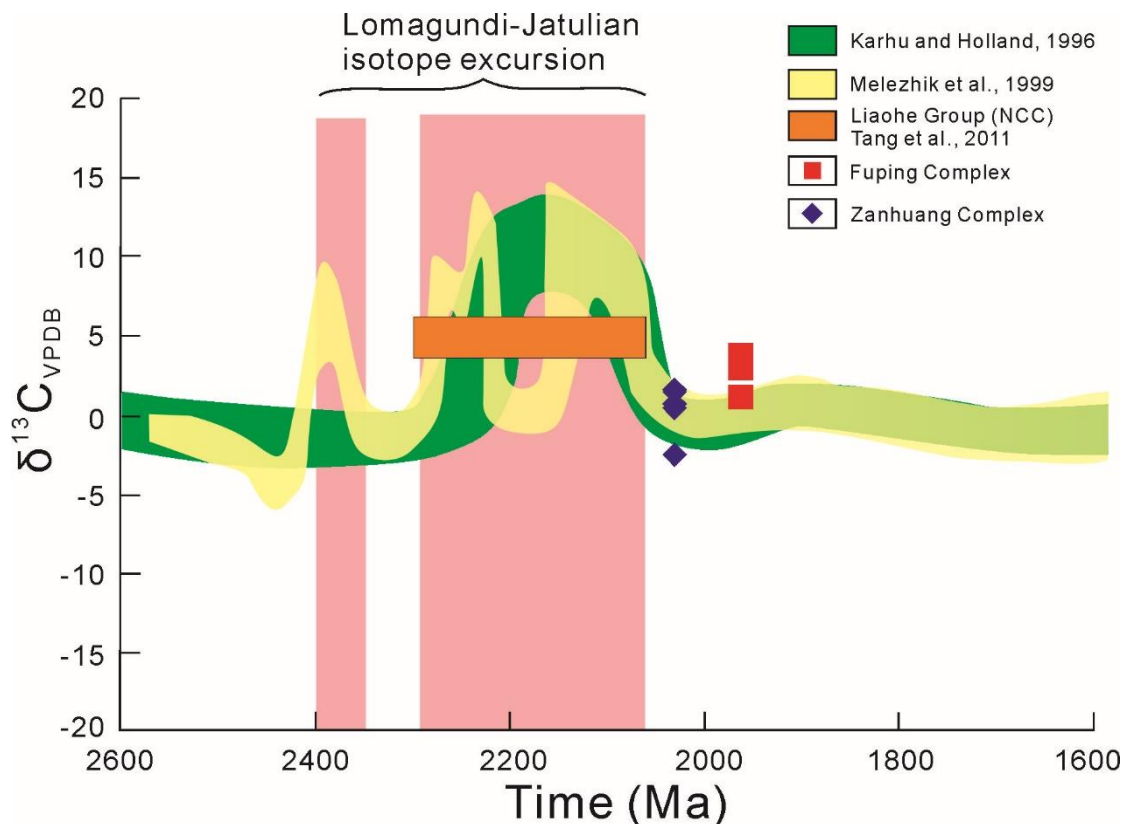


Fig. 5-13 $\delta^{13}\text{C}$ variation of meta-carbonate rocks through Paleoproterozoic, showing the $\delta^{13}\text{C}$ values through the globe (Karhu and Holland, 1996; Melezhik et al., 1999), Liaohe Group in the NCC (Tang et al., 2008) and this study.

In recent studies, the final assembly between the Western and Eastern Blocks

along the TNCO was suggested at 2.0-1.9 Ga, and the 1.9-1.8 Ga metamorphic ages were proposed to record the retrograde cooling (Qian et al., 2013, 2015; Wei et al., 2014; Zhang et al., 2016a). Metamorphic rims of detrital zircons in this study display $^{207}\text{Pb}/^{206}\text{Pb}$ ages varying from 1857 ± 20 Ma to 1898 ± 20 Ma, and the 1.90-1.85 Ga metamorphic overgrowths are interpreted to represent the cooling process along the TNCO. After the closure of the forearc basin in the Fuping area and back-arc basin in the Zhanhuang area, the Western and Eastern Blocks amalgamated and the NCC was incorporated into the global supercontinent Columbia (Rogers and Santosh, 2002, 2009; Zhao et al., 2002b; Meert, 2012; Nance et al., 2014).

5.5 Conclusions

- (1) The correlations between the isotopic results ($\delta^{13}\text{C}$ and $\delta^{18}\text{O}$) and geochemical composition (Mn, Sr, Mn/Sr, Mg/Ca, Ca/Sr and Fe/Sr) suggest that the dolomite marbles from the Zhanhuang Complex were strongly disturbed and that the calc-silicate rocks were moderately affected by the post-depositional processes. The dolomite-calcite marbles display the primary geochemical features without post-depositional effects.
- (2) The protoliths of the impure marbles and calc-silicate rocks are marine carbonates. These rocks formed in a proximal and shallow marine environment, as indicated by their comparable trace elements, carbon and oxygen isotopic compositions, lithology and mineral assemblage.
- (3) Detrital zircon U-Pb age dating of the meta-carbonates from Fuping and Zhanhuang Complexes shows age populations of 2.50-2.57 Ga, 2.2-2.4 Ga, 2.0-2.1 Ga and 1.85-1.90 Ga. The depositional age for the Wanzi Group is further constrained as 1.95-1.93 Ga. In combination with the youngest igneous detrital zircon age of 2033 ± 20 Ma and metamorphic ages, the depositional age of the Central Zhanhuang Domain is inferred to be 2.03-1.90 Ga.
- (4) The Wanzi Group in the Fuping Complex was deposited in a forearc basin during the later period of a protracted subduction cycle, and the Central Zhanhuang

Domain was deposited in a back-arc basin which formed after the 2.0-2.1 Ga continental rifting.

- (5) The dolomite-calcite marbles from the Wanzi Group display relatively higher $\delta^{13}\text{C}$ values (-0.31 ‰ to 3.65 ‰, mean = 2.65 ‰) which are proposed to be affected by the Paleoproterozoic Jatulian Event. The dolomite-calcite marbles from the Zhanhuang Complex preserve the original $\delta^{13}\text{C}$ values (-2.68 ‰ to 1.44 ‰, mean = 0.20 ‰) of marine carbonates.

Chapter 6: Paleoproterozoic (1.96-1.80 Ga) metamorphism in the Fuping Complex

6.1 Introduction

High pressure metamorphism of continental crust is commonly associated with the processes of subduction and collision during continental amalgamation (Brown, 2007; Anderson et al., 2012, Chopin et al., 2012). The petrology, metamorphic P - T conditions and geochronology of high-grade metamorphic rocks have been widely used to understand crustal evolution and geodynamic settings (e.g. Wei and Powell, 2004; Korhonen et al., 2013; Brown, 2014; Tsunogae et al., 2014; Tang et al., 2016b; Zhang et al., 2017b, and references therein). Metamorphism involving near-isothermal decompression (ITD) along clockwise P - T path is usually related to continent-continent collisional environments (England and Thompson, 1984; Brown, 1993). Phase diagrams (pseudosections) based on bulk composition, an internally consistent thermodynamic dataset and phase activity-composition (a - x) models have been widely applied to derive metamorphic P - T conditions (e.g. White et al., 2014; Palin et al., 2016). Recently, Green et al. (2016) proposed a melt model for metabasic rocks, with new computations for high-temperature augitic clinopyroxene and K-, Ti-bearing hornblende. These new activity-composition (a - x) models can be applied to unravel the P - T evolution and role of melt recorded by metabasic rocks such as mafic granulites.

The North China Craton (NCC) witnessed the collisional assembly of major continental blocks at 2.1–1.8 Ga, broadly coeval with the incorporation of the craton within the global supercontinent Columbia (Rogers and Santosh, 2002, 2009; Wilde et al., 2002; Zhao et al., 2002a; Meert, 2012; Nance et al., 2014). However, the timing and tectonic setting of the final assembly of the NCC are debated with several diverse models proposed, including the following: 1) The Trans-North China Orogen (TNCO) represents the final collisional belt between the Eastern and Western Blocks at 1.9–1.8 Ga (Kröner et al., 2005a; Zhao et al., 2005, 2007, 2012; Wang, 2009; Wang

et al., 2010a; Zhang et al., 2009; Trap et al., 2012). 2) After the first-stage of cratonization through microblock amalgamation during late Neoproterozoic (~2.5 Ga), the second-stage of cratonization represented by three mobile belts (Jinyu, Fengzhen and Jiaoliao belts) formed by intraplate rifting-subduction-collision at 2.30–1.97 Ga, with subsequent mantle upwelling causing metamorphism at 1.97–1.82 Ga (Zhai et al., 2005; Zhai, 2011, 2014; Zhai and Santosh, 2011). 3) The TNCO represents a continent–arc–continent collisional orogen at ~2.5 Ga, followed by the final collision at ~1.9 Ga recorded by the Northern Hebei Orogenic Belt and Jiaoliao Orogenic Belt (Kusky and Li, 2003; Li and Kusky, 2007; Kusky et al., 2007; Kusky and Santosh, 2009). 4) Double-sided subduction occurred along the TNCO and the Inner Mongolia Suture Zone (Khondalite Belt) involving the Eastern Block (Yanliao Block), Ordos Block and Yinshan Block and final collisional assembly of the NCC at 2.0–1.85 Ga (Santosh, 2010; Zhang et al., 2016a). Furthermore, the peak metamorphic ages in the suggested tectonic models above are also controversial with two groups of metamorphic ages at 1.95–1.90 Ga (e.g. Qian et al., 2015; Qian and Wei, 2016; Zhang et al., 2016a) and 1.88–1.80 Ga (e.g. Zhao et al., 2002b; Guo et al., 2005; Tang et al., 2015a), both are inferred to represent peak metamorphism.

Paleoproterozoic granulites are widespread in the NCC, including mafic granulites that are well preserved in the basement terranes along the TNCO. These high-grade metamorphic rocks are proposed to have been formed during the collisional event which resulted in the final cratonization of the NCC (e.g. Zhao et al., 2000a, 2000b, 2012; Guo et al., 2015a). The Fuping Complex is one of the important basement terranes within the central segment of the TNCO, where typical mafic and pelitic granulites are exposed. Previous studies only focused on the geochronology of pelitic granulites (Cheng et al., 2004), and *P–T* estimations of mafic granulites involving conventional geothermobarometers (Liu, 1996) and TWQ (Zhao et al., 2000a), without any detailed elucidation of the metamorphic *P–T–t* history based on phase equilibria modelling in combination with zircon geochronology. The objective of this study is therefore to integrate petrologic and phase equilibria studies with zircon U–Pb geochronology in order to understand the metamorphic *P–T*

evolution of the major Paleoproterozoic orogen in the NCC through a systematic investigation of a suite of mafic granulites from the Fuping Complex in the TNCO.

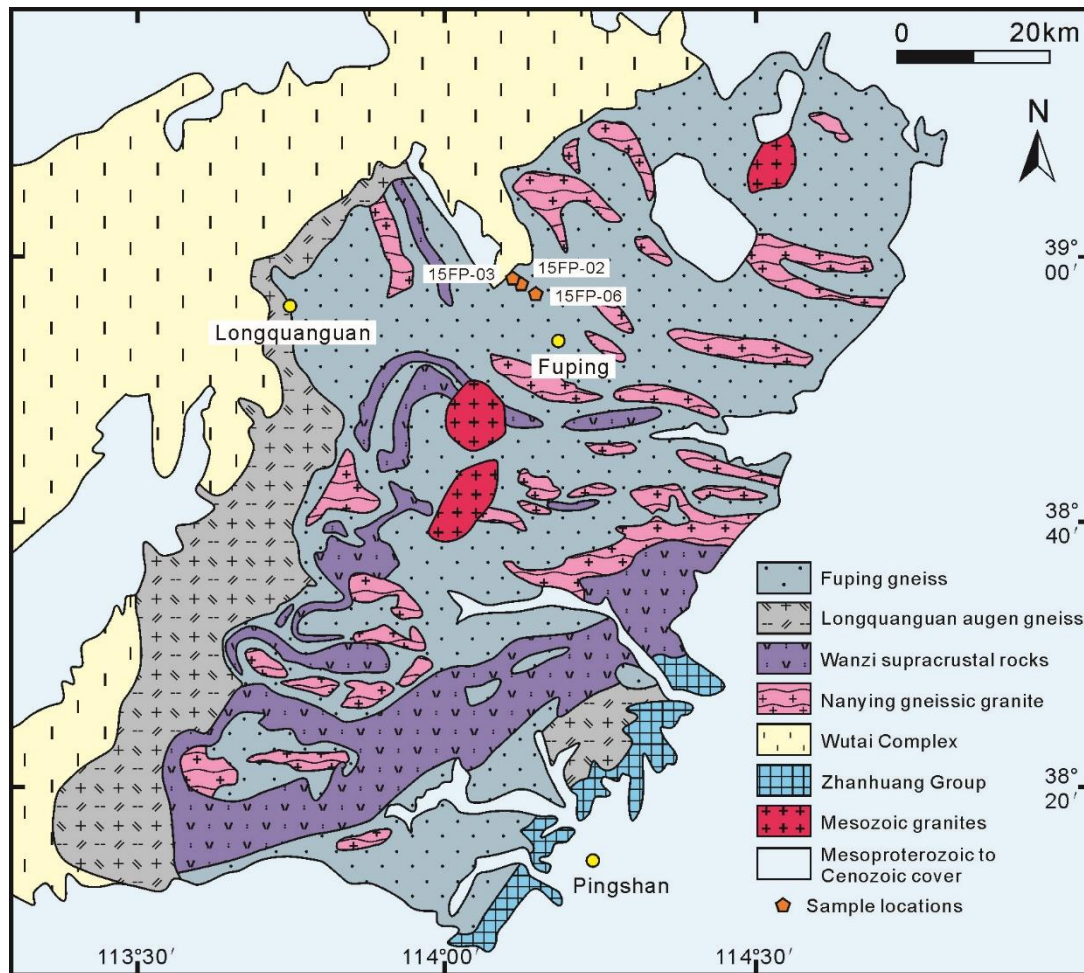


Fig. 6-1 Geological map of the Fuping Complex and the adjacent Wutai Complex (modified after Zhao et al., 2000a).

6.2 Samples and petrography

Three mafic granulite samples collected from the Daliushu area, 10 km NW of Fuping city (Fig. 6-1) were selected for detailed petrological studies. The mafic granulites are exposed as boudins or lenses within the TTG gneisses, and range in width from 0.1 to 2.0 m and length from 1 to 30 m (Fig. 6-2). The granulite boudins are aligned parallel to the foliation of the TTG gneisses (Fig. 6-2a, 6-2c). The detailed sampling locations are 38°54'20.7"N/114°07'22.3"E (15FP-02), 38°55'47.0"N/114°06'01.9"E (15FP-03) and 38°53'01.5"N/114°08'17.4"E (15FP-06). The salient aspects of the petrography of each sample are summarized below:

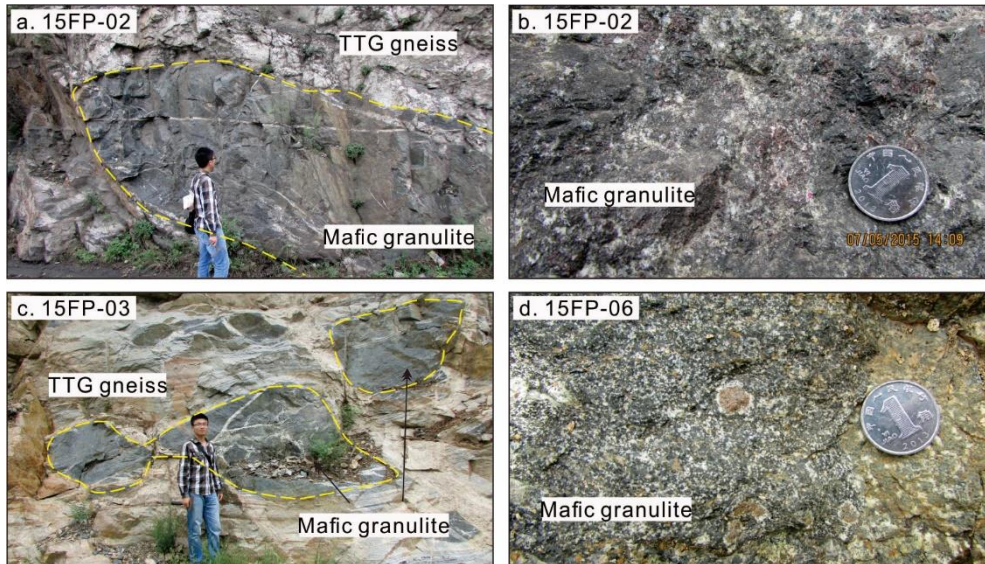


Fig. 6-2 Field photographs of mafic granulite from the Fuping Complex. (a) Mafic granulite sample 15FP-02 occurs as enclave in the TTG gneiss. (b) Sample 15FP-02, showing mineral assemblage of garnet + clinopyroxene + orthopyroxene + plagioclase + quartz. (c) Sample 15FP-03, showing mafic granulite occurs as boudin and enclave in the migmatized TTG gneiss. (d) Sample 15FP-06, showing “white eye” texture in which coarse grained garnets are surrounded by plagioclase + amphibole/pyroxene coronas.

6.2.1 15FP-02

Mafic granulite sample 15FP-02 is massive and dark gray (Fig. 6-2), and dominantly composed of garnet, clinopyroxene, orthopyroxene, plagioclase, quartz, amphibole, biotite, and K-feldspar, with minor ilmenite and magnetite (Fig. 6-3). The hand specimen shows patches of quartz + feldspar aggregates. The porphyroblastic garnets are medium- to coarse-grained (0.2–2.0 mm) and contain minor mineral inclusions of plagioclase, amphibole, quartz, biotite and ilmenite. The orthopyroxene occurs as coarse-grained (0.5–1.0 mm) grain (Fig. 4b) and also as fine-grained (<0.3 mm), xenoblastic intergrowths with plagioclase. The coarse-grained orthopyroxene, together with medium- to coarse-grained garnet, clinopyroxene, amphibole, plagioclase, quartz, K-feldspar, ilmenite, and magnetite, display a near-equigranular granoblastic texture and are inferred to have equilibrated at peak metamorphic conditions. Amphibole occurs as xenoblastic, medium- to fine-grained (<0.5 mm) grains in the matrix. The elongate amphibole, plagioclase

and magnetite symplectite separate the coarse-grained garnet and quartz (Fig. 6-3a). Thin rims of quartz form a moat around porphyroblastic garnet (Fig. 6-3d). Two retrograde textures are observed as amphibole + plagioclase + magnetite (Fig. 6-3a) and orthopyroxene + plagioclase (Fig. 6-3c) symplectites. Biotite and K-feldspar occur as fine grains in the matrix.

6.2.2 15FP-03

Mafic granulite sample 15FP-03 was collected from a boudin in the migmatized TTG gneiss (Fig. 6-2c). Coarse-grained garnet porphyroblasts (0.5–5.0 mm), clinopyroxene, amphibole, plagioclase, quartz, ilmenite and K-feldspar comprise the inferred peak metamorphic mineral assemblage. Garnet hosts minor mineral inclusions of clinopyroxene, quartz and ilmenite (Fig. 6-3e). Amphibole in the matrix ranges from coarse- to fine-grained (<0.5 mm) and also occurs intergrown with plagioclase as a corona around garnet (Fig. 6-3g).

Another retrograde reaction texture occurs in the form of clinopyroxene + plagioclase + magnetite intergrowths which pseudomorph the cores of porphyroblastic garnet, giving an atoll structure (Fig. 6-3h). The fine-grained biotite, quartz, ilmenite and K-feldspar embay the garnet porphyroblast (Fig. 6-3e).

6.2.3 15FP-06

This mafic granulite is massive and dark gray, and contains coarse corona textures around garnet which are visible in hand specimen. The coronas contain plagioclase + amphibole or pyroxene (Fig. 6-2d). The garnet porphyroblasts occur in an equigranular and medium- to coarse-grained matrix assemblage of clinopyroxene + amphibole + plagioclase + quartz + ilmenite + K-feldspar, which is inferred to be the peak metamorphic assemblage (Fig. 6-4). The garnet porphyroblasts host very few mineral inclusions such as amphibole, quartz and ilmenite. Moats of quartz + K-feldspar + plagioclase occur around the porphyroblastic garnet. Two retrograde reaction textures are recognized, the most common one comprises amphibole + plagioclase coronas around the garnet porphyroblasts (Fig. 6-4c). The second type of retrograde texture is represented by

orthopyroxene + clinopyroxene + amphibole + plagioclase symplectite around embayed garnet (Fig. 6-4d).

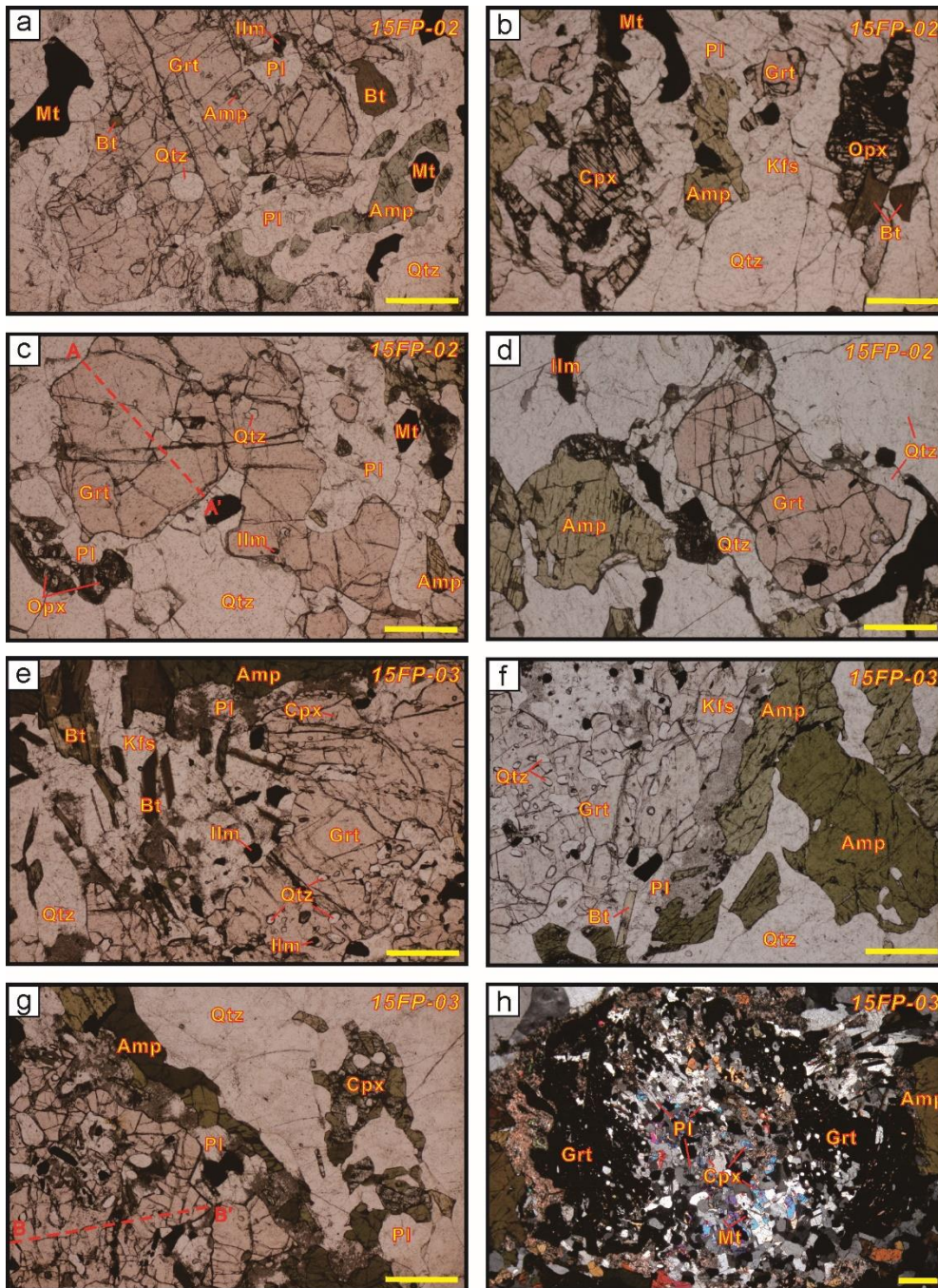


Fig. 6-3 Representative photomicrographs of mafic granulites (15FP-02 and 15FP-03) from the Fuping Complex. (a) Sample 15FP-02, showing peak mineral assemblage of garnet + quartz + magnetite and plagioclase + amphibole + magnetite symplectite between garnet and quartz (plane polarized light). (b) Sample 15FP-02, showing peak mineral assemblage of garnet + clinopyroxene + orthopyroxene + plagioclase + quartz + K-feldspar (plane polarized light). (c) Sample 15FP-02, orthopyroxene + plagioclase symplectite around porphyroblastic garnet (plane

polarized light). The red line is the location of the compositional profile shown in Fig. 6-5a. (d) Sample 15FP-02, showing peak mineral assemblage of garnet + amphibole + quartz + ilmenite and thin rim of quartz moat occurs around porphyroblastic garnet (plane polarized light). (e) Sample 15FP-03, the garnet porphyroblast contains few inclusions of quartz, clinopyroxene and ilmenite, biotite occur as fine-grained mineral in the matrix (plane polarized light). (f) Sample 15FP-03, showing peak mineral assemblage of garnet + amphibole + quartz + K-feldspar and amphibole + plagioclase symplectite around garnet (plane polarized light). (g) Sample 15FP-03, showing equilibrium peak mineral assemblage of garnet + clinopyroxene + plagioclase + quartz, and amphibole + plagioclase symplectite between garnet and quartz. The red line is the location of the compositional profile shown in Fig. 6-5b (plane polarized light). (h) Sample 15FP-03, plagioclase + clinopyroxene pseudomorph after porphyroblastic garnet (crossed polarized light). Scale bars are in 500 μm .

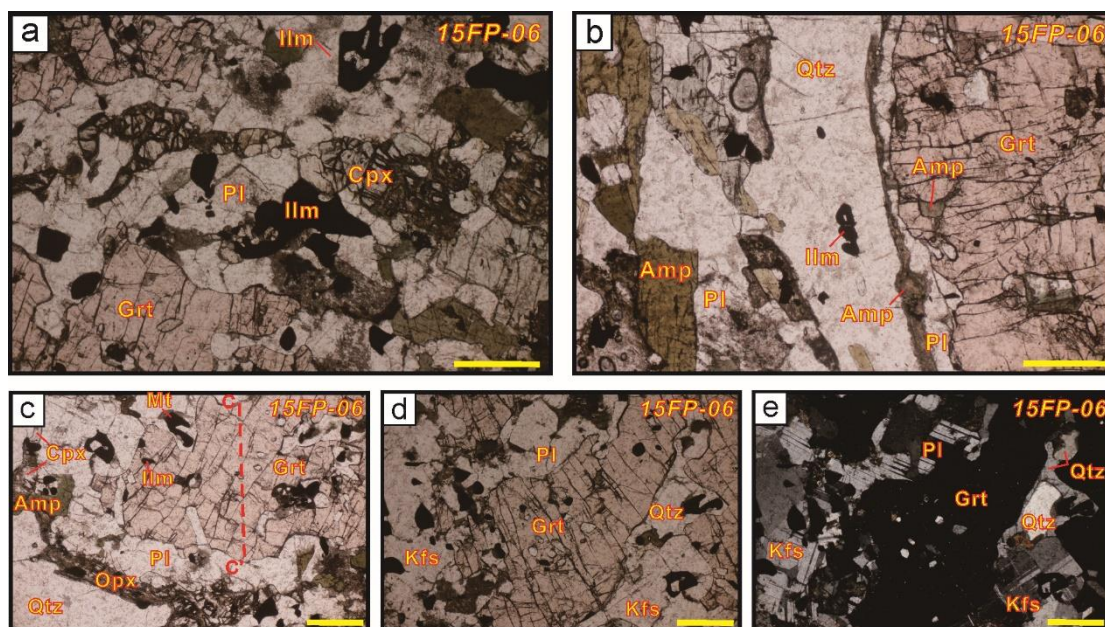


Fig. 6-4 Representative photomicrographs of mafic granulites (15FP-06) from the Fuping Complex. (a) Peak mineral assemblage of garnet + clinopyroxene + plagioclase + quartz + ilmenite (plane polarized light). (b) Amphibole + plagioclase corona around garnet (plane polarized light). (c) Plagioclase + clinopyroxene + orthopyroxene + amphibole symplectite between garnet and quartz, the red line is the location of the compositional profile shown in Fig. 6-5c (plane polarized light). (d) Quartz + K-feldspar + plagioclase moat occurs around porphyroblastic garnet (plane polarized light). (e) Quartz + K-feldspar + plagioclase moat occurs around porphyroblastic garnet (cross polarized light). Scale bars are in 500 μm .

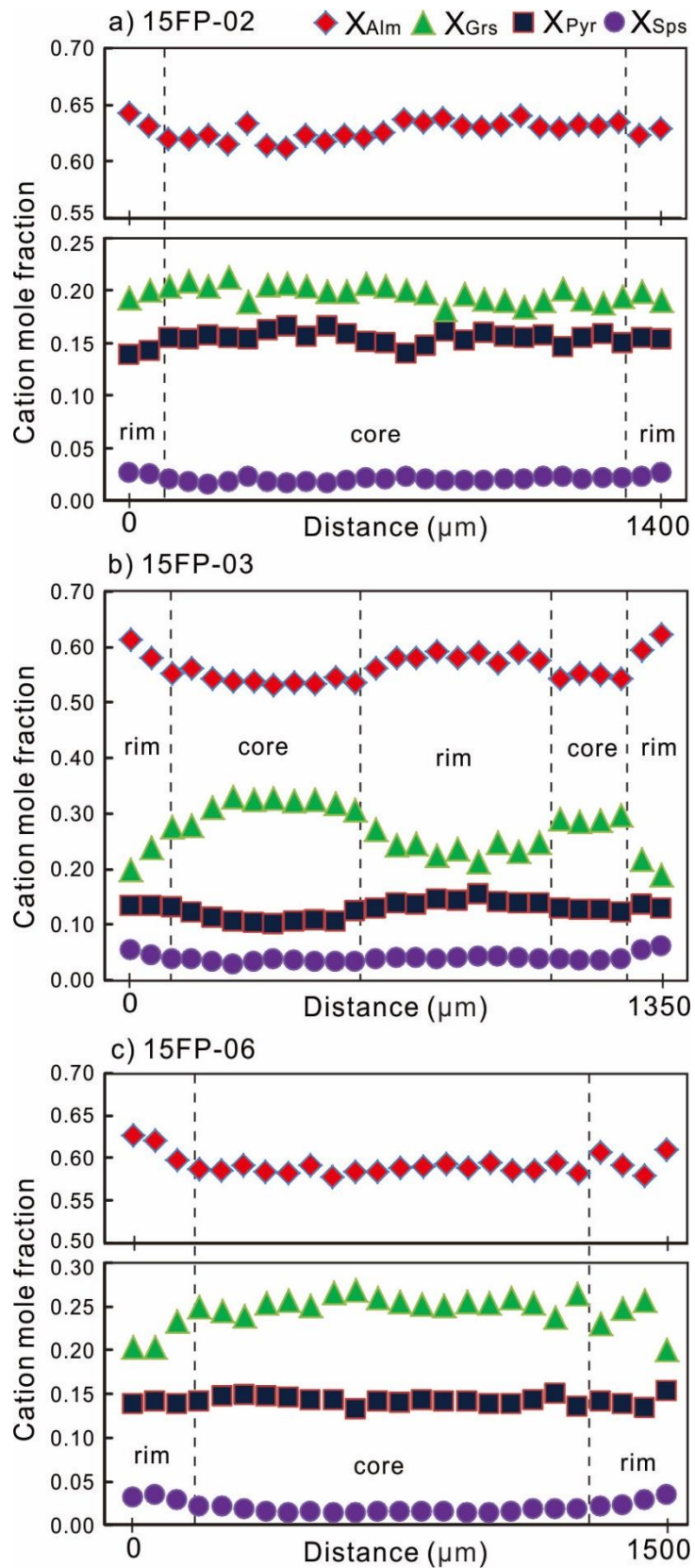


Fig. 6-5 Compositional zoning profiles of the porphyroblastic garnets, showing the approximate boundaries of the core and rim of the grains.

6.3 Analytical results

6.3.1 Mineral chemistry

6.3.1.1 Garnet

The porphyroblastic garnets are compositionally zoned with the rims showing higher X_{Alm} and X_{Sps} , lower X_{Grs} and X_{Pyr} than their cores (Table 6-2, Fig. 6-5). In sample 15FP-02, the garnet grain is characterized by a large relatively homogeneous core domain with slightly lower X_{Alm} (0.61–0.64) and X_{Sps} (0.02) and higher X_{Grs} (0.18–0.21) and X_{Pyr} (0.14–0.17) than those in the rim (Fig. 6-5a). Sample 15FP-03 displays distinct compositional zoning from core ($\text{Alm}_{53-56}\text{Pyr}_{10-13}\text{Grs}_{27-33}\text{Sps}_{3-4}$) to rim ($\text{Alm}_{57-62}\text{Pyr}_{13-16}\text{Grs}_{19-25}\text{Sps}_{4-6}$). The separate core-rim zoning patterns across the grain implies that some grains formed by the coalescence of two garnet grains from separate nuclei (Fig. 6-5b). The garnet porphyroblasts in sample 15FP-06 also have compositional zoning with core ($\text{Alm}_{58-59}\text{Pyr}_{13-15}\text{Grs}_{24-27}\text{Sps}_{1-2}$) and rim ($\text{Alm}_{58-63}\text{Pyr}_{13-15}\text{Grs}_{20-26}\text{Sps}_{2-4}$) (Fig. 6-5c).

6.3.1.2 Amphibole

Amphiboles are dominantly ferropargasite ($\text{Ca}_B \geq 1.50$, $\text{Na}_A + \text{K}_A \geq 0.50$, $\text{Ti} < 0.50$) according to the nomenclature of [Leake et al. \(1997\)](#). In sample 15FP-02, three types of amphibole are identified, the amphibole inclusions display $\text{Si} = 6.27\text{--}6.58$ p.f.u. ($\text{O} = 23$) and $X_{\text{Mg}} = \text{Mg}/(\text{Mg} + \text{Fe}^{2+}) = 0.41\text{--}0.47$, and the coarse- to fine-grained amphiboles in the matrix exhibit $\text{Si} = 6.33\text{--}6.40$ p.f.u. and $X_{\text{Mg}} = 0.39\text{--}0.41$ (Table S1). In sample 15FP-03, the amphibole inclusions and coarse- to fine-grained amphiboles in the matrix show slightly different compositions with $\text{Si} = 6.32\text{--}6.39$ p.f.u. and $X_{\text{Mg}} = 0.40\text{--}0.41$. In sample 15FP-06, the coarse-grained amphibole and fine-grained amphibole corona show Si contents (6.35–6.51 p.f.u.) and variable X_{Mg} values of 0.44–0.45 and 0.41–0.42, respectively (Table 6-3).

6.3.1.3 Clinopyroxene

Clinopyroxenes analyzed in this study are all augite in composition, including those occurring as inclusions in garnet, matrix coarse grains, and symplectites intergrown with plagioclase + orthopyroxene + amphibole (Fig. 6-3). Clinopyroxene

in sample 15FP-02 occurs only as a coarse-grained mineral (Fig. 6-3b) and contains Al contents of 0.08–0.09 p.f.u. (O = 6) and $X_{Mg} = 0.60$. In sample 15FP-03, clinopyroxene occurring as inclusions, matrix grains and in symplectites exhibit slight compositional variation in Al content (0.08–0.09 p.f.u., 0.05–0.07 p.f.u. and 0.07–0.08 p.f.u., respectively) but constant X_{Mg} values (0.58–0.60). In sample 15FP-06, the coarse-grained clinopyroxenes contain Al (0.08–0.09 p.f.u.) and X_{Mg} values of 0.59–0.60. Clinopyroxenes in the clinopyroxene + orthopyroxene + amphibole + plagioclase symplectites have relatively lower Al (0.07–0.08 p.f.u.) and X_{Mg} values of 0.55–0.59 (Table 6-5, Fig. 6-6b).

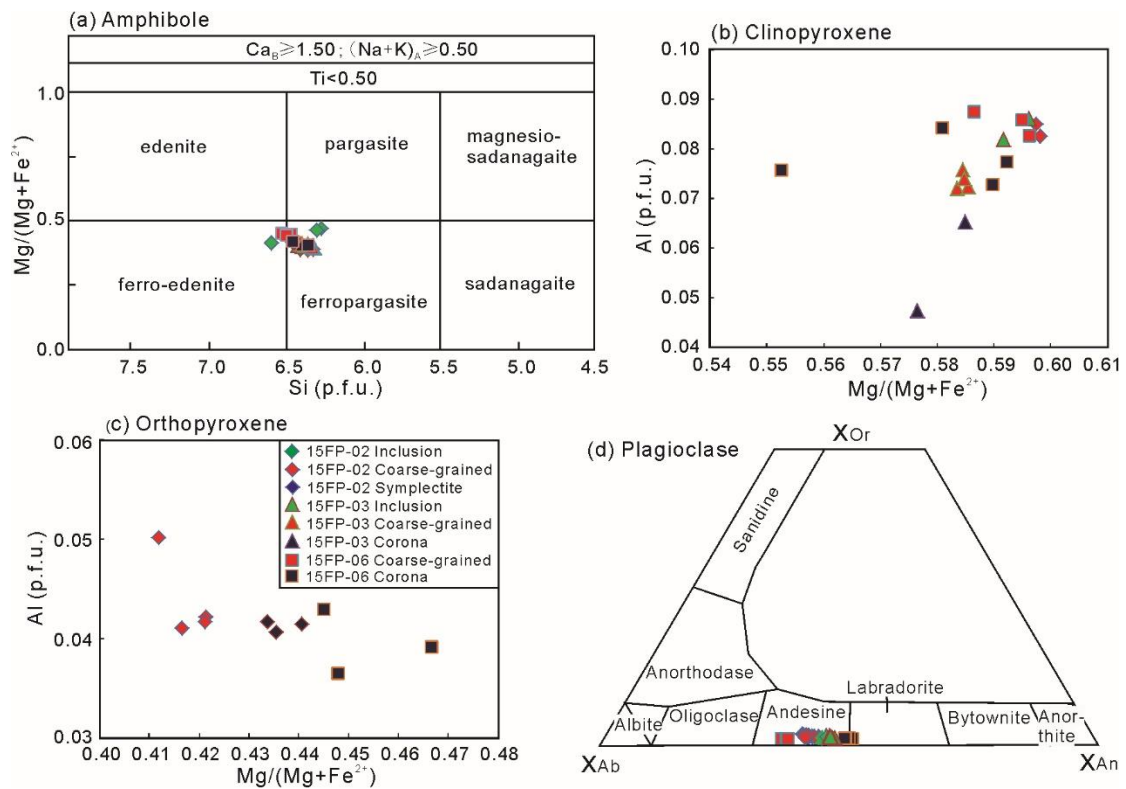


Fig. 6-6 Compositional diagrams of principal minerals in mafic granulites from the Fuping Complex. (a) Classification diagram of amphibole after Leake et al. (1997). (b) Al versus Mg/(Mg+Fe²⁺) plot for clinopyroxene. (c) Al versus Mg/(Mg+Fe²⁺) plot for orthopyroxene. (d) Ternary X_{An}-X_{Ab}-X_{Or} diagram for plagioclase. PG, prograde stage; PK, peak stage; RG, retrograde stage.

6.3.1.4 Orthopyroxene

In sample 15FP-02, the medium- to coarse-grained orthopyroxenes display higher Al (0.04–0.05 p.f.u., O = 6) contents and lower $X_{Mg} = 0.41$ –0.42 than the

symplectitic orthopyroxene which have lower Al (0.04 p.f.u.) and higher $X_{Mg} = 0.43$ –0.44. Orthopyroxene occurs only in symplectites in sample 15FP-06 (Fig. 6-4c), with relatively moderate values of Al (0.04 p.f.u.) and X_{Mg} (0.45–0.47, Fig. 6-6c).

6.3.1.5 Plagioclase

Plagioclase grains in the different samples occur in various textural domains, such as mineral inclusions in garnet, as matrix grains and in fine-grained symplectites/coronas. All plagioclase grains are broadly andesine with $An = 0.37$ –0.50 (Table 6-4, Fig. 6-6d). The plagioclase grains in samples 15FP-02 and 15FP-03 are relatively homogeneous in composition with $An = 0.40$ –0.46. In sample 15FP-06, the symplectitic plagioclase ($An=0.48$ –0.50) contains more calcium than the coarse-grained plagioclase in the matrix ($An=0.37$ –0.43).

6.3.1.6 Other minerals

In mafic granulite samples 15FP-02 and 15FP-03, K-feldspar and biotite are observed. The K-feldspar occurs as medium- to fine-grained mineral in the matrix and shows variable K contents of 0.70–0.92 p.f.u. (Table 6-7). In sample 15FP-02, biotite inclusions in garnet show lower Fe^{2+} (1.24–1.29 p.f.u.) and higher Mg (1.31–1.33 p.f.u.) than the biotites in the matrix ($Fe^{2+} = 1.42$ –1.65 p.f.u., Mg = 1.03–1.09 p.f.u.). The biotites in the matrix in sample 15FP-03 show constant Al contents (1.37–1.38 p.f.u.) and moderate contents of Fe^{2+} (1.28 p.f.u.) and Mg (1.07–1.11 p.f.u.).

Ilmenite and magnetite are common minor constituents in all the mafic granulite samples. The ilmenites exhibit high Ti (0.91–0.98 p.f.u.), variable Fe^{2+} (0.67–1.09 p.f.u.) and minor Mn (0.02–0.05 p.f.u.) (Table 6-6). Magnetite compositions are close to its ideal formulae as Fe_3O_4 with variable Ti (<0.13 p.f.u.) and Fe (2.60–2.98 p.f.u.).

6.3.2 Pseudosection modelling

P – T pseudosection calculations were performed by using THERMOCALC 3.40 (Powell and Holland, 1988, updated July 2016) and the internally consistent thermodynamic dataset of ds62 (Holland and Powell, 2011). The effective bulk-rock

compositions for pseudosection calculation (samples 15FP-02, 15FP-03 and 15FP-06), normalized into mole proportions in the model system, were calculated on the basis of the whole-rock geochemical results (Table 6-1). MnO was neglected because of low concentrations (<0.3 wt.%). Potassium was considered because of the relatively high contents ($K_2O = 0.82\text{--}2.70$ wt.%) as well as the presence of K-feldspar and biotite. Fe_2O_3 was taken into account for the calculations because the rocks contain 4.48–9.22 wt.% Fe_2O_3 and magnetite was present. Fe_2O_3 contents were determined by titration. Water contents in mole $M(H_2O)$ were fixed by $P/T\text{--}M(H_2O)$ diagrams with H_2O contents range from near-anhydrous composition ($H_2O = 0.01$ mol.%) to 5.00 mol.%. Therefore, a model system of NCKFMASHTO ($Na_2O\text{--}CaO\text{--}K_2O\text{--}FeO\text{--}MgO\text{--}Al_2O_3\text{--}SiO_2\text{--}H_2O\text{--}TiO_2\text{--}Fe_2O_3$) was chosen for $P\text{--}T$ pseudosection calculations. The phases considered in the modelling and the corresponding activity-composition (a-x) models used are garnet, orthopyroxene and biotite (White et al., 2014), amphibole, clinopyroxene and melt (Green et al., 2016), plagioclase and K-feldspar (Holland and Powell, 2003), ilmenite (White et al., 2000) and magnetite (White et al., 2002). Quartz and rutile are treated as pure end-member phases.

6.3.2.1 Sample 15FP-02

The peak mineral assemblage in this sample comprises garnet + clinopyroxene + orthopyroxene + amphibole + quartz + plagioclase + K-feldspar + magnetite + ilmenite. A $P\text{--}M(H_2O)$ diagram was constructed at 850 °C which is estimated from garnet-orthopyroxene geothermometry (Table 6-8). The peak mineral assemblage is stable at $M(H_2O)$ contents <0.4 mol.% defined by the orthopyroxene-out and ilmenite-out lines (Fig. 6-7a). Thus a $M(H_2O)$ content of 0.2 mol.% was selected for the subsequent pseudosection calculation for the peak $P\text{--}T$ condition. In the pseudosection, the solidus is predicted at temperatures between 800 °C and 875 °C over the pressure range from 5 kbar to 10 kbar (Fig. 6-7b). The peak assemblage lies within the stable field with $P\text{--}T$ conditions of 8.2–9.2 kbar and 870–882 °C. The upper temperature limit is defined by the amphibole-out line, and the upper and lower pressure limits are defined by the orthopyroxene-out and ilmenite-out lines, respectively.

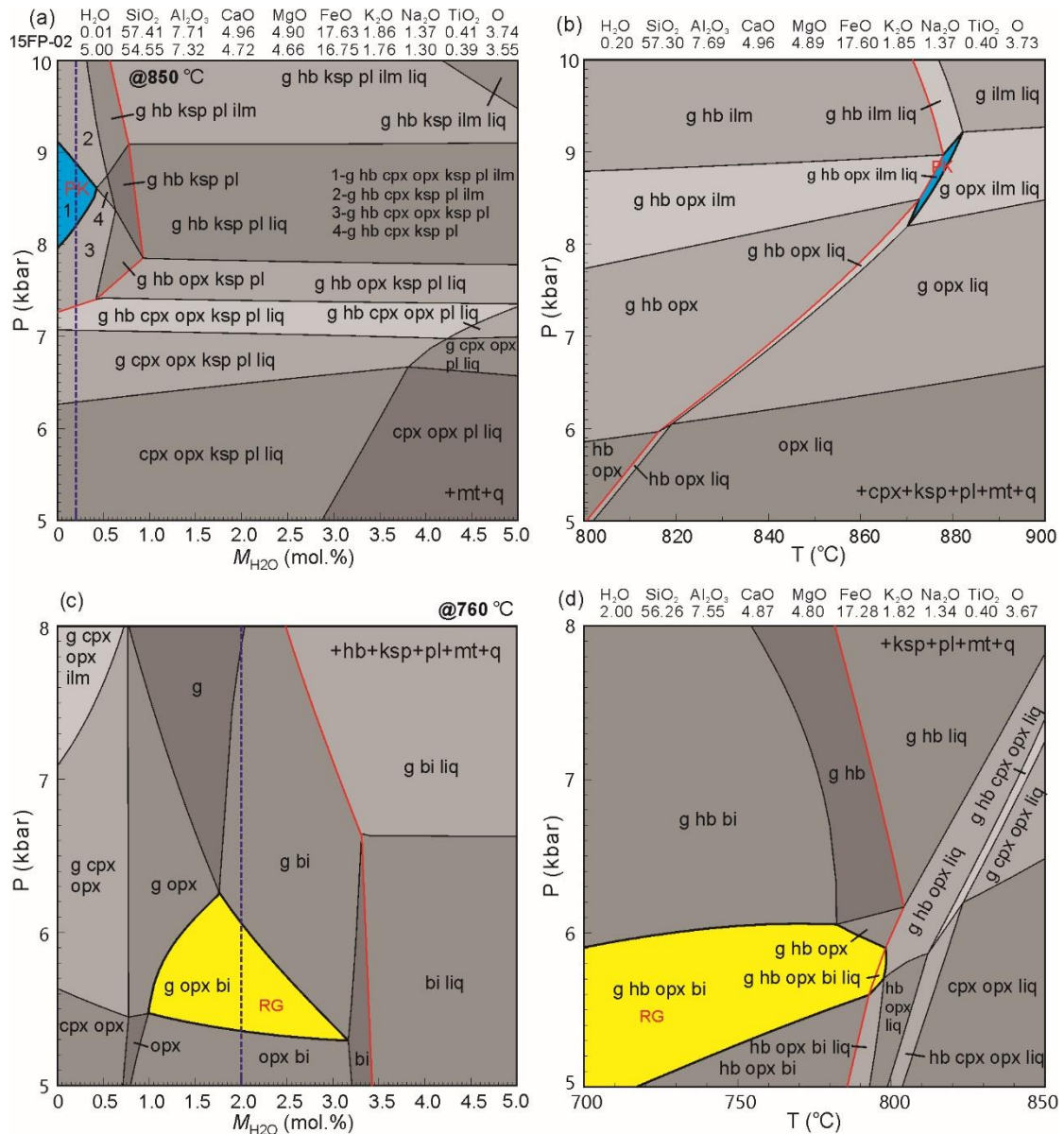


Fig. 6-7 Pseudosections for mafic granulite sample 15FP-02 calculated in the system NCKFMASHTO. (a) P - M_{H_2O} diagram at 850 °C. (b) P - T pseudosection calculated at the adjusted H_2O content of 0.20 mol.%, the stable field for the peak phase assemblage is shown in blue color. (c) P - M_{H_2O} diagram at 760 °C. (d) P - T pseudosection calculated at the adjusted H_2O content of 2.00 mol.%, the stable field for the retrograde phase assemblage is shown in yellow color. Mineral abbreviations: g, garnet; cpx, clinopyroxene; opx, orthopyroxene; hb, amphibole; pl, plagioclase; q, quartz; ksp, K-feldspar; bi, biotite; ilm, ilmenite; mt, magnetite; ru, rutile; liq, liquid. PK, peak stage; RG, retrograde stage.

The retrograde mineral assemblage comprises garnet rim, amphibole + magnetite + plagioclase and orthopyroxene + plagioclase symplectites and fine-grained quartz +

biotite + K-feldspar in the matrix. A P - $M(\text{H}_2\text{O})$ diagram was constructed at 760 °C which is estimated from hornblende-plagioclase geothermometry (Table 6-8). An approximate H_2O content of 2.0 mol.% was used for P - T pseudosection (Fig. 6-7c). In the pseudosection, at higher H_2O content (2.0 mol.%), the solidus is shifted to lower temperature (780–800 °C) at 5–8 kbar (Fig. 6-7d). The garnet-out line at the lower pressure, orthopyroxene-out line at the upper pressure and biotite-out line at the upper temperature define the stable field of retrograde assemblage at P - T conditions of <6.1 kbar and <795 °C.

6.3.2.2 Sample 15FP-03

The peak mineral assemblage in this sample comprises garnet + clinopyroxene + amphibole + quartz + plagioclase + K-feldspar + ilmenite. The T - $M(\text{H}_2\text{O})$ diagram used to constrain the H_2O content was constructed at 11 kbar which was estimated from garnet-clinopyroxene-plagioclase-quartz geobarometry (Table 6-8). The amphibole-out and plagioclase-out lines define the stable field for the peak assemblage at $\text{H}_2\text{O} < 2.5$ mol.%, an appropriate H_2O content of 1.0 mol.% was selected for P - T pseudosection (Fig. 6-8a). The solidus in the pseudosection is located at 807 °C to 865 °C in the pressure range of 5–12 kbar (Fig. 6-8b). At 800–900 °C, plagioclase disappears at pressure above 10.4–11.8 kbar, rutile appears at pressure above 11.2–11.7 kbar, and orthopyroxene appears at pressure below 8.5 kbar. The relevant fields are contoured for garnet X_{Ca} isopleth, where the X_{Ca} decreases as pressure decreases within the pressure range of 8–11 kbar (Fig. 6-8b). The peak field is further constrained by the amphibole-out line at the upper temperature and measured X_{Ca} (0.28–0.34) of garnet core, where peak P - T conditions of 9.6–11.3 kbar and 855–870 °C are inferred.

The retrograde mineral assemblage is inferred to have been garnet + clinopyroxene + amphibole + quartz + plagioclase + biotite + K-feldspar + ilmenite + magnetite. A similar approach of P - $M(\text{H}_2\text{O})$ diagram at 760 °C was used to fix appropriate H_2O content. A small field constrained by the biotite-out, garnet-out and orthopyroxene-in lines was stable at H_2O contents of 3.3–3.7 mol.% (Fig. 6-8c). Thus the corresponding pseudosection was calculated at $\text{H}_2\text{O} = 3.5$ mol.%. The retrograde

phase assemblage is stable at 5.6–5.8 kbar and <795 °C (Fig. 6-8d). The relevant fields are contoured for garnet X_{Ca} isopleth, where the X_{Ca} decreases as pressure decreases in the higher P – T fields than in the retrograde field. The measured X_{Ca} (0.20–0.26) of garnet rim are plotted in the retrograde P – T range (Fig. 6-8d).

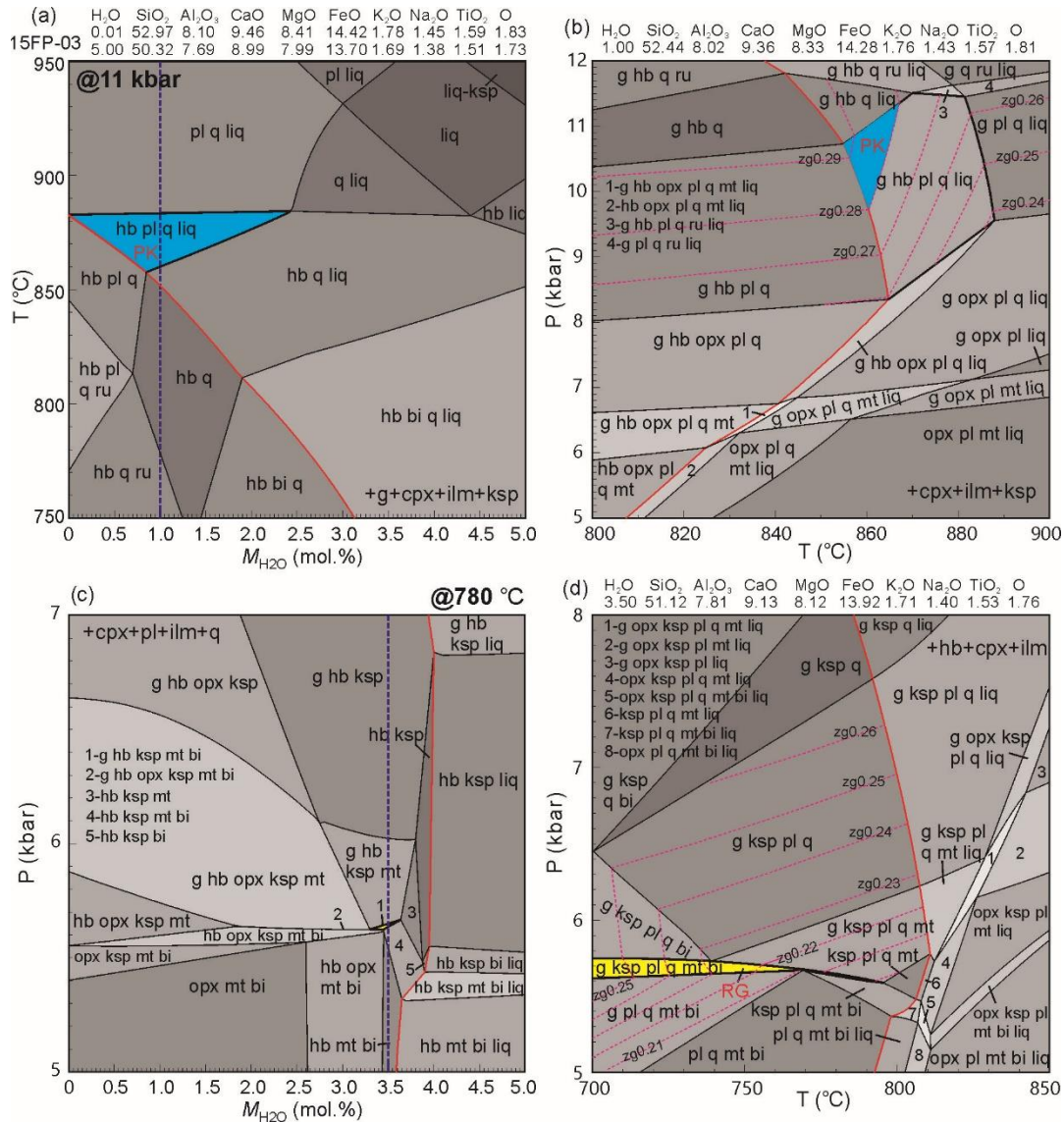


Fig. 6-8 Pseudosections for mafic granulite sample 15FP-03 calculated in the system NCKFMASHTO. (a) T – M_{H_2O} diagram at 11 kbar. (b) P – T pseudosection calculated at the adjusted H_2O content of 1.00 mol.%, the stable field for the peak phase assemblage is shown in blue color. (c) P – M_{H_2O} diagram at 780 °C. (d) P – T pseudosection calculated at the adjusted H_2O content of 3.50 mol.%, the stable field for the retrograde phase assemblage is shown in yellow color. The pseudosections are contoured with compositional isopleths of garnet ($z_g = Ca/(Ca + Mg + Fe^{2+})$). Abbreviations are the same with Fig. 6-7.

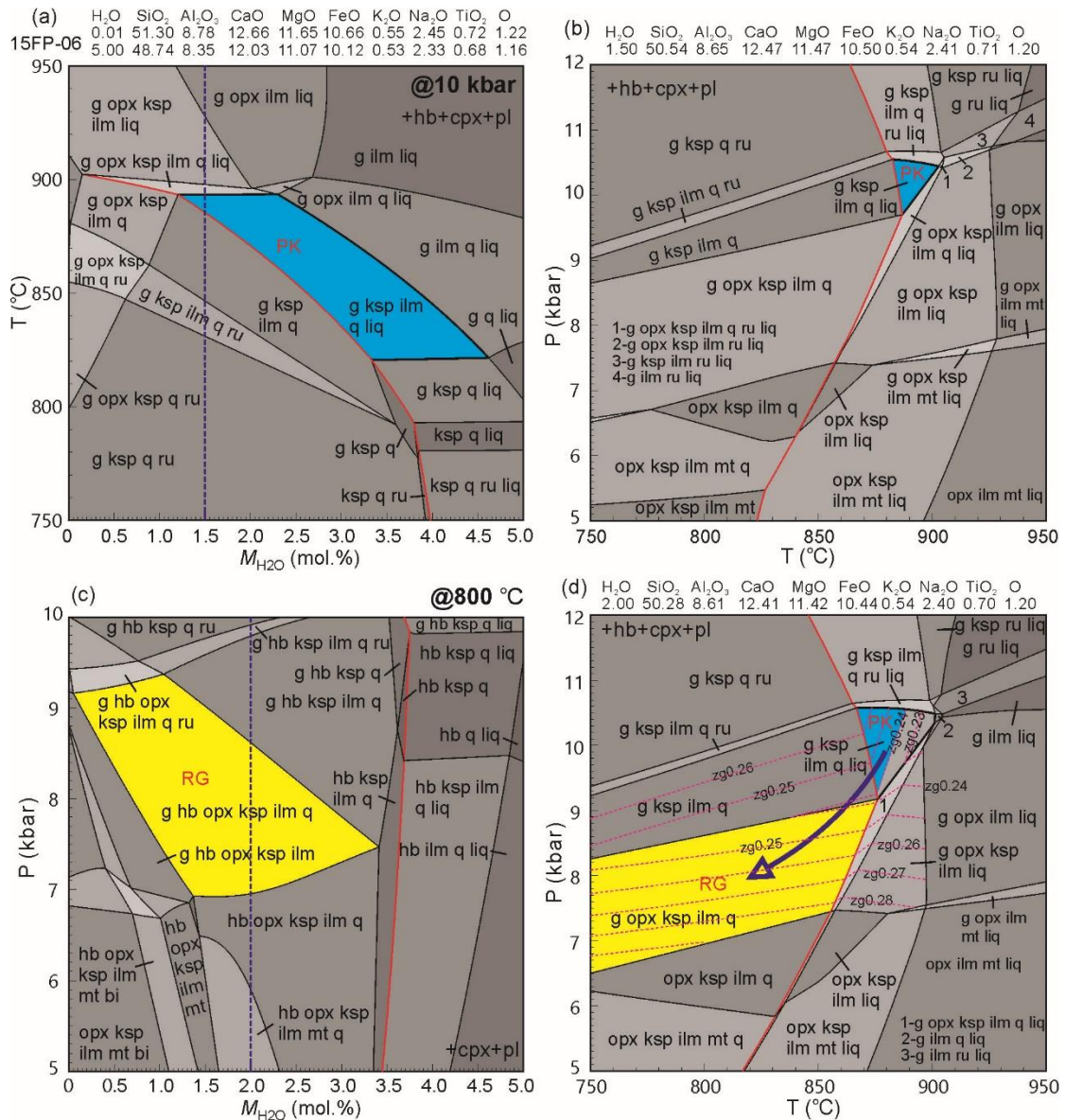


Fig. 6-9 Pseudosections for mafic granulite sample 15FP-06 calculated in the system NCKFMASHTO. (a) T - M_{H_2O} diagram at 10 kbar. (b) P - T pseudosection calculated at the adjusted H_2O content of 1.50 mol.%, the stable field for the peak phase assemblage is shown in blue color. (c) P - M_{H_2O} diagram at 800 °C. (d) P - T pseudosection calculated at the adjusted H_2O content of 2.00 mol.%, the field for the retrograde phase assemblage is shown in yellow color. The pseudosection is contoured with compositional isopleths of garnet ($zg = Ca/(Ca + Mg + Fe^{2+})$). Abbreviations are the same with Fig. 6-7.

6.3.2.3 Sample 15FP-06

The peak mineral assemblage in this sample comprises garnet + clinopyroxene + amphibole + quartz + plagioclase + K-feldspar + ilmenite. A T - $M(H_2O)$ diagram at

10 kbar was used to constrain the H₂O content (Fig. 6-9a). The calculated pseudosection at H₂O = 1.5 mol.% shows that the peak assemblage is stable at pressures of 9.7–10.5 kbar and temperatures of 880–900 °C (Fig. 6-9b). Between 5 kbar and 12 kbar, the temperature of the solidus varies from 820 °C to 880 °C. The stable field for the peak phase assemblage is constrained by the rutile-in and orthopyroxene-in lines, and the field is just above the solidus line.

The retrograde mineral assemblage comprises garnet + clinopyroxene + orthopyroxene + amphibole + quartz + plagioclase + K-feldspar + ilmenite (Fig. 6-4). A *P*–*M*(H₂O) diagram was constructed at 800 °C which is estimated from hornblende-plagioclase geothermometer (Table 6-8). The phase assemblage is stable at pressure 7.0–9.4 kbar and H₂O < 3.4 mol.% (Fig. 6-9c). An approximate H₂O content of 2.0 mol.% was used for the *P*–*T* pseudosection. The retrograde field is subsolidus with pressure lower than 9 kbar and temperature lower than 865 °C. At higher H₂O content, the solidus is shifted to lower temperature (820–865 °C) than that in the peak stage. The H₂O content (2.0 mol.%) is also appropriate for the peak phase assemblage (Fig. 6-9a), where the stable field for the peak phase assemblage shows temperature in the range of 865–900 °C. In the peak field and adjacent fields, the *X*_{Ca} also decreases mainly as pressure decreases. The garnet core compositions (*X*_{Ca} = 0.24–0.27) further constrain the peak field.

6.3.3 Geothermobarometry

The peak metamorphic *P*–*T* conditions are further quantified by conventional geothermobarometry. Temperatures were calculated based on experimental and empirical calibrations of Fe–Mg fractionation for garnet-clinopyroxene pair (Ellis and Green, 1979; Dahl, 1980) and garnet-orthopyroxene pairs (Lee and Ganguly, 1988; Aranovich and Berman, 1997). The garnet-orthopyroxene-plagioclase-quartz geobarometry based on experimental calibration (Perkins and Chipera, 1985) was applied to constrain the peak metamorphic pressure of sample 15FP-02, and garnet-clinopyroxene-plagioclase-quartz geobarometry was used for samples 15FP-03 and 15FP-06. The calculated results are listed in Table 6-8.

The estimated temperature ranges for garnet-orthopyroxene pairs are 772-865 °C at 9 kbar for sample 15FP-02 (Lee and Ganguly, 1988; Aranovich and Berman, 1997). Metamorphic pressure for the garnet-orthopyroxene-plagioclase-quartz assemblages has been refined by Perkins and Chipera (1985), and computation based on this method shows pressure of 9.5–10.2 kbar at 850 °C. We also obtained the pressure ranges of 8.2–10.2 kbar at 850 °C based on the experimental method of Moecher et al. (1988).

From the Fe-Mg exchange thermometry of garnet-clinopyroxene pairs (Ellis and Green, 1979; Dahl, 1980), the peak metamorphic temperatures were estimated at 789–886 °C and 783–859 °C (at 10 kbar) for samples 15FP-03 and 15FP-06, respectively (Table 6-8). Metamorphic pressures were calculated using garnet-clinopyroxene-plagioclase-quartz assemblages based on the method of Eckert et al. (1991), and the results show pressures of 8.9–9.1 kbar (15FP-03) and 9.1–9.3 kbar (15FP-06) at 850 °C. Application of the Moecher et al. (1988) method yields pressure estimates for sample 15FP-03 (9.9–12.3 kbar) and 15FP-06 (9.2–11.3 kbar) that are consistent with the phase equilibria modelling results.

Hornblende-plagioclase geothermometry was applied to estimate the retrograde temperature (Holland and Blundy, 1994). The temperatures for samples 15FP-02, 15FP-03 and 15FP-06 were estimated to be 750–765 °C, 780–795 °C and 800–810 °C, respectively (Table 6-8).

6.3.4 Zircon U-Pb geochronology

Zircons from the three mafic granulite samples (15FP-02, 15FP-03 and 15FP-06) were analyzed by LA-ICP-MS for U-Pb geochronology. Representative cathodoluminescence (CL) images of zircon grains and U-Pb age data plots are shown in Figs. 6-10, 6-11 and 6-12. The age data are given in Table 6-9.

Zircons from sample 15FP-02 are colorless and transparent to translucent. The anhedral to subhedral grains are oval to near-spherical in shape, with lengths of 50–200 µm and length to width ratios vary from 2:1 to 1:1. Under CL images, most zircons show clear core-rim texture with dark core and bright rim, whereas few

zircon grains are structureless with homogeneous gray color or show slightly patchy zoning (Fig. 6-10a). A total of 24 spots from 22 zircons were analyzed. The results from six darker core domains show Th contents from 26.5 to 170.5 ppm, U contents from 280.5 to 869.5 ppm and Th/U ratios vary from 0.17 to 0.36 (except Th/U=0.03 of spot 18). Five cores form a tight group on the concordia and yield weighted mean $^{207}\text{Pb}/^{206}\text{Pb}$ age of 2327 ± 37 Ma (MSWD = 2.0), and spot 12 defines an age at 2245 ± 19 Ma (Fig. 6-10b). The results of 18 analyses on rims, structureless or slightly patchy zoned domains display Th contents from 2.3 to 140.2 ppm, U contents from 184.3 to 1708 ppm and Th/U ratios vary from 0.01 to 0.11 (except Th/U=0.32 of spot 17). These analyses yield a weighted mean $^{207}\text{Pb}/^{206}\text{Pb}$ age of 1831 ± 10 Ma (MSWD = 1.2). The above features of CL image and Th/U ratio suggest magmatic origin for the dark cores and metamorphic origin for the bright rims and the structureless or slightly patchy-zoned zircons. The 2327 ± 37 Ma age is taken to represent the crystallization age of the protolith, and the 1831 ± 10 Ma age is interpreted to represent the zircon overgrowth during the Paleoproterozoic metamorphism.

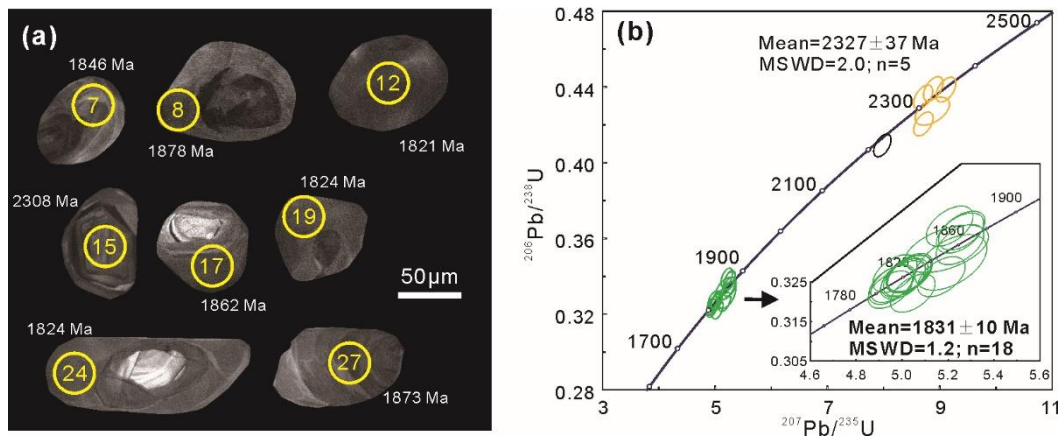


Fig. 6-10 Representative CL images (a) of zircons and concordia plots (b) of the mafic granulite sample 15FP-02.

Zircons from sample 15FP-03 are colorless to light brown, and transparent to translucent. The zircon grains show near-spherical or irregular morphology with a length of 60–200 μm and length to width ratios vary from 2:1 to 1:1. In the CL images, most zircons show clear core-rim texture with tiny dark cores and bright rims,

or are structureless with a homogeneous gray color or fir-tree features (Fig. 6-11a). A total of 30 spots from 29 zircons were analyzed. All analyses show Th contents range from 0.6 to 31.3 ppm, U contents range from 36.3 to 198.3 ppm and Th/U ratios vary from 0.01 to 0.14 (except Th/U=0.25 of spot 09, Th/U=0.32 of spot 17), suggesting metamorphic origin. Four spots with $^{207}\text{Pb}/^{206}\text{Pb}$ ages ranging from 1919 ± 22 Ma to 1937 ± 21 Ma form a coherent tight group and yield a weighted mean $^{207}\text{Pb}/^{206}\text{Pb}$ age of 1924 ± 21 Ma (MSWD = 0.18). Twenty-six spots with $^{207}\text{Pb}/^{206}\text{Pb}$ ages ranging from 1778 ± 24 Ma to 1885 ± 23 Ma cluster at another group (Fig. 6-11b), yielding weighted mean $^{207}\text{Pb}/^{206}\text{Pb}$ age of 1829 ± 8 Ma (MSWD = 0.97). The two ages of 1924 ± 21 Ma and 1829 ± 8 Ma are interpreted to represent two stages of zircon overgrowth during Paleoproterozoic metamorphism.

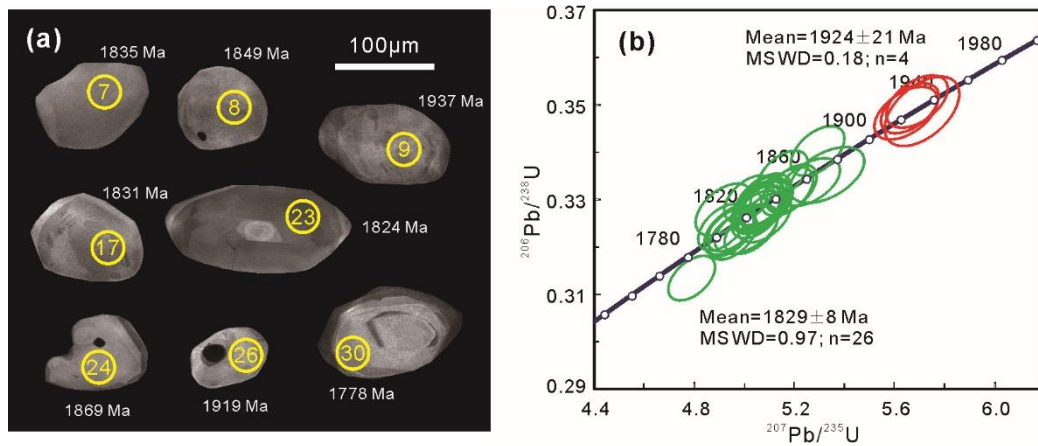


Fig. 6-11 Representative CL images (a) of zircons and concordia plots (b) of the mafic granulite sample 15FP-03.

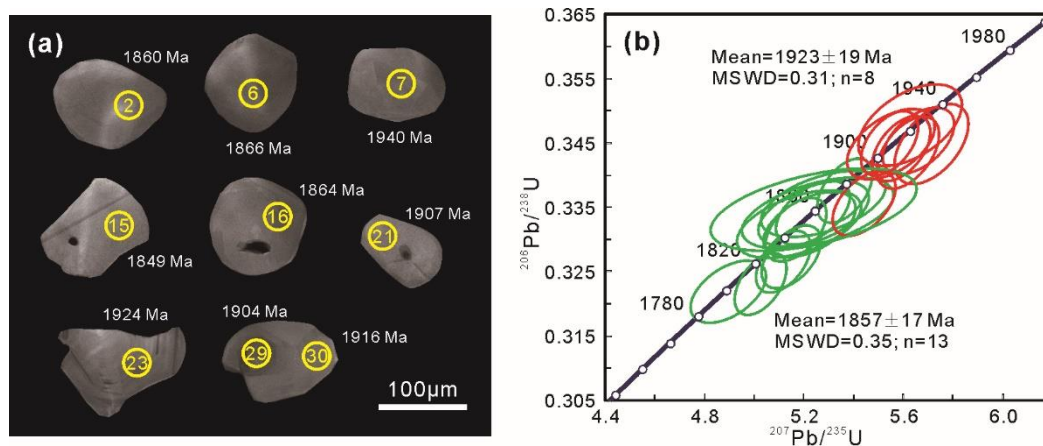


Fig. 6-12 Representative CL images (a) of zircons and concordia plots (b) of the mafic granulite sample 15FP-06.

Zircons from sample 15FP-06 are colorless to light brown, and transparent to translucent. The zircon grains show oval to near-spherical or irregular morphology with a length of 50-150 μm and aspect ratios vary from 2:1 to 1:1. In the CL images, zircon grains share similar features with sample 15FP-03, showing clear core-rim texture with tiny dark core and bright rim, or being structureless with a homogeneous gray color (Fig. 6-12a). A total of 21 spots from 20 zircons were analyzed. The results show Th contents vary from 0.1 to 8.8 ppm, U contents vary from 1.1 to 60.1 ppm and Th/U ratios range from 0.01 to 0.17 (except five grains with Th/U=0.23–0.92), suggesting metamorphic origin. Eight analyses with a $^{207}\text{Pb}/^{206}\text{Pb}$ age range from 1904 ± 22 Ma to 1959 ± 40 Ma yield a weighted mean $^{207}\text{Pb}/^{206}\text{Pb}$ age of 1923 ± 19 Ma (MSWD = 0.31). Thirteen spots display a $^{207}\text{Pb}/^{206}\text{Pb}$ age range from 1804 ± 35 Ma to 1884 ± 22 Ma (Fig. 6-12b), yielding a weighted mean $^{207}\text{Pb}/^{206}\text{Pb}$ age of 1857 ± 17 Ma (MSWD = 0.35). The 1923 ± 19 Ma and 1857 ± 17 Ma ages are interpreted to represent two stages of zircon overgrowth during the Paleoproterozoic metamorphism.

6.4 Discussion

6.4.1 Metamorphic evolution of the mafic granulites

The metamorphic evolution of the mafic granulites in the Fuping Complex is assessed by mineral assemblages, textures and phase equilibria modelling. Melt plays an important role during metamorphism, and the peak phases in the studied rocks are just above the solidus. It is thus inferred that dehydration melting took place by consumption of the hydrous minerals (amphibole and biotite) and quartz from the prograde stage to the peak stage. The presence of melt phase is implied by the following lines of evidence from the field and micro-textures: (i) the patches of quartz + feldspar aggregates in the hand specimen (Fig. 6-2b); (ii) thin rims of quartz moat distribute around porphyroblastic garnet (Fig. 6-3d); (iii) rims of quartz + K-feldspar + plagioclase moat occur around porphyroblastic garnet (Fig. 6-4d, 6-4e).

The P – T pseudosections for the peak and retrograde metamorphic stages are constructed at alternative water contents from P/T – $M(\text{H}_2\text{O})$ diagrams. The results of

phase equilibria modelling for sample 15FP-02 show peak pressure of 8.2–9.2 kbar and temperature of 870–882 °C, followed by the retrograde P – T conditions of <6.1 kbar and <795 °C. Samples 15FP-02 and 15FP-03 share same peak phase assemblage of garnet + clinopyroxene + amphibole + quartz + plagioclase + K-feldspar + ilmenite + melt. The peak and retrograde metamorphic P – T conditions for sample 15FP-03 are estimated at 9.6–11.3 kbar, 855–870 °C and 5.6–5.8 kbar, <795 °C, respectively. The peak assemblage of sample 15FP-06 define P – T conditions of 9.7–10.5 kbar, 880–900 °C, and the retrograde stages based on relatively higher H₂O contents from P/T – M (H₂O) diagrams define P – T conditions of <9 kbar, <865 °C, respectively.

The results of this study suggest a clock-wise P – T path involving decompression and cooling from the peak to retrograde stages. For sample 15FP-02, the P – T trajectory involves the crystallization of melt, appearance of biotite and formation of orthopyroxene coronas. Orthopyroxene is present in the lower pressure field and biotite appears in the lower temperature field in the pseudosection. For sample 15FP-03, orthopyroxene is absent, biotite and amphibole + plagioclase corona are present in the matrix. Thus the P – T trajectory is constrained by the orthopyroxene-in, plagioclase-out and biotite-in lines. Orthopyroxene and biotite display similar distribution with sample 15FP-02 and plagioclase is present in the lower pressure field. For sample 15FP-06, the appearance of orthopyroxene and crystallization of melt constrain the clock-wise P – T path (Fig. 6-9d). The clock-wise P – T trajectories are also constrained by the compositional zoning of garnet, the lower X_{Ca} values of the rims than those in the cores imply decompression after the peak. The wide and homogeneous garnet cores are inferred to have formed in the peak metamorphic stage, and the thin rims during the retrograde cooling with an increase in almandine and decrease in grossular. The zoning patterns of homogeneous garnet cores and thin rims with outward increase of X_{Alm} and X_{Sps} and decrease of X_{Grs} and X_{Pyx} are consistent with diffusional homogenization at high temperature followed by diffusion controlled retrograde reequilibration of the rims (Guilmette et al., 2011; Zhang et al., 2017b). The lower content of calcium (grossular) in the garnet rims

may be attributed to the formation of plagioclase corona around the porphyroblastic garnet. The increase of X_{Fe} and decrease of X_{Ca} in the garnet rims resulted from the Fe-Mg exchange between garnet and matrix minerals (Caddick et al., 2010; Zhang et al., 2015).

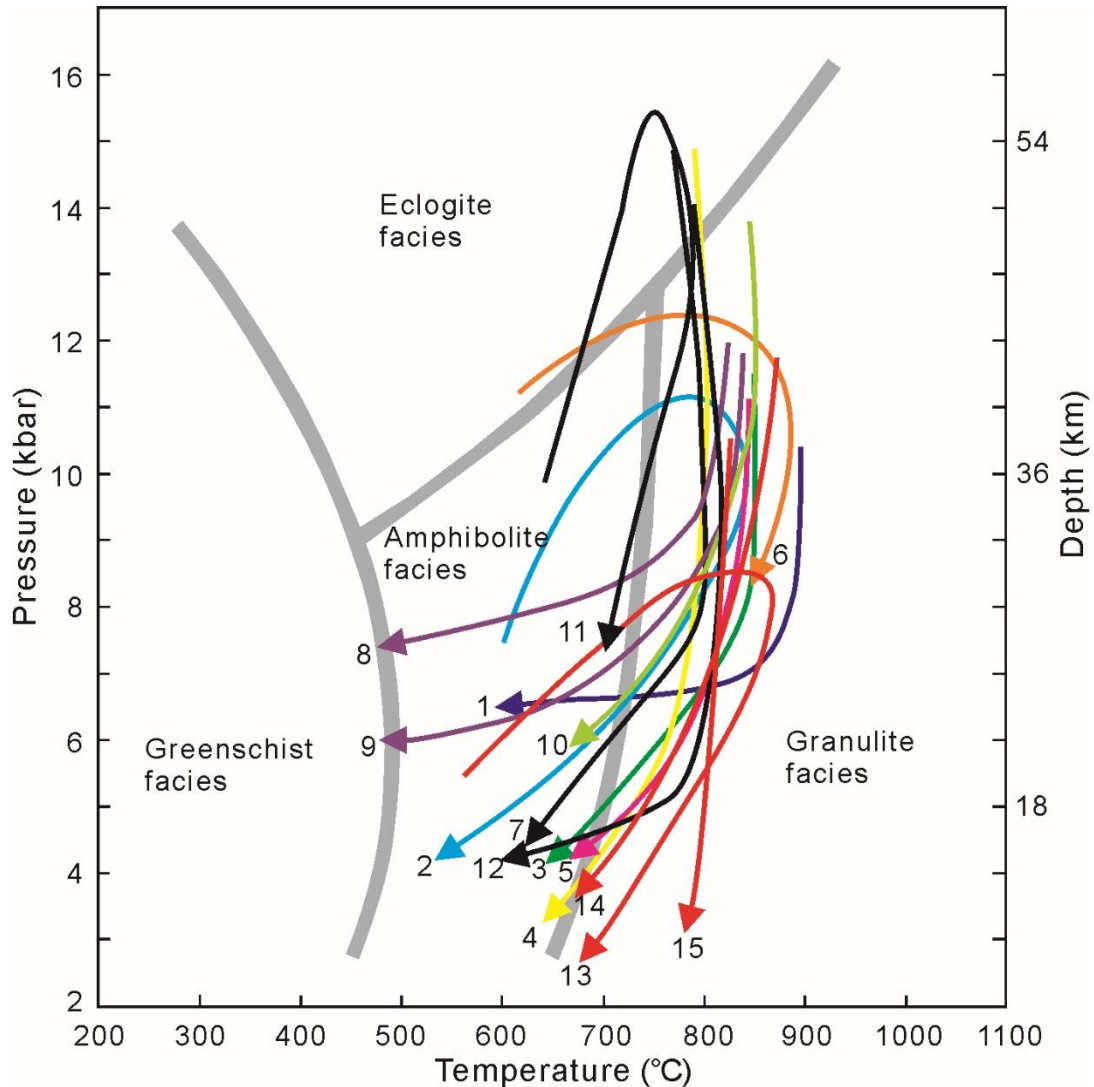


Fig. 6-13 Metamorphic P-T paths of high- and medium-pressure granulites from the TNCO. The P-T paths are shown: 1, Fuping Complex (Zhao et al., 2000a); 2, Fuping Complex (Liu, 1996); 3, Hengshan Complex (Zhao et al., 2000b); 4-5, Hengshan Complex (Zhao et al., 2001b); 6, Hengshan Complex (Guo et al., 1999); 7, Hengshan Complex (O'Brien et al., 2005); 8-9, Xuanhua-Huai'an (Guo et al., 2002); 10, Xuanhua-Huai'an (Zhai et al., 1992); 11, Xuanhua-Chicheng (Zhang et al., 2016b); 12, Chengde Complex (Zhang et al., 2006); 13, sample 15FP-02; 14, sample 15FP-03; 15, sample 15FP-06. P-T grid is after O'Brien and Rötzler (2003).

The inferred clock-wise P – T path in this study is comparable with those recorded by mafic and pelitic granulites in the Fuping, Hengshan, Xuanhua-Huai'an and Chengde Complexes as reported in previous studies (Fig. 6-13). These clock-wise P – T paths of the high-grade metamorphic rocks have been correlated to a collisional setting between the Western and Eastern Blocks along the TNCO (Zhao and Zhai, 2013, and references therein).

6.4.2 Age and tectonic setting of protolith

The mafic granulites are exposed as boudins within the TTG gneisses, suggesting that the protoliths are possibly mafic dykes (Zhang et al., 2006). The zircon cores in sample 15FP-02 display weighted mean $^{207}\text{Pb}/^{206}\text{Pb}$ age of 2327 ± 37 Ma and relatively high Th/U ratios, suggesting that the age marks the timing of intrusion of the mafic dykes. In the Fuping Complex, mafic dykes exposed along the Chengnanzhuang shear zone show emplacement age of ~ 2.31 Ga based on single-zircon Pb-evaporation analyses (Liu et al., 2002). Another pulse of mafic magmatism occurred at 2.1–2.0 Ga with subsequent metamorphism under amphibolite facies (Tang et al., 2015a).

The tectonic setting of the central segment of the TNCO at ~ 2.30 Ga, remains controversial. Zhai and Santosh (2011) proposed that the pull-apart stage in the NCC probably occurred at 2.3–2.0 Ga, including the formation of rifts, their extension and the generation of ancient remnant ocean basins. However, granitic rocks from Hengshan, Lüliang, Huai'an-Xuanhua Complexes record clear arc magmatism at 2.37–2.10 Ga related subduction process (Kröner et al., 2005a; Zhao et al., 2008b; Santosh et al., 2015). In recent studies, the Fuping Complex was suggested to have experienced compressional arc magmatism along the Wutai greenstone belt which marked the amalgamation of several microblocks during the late Neoproterozoic (Zhai and Santosh, 2011; Tang et al., 2016a). The rifting event should have occurred between 2.5–2.1 Ga before the Paleoproterozoic subduction event (2.1–2.0 Ga, Tang et al., 2015a), and thus the protolith (2327 Ma mafic dyke) of the mafic granulite in this study is regarded to have formed in a rifting setting. Liu et al. (2002) suggested

that the ~2.31 mafic dykes formed from underplating of basaltic magmas. Wei et al. (2014) proposed that back-arc extension and arc magmatism might have contributed to the formation of the mafic dykes and felsic magmatic rocks during 2.35–2.0 Ga.

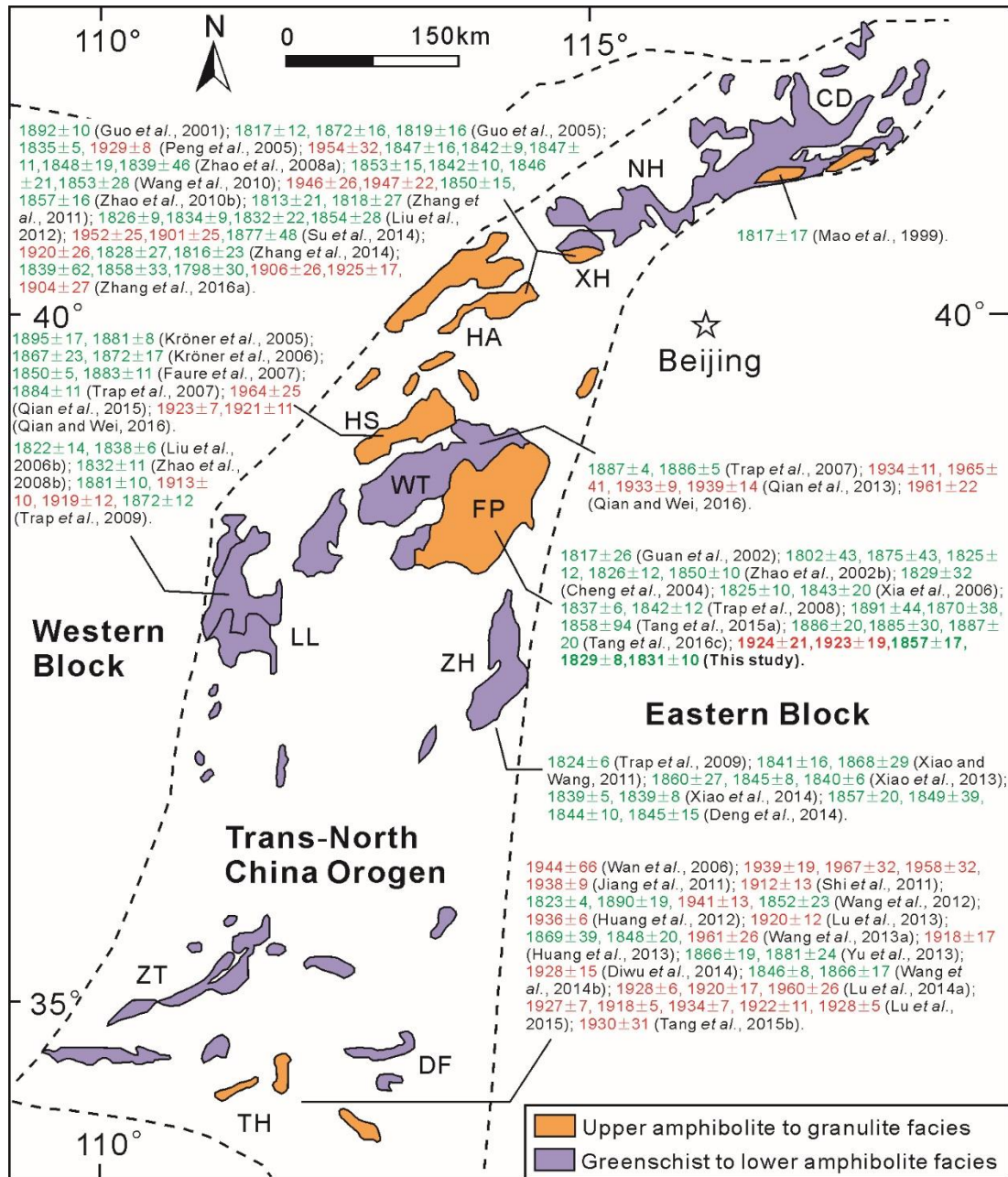


Fig. 6-14 Metamorphic ages of various rock types within the TNCO (after Zhao and Zhai, 2013).

Abbreviations: CD, Chengde; NH, Northern Hebei; XH, Xuanhua; HA, Huai'an; HS, Hengshan; WT, Wutai; FP, Fuping; LL, Lüliang; ZH, Zhanhuang; ZT, Zhongtiao; DF, Dengfeng; TH, Taihua.

6.4.3 Metamorphic ages and implications for the evolution of the TNCO

The long residence in the deep crustal level and presence of melt phase during metamorphism would promote the overgrowth or recrystallization of zircon grains (Hermann et al., 2001; Baldwin and Brown, 2008). Another favorable factor involves metamorphic temperature. Kelsey et al. (2008) proposed that zircon can commence growth from the peak P - T stage of metamorphism and thus record the peak of metamorphism for granulites heated to approximately <900 °C, and zircon might not record the timing of peak P - T conditions if UHT (>900 °C) conditions are reached. Thus, the following two processes are considered most probable for the recrystallization and formation of metamorphic zircon: (i) the peak metamorphic stage with temperature <900 °C and contribution of melt phase; (ii) the retrograde stage across the solidus, further cooling, and decompression process. The metamorphic zircons dated in this study show two groups of metamorphic ages at 1.90–1.96 Ga (peak at 1.92–1.93 Ga) and 1.80–1.89 Ga (peak at 1.83–1.86 Ga). Therefore, the metamorphic ages of 1.93–1.92 Ga would represent the peak granulite-facies stage, and the younger ages (1.83–1.86 Ga) are interpreted to represent the subsequent retrograde metamorphism. Similar multiple zircon growth and recrystallization with non-planar structureless, fir-tree zoned overgrowth and rounded resorption textures are common in high-grade metamorphic rocks (Vavra et al., 1996).

Several recent studies have reported geochronological data relating to the metamorphism of basement terranes in the TNCO (Figs. 6-14, 6-15). Metamorphic zircons from different rock types record age range from 1.96 Ga to 1.80 Ga. The available metamorphic ages from the TNCO show two age peaks at 1.92–1.94 Ga and 1.84–1.85 Ga (Fig. 6-13a). The older group of metamorphic ages (1.96–1.90 Ga) is widespread in most basement terranes in the TNCO (Fig. 6-12) and has been suggested to represent the major collisional event along the three major Paleoproterozoic belts in the NCC (Lu et al., 2015). In the middle segment of TNCO, metamorphic rock from the Fuping, Hengshan, Wutai and Lüliang Complexes also

record metamorphic ages in the range of 1913 ± 10 Ma to 1965 ± 41 Ma (Trap et al., 2009; Qian et al., 2013, 2015; Qian and Wei, 2016; this study). Qian et al. (2015) interpreted the ~ 1.95 Ga metamorphic age to represent the pre-peak/peak metamorphic stage. The Huai'an-Xuanhua Complex exposes typical high-pressure mafic granulites which have been widely recognized to have experienced high pressure granulite-facies metamorphism at 1.96–1.90 Ga (e.g. Su et al., 2014; Zhang et al., 2016a). In the northernmost Huai'an-Xuanhua Complex, the older set of metamorphic ages vary from 1901 ± 25 Ma to 1954 ± 32 Ma (Peng et al., 2005; Zhao et al., 2008a, 2010; Su et al., 2014; Zhang et al., 2014, 2016a).

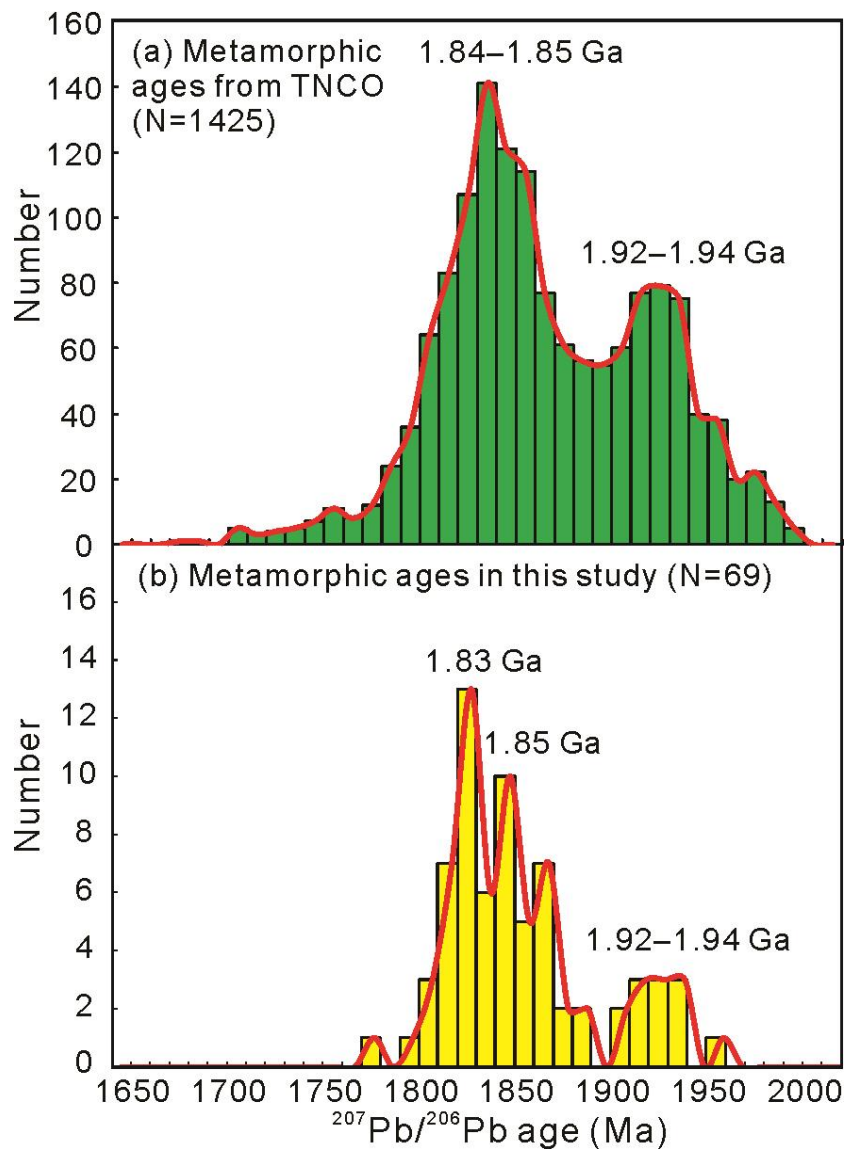


Fig. 6-15 Metamorphic zircon U-Pb age spectra and relative probability plots of various rock types within the TNCO. Data from references are shown in Fig. 6-14.

The widespread metamorphic ages in the various complexes within the TNCO with peaks at peaks at 1.92–1.94 Ga and at 1.84–1.85 Ga are in accordance with the notion that this orogen represents the Paleoproterozoic collisional belt between the Eastern and Western Blocks of the NCC. The metamorphic ages in this study are coeval with the age peaks from other complexes in the TNCO, suggesting that the 1.96–1.90 Ga ages represent the granulite-facies metamorphism and the 1.86–1.83 Ga ages corresponds to the retrograde metamorphism (Zhang et al., 2016a). Following a detailed evaluation of previous tectonic models, Zhang et al. (2016a) suggested a model which envisages subduction from both sides of the Ordos Block by the Yinshan Block and Eastern Block, a model which is similar to the double-side subduction model of Santosh (2010). A similar scenario of collisional assembly between the Longgang and Langrim Blocks along the Jiao-Liao-Ji belt at ~1.90 Ga has been traced from the Eastern Block, with the final cratonization of the NCC at ~1.90 Ga and the incorporation of the NCC into the Columbia supercontinent (Rogers and Santosh, 2002, 2009; Zhao et al., 2002a; Meert, 2012; Nance et al., 2014). The retrograde ages of 1.90–1.80 Ga are considered to be related to the cooling and exhumation of the rocks from the lower crust (Wei et al., 2014).

6.5 Conclusions

- (1) The peak metamorphic P – T conditions of the three mafic granulite samples investigated in this study are estimated at 8.2–9.2 kbar, 870–882 °C (15FP-02), 9.6–11.3 kbar, 855–870 °C (15FP-03) and 9.7–10.5 kbar, 880–900 °C (15FP-06), respectively. The pseudosections for the subsequent retrograde stages based on relatively higher H_2O contents from P/T – $M(H_2O)$ diagrams define the retrograde P – T conditions as <6.1 kbar, <795 °C (15FP-02), 5.6–5.8 kbar, <795 °C (15FP-03), and <9 kbar, <865 °C (15FP-06), respectively. The combined results define clock-wise P – T path involving cooling and decompression from the peak to retrograde stages.
- (2) The field occurrence and age results suggest that the mafic dyke protoliths of the mafic granulite were emplaced at ~2327 Ma, and that these possibly formed in a

rifting setting.

- (3) The metamorphic zircons in this study show two groups of ages at 1.90–1.96 Ga (peak at 1.92–1.93 Ga) and 1.80–1.89 Ga (peak at 1.83–1.86 Ga). The older ages are correlated with the peak granulite-facies metamorphism, and the younger group is interpreted to represent the subsequent retrograde metamorphism.
- (4) A compilation of the available metamorphic ages from various complexes in the TNCO shows two age peaks at 1.92–1.94 Ga and 1.84–1.85 Ga. The 1.96–1.90 Ga ages are correlated with the collisional assembly of the Yinshan, Ordos and Eastern Blocks. The final cratonization of the NCC took place at ~1.90 Ga broadly coeval with the incorporation of the NCC into the Columbia supercontinent.

Chapter 7: Discussion and Conclusions

Based on systematic and detailed studies on different rock types from the Fuping Complex as described in the above chapters, the tectonic settings and evolutionary processes of the central segment of the TNCO are summarized in this chapter.

7.1 Late Neoproterozoic microblock amalgamation of the NCC

Zhai and Santosh (2011) emphasized a microblock model for the cratonization of the NCC involving the subduction-collision of seven ancient microblocks through closure of the intervening oceans as represented by major granite greenstone belts (Fig. 1-2). The granite greenstone belts comprise volcano-sedimentary sequences and tonalite-trondhjemite-granodiorite suites with ages of 2.75–2.6 Ga and 2.6–2.5 Ga (Zhai and Santosh, 2011; Peng et al., 2015; Deng et al., 2016). The systematic petrological, mineral chemical, whole rock geochemical, zircon U-Pb-Hf-O isotopic studies from the Yangmuqiao mafic-ultramafic intrusion and the coeval TTG gneiss presented in Chapter 3 revealed that the Fuping Complex was formed by late Neoproterozoic eastward subduction and accretion between the Ordos and the Qianhuai microblocks along the Wutai greenstone belt which represents the suture of a paleo ocean.

Based on the summary of lithology, geochemistry, geochronology and mineralization from the representative granite greenstone belts (GGBs) (Table 7-1), it is reasonable to envisage that the Neoproterozoic cratonization of the NCC involved two-stages of tectonic process along the 2.6–2.75 Ga GGB and ~2.5 Ga GGBs, similar to those in Neoproterozoic-Phanerozoic orogenic belts such as the Central Asian Orogenic Belt (Windley et al., 2007; Xiao et al., 2010). i) The early Neoproterozoic plume–arc interaction process formed the various lithologies in the Yanlingguan GGB (Fig. 1-2; Polat et al., 2006; Wang et al., 2013b, 2015); ii) The late Neoproterozoic plate subduction, with or without the process of arc-plume interaction, resulted in the accretion of oceanic crust and arc magmatism along the GGBs (e.g. Zhai and Santosh, 2011; Wang et al., 2015; Tang et al., 2016a). The proposed

processes are supported by the following lines of evidence:

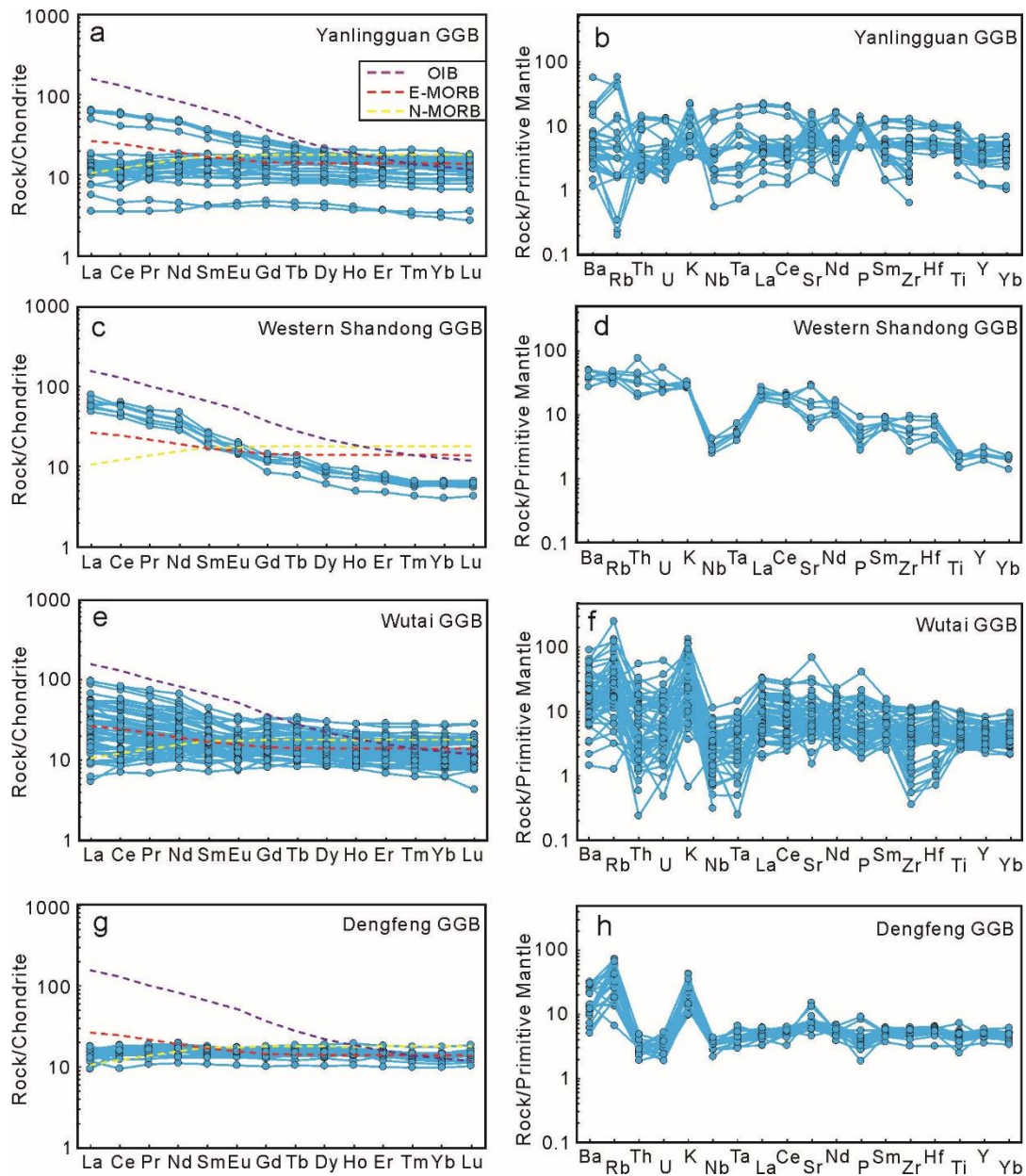


Fig. 7-1 Chondrite-normalized REE diagrams and primitive mantle-normalized trace element spider diagrams for meta-basalts from the Yanlingguan GGB (a-b, data source: Polat et al., 2006; Wang et al., 2013b), the Western Shandong GGB (c-d, data source: Peng et al., 2013a), the Wutai GGB (e-f, data source: Wang et al., 2004, 2014a; Polat et al., 2005) and the Dengfeng GGB (g-h, data source: Diwu et al., 2011; Deng et al., 2016).

(1) Geochemistry of various meta-basalts in all representative GGBs display close affinity with N-MORB, E-MORB, OIB and calc-alkaline basalt (Figs. 7-1, 7-2 and 7-3), implying the existence of oceanic basin between microblocks. Some meta-basalts and all granitoid rocks show arc signature with the enrichment of LREE

and LILE, and depletion of HFSE and HREE, suggesting that subduction tectonics played a major role for the formation of these rocks (Wang et al., 2004, 2013b, 2014a, 2015; Polat et al., 2005, 2006; Diwu et al., 2011; Guo et al., 2013, 2015b, 2016; Peng et al., 2013b, 2015; Liu et al., 2014c; Deng et al., 2016).

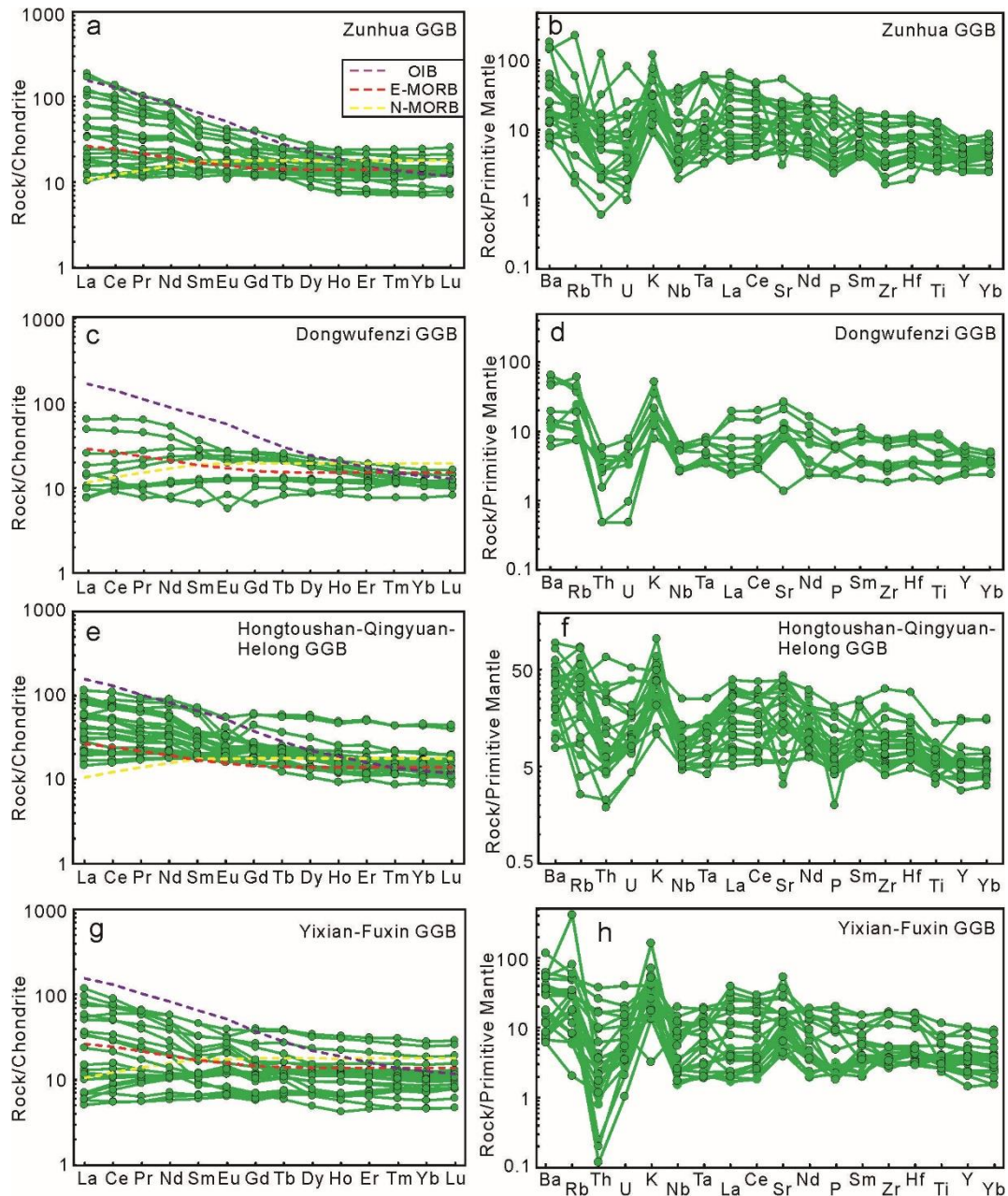


Fig. 7-2 Chondrite-normalized REE diagrams and primitive mantle-normalized trace element spider diagrams for meta-basalts from the Zunhua GGB (a-b, data source: Guo et al., 2013), the Dongwufenzi GGB (c-d, data source: Liu et al., 2014c), the Hongtoushan-Qingyuan-Helong GGB (e-f, data source: Guo et al., 2015b, 2016; Peng et al., 2015) and the Yixian-Fuxin GGB (g-h, data source: Wang et al., 2011, 2015).

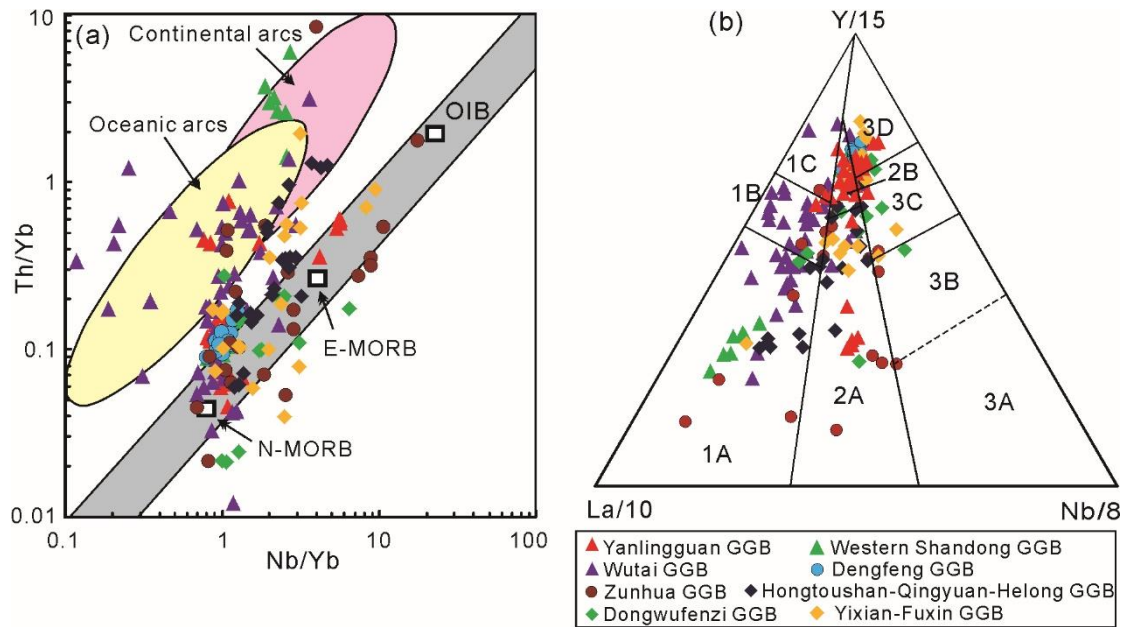


Fig. 7-3 (a) Nb/Yb vs. Th/Yb diagram (Pearce, 2008). (b) La/10-Y/15-Nb/8 triangular diagram, 1A: calc-alkali basalt; 1C: volcanic-arc tholeiite; 1B: overlapped field of 1A and 1C; 2A: continental basalt; 2B: back-arc basin basalt; 3A: alkalic basalt from intercontinental rift; 3B: enriched E-type MORB; 3C: weakly enriched E-type MORB; 3D: N-type MORB (Cabanis and Lecolle, 1989). Data sources are same with those in Figs. 7-1 and 7-2.

(2) The 2.75–2.60 Ga TTG rocks, komatiites, meta-basalts and meta-sedimentary rocks in the Yanlingguan GGB are correlated to the upwelling mantle plume with eruption close to the continental margin within an ocean basin (Wang et al., 2013b). The TTG rocks underwent the 2.63–2.59 Ga metamorphism (Fig. 7-4) which may record the subduction within the oceanic slab or collision (Ren et al., 2016).

(3) The volcano-sedimentary rocks and granitoid rocks in the late Neoproterozoic GGBs display formation age at 2.60–2.48 Ga, and metamorphic age at 2.52–2.47 Ga (Table 7-1 and references therein; Fig. 7-4), corresponding to a typical subduction-collision system. The 2.52–2.47 Ga metamorphism with anticlockwise P–T paths involving isobaric cooling can also occur at the root of magmatic arcs or under back-arc basin setting (Zhao and Zhai, 2013 and references therein).

(4) Several late Neoproterozoic ophiolites were reported along the representative GGBs in the North China Craton, such as the Zunhua ophiolitic mélange within the Zunhua GGB (Kusky and Zhai, 2012), the Wutai, Northern Taihang and Southern Taihang ophiolites within the Wutai GGB (Polat et al., 2005; Kusky and Zhai, 2012),

the Yishui ophiolite in the Western Shandong GGB (Santosh et al., 2016), and the Western Liaoning ophiolite within the Yixian-Fuxin GGB (Kusky and Zhai, 2012). These reports confirm oceanic plate subduction.

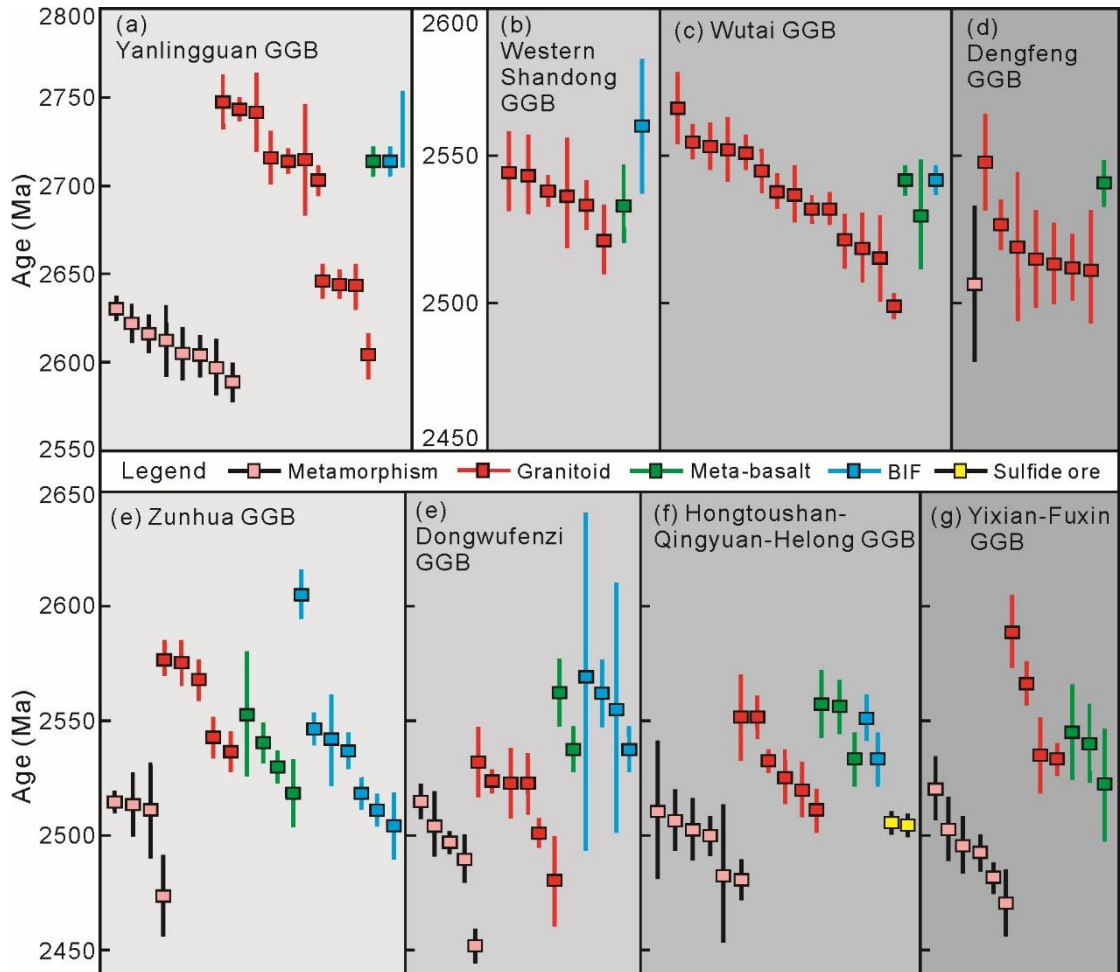


Fig. 7-4 Age distribution of granitoid rocks, meta-basalts, BIFs and sulfide ores from representative GGB of the NCC. Data sources are shown in Table 7-1.

(5) Some of the late granite and pegmatite veins are un-metamorphosed and formed in post-collisional magmatism. Deng et al. (2016) proposed that the granite dyke from the Dengfeng GGB was intruded at 2486 ± 20 Ma. Jian et al. (2012) reported a crystallization age of 2508 ± 17 Ma for a pegmatite from the Dongwufenzi GGB.

(6) Most late Neoproterozoic BIFs in the NCC were proposed to have deposited in back-arc basin or arc-related oceanic slab (Wang et al., 2014a; Zhang et al., 2016c). The late Neoproterozoic komatiite (Dongwufenzi GGB), sanukitoid (Dongwufenzi GGB and Western Shandong GGB), BIF (Zunhua GGB) and VMS deposits

(Hongtoushan-Qingyuan-Helong GGB) were considered to be related to the oceanic slab with the involvement of mantle plume (Zhu et al., 2015).

7.2 Paleoproterozoic rift and subduction processes along the TNCO

Zhai and Santosh (2011) proposed that the pull-apart stage in the NCC probably occurred at 2.3–2.0 Ga, including the formation of rifts, their extension and the generation of ancient remnant ocean basins. The mafic granulites display weighted mean $^{207}\text{Pb}/^{206}\text{Pb}$ age of 2327 ± 37 Ma, marking the timing of intrusion of the mafic dykes. In the Fuping Complex, mafic dykes exposed along the Chengnanzhuang shear zone show emplacement age of ~ 2.31 Ga based on single-zircon Pb-evaporation analyses (Liu et al., 2002). Liu et al. (2002) suggested that the ~ 2.31 mafic dykes formed from underplating of basaltic magmas. Wei et al. (2014) proposed that back-arc extension and arc magmatism might have contributed to the formation of the mafic dykes and felsic magmatic rocks during 2.35–2.0 Ga. Thus the protoliths of the mafic granulites were possibly formed in an extensional setting, representing a rift event of the central domain of the NCC at ca. 2.3 Ga.

Zircons in the granitic, metabasaltic, and metasedimentary samples from the Fuping Complex record an important magmatic event at 2.09–2.03 Ga (Fig. 4-13a). The protolith magmas of the granitoids and metabasalts formed in an arc or subduction related tectonic setting based on geochemical evidences (Figs. 4-9, 4-11). The 2.12–2.02 Ga arc magmatism is commonly present in the Fuping, Wutai and Lüliang Complexes (Guan et al., 2002; Zhao et al., 2002a; Wilde et al., 2005; Liu et al., 2009; Santosh et al., 2016). However, 2.09–2.00 Ga continent rift related magmatism is also present in the Hengshan, Huai'an and Zanhuang Complexes (Yang et al., 2011; Zhao et al., 2011; Zhang et al., 2011; Peng et al., 2012b; Xie et al., 2012). Thus it is reasonable to propose the double subduction and associated rifting model for the 2.1–2.0 Ga evolution of the TNCO: i) The Wutai Complex and the Fuping Complex were separated by the Longquanguan ocean, and the double subduction of the oceanic lithosphere resulted in arc magmatism; (ii) Simultaneously, continental

rifting developed in the Hengshan, Huai'an and Zanhuan Complexes. Detrital zircon U-Pb geochronological study propose that the meta-sedimentary rocks (Wanzi Group) in the Fuping Complex were deposited during 1.95-1.93 Ga, and the Gantaohe Group and the Central Zanhuan Domain in the adjacent Zanhuan Complex were deposited at 2.09-1.85 Ga and 2.03-1.90 Ga, respectively. However, the discrepancy of $\delta^{13}\text{C}$ values between the meta-carbonate samples from the Fuping and Zanhuan Complexes imply that the adjacent two Complexes may not have experience a unified depositional environment in the late Paleoproterozoic. As in the double subduction and rifting model above, the Fuping Complex recorded subduction-related arc magmatism and the Zanhuan Complex witnessed continental rifting process. Thus, it is reasonable to suggest that the Wanzi Group in the Fuping Complex was deposited in a forearc basin during the later period of the continuous subduction, and the protoliths of the meta-sedimentary rocks in the Zanhuan Complex were deposited in a back-arc basin which formed after the 2.0-2.1 Ga continental rifting.

7.3 Paleoproterozoic final collision along the TNCO

The North China Craton (NCC) witnessed the collisional assembly of major continental blocks at 2.1–1.8 Ga, broadly coeval with the incorporation of the craton within the global supercontinent Columbia (Rogers and Santosh, 2002, 2009; Wilde et al., 2002; Zhao et al., 2002b; Meert, 2012; Nance et al., 2014). The peak metamorphic ages within the TNCO from available data are in controversial with two groups at 1.95–1.90 Ga (e.g. Qian et al., 2015; Qian and Wei, 2016; Zhang et al., 2016a) and 1.88–1.80 Ga (e.g. Zhao et al., 2002b, 2008a; Guo et al., 2005; Liu et al., 2012b). The metamorphic zircons from mafic granulites in Chapter 7 show two groups of metamorphic ages at 1.90–1.96 Ga and 1.80–1.89 Ga. The various rock types including gneissic granite, amphibolites and schist in Chapter 4 show identical metamorphic ages varying from 1.89 to 1.83 Ga. Moreover, several metamorphic zircon rims from meta-carbonate samples in Chapter 5 display $^{207}\text{Pb}/^{206}\text{Pb}$ ages varying from 1857 ± 20 Ma to 1898 ± 20 Ma. Thus the metamorphic ages of 1.93–1.92 Ga would represent the peak granulite-facies metamorphism and the younger

ages (1.83–1.86 Ga) are interpreted to represent the subsequent retrograde (low -grade) metamorphism. The various complexes include Huai'an, Xuanhua, Hengshan, Wutai, Fuping, Lüliang and Taihua within the TNCO have recorded the 1.96–1.90 Ga metamorphic ages, implying the collision between the Eastern and Western Blocks of the NCC would have occurred in this period (Peng et al., 2005; Zhao et al., 2008a, 2010; Qian et al., 2013, 2015; Su et al., 2014; Zhang et al., 2014, 2016a; Lu et al., 2015; Qian and Wei, 2016).

A similar scenario of collisional assembly along the Khondalite belt (Inner Mongolia Suture Zone) and the Jiao-Liao-Ji belt have also occurred during 1.95-1.90 Ga (e.g. Li et al., 2004, 2006; Luo et al., 2004; Zhao et al., 2005; Lu et al., 2006; Li and Zhao, 2007; Santosh et al., 2007a, 2007b, 2008, 2012). The Khondalite belt represented by high-pressure (HP) pelitic granulites and ultra-high temperature (UHT) Mg-Al granulites was formed during the continent-continent collision between the Yinshan and Ordos Block at ca. 1.95-1.92 Ga (e.g. Zhao et al., 2005; Santosh et al., 2007a, 2007b, 2008, 2012). The collisional event between the Longgang and Langrim Blocks along the Jiao-Liao-Ji belt has occurred at ~1.90 Ga (Li et al., 2004, 2006; Luo et al., 2004; Lu et al., 2006; Li and Zhao, 2007). Meanwhile, the collisional assembly of the major crustal blocks in the North China Craton might have occurred during 1.93 to 1.90 Ga, marking the final cratonization of the NCC and the incorporation of the NCC into the Columbia supercontinent (Rogers and Santosh, 2002, 2009; Zhao et al., 2002a; Meert, 2012, Nance et al., 2014).

Acknowledgements

First of all, I would like to sincerely thank my supervisors Professor Toshiaki Tsunogae and Professor M. Santosh, for their guidance, encouragement, immense supervision and financial support on this PhD research project. I gratefully thank Professor Toshiaki Tsunogae for sharing his knowledge, guidance in learning metamorphic petrology and THERMOCALC technique, and care during my study in the University of Tsukuba. I also appreciate Professor M. Santosh for his kindly advice in science and my life, buildup and support for my research career, and great efforts to improve my written English. Their dedication in science and conscientious attitude are models for my further research career.

I would like to express my gratefulness to professor Shou-ting Zhang for his supervision during my Master Course. Professor Shou-ting Zhang's guidance in studying mineral deposit and metallogeny are academic enlightenments for my research.

I would also express thanks to Professor Yunpeng Dong from the Northwest University for his help in the fieldwork and zircon analyses. Thanks are given to Dr. Teruyuki Maruoka for his help in carbon and oxygen isotopic analyses. I am grateful to my group members in the University of Tsukuba and China University of Geosciences Beijing for their help in the field and laboratory analyses, and friends in office room 113 for their useful discussion during the research.

Several parties are thanked for their support during my PhD study career, including University of Tsukuba, the China University of Geosciences, State Key Laboratory of Continental Dynamics of Northwest University, Tianjin Institute of Geology and Mineral Resource and Chinese Academy of Geological Sciences.

This study was financially supported through the Grant-in-Aid for Scientific Research (B) from Japan Society for the Promotion of Science (JSPS) to Toshiaki Tsunogae (No. 26302009), Talent Award to M. Santosh under the 1000 Talents Plan of the Chinese Government, the Foreign Expert grant from China University of Geosciences Beijing to M. Santosh, and the award of the China Scholarship Council

(No. 201506400008) to Li Tang for one year's study at the University of Tsukuba, Japan.

At last, I am very much grateful to my parents and every family members for their fully support and encourage in my life. Without them, I would not have got the power to continue my research.

References

- Anbar, A.D., Duan, Y., Lyons, T.W., Arnold, G.L., Kendall, B., Creaser, R.A., Kaufman, A.J., Gordon, G.W., Scott, C., Garvin, J., Buick, R., 2007. A whiff of oxygen before the Great Oxidation Event? *Science* 317, 1903–1906.
- Anderson, J.R., Payne, J.L., Kelsey, D.E., Hand, M., Collins, A.S., Santosh, M., 2012. High-pressure granulites at the dawn of the Proterozoic. *Geology* 40, 431-434.
- Aranovich, L.Y., Berman, R.G., 1997. A new garnet-orthopyroxene thermometer based on reversed Al_2O_3 solubility in $\text{FeO-Al}_2\text{O}_3\text{-SiO}_2$ orthopyroxene. *American Mineralogist* 82, 345-353.
- Baldwin, A., Brown, M., 2008. Age and duration of ultrahigh-temperature metamorphism in the Anápolis-Itaúçu Complex, Southern Brasília Belt, central Brazil-constraints from U-Pb geochronology, mineral rare earth element chemistry and trace-element thermometry. *Journal of Metamorphic Geology* 26, 213–233.
- Barnes, S.J., Naldrett, A.J., Gorton, M.P., 1985. The origin of the fractionation of platinum-group elements in terrestrial magmas. *Chemical Geology* 53, 303-323.
- Barnes, S.J., Maier, W.D., 1999. The fractionation of Ni, Cu, and the noble metals in silicate and sulphide liquids. *Geological Association of Canada Short Course Notes* 13, 69–106.
- Barnes, S.J., Roeder, P.L., 2001. The range of spinel compositions in terrestrial mafic and ultramafic rocks. *Journal of Petrology* 12, 2279–2302.
- Barth, M.G., McDonough, W.F., Rudnick, R.L., 2000. Tracking the budget of Nb and Ta in the continental crust. *Chemical Geology* 165, 197-213.
- Bau, M., Romer, R., Lüders, V., Beukes, N.J., 1999. Pb, O, and C isotopes in silicified Mooidraai dolomite (Transvaal Supergroup, South Africa): implications for the composition of Paleoproterozoic seawater and “dating” the increase of oxygen in the Precambrian atmosphere. *Earth and Planetary Science Letters* 174, 43–57.
- Bekker, A., Karhu, J.A., Kaufman, A.J., 2006. Carbon isotope record for the onset of the Lomagundi carbon isotope excursion in the Great Lakes area, North America. *Precambrian Research* 148, 145-180.
- Berly, T.J., Hermann, J., Arculus, R.J., Lapierre, H., 2006. Supra-subduction zone pyroxenites

- from San Jorge and Santa Isabel (Solomon Island). *Journal of Petrology* 47, 1531–1555.
- Black, L.P., Kamo, S.L., Allen, C.M., Davis, D.W., Aleinikoff, J.N., Valley, J.W., Mundil, R., Campbell, I.H., Korsch, R.J., Williams, I.S., 2004. Improved $^{206}\text{Pb}/^{238}\text{U}$ microprobe geochronology by the monitoring of a trace-element related matrix effect; SHRIMP, ID-TIMS, ELA-ICP-MS and oxygen isotope documentation for a series of zircon standards. *Chemical Geology* 205, 115–140.
- Blichert-Toft, J., Albarède, F., 1997. The Lu–Hf geochemistry of chondrites and the evolution of the mantle–crust system. *Earth and Planetary Science Letters* 148, 243–258.
- Brown, M., 1993. P–T–t evolution of orogenic belts and the causes of regional metamorphism. *Journal of the Geological Society, London*, 150, 227–241.
- Brown, M., 2007. Metamorphic conditions in orogenic belts: a record of secular change. *International Geology Review*, 49, 193–234.
- Brown, M., 2014. The contribution of metamorphic petrology to understanding lithosphere evolution and geodynamics. *Geoscience Frontiers*, 5, 553–569.
- Cabanis, B., Lecolle, M., 1989. Le diagramme La/10-Y/15-Nb/8: un outil pour la discrimination des séries volcaniques et la mise en évidence des processus de mélange et/ou de contamination crustale. *Comptes Rendus de L' Academie Des Sciences Series II* 309, 2023–2029.
- Caddick, M.J., Konopásek, J., Thompson, A.B., 2010. Preservation of garnet growth zoning and the duration of prograde metamorphism. *Journal of Petrology* 51, 2327–2347.
- Chen, Y.J., Liu, C.Q., Chen, H.Y., Zhang, Z.J., Li, C., 2000. Carbon isotope geochemistry of graphite deposits and ore-bearing khondalite series in North China: implications for several geoscientific problems. *Acta Petrologica Sinica* 2, 233–244. (in Chinese with English abstract).
- Cheng, Y.Q., Yang, C.H., Wan, Y.S., Liu, Z.X., Zhang, X.P., Du, L.L., Zhang, S.G., Wu, J.S., Gao, J.F., 2004. Precambrian Geology and Anatexis and Its Reworking in the Crustal Rocks at the Central-Northern Segments of the Taihangshan Mountain. Geological Publishing House, Beijing, p. 1–191 (in Chinese).
- Chopin, F., Schulmann, K., Štípská, P., Martelat, J. E., Pitra, P., Lexa, O., Petri, B., 2012. Microstructural and metamorphic evolution of a high-pressure granitic orthogneiss during

- continental subduction (Orlica–Śnieżnik dome, Bohemian Massif). *Journal of Metamorphic Geology* 30, 347-376.
- Chu, N.C., Taylor, R.N., Chavagnac, V., Nesbitt, R.W., Boela, R.M., Milton, J.A., Germain, C.R., Bayon, G., Burton, K., 2002. Hf isotope ratio analysis using multi-collector inductively coupled plasma mass spectrometry: an evaluation of isobaric interference corrections. *Journal of Analytical Atomic Spectrometry* 17, 1567–1574.
- Condie, K.C., 1993. *Plate Tectonics, Crustal Evolution*, 3rd ed. Pergamon Press, Oxford.
- Condie, K.C., 2000. Episodic continental growth models: afterthoughts and extensions. *Tectonophysics* 322, 153–162.
- Coplen, T.B., Hoppo, J.A., Böhlke, J.K., Peiser, H. S., Rieder, S.E., Krouse, H. R., Rosman, K., Ding, T., Vocke, R., Révész, K., Lamberty, A., Taylor, P., De Bièvre, P., 2002. *Compilation of Minimum and Maximum Isotope Ratios of Selected Elements in Naturally Occurring Terrestrial Materials and Reagents*. U.S. Dept. of the Interior, U.S. Geological Survey.
- Coplen, T.B., Brand, W.A., Gehre, M., Gröning, M., Meijer, H.A., Toman, B., Verkouteren, R.M., 2006. New guidelines for $\delta^{13}\text{C}$ measurements. *Analytical Chemistry* 78, 2439-2441.
- Dahl, P.S., 1980. The thermal-compositional dependence of Fe^{2+} -Mg distributions between coexisting garnet and pyroxene: applications to geothermometry. *American Mineralogist* 65, 852-866.
- Dai, Y.P., Zhang, L.C., Wang, C., Liu, L., Cui, M., Zhu, M., Xiang, P., 2012. Genetic type, formation age and tectonic setting of the Waitoushan banded iron formation, Benxi, Liaoning Province. *Acta Petrologica Sinica* 28, 3574–3594. (in Chinese with English abstract).
- Dai, Y.P., Zhang, L.C., Zhu, M., Wang, C., Liu, L., 2013. Chentaigou BIF-type iron deposit, Anshan area associated with Archean crustal growth: Constraints from zircon U-Pb dating and Hf isotope. *Acta Petrologica Sinica* 29, 2537–2550. (in Chinese with English abstract).
- Day, J.M., Pearson, D.G., Hulbert, L.J., 2008. Rhenium–osmium isotope and platinum-group element constraints on the origin and evolution of the 1.27 Ga Muskox layered intrusion. *Journal of Petrology* 49, 1255-1295.
- DeBari, S.M., Coleman, R.G., 1989. Examination of the deep levels of an island-arc: evidence from the Tunisia ultramafic–mafic assemblage, Tonis, Alaska. *Journal of Geophysical Research* 94, 4373–4391.

- Deng, H., Kusky, T., Polat, A., Wang, J.P., Wang, L., Fu, J.M., Wang, Z.S., Yuan, Y., 2014. Geochronology, mantle source composition and geodynamic constraints on the origin of Neoproterozoic mafic dikes in the Zanhuang Complex, Central Orogenic Belt, North China Craton. *Lithos* 205, 359-378.
- Deng, H., Kusky, T., Polat, A., Wang, C., Wang, L., Li, Y., Wang, J., 2016. A 2.5 Ga fore-arc subduction-accretion complex in the Dengfeng Granite-Greenstone Belt, Southern North China Craton. *Precambrian Research* 275, 241-264.
- Dhuime, B., Bosch, D., Bodinier, J.L., Garrido, C.J., Bruguier, O., Hussain, S.S., Dawood, H., 2007. Multistage evolution of the Jijal ultramafic–mafic complex (Kohistan, N Pakistan): implications for building the roots of island arcs. *Earth and Planetary Science Letters* 261, 179–200.
- Diwu, C.R., Sun, Y., Guo, A., Wang, H., Liu, X., 2011. Crustal growth in the North China Craton at ~ 2.5 Ga: Evidence from in situ zircon U–Pb ages, Hf isotopes and whole-rock geochemistry of the Dengfeng complex. *Gondwana Research* 20, 149-170.
- Diwu, C.R., Sun, Y., Zhao, Y., Lai, S.C., 2014. Early Paleoproterozoic (2.45–2.20 Ga) magmatic activity during the period of global magmatic shutdown: Implications for the crustal evolution of the southern North China Craton. *Precambrian Research* 255, 627-640.
- Du, L.L., Yang, C.H., Wyman, D.A., Nutman, A.P., Lu, Z.L., Song, H.X., Xie, H.Q., Wan, Y.S., Zhao, L., Geng, Y.S., Ren, L.D., 2016. 2090–2070 Ma A-type granitoids in Zanhuang Complex: Further evidence on a Paleoproterozoic rift-related tectonic regime in the Trans-North China Orogen. *Lithos* 254-255, 18-35.
- Eckert, J.O., Newton, R.C., Kleppa, O.J., 1991. The H of reaction and recalibration of garnet-pyroxene-plagioclase-quartz geobarometers in the CMAS system by solution calorimetry. *American Mineralogist* 76, 148-160.
- Ellis, D.J., Green, D.H., 1979. An experimental study of the effect of Ca upon garnet-clinopyroxene Fe-Mg exchange equilibria. *Contributions to Mineralogy and Petrology* 71, 13-22.
- England, P.C., Thompson, A., 1984. Pressure-temperature-time paths of regional metamorphism I. Heat transfer during the evolution of regions of thickened continental crust. *Journal of Petrology* 25, 894-928.

- Eyuboglu, Y., Santosh, M., Bektas, O., Chung, S.L., 2011. Late Triassic subduction-related ultramafic–mafic magmatism in the Amasya region (eastern Pontides, N. Turkey): Implications for the ophiolite conundrum in Eastern Mediterranean. *Journal of Asian Earth Sciences* 42, 234–257.
- Faure, M., Trap, P., Lin, W., Monié P., Bruguier, O., 2007. Polyorogenic evolution of the Paleoproterozoic Trans-North China Belt, new insights from the Lüliangshan–Hengshan–Wutaishan and Fuping massifs. *Episodes* 30, 1–12.
- Frost, B.R., Barnes, C.G., Collins, W.J., Arculus, R.J., Ellis, D.J., Frost, C.D., 2001. A geochemical classification for granitic rocks. *Journal of Petrology* 42, 2033–2048.
- Garuti, G., Fershtater, G., Bea, F., Montero, P., Pushkarev, E.V., Zaccarini, F., 1997. Platinum-group elements as petrological indicators in mafic-ultramafic complexes of the central and southern Urals: preliminary results. *Tectonophysics* 276, 181–194.
- Gehre, M., Strauch, G., 2003. High-temperature elemental analysis and pyrolysis techniques for stable isotope analysis. *Rapid communications in mass spectrometry* 17, 1497–1503.
- Geng, Y.S., Wan, Y.S., Shen, Q.H., Li, H.M., Zhang, R.X., 2000. Chronological framework of the early Precambrian important events in the Lüliang area, Shanxi province. *Acta Geologica Sinica* 74, 216–223. (in Chinese with English abstract).
- Geng, Y.S., Liu, F.L., Yang, C.H., 2006. Magmatic event at the end of the Archean in eastern Hebei province and its geological implication. *Acta geologica Sinica (English Edition)* 80, 819–833.
- Geng, Y.S., Du, L.L., Ren, L.D., 2012. Growth and reworking of the early Precambrian continental crust in the North China Craton: constraints from zircon Hf isotopes. *Gondwana Research* 21, 517–529.
- Green, E.C.R., White, R.W., Diener, J.F.A., Powell, R., Holland, T.J.B., Palin, R.M., 2016. Activity–composition relations for the calculation of partial melting equilibria in metabasic rocks. *Journal of Metamorphic Geology* 34, 845–869.
- Griffin, W.L., Pearson, N.J., Belousova, E., Jackson, S.E., van Achterbergh, E., O'Reilly, S.Y., Shee, S.R., 2000. The Hf isotope composition of cratonic mantle: LA-MC-ICPMS analysis of zircon megacrysts in kimberlites. *Geochimica et Cosmochimica Acta* 64, 133–147.

- Griffin, W.L., Wang, X., Jackson, S.E., Pearson, N.J., O'Reilly, S.Y., Xu, X., Zhou, X., 2002. Zircon chemistry and magma mixing, SE China: in-situ analysis of Hf isotopes. Tonglu and Pingtan igneous complexes. *Lithos* 61, 237–269.
- Guan, H., Sun, M., Wilde, S.A., Zhou, X.H., Zhai, M.G., 2002. SHRIMP U–Pb zircon geochronology of the Fuping Complex: implications for formation and assembly of the North China Craton. *Precambrian Research* 113, 1–18.
- Guan, P., Wang, Y., 2009. A review on the global Palaeoproterozoic positive $\delta^{13}\text{C}$ excursion: Data analysis and matter comment. *Acta Scientiarum Naturalium Universitatis Pekinensis* 45, 906-914. (in Chinese with English abstract).
- Guilmette, C., Indares, A., Hébert, R., 2011. High-pressure anatexitic paragneisses from the Namche Barwa, Eastern Himalayan Syntaxis: Textural evidence for partial melting, phase equilibria modelling and tectonic implications. *Lithos* 124, 66-81.
- Guo, J.H., Zhai, M.G., Li, Y.G., Li, J.H., 1999. Metamorphism, PT paths and tectonic significance of garnet amphibolite and granulite from Hengshan, North China Craton. *Chinese Journal of Geology* 34, 311-325. (in Chinese with English abstract).
- Guo, J.H., Zhai, M.G., Xu, R., 2001. Timing of the granulite facies metamorphism in the Sanggan area, North China craton: zircon U-Pb geochronology. *Science in China Series D: Earth Sciences*, 44, 1010-1018.
- Guo, J.H., O'Brien, P.J., Zhai, M.G., 2002. High-pressure granulites in the Sanggan area, North China Craton: metamorphic evolution, P–T paths and geotectonic significance. *Journal of Metamorphic Geology* 20, 741–756.
- Guo, J.H., Sun, M., Zhai, M.G., 2005. Sm–Nd and SHRIMP U–Pb zircon geochronology of high-pressure granulites in the Sanggan area, North China Craton: timing of Paleoproterozoic continental collision. *Journal of Asian Earth Sciences* 24, 629–642.
- Guo, R., Liu, S., Santosh, M., Li, Q., Bai, X., Wang, W., 2013. Geochemistry, zircon U–Pb geochronology and Lu–Hf isotopes of metavolcanics from eastern Hebei reveal Neoproterozoic subduction tectonics in the North China Craton. *Gondwana Research* 24, 664-686.
- Guo, J.H., Zhai, M.G., Peng, P., Jiao, S., Zhao, L., Wang, H., 2015a. Paleoproterozoic granulites in the North China Craton and their geological implications. In *Precambrian Geology of China* (pp. 137-169). Springer Berlin Heidelberg.

- Guo, B., Liu, S., Zhang, J., Yan, M., 2015b. Zircon U–Pb–Hf isotope systematics and geochemistry of Helong granite-greenstone belt in Southern Jilin Province, China: Implications for Neoproterozoic crustal evolution of the northeastern margin of North China Craton. *Precambrian Research* 271, 254-277.
- Guo, B., Liu, S., Zhang, J., Wang, W., Fu, J., Wang, M., 2016. Neoproterozoic Andean-type active continental margin in the northeastern North China Craton: Geochemical and geochronological evidence from metavolcanic rocks in the Jiapigou granite-greenstone belt, Southern Jilin Province. *Precambrian Research* 285, 147-169.
- Han, B.F., Xu, Z., Ren, D., Li, L.L., Yang, J.H., Yang, Y.H., 2012. Crustal growth and intracrustal recycling in the middle segment of the Trans-North China Orogen, North China Craton: a case study of the Fuping Complex. *Geological Magazine* 149, 729–742.
- Han, C., Xiao, W., Su, B., Chen, Z., Zhang, X., Ao, S., Zhang, J., Zhang, Z., Wan, B., Song, D., Wang, Z., 2014. Neoproterozoic Algoma-type banded iron formations from Eastern Hebei, North China Craton: SHRIMP U-Pb age, origin and tectonic setting. *Precambrian Research* 251, 212-231.
- Hawkesworth, C.J., Kemp, A.I.S., 2006. Using hafnium and oxygen isotopes in zircons to unravel the record of crustal evolution. *Chemical Geology* 226, 144-162.
- He, X.F., Santosh, M., Bockmann, K., Kelsey, D.E., Hand, M., Hu, J., Wan, Y., 2016. Petrology, phase equilibria and monazite geochronology of granulite-facies metapelites from deep drill cores in the Ordos Block of the North China Craton. *Lithos* 262, 44-57.
- Heinonen, A., Andersen, T., Rönkä O.T., Whitehouse, M., 2015. The source of Proterozoic anorthosite and rapakivi granite magmatism: evidence from combined in situ Hf–O isotopes of zircon in the Ahvenisto complex, southeastern Finland. *Journal of the Geological Society* 172, 103-112.
- Helmy, H.M., El Mahallawi, M.M., 2003. Gabbro Akarem mafic–ultramafic complex, Eastern Desert, Egypt: A late Precambrian analogue of Alaskan-type Complexes. *Mineralogy and Petrology* 77, 85–108.
- Hermann, J., Rubatto, D., Korsakov, A., 2001. Multiple zircon growth during fast exhumation of diamondiferous, deeply subducted continental crust (Kokchetav Massif, Kazakhstan). *Contributions to Mineralogy and Petrology* 141, 66–82.

- Himmelberg, G.R., Loney, R.A., Craig, J.T., 1986. Petrogenesis of the ultramafic complex at the Blashke Islands, Southern Alaska: US Geological Survey Bulletin 1662, Washington, D.C., U.S. Government Printing Office, p. 1–14.
- Himmelberg, G.R., Loney, R.A., 1995. Characteristics and petrogenesis of Alaskan-type ultramafic–mafic intrusions, southeastern Alaska. U.S. Geological Survey Professional Paper 1564, 1–47.
- Holland, T., Blundy, J., 1994. Non-ideal interactions in calcic amphiboles and their bearing on amphibole-plagioclase thermometry. *Contributions to Mineralogy and Petrology* 116, 433–447.
- Holland, T.J.B., Powell, R., 2003. Activity–composition relations for phases in petrological calculations: an asymmetric multicomponent formulation. *Contributions to Mineralogy and Petrology* 145, 492–501.
- Holland, T.J.B., Powell, R., 2011. An improved and extended internally consistent thermodynamic dataset for phases of petrological interest, involving a new equation of state for solids. *Journal of Metamorphic Geology* 29, 333–383.
- Hoskin, P.W.O., Schaltegger, U., 2003. The composition of zircon and igneous and metamorphic petrogenesis. *Reviews in mineralogy and geochemistry* 53, 27–62.
- Huang, D.M., Zhang, D.H., Wang, S.Y., Zhang, Y.X., Dong, C.Y., Liu, D.Y., Wan, Y.S., 2012. 2.3 Ga magmatism and 1.94 Ga metamorphism in the Xiatang area, southern margin of the North China Craton—evidence from whole-rock geochemistry and zircon geochronology and Hf isotopes. *Geological Review* 58, 565–576. (in Chinese with English abstract)
- Huang, X.L., Wilde, S.A., Zhong, J.W., 2013. Episodic crustal growth in the southern segment of the Trans-North China Orogen across the Archean-Proterozoic boundary. *Precambrian Research* 233, 337–357.
- Jahn, B.M., Liu, D.Y., Wan, Y.S., Song, B., Wu, J.S., 2008. Archean crustal evolution of the Jiaodong Peninsula, China, as revealed by zircon SHRIMP geochronology, elemental and Nd-isotope geochemistry. *American Journal of Science* 308, 232–269.
- Jian, P., Kröner, A., Windley, B.F., Zhang, Q., Zhang, W., Zhang, L.Q., 2012. Episodic mantle melting–crustal reworking in the late Neoproterozoic of the northwestern North China Craton: Zircon ages of magmatic and metamorphic rocks from the Yinshan Block. *Precambrian*

Research 222-223, 230-254.

- Jiang, Z.S., Wang, G.D., Xiao, L.L., Diwu, C.R., Lu, J.S., Wu, C.M., 2011. Paleoproterozoic metamorphic P-T-t path and tectonic significance of the Luoning metamorphic complex at the southern terminal of the Trans-North China Orogen, Henan Province. *Acta Petrologica Sinica* 27, 3701-3717. (in Chinese with English abstract).
- Kamenetsky, V.S., Crawford, A.J., Meffre, S., 2001. Factors controlling chemistry of magmatic spinel: An empirical study of associated olivine, Cr-spinel and melt inclusions from primitive rocks. *Journal of Petrology* 42, 655–671.
- Karhu, J.A., Holland, H.D., 1996. Carbon isotopes and the rise of atmospheric oxygen. *Geology* 24, 867-870.
- Kelsey, D.E., Clark, C., Hand, M., 2008. Thermobarometric modelling of zircon and monazite growth in melt-bearing systems: Examples using model metapelitic and metapsammitic granulites. *Journal of Metamorphic Geology* 26, 199–212.
- Kemp, A.I.S., Hawkesworth, C.J., Foster, G.L., Paterson, B.A., Woodhead, J.D., Hergt, J.M., Whitehouse, M.J., 2007. Magmatic and crustal differentiation history of granitic rocks from Hf-O isotopes in zircon. *Science* 315, 980-983.
- Konhauser, K.O., Pecoits, E., Lalonde, S.V., Papineau, D., Nisbet, E.G., Barley, M.E., Arndt, N.T., Zahnle, K., Kamber, B.S., 2009. Oceanic nickel depletion and a methanogen famine before the Great Oxidation Event. *Nature* 458, 750–753.
- Korhonen, F.J., Brown, M., Clark, C., Bhattacharya, S., 2013. Osumilite–melt interactions in ultrahigh temperature granulites: phase equilibria modelling and implications for the P–T–t evolution of the Eastern Ghats Province, India. *Journal of Metamorphic Geology* 31, 881-907.
- Krogh, E.J., 1988. The garnet-clinopyroxene Fe-Mg geothermometer—a reinterpretation of existing experimental data. *Contributions to Mineralogy and Petrology* 99, 44-48.
- Kröner, A., Wilde, S.A., Li, J.H., Wang, K.Y., 2005a. Age and evolution of a late Archaean to early Palaeozoic upper to lower crustal section in the Wutaishan/Hengshan/Fuping terrain of northern China. *Journal of Asian Earth Sciences* 24, 577–595.
- Kröner, A., Wilde, S.A., O'Brien, P.J., Li, J.H., Passchier, C.W., Walte, N.P., Liu, D.Y., 2005b. Field relationships, geochemistry, zircon ages and evolution of a late Archean to

- Paleoproterozoic lower crustal section in the Hengshan Terrain of Northern China. *Acta Geologica Sinica (English Edition)* 79, 605–629.
- Kröner, A., Wilde, S.A., Zhao, G.C., O'Brien, P.J., Sun, M., Liu, D.Y., Wan, Y.S., Liu, S.W., Guo, J.H., 2006. Zircon geochronology of mafic dykes in the Hengshan Complex of northern China: evidence for late Paleoproterozoic rifting and subsequent high-pressure event in the North China Craton. *Precambrian Research* 146, 45-67.
- Kusky, T.M., Li, J.H., 2003. Paleoproterozoic tectonic evolution of the North China Craton. *Journal of Asian Earth Sciences* 22, 23–40.
- Kusky, T.M., Li, J.H., Santosh, M., 2007. The Paleoproterozoic North Hebei Orogen: North China Craton's Collisional Suture with the Columbia Supercontinent. *Gondwana Research* 12, 4–28.
- Kusky, T.M., Santosh, M., 2009. The Columbia connection in North China. *Geological Society, London, Special Publications*, 323, 49-71.
- Kusky, T.M., Zhai, M.G., 2012. The Neoproterozoic ophiolite in the North China Craton: Early Precambrian plate tectonics and scientific debate. *Journal of Earth Science* 23, 277–284
- Leake, B.E., Woolley, A.R., Arps, C.E.S., Birch, W.D., Gilbert, M.C., Grice, J.D., Hawthorne, F.C., Kato, A., Kisch, H.J., Krivovichev, V.G., Linthout, K., Laird, J., Mandarino, J.A., Maresch, W.V., Nickel, E.H., Rock, N.M.S., Schumacher, J.C., Smith, D.C., Stephenson, N.C.N., Ungaretti, L., Whittaker, E.J.W., Guo, Y., 1997. Nomenclature of amphiboles: report of the subcommittee on amphiboles of the International Mineralogical Association, Commission on New Minerals and Mineral Names. *American Mineralogist* 82, 1019–1037.
- Lee, H.Y., Ganguly, J., 1988. Equilibrium compositions of coexisting garnet and orthopyroxene: experimental determinations in the system FeO-MgO-Al₂O₃-SiO₂, and applications. *Journal of Petrology* 29, 93-113.
- Li, J.H., Kusky, T.M., 2007. A late Archean foreland fold and thrust belt in the North China Craton: implications for early collisional tectonics. *Gondwana Research* 12, 47–66.
- Li, S.S., Santosh, M., Cen, K., Teng, X.M., He, X.F., 2016. Neoproterozoic convergent margin tectonics associated with microblock amalgamation in the North China Craton: Evidence from the Yishui Complex. *Gondwana Research* 38, 113–131.
- Li, S.Z., Zhao, G.C., 2007. SHRIMP U–Pb zircon geochronology of the Liaoji granitoids:

- constraints on the evolution of the Paleoproterozoic Jiao-Liao-Ji belt in the Eastern Block of the North China Craton. *Precambrian Research* 158, 1–16.
- Li, S.Z., Zhao, G.C., Sun, M., Wu, F.Y., Liu, J.Z., Hao, D.F., Han, Z.Z., Luo, Y., 2004. Mesozoic, not Paleoproterozoic SHRIMP U–Pb zircon ages of two Liaoji granites, Eastern Block, North China Craton. *International Geology Review* 46, 162–176.
- Li, S.Z., Zhao, G.C., Min, S., Luo, Y., Han, Z.Z., Zhao, G.T., Hao, D.F., 2006. Are the South and North Liaohe Groups different exotic terranes? — Nd isotope constraints on the Jiao-Liao-Ji orogen. *Gondwana Research* 9, 198–208.
- Li, X.H., Li, W.X., Li, Q.L., Wang, X.C., Liu, Y., Yang, Y.H., 2010a. Petrogenesis and tectonic significance of the 850 Ma Gangbian alkaline complex in South China: evidence from in situ zircon U–Pb dating, Hf–O isotopes and whole-rock geochemistry. *Lithos* 114, 1–15.
- Li, X.H., Long, W.G., Li, Q.L., Liu, Y., Zheng, Y.F., Yang, Y.H., Chamberlain, K.R., Wan, D.F., Guo, C.H., Wang, X.C., Tao, H., 2010b. Penglai zircon megacrysts: a potential new working reference material for microbeam determination of Hf–O isotopes and U–Pb age. *Geostandards and Geoanalytical Research* 34, 117–134.
- Li, G.Z., Li, C., Ripley, E.M., Kamo, S., Su, S.G., 2012. Geochronology, petrology and geochemistry of the Nanlinshan and Banpo mafic–ultramafic intrusions: implications for subduction initiation in the eastern Paleo-Tethys. *Contributions to Mineralogy and Petrology* 164, 773–788.
- Liu, C.H., Zhao, G.C., Sun, M., Wu, F., Yang, J., Yin, C., Leung, W.H., 2011. U–Pb and Hf isotopic study of detrital zircons from the Yejishan Group of the Lüliang Complex: constraints on the timing of collision between the Eastern and Western Blocks, North China Craton. *Sedimentary Geology* 236, 129–140.
- Liu, C.H., Zhao, G.C., Liu, F., Sun, M., Zhang, J., Yin, C.Q., 2012a. Zircons U–Pb and Lu–Hf isotopic and whole-rock geochemical constraints on the Gantaohe Group in the Zhanhuang Complex: implications for the tectonic evolution of the Trans-North China Orogen. *Lithos* 146, 80–92.
- Liu, C.H., Zhao, G.C., Sun, M., Zhang, J., Yin, C.Q., 2012b. U–Pb geochronology and Hf isotope geochemistry of detrital zircons from the Zhongtiao Complex: constraints on the tectonic evolution of the Trans-North China Orogen. *Precambrian Research* 222, 159–172.

- Liu, L., Zhang, L.C., Dai, Y., Wang, C., Li, Z., 2012c. Formation age, geochemical signatures and geological significance of the Sanheming BIF-type iron deposit in the Guyang greenstone belt, Inner Mongolia. *Acta Petrologica Sinica* 28, 3623–3637. (in Chinese with English abstract).
- Liu, C.H., Zhao, G.C., Liu, F., Shi, J., 2014a. Geochronological and geochemical constraints on the Lüliang Group in the Lüliang Complex: implications for the tectonic evolution of the Trans-North China Orogen. *Lithos* 198, 298–315.
- Liu, C.H., Zhao, G.C., Liu, F.L., Han, Y.G., 2014b. Nd isotopic and geochemical constraints on the provenance and tectonic setting of the low-grade meta-sedimentary rocks from the Trans-North China Orogen, North China Craton. *Journal of Asian Earth Sciences* 94, 173–189.
- Liu, C.H., Zhao, G.C., Liu, F.L., Shi, J.R., 2016. Constraints of volcanic rocks of the Wutai complex (Shanxi Province, Northern China) on a giant late Neoproterozoic intra-oceanic arc system in the Trans-North China Orogen. *Journal of Asian Earth Sciences*. <http://dx.doi.org/10.1016/j.jseas.2016.04.006>.
- Liu, L., Zhang, L., Dai, Y., 2014c. Formation age and genesis of the banded iron formations from the Guyang Greenstone Belt, Western North China Craton. *Ore Geology Reviews* 63, 388–404.
- Liu, D.Y., Nutman, A.P., Compston, W., Wu, J.S., Shen, Q.H., 1992. Remnants of ≥ 3800 Ma crust in the Chinese part of the Sino-Korean craton. *Geology* 20, 339–342.
- Liu, S.W., 1996. Study on the P-T path of granulites in Fuping area, Hebei province. *Geological Journal of Universities*, 1, 75–84.
- Liu, S.W., Liang, H.H., 1997. Metamorphism of Al-rich gneisses from the Fuping Complex, Taihang Mountain, China. *Acta Petrologica Sinica* 13, 303–312. (in Chinese with English abstract).
- Liu, S.W., Pan, Y.M., Li, J., Li, Q., Zhang, J., 2002. Geological and isotopic geochemical constraints on the evolution of the Fuping Complex, North China Craton. *Precambrian Research* 117, 41–56.
- Liu, S.W., Pan, Y.M., Xie, Q.L., Zhang, J., Li, Q.G., 2004. Archean geodynamics in the Central Zone, North China Craton: constraints from geochemistry of two contrasting series of

- granitoids in the Fuping and Wutai Complexes. *Precambrian Research* 130, 229–249.
- Liu, S.W., Pan, Y.M., Xie, Q.L., Zhang, J., Li, Q.G., Yang, B., 2005. Geochemistry of the Paleoproterozoic Nanying granitic gneisses in the Fuping Complex: implications for the tectonic evolution of the Central Zone, North China Craton. *Journal of Asian Earth Sciences* 24, 643–658.
- Liu, S.W., Zhao, G.C., Wilde, S. A., Shu, G., Sun, M., Li, Q., Tian, W., Zhang, J., 2006. Th–U–Pb monazite geochronology of the Lüliang and Wutai Complexes: constraints on the tectonothermal evolution of the Trans-North China Orogen. *Precambrian Research* 148, 205-224.
- Liu, S.W., Li, Q.G., Liu, C.H., Lü Y.J., Zhang, F., 2009. Guandishan granitoids of the Paleoproterozoic Lüliang metamorphic complex in the Trans - North China Orogen: SHRIMP zircon ages, petrogenesis and tectonic implications. *Acta Geologica Sinica - English Edition* 83, 580-602.
- Liu, X.C., Hu, J., Zhao, Y., Lou, Y., Wei, C., Liu, X., 2009. Late Neoproterozoic/Cambrian high-pressure mafic granulites from the Grove Mountains, East Antarctica: P–T–t path, collisional orogeny and implications for assembly of East Gondwana. *Precambrian Research* 174, 181-199.
- Liu, L., Yang, X., 2015. Temporal, environmental and tectonic significance of the Huoqiu BIF, southeastern North China Craton: Geochemical and geochronological constraints. *Precambrian Research* 261, 217-233.
- Lu, X.P., Wu, F.Y., Guo, J.H., Wilde, S.A., Yang, J.H., Liu, X.M., Zhang, X.O., 2006. Zircon U–Pb geochronological constraints on the Palaeoproterozoic crustal evolution of the Eastern block in the North China Craton. *Precambrian Research* 146, 138–164.
- Lu, J.S., Wang, G.D., Wang, H., Chen, H.X., Wu, C.M., 2013. Metamorphic P-T-t paths retrieved from the amphibolites, Lushan terrane, Henan Province and reappraisal of the Paleoproterozoic tectonic evolution of the Trans-North China Orogen. *Precambrian Research* 238, 61-77.
- Lu, J.S., Wang, G.D., Wang, H., Chen, H.X., Wu, C.M., 2014a. Palaeoproterozoic metamorphic evolution and geochronology of the Wugang block, southeastern terminal of the Trans-North China Orogen. *Precambrian Research* 251, 197-211.

- Lu, J.S., Wang, G.D., Wang, H., Chen, H.X., Peng, T., Wu, C.M., 2015. Zircon SIMS U–Pb geochronology of the Lushan terrane: dating metamorphism of the southwestern terminal of the Palaeoproterozoic Trans-North China Orogen. *Geological Magazine*, 152, 367–377.
- Lu, Z.L., Song, H.X., Du, L.L., Ren, L.D., Geng, Y.S., Yang, C.H., 2014b. Delineation of the ca. 2.7Ga TTG gneisses in the Fuping Complex, North China Craton and its geological significance. *Acta Petrologica Sinica* 30, 2872–2884. (in Chinese with English abstract).
- Ludwig, K.R., 2003. *ISOPLLOT 3.0: A Geochronological Toolkit for Microsoft Excel*. Berkeley Geochronology Center, Special Publication No. 4.
- Luo, Y., Sun, M., Zhao, G.C., Li, S.Z., Xu, P., Ye, K., Xia, X.P., 2004. LA–ICP–MS U–Pb zircon ages of the Liaohe Group in the Eastern Block of the North China Craton: constraints on the evolution of the Jiao-Liao-Ji Belt. *Precambrian Research* 134, 349–371.
- Ma, X., Guo, J., Liu, F., Qian, Q., Fan, H., 2013a. Zircon U–Pb ages, trace elements and Nd–Hf isotopic geochemistry of Guyang sanukitoids and related rocks: Implications for the Archean crustal evolution of the Yinshan Block, North China Craton. *Precambrian Research* 230, 61–78.
- Ma, X., Fan, H.R., Santosh, M., Guo, J., 2013b. Geochemistry and zircon U–Pb chronology of charnockites in the Yinshan Block, North China Craton: tectonic evolution involving Neoproterozoic ridge subduction. *International Geology Review* 55, 1688–1704.
- Ma, X., Fan, H.R., Santosh, M., Guo, J., 2014. Chronology and geochemistry of Neoproterozoic BIF-type iron deposits in the Yinshan Block, North China Craton: implications for oceanic ridge subduction. *Ore Geology Reviews* 63, 405–417.
- Manikyamba, C., Kerrich, R., 2012. Eastern Dharwar Craton, India: Continental lithosphere growth by accretion of diverse plume and arc terranes. *Geosciences Frontiers* 3, 225–240.
- Mao, D.B., Zhong, C.T., Chen, Z.H., Lin, Y.X., Li, H.M., Hu, X.D., 1999. Isotopic ages and geological implications of high-pressure mafic granulites in the northern Chengde area, Hebei Province, China. *Acta Petrologica Sinica* 15, 524–534. (in Chinese with English abstract).
- Maruoka, T., Koeberl, C., Matsuda, J.I., Syono, Y., 2003. Carbon isotope fractionation between graphite and diamond during shock experiments. *Meteoritics & Planetary Science* 38, 1255–1262.

- McLennan, S.M., 1989. Rare earth elements in sedimentary rocks; influence of provenance and sedimentary processes. *Reviews in Mineralogy and Geochemistry* 21, 169-200.
- Meert, J.G., 2012. What's in a name? The Columbia (Paleopangaea/Nuna) supercontinent. *Gondwana Research* 21, 987–993.
- Melezhik, V.A., Fallick, A.E., Medvedev, P.V., Makarikhin, V.V., 1999. Extreme $^{13}\text{C}_{\text{carb}}$ enrichment in ca. 2.0 Ga magnesite–stromatolite–dolomite–red beds' association in a global context: a case for the world-wide signal enhanced by a local environment. *Earth-Science Reviews* 48, 71-120.
- Melezhik, V.A., Fallick, A.E., 2003. $\delta^{13}\text{C}$ and $\delta^{18}\text{O}$ variations in primary and secondary carbonate phases: several contrasting examples from Palaeoproterozoic ^{13}C -rich metamorphosed dolostones. *Chemical Geology* 201, 213-228.
- Melezhik, V., Fallick, A.E., Pokrovsky, B.G., 2005. Enigmatic nature of thick sedimentary carbonates depleted in ^{13}C beyond the canonical mantle value: the challenges to our understanding of the terrestrial carbon cycle. *Precambrian Research* 137, 131-165.
- Moecher, D.P., Essene, E.J., Anovitz, L.M., 1988. Calculation and application of clinopyroxene-garnet-plagioclase-quartz geobarometers. *Contributions to Mineralogy and Petrology* 100, 92-106.
- Mohanty, S.P., Barik, A., Sarangi, S., Sarkar, A., 2015. Carbon and oxygen isotope systematics of a Paleoproterozoic cap-carbonate sequence from the Sausar Group, Central India. *Palaeogeography, Palaeoclimatology, Palaeoecology* 417, 195-209.
- Nakamura, H., Iwamori, H., 2009. Contribution of slab-fluid in arc magmas beneath the Japan arcs. *Gondwana Research* 16, 431–445.
- Nance, R.D., Murphy, J.B., Santosh, M., 2014. The supercontinent cycle: a retrospective essay. *Gondwana Research* 25, 4–29.
- Nutman, A.P., Wan, Y.S., Du, L.L., Friend, C.R.L., Dong, C.Y., Xie, H.Q., Wang, W., Sun, H.Y., Liu, D.Y., 2011. Multistage late Neoproterozoic crustal evolution of the North China Craton, eastern Hebei. *Precambrian Research* 189, 43–65.
- Nutman, A.P., Maciejowski, R., Wan, Y.S., 2014. Protoliths of enigmatic Archaean gneisses established from zircon inclusion studies: Case study of the Caozhuang quartzite, E. Hebei, China. *Geoscience Frontiers* 5, 445-455.

- O'Brien, P.J., Rötzler, J., 2003. High-pressure granulites: formation, recovery of peak conditions and implications for tectonics. *Journal of Metamorphic Geology* 21, 3-20.
- O'Brien, P.J., Walte, N., Li, J.H., 2005. The petrology of two distinct granulite types in the Hengshan Mts, China, and tectonic implications. *Journal of Asian Earth Sciences*, 24, 615-627.
- Palin, R.M., White, R.W., Green, E.C.R., Diener, J.F.A., Powell, R., Holland, T.J.B., 2016. High-grade metamorphism and partial melting of basic and intermediate rocks. *Journal of Metamorphic Geology* 34, 871–892.
- Parlak, O., Höck, V., Delaloye, M., 2002. The supra-subduction zone Pozanti–Karsanti ophiolite, southern Turkey: evidence for high-pressure crystal fractionation of ultramafic cumulates. *Lithos* 65, 205–224.
- Paula-Santos, G.M., Babinski, M., Kuchenbecker, M., Caetano-Filho, S., Trindade, R.I., Pedrosa-Soares, A.C., 2015. New evidence of an Ediacaran age for the Bambuí Group in southern São Francisco craton (eastern Brazil) from zircon U–Pb data and isotope chemostratigraphy. *Gondwana Research* 28, 702-720.
- Pearce, J.A., Harris, N.B.W., Tindle, A.G., 1984. Trace element discrimination diagrams for the tectonic interpretation of granitic rocks. *Journal of Petrology* 25, 956–983.
- Pearce, J.A., 1996. A User's Guide to Basalt Discrimination Diagrams. In: Wyman, D.A. (Ed.), *Trace Element Geochemistry of Volcanic Rocks: Applications for Massive Sulphide Exploration Geological Association of Canada, Short Course Notes*, vol. 12, pp. 79–113.
- Pearce, J.A., Robinson, P.T., 2010. The Troodos ophiolitic complex probably formed in a subduction initiation, slab edge setting. *Gondwana Research* 18, 60–81.
- Perkins D., Chipera, S.J., 1985. Garnet-orthopyroxene-plagioclase-quartz barometry: refinement and application to the English River subprovince and the Minnesota River valley. *Contributions to Mineralogy and Petrology* 89, 69-80.
- Pettigrew, N.T., Hattori, K.H., 2006. The Quetico intrusions of Western Superior Province: Neo-Archean examples of Alaskan/Ural-type mafic-ultramafic intrusions. *Precambrian Research* 149, 21–42.
- Peng, P., Zhai, M.G., Zhang, H., Guo, J.H., 2005. Geochronological constraints on the Paleoproterozoic evolution of the North China Craton: SHRIMP zircon ages of different

- types of mafic dikes. *International Geology Review*, 47, 492-508.
- Peng, T.P., Fan, W.M., Peng, P.X., 2012a. Geochronology and geochemistry of late Archean adakitic plutons from the Taishan granite–greenstone Terrain: implications for tectonic evolution of the eastern North China Craton. *Precambrian Research* 208–211, 53–71.
- Peng, P., Guo, J.H., Zhai, M.G., Windly, B.F., Li, T.S., Liu, F., 2012b. Genesis of the Hengling magmatic belt in the North China Craton: implications for Paleoproterozoic tectonics. *Lithos* 148, 27-44.
- Peng, T., Wilde, S. A., Fan, W., eng, B., 2013a. Late Neoproterozoic potassic high Ba–Sr granites in the Taishan granite–greenstone terrane: Petrogenesis and implications for continental crustal evolution. *Chemical Geology* 344, 23-41.
- Peng, T., Wilde, S. A., Fan, W., Peng, B., 2013b. Neoproterozoic siliceous high-Mg basalt (SHMB) from the Taishan granite–greenstone terrane, Eastern North China Craton: Petrogenesis and tectonic implications. *Precambrian Research* 228, 233-249.
- Peng, P., Wang, C., Wang, X., Yang, S., 2015. Qingyuan high-grade granite–greenstone terrain in the Eastern North China Craton: Root of a Neoproterozoic arc. *Tectonophysics* 662, 7-21.
- Polat, A., Kusky, T., Li, J., Fryer, B., Kerrich, R., Patrick, K., 2005. Geochemistry of Neoproterozoic (ca. 2.55–2.50 Ga) volcanic and ophiolitic rocks in the Wutaishan greenstone belt, central orogenic belt, North China craton: implications for geodynamic setting and continental growth. *Geological Society of America Bulletin* 117, 1387-1399.
- Polat, A., Li, J., Fryer, B., Kusky, T., Gagnon, J., Zhang, S., 2006. Geochemical characteristics of the Neoproterozoic (2800–2700 Ma) Taishan greenstone belt, North China Craton: evidence for plume–craton interaction. *Chemical Geology* 230, 60-87.
- Powell, R., 1985. Regression diagnostics and robust regression in geothermometer/geobarometer calibration: the garnet-clinopyroxene geothermometer revisited. *Journal of Metamorphic Geology* 3, 231-243.
- Powell, R., Holland, T.J.B., 1988. An internally consistent thermodynamic dataset with uncertainties and correlations: 3. Application, methods, worked examples and a computer program. *Journal of Metamorphic Geology* 6, 173–204.
- Prave, A.R., Fallick, A.E., Thomas, C.W., Graham, C.M., 2009. A composite C-isotope profile for the Neoproterozoic Dalradian Supergroup of Scotland and Ireland. *Journal of the Geological*

- Society 166, 845-857. Pearce, J.A., Peate, D.W., 1995. Tectonic implications of the composition of volcanic arc magmas. *Annual Review of Earth and Planetary Sciences* 23, 251–285.
- Puchtel, I.S., Hofmann, A.W., Amelin, Y.V., Garbe-Schönberg, C.D., Samsonov, A.V., Shchipansky, A.A., 1999. Combined mantle plume-island arc model for the formation of the 2.9 Ga Sumozero-Kenozero greenstone belt, SE Baltic Shield: Isotope and trace element constraints. *Geochimica et Cosmochimica Acta* 63, 3579-3595.
- Qian, J.H., Wei, C.J., Zhou, X.W., Zhang, Y., 2013. Metamorphic P–T paths and New Zircon U–Pb age data for garnet–mica schist from the Wutai Group, North China Craton. *Precambrian Research* 233, 282-296.
- Qian, J.H., Wei, C.J., Clarke, G.L., Zhou, X., 2015. Metamorphic evolution and Zircon ages of Garnet–orthoamphibole rocks in southern Hengshan, North China Craton: Insights into the regional Paleoproterozoic P–T–t history. *Precambrian Research* 256, 223-240.
- Qian, J.H., Wei, C.J., 2016. P–T–t evolution of garnet amphibolites in the Wutai–Hengshan area, North China Craton: insights from phase equilibria and geochronology. *Journal of Metamorphic Geology* 34, 423–446.
- Ren, L.D., Geng, Y.S., Du, L.L., Wang, Y.B., Guo, J.J., 2013. SHRIMP data on zircons from the Wanzi series: Constraints on the rock formation time and implications of migmatization at 2.1–2.0 Ga in the Fuping Complex, North China Craton. *Journal of Asian Earth Sciences* 72, 203-215.
- Ren, P., Xie, H., Wang, S., Nutman, A., Dong, C., Liu, S., Xie, S., Che, X., Song, Z., Ma, M., Liu, D., Wan, Y.S., 2016. A ca. 2.60 Ga tectono-thermal event in Western Shandong Province, North China Craton from zircon U-Pb-O isotopic evidence: Plume or convergent plate boundary process. *Precambrian Research* 281, 236–252.
- Rogers, J.J.W., Santosh, M., 2002. Configuration of Columbia, a Mesoproterozoic supercontinent. *Gondwana Research* 5, 5–22.
- Rogers, J.J.W., Santosh, M., 2003. Supercontinents in Earth history. *Gondwana Research* 6, 357–368.
- Rogers, J.J.W., Santosh, M., 2009. Tectonics and surface effects of the supercontinent Columbia. *Gondwana Research* 15, 373–380.

- Rudnick, R.L., Gao, S., 2003. Composition of the continental crust. *Treatise on geochemistry* 3, 1-64.
- Rumble, D., Wang, Q., Zhang, R., 2000. Stable isotope geochemistry of marbles from the coesite UHP terrains of Dabieshan and Sulu, China. *Lithos* 52, 79-95.
- Said, N., Kerrich, R., Maier, W.D., McCuaig, C., 2011. Behaviour of Ni–PGE–Au–Cu in mafic–ultramafic volcanic suites of the 2.7 Ga Kambalda sequence, Kalgoorlie terrane, Yilgarn craton. *Geochimica et Cosmochimica Acta* 75, 2882-2910.
- Samuel, V.O., Santosh, M., Liu, S., Wang, W., Sajeev, K., 2014. Neoproterozoic continental growth through arc magmatism in the Nilgiri Block, southern India. *Precambrian Research* 245, 146-173.
- Santos, R.V., dos Santos, E. J., de Souza Neto, J.A., Carmona, L.C.M., Sial, A.N., Mancini, L.H., Santos, L.C.M.L., Nascimento, G.H., Mendes, L.U.S., Anastácio, E.M.F., 2013. Isotope geochemistry of Paleoproterozoic metacarbonates from Itatuba, Borborema Province, Northeastern Brazil: evidence of marble melting within a collisional suture. *Gondwana Research* 23, 380-389.
- Santosh, M., 2010. Assembling North China Craton within the Columbia supercontinent: the role of double-sided subduction. *Precambrian Research* 178, 149–167.
- Santosh, M., Tsunogae, T., Li, J.H., 2007a. Discovery of sapphirine-bearing Mg–Al granulites in the North China Craton: implications for Paleoproterozoic ultrahigh temperature metamorphism. *Gondwana Research* 11, 263–285.
- Santosh, M., Wilde, S.A., Li, J.H., 2007b. Timing of Paleoproterozoic ultrahigh temperature metamorphism in the North China Craton: evidence from SHRIMP U–Pb zircon geochronology. *Precambrian Research* 159, 178–196.
- Santosh, M., Tsunogae, T., Ohyama, H., Sato, K., Li, J.H., Liu, S.J., 2008. Carbonic metamorphism at ultrahigh-temperatures: evidence from North China Craton. *Earth and Planetary Science Letters* 266, 149–165.
- Santosh, M., Liu, S.J., Tsunogae, T., Li, J.H., 2012. Paleoproterozoic ultrahigh-temperature granulites in the North China Craton: Implications for tectonic models on extreme crustal metamorphism. *Precambrian Research* 222–223, 77–106.
- Santosh, M., Yang, Q.Y., Teng, X., Tang, L., 2015. Paleoproterozoic crustal growth in the North

- China Craton: evidence from the Liliang Complex. *Precambrian Research* 263, 197–231.
- Santosh, M., Teng, X.M., He, X.F., Tang, L., Yang, Q.Y., 2016. Discovery of Neoproterozoic suprasubduction zone ophiolite suite from Yishui Complex in the North China Craton. *Gondwana Research* 38, 1-27.
- Scherer, E., Munker, C., Mezger, K., 2001. Calibration of the lutetium–hafnium clock. *Science* 293, 683–687.
- Schidlowski, M., Eichmann, R., Junge, C.E., 1975. Precambrian sedimentary carbonates: carbon and oxygen isotope geochemistry and implications for the terrestrial oxygen budget. *Precambrian Research* 2, 1-69.
- Shan, H.X., Zhai, M.G., Oliveira, E.P., Santosh, M., Wang, F., 2015. Convergent margin magmatism and crustal evolution during Archean-Proterozoic transition in the Jiaobei terrane: Zircon U–Pb ages, geochemistry, and Nd isotopes of amphibolites and associated grey gneisses in the Jiaodong complex, North China Craton. *Precambrian Research* 264, 98-118.
- Shen, Q.H., Zhao, Z.R., Song, H.X., 2007. Geology, Petrochemistry and SHRIMP zircon U–Pb dating of the Mashan and Xueshan granitoids in Yishui County, Shandong Province. *Geological Review* 53, 180–186. (in Chinese with English abstract).
- Shi, Y., Yu, J.H., Xu, X.S., Tang, H.F., Qiu, J.S., Chen, L.H., 2011. U–Pb ages and Hf isotope compositions of zircons of Taihua Group in Xiaoqinling area, Shaanxi Province. *Acta Petrologica Sinica* 27, 3095-3108. (in Chinese with English abstract).
- Shields, G., Veizer, J., 2002. Precambrian marine carbonate isotope database: Version 1.1. *Geochemistry, Geophysics, Geosystems* 3, 1-12.
- Singh, M.R., Manikyamba, C., Ray, J., Ganguly, S., Santosh, M., Saha, A., Rambabu, S., Sawant, S.S., 2015. Major, trace and platinum group element (PGE) geochemistry of Archean Iron Ore Group and Proterozoic Malangtoli metavolcanic rocks of Singhbhum Craton, Eastern India: Inferences on mantle melting and sulphur saturation history. *Ore Geology Reviews*. <http://dx.doi.org/10.1016/j.oregeorev.2015.04.024>.
- Singh, A.K., Tewari, V.C., Sial, A.N., Khanna, P.P., Singh, N.I., 2016. Rare earth elements and stable isotope geochemistry of carbonates from the mélange zone of Manipur ophiolitic Complex, Indo-Myanmar Orogenic Belt, Northeast India. *Carbonates and Evaporites* 31,

139-151.

- Snoke, A.W., Quick, J.E., Bowman, H.R., 1981. Bear Mountain igneous complex, Klamath Mountains, California: An ultrabasic to silicic calc-alkaline suite. *Journal of Petrology* 22, 501–552.
- Soesoo, A., Bons, P.D., Gray, D.R., Foster, D.A., 1997. Divergent double subduction: tectonic and petrologic consequences. *Geology* 25, 755–758.
- Song, H.X., Yang, C.H., Du, L.L., Ren, L.D., Wang, H., 2011. Carbon and oxygen isotopic characteristics of several Paleoproterozoic carbonate strata in North China Craton. *Acta Petrologica et Mineralogica* 30, 865-872. (in Chinese with English abstract).
- Spencer, C.J., Thomas, R.J., Roberts, N.M., Cawood, P.A., Millar, I., Tapster, S., 2015. Crustal growth during island arc accretion and transcurrent deformation, Natal Metamorphic Province, South Africa: new isotopic constraints. *Precambrian Research* 265, 203-217.
- Su, B.X., Qin, K.Z., Sakyi, P.A., Malaviarachchi, S.P., Liu, P.P., Tang, D.M., Xiao, Q.H., Sun, H., Ma, Y.G., Mao, Q., 2012. Occurrence of an Alaskan-type complex in the Middle Tianshan Massif, Central Asian Orogenic Belt: inferences from petrological and mineralogical studies. *International Geology Review* 54, 249-269.
- Su, Y., Zheng, J., Griffin, W. L., Zhao, J., Li, Y., Wei, Y., Huang, Y., 2014. Zircon U–Pb ages and Hf isotope of gneissic rocks from the Huai’an Complex: Implications for crustal accretion and tectonic evolution in the northern margin of the North China Craton. *Precambrian Research* 255, 335-354.
- Sun, S.S., McDonough, W.F., 1989. Chemical and isotopic systematics of oceanic basalts: implications for mantle composition and processes. Geological Society, London, Special Publications 42, 313–345.
- Sun, M., Armstrong, R.L., Lambert, R.S.J., 1992. Petrochemistry and Sr, Pb and Nd isotopic geochemistry of Early Precambrian rocks, Wutaishan and Taihangshan areas, China. *Precambrian Research* 56, 1–31.
- Swart, P.K., 2015. The geochemistry of carbonate diagenesis: The past, present and future. *Sedimentology* 62, 1233-1304.
- Tam, P.Y., Zhao, G.C., Liu, F.L., Zhou, X., Sun, M., Li, S., 2011. Timing of metamorphism in the Paleoproterozoic Jiao-Liao-Ji Belt: new SHRIMP U–Pb zircon dating of granulites, gneisses

- and marbles of the Jiaobei massif in the North China Craton. *Gondwana Research* 19, 150-162.
- Tang, J., Zheng, Y.F., Wu, Y.B., Gong, B., 2006. Zircon SHRIMP U–Pb dating, C and O isotopes for impure marbles from the Jiaobei terrane in the Sulu orogen: implication for tectonic affinity. *Precambrian Research* 144, 1-18.
- Tang, H.S., Chen, Y. J., Wu, G., Lai, Y., 2008. The C–O isotope composition of the Liaohe Group, northern Liaoning province and its geologic implications. *Acta Petrologica Sinica* 24, 129-138. (in Chinese with English abstract).
- Tang, L., Santosh, M., Teng, X.M., 2015a. Paleoproterozoic (ca. 2.1–2.0 Ga) arc magmatism in the Fuping Complex: Implications for the tectonic evolution of the Trans-North China Orogen. *Precambrian Research* 268, 16-32.
- Tang, L., Santosh, M., Dong, Y.P., 2015b. Tectonic evolution of a complex orogenic system: evidence from the northern Qinling belt, central China. *Journal of Asian Earth Sciences*, 113, 544-559.
- Tang, L., Santosh, M., Tsunogae, T., Teng, X.M., 2016a. Late Neoproterozoic arc magmatism and crustal growth associated with microblock amalgamation in the North China Craton: Evidence from the Fuping Complex. *Lithos* 248-251, 324-338.
- Tang, L., Santosh, M., Dong, Y.P., Tsunogae, T., Zhang, S.T., Cao, H.W., 2016b. Early Paleozoic tectonic evolution of the North Qinling orogenic belt: Evidence from geochemistry, phase equilibrium modelling and geochronology of metamorphosed mafic rocks from the Songshugou ophiolite. *Gondwana Research* 30, 48-64.
- Tang, L., Santosh, M., Tsunogae, T., Teruyuki, M., 2016c. Paleoproterozoic meta-carbonates from the central segment of the Trans-North China Orogen: Zircon U–Pb geochronology, geochemistry, and carbon and oxygen isotopes. *Precambrian Research* 284, 14-29.
- Tang, L., Santosh, M., 2017a. Neoproterozoic granite-greenstone belts and related ore mineralization in the North China Craton: An overview. *Geoscience Frontiers*, doi:10.1016/j.gsf.2017.04.002.
- Tang, L., Santosh, M., Tsunogae, T., Koizumi, T., Hu, X.K., Teng, X.M., 2017b. Petrology, phase equilibria modelling and zircon U–Pb geochronology of Paleoproterozoic mafic granulites from the Fuping Complex, North China Craton. *Journal of Metamorphic Geology*,

doi:10.1111/jmg.12243.

- Teng, X.M., Santosh, M., 2015. A long-lived magma chamber in the Paleoproterozoic North China Craton: Evidence from the Damiao gabbro-anorthosite suite. *Precambrian Research* 256, 79–101.
- Trap, P., Faure, M., Lin, W., Monié P., 2007. Late Paleoproterozoic (1900–1800 Ma) nappe stacking and polyphase deformation in the Hengshan–Wutaishan area: implications for the understanding of the Trans-North-China Belt, North China Craton. *Precambrian Research* 156, 85–106.
- Trap, P., Faure, M., Lin, W., Bruguier, O., Monie, P., 2008. Contrasted tectonic styles for the Paleoproterozoic evolution of the North China Craton. Evidence for a 2.1 Ga thermal and tectonic event in the Fuping Massif. *Journal of Structural Geology* 30, 1109–1125.
- Trap, P., Faure, M., Lin, W., Monié P., Meffre, S., Melleton, J., 2009. The Zhanhuang Massif, the second and eastern suture zone of the Paleoproterozoic Trans-North China Orogen. *Precambrian Research* 172, 80-98.
- Trap, P., Faure, M., Lin, W., Le Breton, N., Monié P., 2012. Paleoproterozoic tectonic evolution of the Trans-North China Orogen: toward a comprehensive model. *Precambrian Research* 222, 191-211.
- Tsunogae, T., Liu, S.J., Santosh, M., Shimizu, H., Li, J.H., 2011. Ultrahigh-temperature metamorphism in Daqingshan, Inner Mongolia Suture Zone, North China Craton. *Gondwana Research* 20, 36-47.
- Tsunogae, T., Dunkley, D.J., Horie, K., Endo, T., Miyamoto, T., Kato, M., 2014. Petrology and SHRIMP zircon geochronology of granulites from Vesleknausen, Lützow-Holm Complex, East Antarctica: Neoproterozoic high-grade metamorphism. *Geoscience Frontiers*, 5, 167-182.
- Valley, J.W., Kinny, P.D., Schulze, D.J., Spicuzza, M.J., 1998. Zircon megacrysts from kimberlite: oxygen isotope variability among mantle melts. *Contributions to Mineralogy and Petrology* 133, 1–11.
- Valley, J.W., Lackey, J.S., Cavosie, A.J., Clechenko, C.C., Spicuzza, M.J., Basei, M.A.S., Bindeman, I.N., Ferreira, V.P., Sial, A.N., King, E.M., Peck, W.H., Sinha, A.K., Wei, C.S., 2005. 4.4 billion years of crustal maturation: oxygen isotopes in magmatic zircon.

Contributions to Mineralogy and Petrology 150, 561–580.

- Vavra, G., Gebauer, D., Schmid, R., Compston, W., 1996. Multiple zircon growth and recrystallization during polyphase Late Carboniferous to Triassic metamorphism in granulites of the Ivrea Zone (Southern Alps): an ion microprobe (SHRIMP) study. Contributions to Mineralogy and Petrology 122, 337-358.
- Veizer, J., 1983. Trace elements and isotopes in sedimentary carbonates. Reviews in Mineralogy and Geochemistry 11, 265-299.
- Veizer, J., Hoefs, J., Lowe, D.R., Thurston, P.C., 1989. Geochemistry of Precambrian carbonates: II. Archean greenstone belts and Archean sea water. Geochimica et Cosmochimica Acta 53, 859-871.
- Veizer, J., Plumb, K.A., Clayton, R.N., Hinton, R.W., Grotzinger, J.P., 1992. Geochemistry of Precambrian carbonates: V. Late Paleoproterozoic seawater. Geochimica et Cosmochimica Acta 56, 2487-2501.
- Veizer, J., Ala, D., Azmy, K., Bruckschen, P., Buhl, D., Bruhn, F., Carden, G.A., Diener, A., Ebner, S., Godderis, Y., Jasper, T., Korte, C., Pawellek, F., Podlaha, O.G., Strauss, H., 1999. $^{87}\text{Sr}/^{86}\text{Sr}$, $\delta^{13}\text{C}$ and $\delta^{18}\text{O}$ evolution of Phanerozoic seawater. Chemical Geology 161, 59-88.
- Verma, S.P., Guevara, M., Agrawal, S., 2006. Discriminating four tectonic settings: Five new geochemical diagrams for basic and ultrabasic volcanic rocks based on log-ratio transformation of major element data. Journal of Earth System Science 115, 485–528.
- Wan, Y.S., Wilde, S.A., Liu, D., Yang, C., Song, B., Yin, X., 2006. Further evidence for ~1.85 Ga metamorphism in the Central Zone of the North China Craton: SHRIMP U–Pb dating of zircon from metamorphic rocks in the Lushan area, Henan Province. Gondwana Research 9, 189-197.
- Wan, Y.S., Liu, D.Y., Wang, S.J., Yang, E.X., Wang, W., Dong, C.Y., Zhou, H.Y., Du, L.L., Yang, Y.H., Diwu, C.R., 2011. 2.7 Ga juvenile crust formation in the North China Craton (Taishan-Xintai area, western Shandong Province): further evidence of an understated event from U–Pb dating and Hf isotopic composition of zircon. Precambrian Research 186, 169–180.
- Wan, Y.S., Dong, C.Y., Liu, D.Y., Kröner, A., Yang, C.H., Wang, W., Du, L.L., Xie, H.Q., Ma, M.Z., 2012. Zircon ages and geochemistry of late Neoproterozoic syenogranites in the North

- China Craton: a review. *Precambrian Research* 222, 265-289.
- Wang, A.D, Liu, Y.C., 2012. Neoproterozoic (2.5–2.8 Ga) crustal growth of the North China Craton revealed by zircon Hf isotope: a synthesis. *Geoscience Frontiers* 3, 147-173.
- Wang, G.D., Lu, J.S., Wang, H., Chen, H.X., Xiao, L.L., Diwu, C.R., Ji, J., Wu, C.M., 2013a. LA-ICP-MS U-Pb dating of zircons and $^{40}\text{Ar}/^{39}\text{Ar}$ dating of amphiboles of the Taihua Metamorphic Complex, Mt. Huashan, southern terminal of the Palaeoproterozoic Trans-North China Orogen. *Acta Petrologica Sinica* 29, 3099-3114. (in Chinese with English abstract).
- Wang, W., Yang, E., Zhai, M., Wang, S., Santosh, M., Du, L., Xie, H., Lv, B., Wan, Y., 2013b. Geochemistry of ~2.7 Ga basalts from Taishan area: Constraints on the evolution of early Neoproterozoic granite-greenstone belt in western Shandong Province, China. *Precambrian Research* 224, 94-109.
- Wang, C., Zhang, L., Lan, C., Dai, Y., 2014a. Petrology and geochemistry of the Wangjiazhuang banded iron formation and associated supracrustal rocks from the Wutai greenstone belt in the North China Craton: implications for their origin and tectonic setting. *Precambrian Research* 255, 603-626.
- Wang, G.D., Wang, H., Chen, H.X., Lu, J.S., Wu, C.M., 2014b. Metamorphic evolution and zircon U-Pb geochronology of the Mts. Huashan amphibolites: insights into the Palaeoproterozoic amalgamation of the North China Craton. *Precambrian Research* 245, 100-114.
- Wang, K.Y., Li, J.L., Liu, L.Q., 1991. Petrogenesis of the Fuping grey gneisses: *Scientia Geologica Sinica* 26, 254–267. (in Chinese with English abstract).
- Wang, K.Y., Li, J.L., Hao, J., Li, J.H., Zhou, S.P., 1996. The Wutaishan mountain belt within the Shanxi Province, Northern China: a record of late Archean collision tectonics. *Precambrian Research* 78, 95–103.
- Wang, Z.H., 2009. Tectonic evolution of the Hengshan–Wutai–Fuping Complexes and its implication for the Trans-North China Orogen. *Precambrian Research* 131, 323–343.
- Wang, Z.H., 2010. Reply to the comment by Zhao et al. on: “Tectonic evolution of the Hengshan–Wutai–Fuping complexes and its implication for the Trans-North China Orogen” [*Precambrian Res.* 170 (2009) 73–87]. *Precambrian Research* 176, 99-104.
- Wang, Z.H., Wilde, S.A., Wang, K., Yu, L., 2004. A MORB-arc basalt-adakite association in the

- 2.5 Ga Wutai greenstone belt: late Archean magmatism and crustal growth in the North China Craton. *Precambrian Research* 131, 323–343.
- Wang, Z.H., Wilde, S.A., Wan, J.L., 2010a. Tectonic setting and significance of 2.3–2.1 Ga magmatic events in the Trans-North China Orogen: new constraints from the Yanmenguan mafic–ultramafic intrusion in the Hengshan–Wutai–Fuping Area. *Precambrian Research* 178, 27–42.
- Wang, J., Wu, Y., Gao, S., Peng, M., Liu, X., Zhao, L., Zhou, L., Hu, Z., Gong, H., Liu, Y., 2010b. Zircon U–Pb and trace element data from rocks of the Huai’an Complex: new insights into the late Paleoproterozoic collision between the Eastern and Western Blocks of the North China Craton. *Precambrian Research* 178, 59–71.
- Wang, Y., Zhang, Y., Zhao, G., Fan, W., Xia, X., Zhang, F., Zhang, A., 2009. Zircon U–Pb geochronological and geochemical constraints on the petrogenesis of the Taishan sanukitoids (Shandong): implications for Neoproterozoic subduction in the Eastern Block, North China Craton. *Precambrian Research* 174, 273–286.
- Wang, W., Wang, S., Liu, D., Li, P., Dong, C., Xie, H., Ma, M., Wan, Y., 2010c. Formation age of the Neoproterozoic Jining Group (banded iron formation) in the western Shandong Province: Constraints from SHRIMP zircon U–Pb dating. *Acta Petrologica Sinica* 26, 1175–1181.
- Wang, W., Liu, S., Bai, X., Yang, P., Li, Q., Zhang, L., 2011. Geochemistry and zircon U–Pb–Hf isotopic systematics of the Neoproterozoic Yixian–Fuxin greenstone belt, northern margin of the North China Craton: implications for petrogenesis and tectonic setting. *Gondwana Research* 20, 64–81.
- Wang, W., Liu, S.W., Santosh, M., Wang, G., Bai, X., Guo, R., 2015. Neoproterozoic intra-oceanic arc system in the Western Liaoning Province: Implications for Early Precambrian crustal evolution in the Eastern Block of the North China Craton. *Earth-Science Reviews* 150, 329–364.
- Wang, Y.J., Fan, W.M., Zhang, Y., Guo, F., 2003. Structural evolution and $^{40}\text{Ar}/^{39}\text{Ar}$ dating of the Zanhuang metamorphic domain in the North China Craton: constraints on Paleoproterozoic tectonothermal overprinting. *Precambrian Research* 122, 159–182.
- Wei, C.J., Qian, J.H., Zhou, X.W., 2014. Paleoproterozoic crustal evolution of the Hengshan–Wutai–Fuping region, North China Craton. *Geoscience Frontiers* 5, 485–497.

- White, R.W., Powell, R., Holland, T.J.B., Worley, B.A., 2000. The effect of TiO₂ and Fe₂O₃ on metapelitic assemblages at greenschist and amphibolite facies conditions: mineral equilibria calculations in the system K₂O-FeO-MgO-Al₂O₃-SiO₂-H₂O-TiO₂-Fe₂O₃. *Journal of Metamorphic Geology* 18, 497–511.
- White, R.W., Powell, R., Clarke, G.L., 2002. The interpretation of reaction textures in Fe-rich metapelitic granulites of the Musgrave Block, central Australia: constraints from mineral equilibria calculations in the system K₂O-FeO-MgO-Al₂O₃-SiO₂-H₂O-TiO₂-Fe₂O₃. *Journal of Metamorphic Geology* 20, 41–55.
- White, R.W., Powell, R., Holland, T.J.B., Johnson, T.E., Green, E.C.R., 2014. New mineral activity–composition relations for thermodynamic calculations in metapelitic systems. *Journal of Metamorphic Geology* 32, 261–286.
- Wiedenbeck, M., Hanchar, J.M., Peck, W.H., Sylvester, P., Valley, J., Whitehouse, M., Kronz, A., Morishita, Y., Nasdala, L., Fiebig, J., 2004. Further characterisation of the 91500 zircon crystal. *Geostandards and Geoanalytical Research* 28, 9–39.
- Wilde, S.A., Cawood, P., Wang, K.Y., 1997. The relationship and timing of granitoid evolution with respect to felsic volcanism in the Wutai Complex, North China Craton. In: Qian, X.L., You, Z.D., Halls, H.C. (Eds.), *Proceedings of the 30th IGC. Precambrian Geology and Metamorphic Petrology* 17, 75–88.
- Wilde, S.A., Zhao, G.C., Wang, K.Y., Sun, M., 2004. First precise SHRIMP U–Pb zircon ages for the Hutuo Group, Wutaishan: further evidence for the Palaeoproterozoic amalgamation of the North China Craton. *Chinese Science Bulletin* 49, 83–90.
- Wilde, S.A., Cawood, P.A., Wang, K.Y., Nemchin, A.A., 2005. Granitoid evolution in the Late Archaean Wutai Complex, North China Craton. *Journal of Asian Earth Sciences* 24, 597–613.
- Windley, B.F., 1993. Uniformitarianism today: plate tectonics is the key to the past. *Journal Geological Society of London* 150, 7–19.
- Windley, B.F., Alexeiev, D., Xiao, W., Kröner, A., Badarch, G., 2007. Tectonic models for accretion of the Central Asian Orogenic Belt. *Journal of the Geological Society* 164, 31–47.
- Windley, B.F., Garde, A.A., 2009. Arc-generated blocks with crustal sections in the North Atlantic craton of West Greenland: crustal growth in the Archean with modern analogues. *Earth-Science Reviews* 93, 1–30.

- Wood, P.A., 1980. The application of a Th–Hf–Ta diagram to problems of tectonomagmatic classification and to establishing the nature of crustal contamination of basaltic lavas of the British Tertiary Volcanic Province. *Earth and Planetary Science Letters* 50, 11–30.
- Woodhead, J., Hergt, J., Shelley, M., Eggins, S., Kemp, R., 2004. Zircon Hf-isotope analysis with an excimer laser, depth profiling, ablation of complex geometries, and concomitant age estimation. *Chemical Geology* 209, 121–135.
- Wu, C.H., Li, S.X., Gao, J.F., 1986. Archean and Paleoproterozoic metamorphic regions in the North China Craton. In: Dong, S.B. (Ed.), *Metamorphism and Crustal Evolution of China*. Geological Publishing House, Beijing, pp. 1–89. (in Chinese with English abstract).
- Wu, J.S., Geng, Y.S., Xu, H.F., Jin, L.G., He, S.Y., Sun, S.W., 1989. Metamorphic geology of the Fuping Group. *Tianjin Institute of Geology Bulletin*, 19, 1-213. (in Chinese with English abstract).
- Wu, F.Y., Zhao, G.C., Wilde, S.A., Sun, D.Y., 2005. Nd isotopic constraints on crustal formation in the North China Craton. *Journal of Asian Earth Sciences* 24, 523–545.
- Wu, J.S., Geng, Y.S., Shen, Q.H., Wan, Y.S., Liu, D.Y., Song, B., 1998. Archaean geology characteristics and tectonic evolution of China-Korea Paleo-continent. Geological Publishing House, Beijing, pp. 1-211. (in Chinese with English abstract).
- Xia, X.P., Sun, M., Zhao, G.C., Wu, F.Y., Xu, P., Zhang, J., He, X.H., Zhang, J.H., 2006. U–Pb and Hf Isotope Study of Detrital Zircons from the Wanzi Supracrustals: constraints on the tectonic setting and evolution of the Fuping Complex, Trans-North China Orogen. *Acta Geologica Sinica (English Edition)*, 80, 844–863.
- Xiao, L.L., Wang, G.D., 2011. Zircon U–Pb dating of metabasic rocks in the Zanhuang metamorphic complex and its geological significance. *Acta Petrologica et Mineralogica*, 30, 781-794. (in Chinese with English abstract).
- Xiao, L.L., Wu, C.M., Zhao, G.C., Guo, J.H., Ren, L.D., 2011. Metamorphic P–T paths of the Zanhuang amphibolites and metapelites: constraints on the tectonic evolution of the Paleoproterozoic Trans-North China Orogen. *International Journal of Earth Sciences* 100, 717–739.
- Xiao, L.L., Wang, G.D., Wang, H., Jiang, Z.S., Diwu, C.R., Wu, C.M., 2013. Zircon U–Pb geochronology of the Zanhuang metamorphic complex: reappraisal of the Palaeoproterozoic

- amalgamation of the Trans-North China Orogen. *Geological Magazine*, 150, 756-764.
- Xiao, L.L., Liu, F.L., Chen, Y., 2014. Metamorphic P–T–t paths of the Zanhuang metamorphic complex: Implications for the Paleoproterozoic evolution of the Trans-North China Orogen. *Precambrian Research* 255, 216-235.
- Xiao, W.J., Windley, B.F., Hao, J., Zhai, M.G., 2003. Accretion leading to collision and the Permian Solonker suture, Inner Mongolia, China: termination of the Central Asian orogenic belt. *Tectonics* 22, 1–20.
- Xiao, W.J., Huang, B.C., Han, C.M., Sun, S., Li, J.L., 2010. A review of the western part of the Altaids: a key to understanding the architecture of accretionary orogens. *Gondwana Research* 18, 253-273.
- Xie, H.Q., Liu, D.Y., Yin, X.Y., Zhou, H.Y., Yang, C.H., Du, L.L., Wan, Y.S., 2012. Formation age and tectonic environment of the Gantaohu Group, North China Craton: Geology geochemistry, SHRIMP zircon geochronology and Hf–Nd isotopic systematics. *Chinese Science Bulletin* 57, 4735–4745.
- Yang, C.H., Du, L.L., Ren, L.D., Song, H.X., Wan, Y.S., Xie, H.Q., Liu, Z.X., 2011. The age and petrogenesis of the Xuting granite in the Zanhuang Complex, Hebei Province: constraints on the structural evolution of the Trans-North China Orogen, North China Craton. *Acta Petrologica Sinica* 27, 1003–1016. (in Chinese with English abstract).
- Yang, X., Liu, L., Lee, I., Wang, B., Du, Z., Wang, Q., Wang, Y., Sun, W., 2014. A review on the Huoqiu banded iron formation (BIF), southeast margin of the North China Craton: Genesis of iron deposits and implications for exploration. *Ore Geology Reviews* 63, 418-443.
- Yang, Q.Y., Santosh, M., 2015. Charnokite magmatism during a transitional phase: Implications for late Paleoproterozoic ridge subduction in the North China Craton. *Precambrian Research* 261, 188-216.
- Yang, Q.Y., Santosh, M., Collins, A.S., Teng, X.M., 2016. Microblock amalgamation in the North China Craton: Evidence from Neoproterozoic magmatic suite in the western margin of the Jiaoliao Block. *Gondwana Research* 31, 96-123.
- Yu, J.H., Wang, D., Wang, C., 1997. Ages of the Lüliang Group and its main metamorphism in the Lüliang Mountains, Shanxi: evidence from single-grain zircon U–Pb ages. *Geological Review* 43, 403–408. (in Chinese with English abstract).

- Yu, X., Liu, J., Li, C., Chen, S., Dai, Y., 2013. Zircon U–Pb dating and Hf isotope analysis on the Taihua Complex: Constraints on the formation and evolution of the Trans-North China Orogen. *Precambrian Research* 230, 31–44.
- Yuan, H.L., Gao, S., Liu, X.M., Li, H.M., Günther, D., Wu, F.Y., 2004. Accurate U–Pb age and trace element determinations of zircon by laser ablation-inductively coupled plasma-mass spectrometry. *Geostandards and Geoanalytical Research* 28, 353–370.
- Yuan, H.L., Gao, S., Dai, M.N., Zong, C.L., Günther, D., Fontaine, G.H., Liu, X.M., Diwu, C.R., 2008. Simultaneous determinations of U–Pb age, Hf isotopes and trace element compositions of zircon by excimer laser-ablation quadrupole and multiple-collector ICP-MS. *Chemical Geology* 247, 100–118.
- Zhai, M.G., 2011. Cratonization and the Ancient North China Continent: A summary and review. *Science China Earth Sciences* 54, 1110–1120.
- Zhai, M.G., 2014. Multi-stage crustal growth and cratonization of the North China Craton. *Geoscience Frontiers* 5, 457–469.
- Zhai, M.G., Santosh, M., 2011. The early Precambrian odyssey of the North China Craton: a synoptic overview. *Gondwana Research* 20, 6–25.
- Zhai, M.G., Guo, J.H., Yan, Y.H., 1992. Discovery and preliminary study of the Archean high-pressure granulites in the North China. *Science in China*, 12, 1325–1330. (in Chinese with English abstract).
- Zhai, M.G., Bian, A.G., Zhao, T.P., 2000. The amalgamation of the supercontinent of North China Craton at the end of Neo-Archaean and its breakup during late Palaeoproterozoic and Mesoproterozoic. *Science in China (Series D-Earth Science)* 43, 219–232. (in Chinese with English abstract).
- Zhai, M.G., Guo, J.H., Liu, W.J., 2005. Neoproterozoic to Paleoproterozoic continental evolution and tectonic history of the North China Craton: a review. *Journal of Asian Earth Sciences*, 24, 547–561.
- Zhai, M.G., Peng, P., 2007. Paleoproterozoic events in North China Craton. *Acta Petrologica Sinica* 23, 2665–2682. (in Chinese with English abstract).
- Zhang, F.Q., Liu, J.Z., Ouyang, Z.Y., 1998. Tectonic framework of greenstones in the basement of the North China Craton. *Acta Geophysica Sinica* 41, 99–107. (in Chinese with English

abstract).

- Zhang, H.F., Zhai, M.G., Santosh, M., Diwu, C.R., Li, S.R., 2011. Geochronology and petrogenesis of Neoproterozoic potassic meta-granites from Huai'an Complex: implications for the evolution of the North China Craton. *Gondwana Research* 20, 82-105.
- Zhang, H.F., Zhai, M.G., Santosh, M., Wang, H.Z., Zhao, L., Ni, Z.Y., 2014. Paleoproterozoic granulites from the Xinghe graphite mine, North China Craton: Geology zircon U–Pb geochronology and implications for the timing of deformation, mineralization and metamorphism. *Ore Geology Reviews*, 63, 478-497.
- Zhang, H.F., Wang, H.Z., Santosh, M., Zhai, M.G., 2016a. Zircon U–Pb ages of Paleoproterozoic mafic granulites from the Huai'an terrane, North China Craton (NCC): Implications for timing of cratonization and crustal evolution history. *Precambrian Research* 272, 244-263.
- Zhang, D.D., Guo, J.H., Tian, Z.H., Liu, F., 2016b. Metamorphism and P-T evolution of high pressure granulite in Chicheng, northern part of the Paleoproterozoic Trans-North China Orogen. *Precambrian Research*. <http://dx.doi.org/10.1016/j.precamres.2016.04.009>.
- Zhang, L., Wang, C., Zhu, M., Huang, H., Peng, Z., 2016c. Neoproterozoic Banded Iron Formations in the North China Craton: Geology, Geochemistry, and Its Implications. In *Main Tectonic Events and Metallogeny of the North China Craton*. Springer Singapore, p. 85-103.
- Zhang, J., Zhao, G.C., Sun, M., Wilde, S.A., Li, S.Z., Liu, S.W., 2006. High-pressure mafic granulites in the Trans-North China Orogen: tectonic significance and age. *Gondwana Research* 9, 349-362.
- Zhang, J., Zhao, G.C., Li, S.Z., Sun, M., Liu, S.W., Wilde, S.A., Kröner, A., Yin, C.Q., 2007. Deformation history of the Hengshan Complex: implications for the tectonic evolution of the Trans-North China Orogen. *Journal of Structural Geology* 29, 933–949.
- Zhang, J., Zhao, G.C., Li, S.Z., Sun, M., Wilde, S.A., Liu, S.W., Yin, C.Q., 2009. Polyphase deformation of the Fuping complex, Trans-North China Orogen: structures, SHRIMP UePb zircon ages and tectonic implications. *Journal of Structure Geology* 31, 177-193.
- Zhang, J., Zhao, G.C., Li, S.Z., Sun, M., Liu, S.W., 2012. Structural and aeromagnetic studies of the Wutai Complex: implications for the Tectonic Evolution of the Trans-North China Orogen. *Precambrian Research* 222-223, 212-229.
- Zhang, Z.M., Xiang, H., Dong, X., Ding, H., He, Z., 2015. Long-lived high-temperature

- granulite-facies metamorphism in the Eastern Himalayan orogen, south Tibet. *Lithos* 212, 1-15.
- Zhang, K.J., Li, Q.H., Yan, L.L., Zeng, L., Lu, L., Zhang, Y.X., Hui, J., Jin, X., Tang, X.C., 2017a. Geochemistry of limestones deposited in various plate tectonic settings. *Earth-Science Reviews* 167, 27-46.
- Zhang, Z.M., Xiang, H., Dong, X., Li, W., Ding, H., Gou, Z., Tian, Z., 2017b. Oligocene HP metamorphism and anatexis of the Higher Himalayan Crystalline Sequence in Yadong region, east-central Himalaya. *Gondwana Research* 41, 176-187.
- Zhao, G.C., 2014. Jiangnan Orogen in South China: Developing from divergent double subduction. *Gondwana Research* 27, 1173–1180.
- Zhao, G.C., Zhai, M.G., 2013. Lithotectonic elements of Precambrian basement in the North China Craton: review and tectonic implications. *Gondwana Research* 23, 1207–1240.
- Zhao, G.C., Cawood, P.A., Lu, L.Z., 1999. Petrology and P–T history of the Wutai amphibolites: implications for tectonic evolution of the Wutai Complex, China. *Precambrian Research* 93, 181–199.
- Zhao, G.C., Wilde, S.A., Cawood, P.A., Lu, L.Z., 2000a. Petrology and P–T path of the Fuping mafic granulites: implications for tectonic evolution of the central zone of the North China Craton. *Journal of Metamorphic Geology* 18, 375–391.
- Zhao, G.C., Cawood, P.A., Wilde, S.A., Sun, M., Lu, L., 2000b. Metamorphism of basement rocks in the Central Zone of the North China Craton: implications for Paleoproterozoic tectonic evolution. *Precambrian Research* 103, 55-88.
- Zhao, G.C., Wilde, S.A., Cawood, P.A., Sun, M., 2001a. Archean blocks and their boundaries in the North China Craton: lithological, geochemical, structural and P–T path constraints and tectonic evolution. *Precambrian Research* 107, 45–73.
- Zhao, G.C., Cawood, P.A., Wilde, S.A., Lu, L., 2001b. High-pressure granulites (retrograded eclogites) from the Hengshan Complex, North China Craton: petrology and tectonic implications. *Journal of Petrology* 42, 1141-1170.
- Zhao, G.C., Wilde, S.A., Cawood, P.A., Sun, M., 2002a. SHRIMP U–Pb zircon ages of the Fuping Complex: implications for Late Archean to Paleoproterozoic accretion and assembly of the North China Craton. *American Journal of Science*, 302, 191–226.

- Zhao, G.C., Cawood, P.A., Wilde, S.A., Sun, M., 2002b. Review of global 2.1–1.8 Ga orogens: implications for a pre-Rodinia supercontinent. *Earth-Science Reviews*, 59, 125–162.
- Zhao, G.C., Sun, M., Wilde, S.A., Li, S.Z., 2005. Late Archean to Paleoproterozoic evolution of the North China Craton: key issues revisited. *Precambrian Research* 136, 177–202.
- Zhao, G.C., Kroner, A., Wilde, S.A., Sun, M., Li, S.Z., Li, X.P., Zhang, J., Xia, X.P., He, Y.H., 2007. Lithotectonic elements and geological events in the Hengshan–Wutai–Fuping belt: a synthesis and implications for the evolution of the Trans-North China Orogen. *Geological Magazine*, 144, 753–775.
- Zhao, G.C., Wilde, S.A., Sun, M., Guo, J., Kröner, A., Li, S., Li, X., Zhang, J., 2008a. SHRIMP U–Pb zircon geochronology of the Huai'an Complex: constraints on late Archean to Paleoproterozoic magmatic and metamorphic events in the Trans-North China Orogen. *American Journal of Science*, 308, 270–303.
- Zhao, G.C., Wilde, S.A., Sun, M., Li, S.Z., Li, X.P., Zhang, J., 2008b. SHRIMP U–Pb zircon ages of granitoid rocks in the Lüliang Complex: implications for the accretion and evolution of the Trans-North China Orogen. *Precambrian Research* 160, 213–226.
- Zhao, G.C., Li, S.Z., Zhang, J., Sun, M., Xia, X.P., 2010. A comment on “Tectonic evolution of the Hengshan–Wutai–Fuping complexes and its implication for the Trans-North China Orogen”. *Precambrian Research* 176, 94–98.
- Zhao, G.C., Cawood, P.A., Li, S.Z., Wilde, S.A., Sun, M., Zhang, J., He, Y.H., Yin, C.Q., 2012. Amalgamation of the North China Craton: key issues and discussion. *Precambrian Research* 222–223, 55–76.
- Zhao, R.F., Guo, J.H., Peng, P., Liu, F., 2011. 2.1 Ga crustal remelting event in Hengshan Complex: evidence from zircon UePb dating and Hf-Nd isotopic study on potassic granites. *Acta Petrologica Sinica* 27, 1607–1623. (in Chinese with English abstract).
- Zhu, M.T., Zhang, L.C., Dai, Y.P., Wang, C.L., 2015. In situ zircon U–Pb dating and O isotopes of the Neoproterozoic Hongtoushan VMS Cu–Zn deposit in the North China Craton: Implication for the ore genesis. *Ore Geology Reviews* 67, 354–367.

Appendix I: Methodology

I.1 Field investigation

Field investigation is one of the significant components of this PhD study. Four field investigations were carried out in the Fuping Complex and once in the Zanhuang Complex to fulfill the objectives of this thesis, 90 samples on different rock types were collected for further petrographic, geochemical and geochronological studies.

The first fieldwork was undertaken in June 2014. I carried out investigations on the geological relationship and spatial distribution of different rocks in the southern part of the Fuping Complex. Meanwhile, I focused on the occurrences of the Nanying gneissic granites and associated amphibolite. Eighteen samples were collected.

The second fieldwork was undertaken in August 2014. On the basis of the first fieldwork, I found another two types of amphibolite were cropped out in the Fuping Complex: BIF related amphibolite and marble related amphibolite. I mainly focused on investigation and comparison on the three types of amphibolites mentioned above. Furthermore, I carried out detailed investigation on the Yangmuqiao mafic-ultramafic intrusion in the western part of the Fuping Complex and meta-sedimentary rocks in the Wanzi Group. As a result, thirty samples were collected.

The third fieldwork was carried out in June 2015. Zanhuang Complex is adjacent to the Fuping Complex. I mainly focused on the meta-sedimentary rocks in the Central Zanhuang Domain of the Zanhuang Complex, especially marbles. Marbles are exposed in the Central Zanhuang Domain and Wanzi Group in the Fuping Complex. I investigated their field occurrences and relationships. Twelve samples were collected.

The fourth fieldwork was carried out in July 2015. Based on the previous three times of field work, this field work mainly focused on the mafic granulite in the northern part of the Fuping Complex, and marbles and calc-silicates in the southern part of the Fuping Complex. The spatial distributions of the mafic granulites and their relationship with the wall rock TTG gneisses were investigated. Field

occurrences of meta-carbonates (marbles and calc-silicates were compared with marbles exposed in the Central Zhanhuang Domain. As a result, thirty samples were collected.

I.2 Petrology and EMPA

Electron microprobe analysis (EMPA) for mineral chemistry was carried out using an electron microprobe analyzer (JEOL JXA8530F) at the Chemical Analysis Division of the Research Facility Center for Science and Technology, University of Tsukuba, Japan. The analyses were performed under conditions of 15 kV accelerating voltage and 10 nA sample current, and the data were regressed using an oxide-ZAF correction program supplied by JEOL.

I.3 Pseudosection modelling

P-T pseudosection calculations were performed by using THERMOCALC 3.33 (Powell and Holland, 1988, updated October 2009) and the internally consistent thermodynamic dataset of tcds55s (Holland and Powell, 1998). The effective bulk-rock compositions for pseudosection calculation, normalized into mole proportions in the model system, were calculated on the basis of the bulk-rock geochemical results. A model system of NCKFMASHTO ($\text{Na}_2\text{O}-\text{CaO}-\text{K}_2\text{O}-\text{FeO}-\text{MgO}-\text{Al}_2\text{O}_3-\text{SiO}_2-\text{H}_2\text{O}-\text{TiO}_2-\text{Fe}_2\text{O}_3$) was chosen for P-T pseudosection calculations for samples 15FP-02 and 15FP-03. The pseudosection calculations for sample 15FP-06 were undertaken in the system NCFMASHTO ($\text{Na}_2\text{O}-\text{CaO}-\text{FeO}-\text{MgO}-\text{Al}_2\text{O}_3-\text{SiO}_2-\text{H}_2\text{O}-\text{TiO}_2-\text{Fe}_2\text{O}_3$). The phases considered in the modelling and the corresponding activity-composition (a-x) models used are garnet, orthopyroxene and biotite (White et al., 2014), amphibole, clinopyroxene and melt (Green et al., 2016), plagioclase and K-feldspar (Holland and Powell, 2003), ilmenite (White et al., 2000) and magnetite (White et al., 2002). Quartz and rutile are treated as pure end-member phases.

I.4 Whole rock geochemistry

Whole rock major, trace and platinum-group elements were measured at the National Research Center for Geoanalysis, Chinese Academy of Geological Sciences,

Beijing. Fresh rock chips were initially reduced to avoid surface alteration or weathering. Contents of major elemental oxides were analyzed by X-ray fluorescence (XRF) spectrometry (PW4400) with analytical uncertainties <5%, and trace elements were measured by PE300D inductive coupled plasma mass spectrometry (ICP-MS). Trace and rare earth elements were analyzed with analytical uncertainties 10% for elements with abundances <10 ppm, and approximately 5% for those >10 ppm. The concentrations of PGE in mafic-ultramafic samples were measured by the combination of NiS bead pre-concentration, Te co-precipitation and ICP-MS analysis.

I.5 Zircon U-Pb geochronology and Hf-O isotopes

Zircon grains were separated using conventional heavy fraction, magnetic techniques and hand picking under a binocular microscope at the Yu'neng Geological and Mineral Separation Survey Center, Lang-fang, China. The zircon grains were mounted in epoxy resin disks and then polished to expose the crystals approximately half way along with the standard TEMORA1 (417Ma; [Black et al., 2004](#)). Pre-analytical cathodoluminescence (CL), transmitted and reflected light images were obtained to investigate the internal structures of zircons.

Zircon U-Pb and Lu-Hf isotopic analyses were performed at the State Key Laboratory of Continental Dynamics of Northwest University, China. The detailed analytical procedures for zircon U-Pb dating are same with those described in [Yuan et al. \(2004\)](#). On an Agilent 7500a ICP-MS instrument, the laser spot diameter and frequency was set to be 30 μm and 10 Hz, respectively. Harvard zircon 91500 was used as external standard with a recommended $^{206}\text{Pb}/^{238}\text{U}$ age of 1065.4 ± 0.6 Ma ([Wiedenbeck et al., 2004](#)) to correct instrumental mass bias and depth-dependent elemental and isotopic fractionation, the standard silicate glass NIST 610 and GJ-1 were used to optimize the instrument. U-Th-Pb concentrations were calibrated by using ^{29}Si as an internal standard and NIST 610 as an external standard. Data calculation and concordia diagram plot were carried out using the GLITTER program and ISOPLOT version 4.15 ([Ludwig, 2003](#)). Lu-Hf isotopes were measured on the

same or adjacent domains of the same grains from where the U-Pb dating were done, using Nu Plasma HR multi-collector laser-ablation inductively coupled plasma mass spectrometry (MC-LA-ICPMS) with laser ablation diameter of 45 μm . Detailed working conditions and analytical procedures have been described by Yuan et al. (2008). Recommended $^{176}\text{Lu}/^{175}\text{Lu}$ ratio of 0.02669 (DeBievre and Taylor, 1993) was used to calculate $^{176}\text{Lu}/^{177}\text{Hf}$ ratios, and the $^{176}\text{Yb}/^{172}\text{Yb}$ ratio of 0.5886 (Chu et al., 2002) was used to calculate mean βYb value from ^{172}Yb and ^{173}Yb . Zircon 91500 was used as the reference standard, with a weighted mean $^{176}\text{Hf}/^{177}\text{Hf}$ ratio of 0.282306 ± 10 (Woodhead et al., 2004). Calculation of initial $^{176}\text{Hf}/^{177}\text{Hf}$ was based on the reference to the chondritic reservoir (Blichert-Toft and Albarède, 1997). Hf model age (T_{DM}) was calculated with respect to the depleted mantle with present-day $^{176}\text{Hf}/^{177}\text{Hf} = 0.28325$ and $^{176}\text{Lu}/^{177}\text{Hf} = 0.0384$ (Griffin et al., 2000), and two-stage Hf model age (T_{DM}^{C}) was calculated with respect to the average continental crust with a $^{176}\text{Lu}/^{177}\text{Hf}$ ratio of 0.015 (Griffin et al., 2002), using the ^{176}Lu decay constant of $1.865 \times 10^{-11} \text{ year}^{-1}$ (Scherer et al., 2001).

Zircon oxygen isotope studies were conducted by the Cameca IMS 1280 ion microprobe housed at the Institute of Geology and Geophysics, Chinese Academy of Sciences, Beijing. Detailed working conditions and analytical procedures are the same as those described by Li et al. (2010a). The Cs^+ primary ion beam was accelerated at 10 kV, with an intensity of ca. 2 nA and rastered over a 10 μm area. The spot is about 20 μm in diameter (10 μm beam diameter and 10 μm raster). The instrumental mass fractionation factor (IMF) was corrected using Penglai zircon standard with $(\delta^{18}\text{O})_{\text{VSMOW}} = 5.31 \pm 0.10 \text{ ‰}$ (Li et al., 2010b). Measured $^{18}\text{O}/^{16}\text{O}$ was normalized by using Vienna Standard Mean Ocean Water (VSMOW) compositions, and then corrected for the instrumental mass fractionation factor. The internal precision of a single analysis was generally better than 0.2 ‰ for $^{18}\text{O}/^{16}\text{O}$ ratio. Values of $\delta^{18}\text{O}$ were standardized to VSMOW, and the $\delta^{18}\text{O}$ values were reported in standard per mil notation.

I.6 C-O isotopes

Carbonate minerals (calcite and dolomite) in marble and calc-silicate rock samples were separated for carbon and oxygen isotopic analyses. Fresh rock samples were crushed, followed by hand picking of calcite and dolomite under a binocular microscope. The isotopic compositions of carbon and oxygen were measured at the Stable Isotope Lab of the Faculty of Life and Environmental Sciences, University of Tsukuba, using continuous flow stable isotope ratio mass spectrometer (IsoPrime-EA and Isoprime Ltd). Detailed analytical procedures and conditions for carbon isotopic analyses are same with those described in [Maruoka et al. \(2003\)](#). The $\delta^{13}\text{C}$ values, compared with those of the reference gas, were converted to those of V-PDB (Vienna-Pee Dee Belemnite) scale based on two reference standards (NBS-19: +1.95‰; IAEA-CH-7: -32.151‰, [Coplen et al., 2006](#)). For oxygen isotope, the analytical methods (Maruoka, in preparation) are modified after the procedures of [Gehre and Strauch \(2003\)](#). The $\delta^{18}\text{O}$ values are also reported as V-PDB scale based on two reference standards (NBS-19: -2.2‰; NBS-18: -23.0‰, [Coplen et al., 2002](#)).

Appendix II: Analytical data

Table 3-1 Details of samples from the Fuping TTG gneiss and Yangmuqiao mafic-ultramafic intrusion.

Sample	Location	Coordinate	Rock type	Mineral assemblage
FP-6-1	Nanxiazhuang	N38 °26'08"; E113 °40'57"	TTG gneiss	Pl+Qtz+Bt+Kfs+Hbl+Mt
FP-7	Dongping	N38 °27'07"; E114 °40'36"	TTG gneiss	Pl+Qtz+Bt+Kfs+Hbl+Mt
FP-24	Yangmuqiao	N38 °37'50"; E113 °38'01"	Hornblendite	Hbl+Pl+Bt
FP-25-2	Niujuange	N38 °38'23"; E113 °37'39"	Hornblendite	Hbl+Bt+Pl
FP-28	Yangmuqiao	N38 °37'38"; E113 °38'50"	Pyroxene hornblendite	Hbl+Cpx+Pl+Chr+Bt+Chl
FP-29-1	Yangmuqiao	N38 °37'41"; E113 °37'42"	Pyroxene hornblendite	Hbl+Cpx+Pl+Chr+Bt+ hl

Mineral abbreviations: Hbl, hornblende; Pl, plagioclase; Bt, biotite; Cpx, Clinopyroxene; Qtz, quartz; Chr, chromite; Chl, chlorite; Kfs, K-feldspar; Mt-magnetite; Ilm, ilmenite.

Table 3-2 EMPA data of hornblende.

No.	1	2	3	15	17	18	19	20	21	22	23	24
Sample	FP-28	FP-28	FP-28	FP-28	FP-28	FP-28	FP-28	FP-28	FP-28	FP-28	FP-28	FP-28
SiO ₂	47.85	47.64	47.71	46.89	46.24	48.75	49.36	49.83	48.33	48.32	49.38	55.82

Al ₂ O ₃	8.68	8.47	8.73	9.73	10.07	7.48	7.17	6.87	8.23	8.16	7.49	2.03
TiO ₂	0.55	0.52	0.54	0.59	0.50	0.36	0.44	0.31	0.47	0.45	0.47	0.07
Cr ₂ O ₃	0.94	0.98	0.96	0.80	0.85	0.93	0.90	0.95	0.55	0.50	0.49	0.14
FeO	10.46	10.48	10.62	11.27	10.99	10.13	9.82	9.77	10.45	10.48	10.36	7.90
MnO	0.17	0.24	0.22	0.24	0.22	0.21	0.15	0.14	0.25	0.16	0.22	0.14
NiO	-	0.10	-	0.09	0.06	-	-	0.01	0.07	0.01	0.04	0.04
MgO	14.72	14.59	14.45	14.04	14.11	15.54	15.53	15.51	15.08	15.03	15.73	18.99
CaO	12.24	12.27	12.44	12.28	12.50	12.51	12.54	12.51	12.43	12.48	12.58	12.82
Na ₂ O	1.21	1.25	1.27	1.42	1.43	1.02	1.04	1.00	1.23	1.20	1.11	0.35
K ₂ O	0.62	0.62	0.64	0.72	0.77	0.46	0.39	0.41	0.56	0.55	0.50	0.08
Total	97.42	97.15	97.57	98.08	97.73	97.39	97.34	97.32	97.65	97.33	98.35	98.37
Si	6.95	6.95	6.93	6.81	6.74	7.06	7.13	7.19	7.00	7.01	7.08	7.80
Al	1.48	1.45	1.49	1.67	1.73	1.28	1.22	1.17	1.40	1.39	1.26	0.33
Ti	0.06	0.06	0.06	0.06	0.05	0.04	0.05	0.03	0.05	0.05	0.05	0.01
Cr	0.11	0.11	0.11	0.09	0.10	0.11	0.10	0.11	0.06	0.06	0.06	0.02
Fe ²⁺	1.27	1.28	1.29	1.37	1.34	1.23	1.18	1.18	1.26	1.27	1.24	0.92
Mn	0.02	0.03	0.03	0.03	0.03	0.03	0.02	0.02	0.03	0.02	0.03	0.02

Ni	-	0.01	-	0.01	0.01	-	-	-	0.01	-	-	-
Mg	3.18	3.17	3.13	3.04	3.07	3.35	3.34	3.33	3.25	3.25	3.36	3.95
Ca	1.90	1.92	1.94	1.91	1.95	1.94	1.94	1.93	1.93	1.94	1.93	1.92
Na	0.34	0.35	0.36	0.40	0.40	0.29	0.29	0.28	0.35	0.34	0.31	0.10
K	0.11	0.12	0.12	0.13	0.14	0.08	0.07	0.08	0.10	0.10	0.09	0.01
Total	15.43	15.45	15.45	15.52	15.56	15.40	15.35	15.32	15.44	15.43	15.41	15.08

Table 3-2 continued

No.	25	26	30	31	32	42	43	58	59	60	68	69	70
Sample	FP-28	FP-28	FP-28	FP-28	FP-28	FP-28	FP-28	FP-28	FP-28	FP-28	FP-28	FP-28	FP-28
SiO ₂	55.33	55.20	52.12	52.65	51.56	50.63	51.11	54.30	54.25	54.41	54.05	54.65	53.99
Al ₂ O ₃	2.17	2.02	5.32	4.72	5.90	6.28	6.19	3.06	2.89	2.70	2.91	2.78	2.90
TiO ₂	0.09	0.11	0.26	0.20	0.27	0.30	0.30	0.14	0.11	0.01	0.15	0.13	0.07
Cr ₂ O ₃	0.11	0.12	0.26	0.22	0.23	0.71	0.49	0.30	0.21	0.25	0.32	0.23	0.29
FeO	7.78	7.83	8.23	8.02	8.43	8.48	8.38	8.27	8.26	8.16	8.19	8.14	8.36
MnO	0.21	0.24	0.20	0.10	0.20	0.22	0.20	0.19	0.15	0.22	0.16	0.17	0.22
NiO	0.03	-	-	0.03	-	-	0.01	0.06	0.13	0.02	0.04	-	-

MgO	19.06	18.85	17.50	17.93	17.48	16.47	16.98	17.87	18.09	17.99	18.04	17.89	18.08
CaO	12.81	12.82	12.65	12.79	12.80	12.51	12.49	12.80	12.77	12.82	12.70	13.04	12.80
Na ₂ O	0.31	0.31	0.74	0.73	0.90	0.94	0.86	0.45	0.42	0.36	0.36	0.28	0.33
K ₂ O	0.10	0.09	0.25	0.28	0.30	0.33	0.31	0.16	0.15	0.13	0.12	0.15	0.14
Total	98.01	97.58	97.51	97.66	98.05	96.86	97.31	97.60	97.42	97.07	97.03	97.45	97.19
Si	7.76	7.78	7.41	7.46	7.31	7.28	7.30	7.68	7.69	7.73	7.69	7.73	7.68
Al	0.36	0.34	0.89	0.79	0.99	1.06	1.04	0.51	0.48	0.45	0.49	0.46	0.49
Ti	0.01	0.01	0.03	0.02	0.03	0.03	0.03	0.01	0.01	-	0.02	0.01	0.01
Cr	0.01	0.01	0.03	0.02	0.03	0.08	0.06	0.03	0.02	0.03	0.04	0.03	0.03
Fe ²⁺	0.91	0.92	0.98	0.95	1.00	1.02	1.00	0.98	0.98	0.97	0.97	0.96	0.99
Mn	0.03	0.03	0.02	0.01	0.02	0.03	0.02	0.02	0.02	0.03	0.02	0.02	0.03
Ni	-	-	-	-	-	-	-	0.01	0.02	-	-	-	-
Mg	3.98	3.96	3.70	3.79	3.69	3.53	3.61	3.77	3.82	3.81	3.82	3.77	3.83
Ca	1.93	1.93	1.92	1.94	1.94	1.93	1.91	1.94	1.94	1.95	1.93	1.98	1.95
Na	0.09	0.08	0.20	0.20	0.25	0.26	0.24	0.12	0.12	0.10	0.10	0.08	0.09
K	0.02	0.02	0.05	0.05	0.05	0.06	0.06	0.03	0.03	0.02	0.02	0.03	0.03
Total	15.09	15.08	15.23	15.24	15.31	15.28	15.27	15.11	15.12	15.09	15.10	15.06	15.12

Table 3-2 continued

No.	86	87	88	89	90	91	92	97	98	99	100	101	102
Sample	FP-24	FP-24	FP-24	FP-24	FP-24	FP-24	FP-24	FP-25	FP-25	FP-25	FP-25	FP-25	FP-25
SiO ₂	47.38	48.94	50.00	50.22	49.14	49.30	49.42	52.47	52.81	51.03	50.98	51.03	50.57
Al ₂ O ₃	8.51	7.51	6.56	6.59	6.53	6.88	6.85	3.70	3.93	4.91	5.56	5.50	5.52
TiO ₂	0.78	0.55	0.56	0.53	0.48	0.58	0.52	0.14	0.10	0.16	0.23	0.17	0.26
Cr ₂ O ₃	0.24	0.19	0.32	0.21	0.16	0.26	0.29	0.07	0.07	0.12	0.31	0.22	0.27
FeO	10.94	10.66	9.80	9.99	10.14	9.98	10.10	10.00	10.30	10.74	10.81	10.76	10.32
MnO	0.23	0.20	0.21	0.21	0.17	0.20	0.20	0.20	0.30	0.24	0.31	0.26	0.34
NiO	0.06	0.08	-	0.05	0.11	0.03	0.06	0.03	-	0.03	0.02	0.04	0.05
MgO	14.91	15.41	16.21	16.35	16.04	15.86	15.78	16.55	16.47	15.93	15.68	15.71	15.93
CaO	11.71	11.70	11.62	11.70	11.85	11.68	11.80	12.51	12.37	12.41	12.31	12.43	12.40
Na ₂ O	1.66	1.44	1.26	1.30	1.27	1.35	1.32	0.51	0.46	0.66	0.65	0.62	0.65
K ₂ O	0.30	0.23	0.18	0.18	0.21	0.22	0.23	0.19	0.18	0.26	0.30	0.27	0.26
Total	96.72	96.91	96.71	97.33	96.11	96.33	96.56	96.34	96.99	96.50	97.15	97.02	96.57
Si	6.93	7.11	7.23	7.22	7.18	7.17	7.18	7.59	7.59	7.42	7.37	7.38	7.34
Al	1.47	1.29	1.12	1.12	1.12	1.18	1.17	0.63	0.66	0.84	0.95	0.94	0.94

Ti	0.09	0.06	0.06	0.06	0.05	0.06	0.06	0.01	0.01	0.02	0.02	0.02	0.03
Cr	0.03	0.02	0.04	0.02	0.02	0.03	0.03	0.01	0.01	0.01	0.04	0.03	0.03
Fe ²⁺	1.34	1.29	1.18	1.20	1.24	1.21	1.23	1.21	1.24	1.31	1.31	1.30	1.25
Mn	0.03	0.02	0.03	0.03	0.02	0.02	0.02	0.02	0.04	0.03	0.04	0.03	0.04
Ni	0.01	0.01	-	0.01	0.01	-	0.01	-	-	-	-	-	0.01
Mg	3.25	3.33	3.49	3.50	3.49	3.44	3.42	3.57	3.53	3.45	3.38	3.38	3.45
Ca	1.83	1.82	1.80	1.80	1.85	1.82	1.84	1.94	1.90	1.93	1.90	1.92	1.93
Na	0.47	0.40	0.35	0.36	0.36	0.38	0.37	0.14	0.13	0.18	0.18	0.17	0.18
K	0.06	0.04	0.03	0.03	0.04	0.04	0.04	0.03	0.03	0.05	0.06	0.05	0.05
Total	15.50	15.40	15.33	15.35	15.39	15.37	15.37	15.16	15.14	15.25	15.24	15.23	15.26

Table 3-3 EMPA data of clinopyroxene.

No.	44	45	46	47	48	49	50	64	65	66	67	71	72	73
Sample	FP-28	FP-28	FP-28	FP-28	FP-28	FP-28	FP-28	FP-28	FP-28	FP-28	FP-28	FP-28	FP-28	FP-28
SiO ₂	53.94	54.02	54.52	54.42	54.55	53.27	53.71	54.56	54.37	54.29	54.39	53.24	53.42	53.31
Al ₂ O ₃	1.11	1.03	1.02	0.95	1.01	0.05	0.10	0.94	1.12	1.09	1.07	0.03	0.06	0.10
TiO ₂	-	-	0.02	-	0.05	-	0.05	0.02	0.02	-	0.02	-	0.04	-

Cr ₂ O ₃	0.16	0.09	0.16	0.16	0.20	0.37	0.09	0.07	0.08	0.05	0.10	0.26	0.22	0.12
FeO	6.13	5.84	5.77	5.86	5.64	9.13	9.25	5.67	5.79	5.88	5.93	9.44	9.68	9.53
MnO	0.17	0.22	0.26	0.21	0.22	0.56	0.31	0.24	0.18	0.24	0.21	0.46	0.32	0.29
NiO	0.01	0.01	-	0.03	0.07	0.08	0.03	0.02	-	-	0.06	-	0.06	0.03
MgO	14.13	14.52	14.77	14.52	14.49	12.06	12.23	14.60	14.30	14.30	14.53	11.84	12.01	12.08
CaO	23.54	23.68	23.70	23.82	23.85	24.51	24.53	23.82	23.73	23.30	23.91	24.28	24.22	24.39
Na ₂ O	0.66	0.72	0.75	0.63	0.62	0.21	0.14	0.54	0.62	0.69	0.69	0.20	0.16	0.15
K ₂ O	0.02	-	0.01	0.01	0.02	0.01	0.03	-	-	-	0.01	0.03	-	0.01
Total	99.85	100.12	100.98	100.62	100.73	100.24	100.47	100.48	100.19	99.84	100.91	99.76	100.18	100.00
Si	2.00	1.99	1.99	2.00	2.00	2.00	2.01	2.00	2.00	2.00	1.99	2.01	2.01	2.01
Al	0.05	0.04	0.04	0.04	0.04	-	-	0.04	0.05	0.05	0.05	-	-	-
Cr	-	-	-	-	0.01	0.01	-	-	-	-	-	0.01	0.01	-
Fe ²⁺	0.19	0.18	0.18	0.18	0.17	0.29	0.29	0.17	0.18	0.18	0.18	0.30	0.30	0.30
Mn	0.01	0.01	0.01	0.01	0.01	0.02	0.01	0.01	0.01	0.01	0.01	0.01	0.01	0.01
Mg	0.78	0.80	0.80	0.79	0.79	0.68	0.68	0.80	0.78	0.79	0.79	0.67	0.67	0.68
Ca	0.93	0.94	0.93	0.94	0.94	0.99	0.98	0.94	0.93	0.92	0.94	0.98	0.97	0.98
Na	0.05	0.05	0.05	0.04	0.04	0.02	0.01	0.04	0.04	0.05	0.05	0.01	0.01	0.01

Total	4.00	4.01	4.01	4.00	4.00	4.00	3.99	4.00	4.00	4.00	4.01	3.99	3.99	4.00
En	0.41	0.42	0.42	0.42	0.42	0.35	0.35	0.42	0.41	0.42	0.41	0.34	0.34	0.35
Wo	0.49	0.49	0.49	0.49	0.49	0.51	0.50	0.49	0.49	0.49	0.49	0.50	0.50	0.50
Fs	0.10	0.09	0.09	0.09	0.09	0.15	0.15	0.09	0.09	0.10	0.09	0.15	0.16	0.15

Table 3-3 EMPA data of chromite and plagioclase.

No.	1	2	3	4	5	6	7	8	4	5	13	14
Sample	FP-28	FP-28	FP-28	FP-28	FP-28	FP-28	FP-28	FP-28	FP-28	FP-28	FP-28	FP-28
Comment	Chr	Chr	Chr	Chr	Chr	Chr	Chr	Chr	Pl	Pl	Pl	Pl
SiO ₂	0.12	0.13	0.07	0.09	0.16	0.11	0.13	0.11	62.45	60.98	65.71	65.28
Al ₂ O ₃	6.30	6.09	5.71	5.55	5.55	5.49	3.85	3.96	23.55	24.25	21.71	22.03
TiO ₂	0.25	0.20	0.12	0.18	0.22	0.13	0.16	0.17	-	0.01	-	-
Cr ₂ O ₃	50.44	49.90	51.38	52.04	51.60	51.80	51.88	52.53	0.01	0.01	0.05	0.03
Fe ₂ O ₃	1.13	1.61	-	2.26	-	-	-	-	-	-	-	-
FeO	36.79	36.25	37.36	35.15	36.57	35.93	36.42	35.85	0.22	0.51	0.21	0.29
MnO	1.50	1.44	1.46	1.47	1.37	1.46	2.40	2.44	0.03	0.02	0.01	-
NiO	-	-	0.01	0.02	0.02	0.02	0.01	-	0.05	-	0.07	-

MgO	0.69	0.70	0.70	0.68	0.77	0.76	0.28	0.31	0.07	0.21	0.01	0.06
CaO	0.08	0.07	0.05	0.11	0.17	0.15	0.20	0.26	3.97	0.97	1.37	1.37
Na ₂ O	0.15	0.16	0.10	0.11	0.08	0.15	0.09	0.19	8.68	7.88	9.95	9.84
K ₂ O	0.01	0.02	0.01	-	-	0.01	0.01	0.01	0.87	3.15	0.94	1.12
ZnO	1.55	1.78	1.51	1.71	1.45	1.77	1.62	1.94	-	-	-	-
Total	98.99	98.35	98.47	99.36	97.96	97.77	97.04	97.73	99.89	97.98	100.01	100.01
Si	-	-	-	-	0.01	-	-	-	2.77	2.77	2.89	2.88
Al	0.28	0.27	0.25	0.24	0.25	0.25	0.18	0.18	1.23	1.30	1.13	1.14
Ti	0.01	0.01	-	0.01	0.01	-	-	-	-	-	-	-
Cr	1.49	1.48	1.53	1.53	1.54	1.55	1.59	1.60	-	-	-	-
Fe ³⁺	0.03	0.05	-	0.06	-	-	-	-	-	-	-	-
Fe ²⁺	1.15	1.14	1.18	1.09	1.16	1.14	1.18	1.15	0.01	0.02	0.01	0.01
Mn	0.05	0.05	0.05	0.05	0.04	0.05	0.08	0.08	-	-	-	-
Mg	0.04	0.04	0.04	0.04	0.04	0.04	0.02	0.02	-	0.01	-	-
Ca	-	-	-	-	0.01	0.01	0.01	0.01	0.19	0.05	0.06	0.06
Na	0.01	0.01	0.01	0.01	0.01	0.01	0.01	0.01	0.75	0.69	0.85	0.84
K	-	-	-	-	-	-	-	-	0.05	0.18	0.05	0.06

Zn	0.04	0.05	0.04	0.05	0.04	0.05	0.05	0.05	-	-	-	-
Total	3.10	3.10	3.11	3.08	3.10	3.10	3.11	3.11	5.01	5.02	5.00	5.00

Table 3-3 continued

No.	27	28	29	61	62	63	93	94	95	107	108	109
Sample	FP-28	FP-28	FP-28	FP-28	FP-28	FP-28	FP-24	FP-24	FP-24	FP-25	FP-25	FP-25
Comment	P1	P1	P1	P1	P1	P1	P1	P1	P1	P1	P1	P1
SiO ₂	63.18	63.27	63.42	62.21	62.10	62.77	63.05	62.81	62.49	59.76	59.15	59.27
Al ₂ O ₃	23.06	22.60	22.92	23.16	23.37	23.57	23.07	22.81	23.03	24.92	24.95	24.90
TiO ₂	-	0.04	-	0.02	-	-	-	0.05	-	0.04	-	-
Cr ₂ O ₃	-	0.03	0.02	-	-	-	-	-	0.01	-	0.03	-
FeO	0.06	0.12	0.08	0.14	0.13	0.12	0.14	0.18	0.14	0.25	0.27	0.21
MnO	-	-	0.02	-	0.02	0.02	0.01	0.03	0.01	0.03	0.03	-
NiO	-	-	-	-	0.02	-	-	-	-	-	0.03	-
MgO	0.02	0.02	-	-	0.02	0.03	-	0.04	0.04	-	-	0.06
CaO	4.05	4.09	4.08	4.48	4.62	4.66	4.13	4.20	4.18	6.18	6.30	6.25

Na ₂ O	9.43	9.37	9.28	8.97	8.75	8.92	8.92	9.18	9.03	7.70	7.69	7.88
K ₂ O	0.17	0.17	0.18	0.21	0.24	0.19	0.04	0.07	0.05	0.31	0.12	0.12
Total	99.97	99.71	100.01	99.19	99.28	100.29	99.36	99.36	98.97	99.18	98.55	98.67
Si	2.80	2.81	2.80	2.78	2.77	2.77	2.80	2.80	2.79	2.68	2.67	2.68
Al	1.20	1.18	1.19	1.22	1.23	1.23	1.21	1.20	1.21	1.32	1.33	1.32
Fe ²⁺	-	-	-	0.01	-	-	0.01	0.01	0.01	0.01	0.01	0.01
Ca	0.19	0.19	0.19	0.21	0.22	0.22	0.20	0.20	0.20	0.30	0.30	0.30
Na	0.81	0.81	0.80	0.78	0.76	0.76	0.77	0.79	0.78	0.67	0.67	0.69
K	0.01	0.01	0.01	0.01	0.01	0.01	-	-	-	0.02	0.01	0.01
Total	5.01	5.01	5.00	5.01	5.00	5.00	4.98	5.00	4.99	5.00	5.00	5.01

Table 3-4 EMPA data of biotite and titanite.

No.	33	34	35	80	81	82	83	84	85	6	112	113	114
Sample	FP-24	FP-24	FP-24	FP-24	FP-24	FP-24	FP-24	FP-24	FP-24	FP-25	FP-25	FP-25	FP-25
Comment	Bt	Bt	Bt	Bt	Bt	Bt	Bt	Bt	Bt	Ti	Ti	Ti	Ti
SiO ₂	37.40	37.27	37.47	37.71	37.46	37.85	37.49	36.61	37.00	30.49	30.50	30.87	30.61
Al ₂ O ₃	15.90	15.98	15.71	14.38	14.40	14.51	14.38	14.31	14.37	1.12	0.84	1.13	0.82

TiO ₂	1.74	1.59	1.62	2.45	2.24	2.37	2.44	2.06	2.13	37.18	38.32	37.12	38.45
Cr ₂ O ₃	0.93	0.83	0.99	0.38	0.30	0.31	0.29	0.29	0.25	0.53	0.02	0.03	-
FeO	11.35	11.62	11.65	12.60	12.23	12.29	12.46	12.06	11.93	0.46	0.20	0.49	0.28
MnO	0.16	0.12	0.16	0.10	0.08	0.04	0.13	0.11	0.13	0.05	0.07	0.02	0.03
NiO	0.09	0.10	0.06	0.11	0.08	0.13	0.04	0.10	0.11	-	-	-	0.05
MgO	16.51	16.60	16.79	16.58	16.48	16.57	16.69	16.95	16.54	0.01	0.02	0.18	-
CaO	0.11	0.10	0.09	-	0.01	0.01	0.01	0.10	0.08	28.33	28.19	28.07	27.94
Na ₂ O	0.17	0.18	0.21	0.58	0.54	0.56	0.49	0.48	0.50	0.04	0.04	0.04	-
K ₂ O	8.87	8.74	8.94	8.62	8.76	8.69	8.64	8.44	8.36	0.02	-	0.02	0.02
Total	93.26	93.13	93.68	93.51	92.59	93.31	93.05	91.51	91.39	98.23	98.21	97.96	98.20
Si	2.80	2.80	2.80	2.83	2.84	2.84	2.83	2.81	2.83	1.01	1.01	1.03	1.02
Al	1.40	1.41	1.38	1.27	1.29	1.28	1.28	1.29	1.30	0.04	0.03	0.04	0.03
Ti	0.10	0.09	0.09	0.14	0.13	0.13	0.14	0.12	0.12	0.93	0.96	0.93	0.96
Cr	0.05	0.05	0.06	0.02	0.02	0.02	0.02	0.02	0.02	0.01	-	-	-
Fe ²⁺	0.71	0.73	0.73	0.79	0.78	0.77	0.79	0.77	0.76	0.01	0.01	0.01	0.01
Mn	0.01	0.01	0.01	0.01	0.01	-	0.01	0.01	0.01	-	-	-	-
Ni	0.01	0.01	-	0.01	-	0.01	-	0.01	0.01	-	-	-	-

Mg	1.84	1.85	1.87	1.85	1.86	1.85	1.87	1.94	1.89	-	-	0.01	-
Ca	0.01	0.01	0.01	-	-	-	-	0.01	0.01	1.01	1.00	1.00	0.99
Na	0.03	0.03	0.03	0.08	0.08	0.08	0.07	0.07	0.07	-	-	-	-
K	0.85	0.84	0.85	0.83	0.85	0.83	0.83	0.83	0.82	-	-	-	-
Total	7.81	7.81	7.83	7.84	7.84	7.83	7.84	7.87	7.83	3.03	3.02	3.02	3.01

Table 3-5 Whole-rock major, trace and platinum-group elements (PGE) data.

Sample	FP-6-1	FP-7	FP-24	FP-25-2	FP-28	FP-29-1
Rock type	TTG gneiss	TTG gneiss	Hornblendite	Hornblendite	Pyroxene hornblendite	
Major elements (wt.%)						
SiO ₂	71.02	63.20	49.12	50.65	50.28	47.20
Al ₂ O ₃	15.17	16.80	6.81	5.66	7.10	7.32
CaO	2.96	3.57	11.74	12.71	12.36	14.00
Fe ₂ O ₃	0.10	1.79	3.23	3.32	0.68	2.76
FeO	2.05	2.95	6.95	7.42	8.28	8.75
K ₂ O	1.42	2.32	0.41	0.33	0.53	0.63
MgO	1.13	2.74	15.85	15.20	15.08	13.21

MnO	0.04	0.07	0.19	0.26	0.18	0.21
Na ₂ O	4.84	3.96	1.23	0.62	1.11	1.08
P ₂ O ₅	0.10	0.27	0.31	0.17	0.10	0.34
TiO ₂	0.28	0.65	0.71	0.48	0.49	0.78
CO ₂	0.75	0.33	0.43	0.09	0.34	0.43
H ₂ O+	0.38	0.68	0.66	0.66	0.72	0.88
LOI	0.33	0.88	1.74	1.52	1.50	1.82
Total	100.57	100.21	99.38	99.09	98.75	99.41
Mg#	49	52	74	72	75	68
Trace elements (ppm)						
Cr	10.5	42.6	1806	2477	4467	1512
Mn	285	502	1550	2128	1436	1758
Ni	10.2	29.4	342	170	248	112
Ga	19.5	22.0	11.9	11.4	10.5	13.2
Rb	66.0	111	17.7	4.8	17.0	13.5
Sr	245	412	160	217	145	148
Cs	2.13	1.65	1.57	0.09	0.42	0.12

Ba	222	766	129	150	146	78.4
Pb	9.06	11.0	3.35	3.86	13.1	2.74
Th	6.72	4.71	0.87	0.72	1.36	1.06
U	0.42	0.72	0.41	0.57	0.46	0.50
Nb	3.49	6.62	4.25	1.75	2.05	3.43
Ta	0.39	0.54	0.28	0.14	0.18	0.27
Zr	143	188	54.4	46.5	54.1	49.6
Hf	3.78	4.90	1.90	1.40	1.58	2.03
Ti	1772	4061	4262	2766	2843	4566
La	21.5	38.6	14.5	26.6	8.27	17.1
Ce	40.2	89.9	39.2	71.1	19.9	47.6
Pr	4.48	10.2	5.32	8.93	2.48	6.47
Nd	16.1	39.1	24.5	38.6	10.5	28.0
Sm	2.64	5.94	5.18	7.46	2.46	5.77
Eu	0.56	1.30	1.47	1.98	0.66	1.50
Gd	1.98	3.76	4.19	5.46	2.63	5.32
Tb	0.27	0.42	0.62	0.71	0.42	0.83

Dy	1.27	2.04	2.94	2.80	2.34	4.03
Ho	0.22	0.38	0.49	0.40	0.46	0.71
Er	0.59	0.94	1.34	1.12	1.33	2.05
Tm	0.08	0.13	0.18	0.11	0.20	0.26
Yb	0.50	0.82	1.15	0.74	1.23	1.65
Lu	0.08	0.12	0.16	0.10	0.17	0.24
Sc	4.19	8.09	38.4	47.0	49.4	64.6
Y	5.49	8.42	13.8	11.0	12.9	19.8
ΣREE	90.47	193.65	101.24	166.11	53.05	121.53
[La/Yb] _N	30.84	33.77	9.04	25.78	4.82	7.43
Platinum-group elements (ppb)						
Os			0.19	0.23	0.56	0.87
Ir			0.12	0.23	0.39	0.65
Ru			0.25	0.26	0.74	0.87
Rh			0.24	0.31	0.27	0.68
Pd			1.83	1.49	2.45	3.88
Pt			2.03	2.77	3.00	3.34

Table 3-6 Zircon U-Pb analytical data.

Sample	Element concentration (ppm)				Isotope ratios ($\pm 1\sigma$)						Age (Ma $\pm 1\sigma$)			Concordance (%)			
	Spots	Pb ^T	Th	U	Th/U	²⁰⁷ Pb/ ²⁰⁶ Pb	1 σ	²⁰⁷ Pb/ ²³⁵ U	1 σ	²⁰⁶ Pb/ ²³⁸ U	1 σ	²⁰⁷ Pb/ ²⁰⁶ Pb	1 σ		²⁰⁷ Pb/ ²³⁵ U	1 σ	²⁰⁶ Pb/ ²³⁸ U
FP-7																	
FP-7-01	49	73	70	1.04	0.1686	0.0042	11.1951	0.1802	0.4817	0.0056	2544	41	2540	15	2535	24	100
FP-7-02	161	169	269	0.63	0.1674	0.0041	11.0889	0.1640	0.4804	0.0052	2532	40	2531	14	2529	23	100
FP-7-03	85	122	123	0.99	0.1678	0.0040	11.1497	0.1517	0.4819	0.0050	2536	39	2536	13	2535	22	100
FP-7-04	142	156	224	0.70	0.1670	0.0038	10.9512	0.1282	0.4757	0.0044	2528	38	2519	11	2509	19	99
FP-7-05	76	142	142	1.00	0.1627	0.0041	9.4107	0.1558	0.4196	0.0048	2484	42	2379	15	2259	22	90
FP-7-06	96	191	132	1.45	0.1678	0.0039	11.0704	0.1422	0.4786	0.0047	2536	38	2529	12	2521	21	99
FP-7-07	95	127	140	0.91	0.1675	0.0039	11.1182	0.1378	0.4814	0.0047	2533	38	2533	12	2533	20	100
FP-7-08	88	138	125	1.10	0.1683	0.0040	11.1956	0.1483	0.4826	0.0049	2541	39	2540	12	2538	21	100
FP-7-09	242	246	462	0.53	0.1648	0.0040	10.7517	0.1561	0.4732	0.0051	2506	40	2502	13	2498	22	100
FP-7-10	109	157	214	0.74	0.1703	0.0046	11.1325	0.2188	0.4741	0.0064	2561	44	2534	18	2502	28	98
FP-7-11	66	81	102	0.79	0.1682	0.0041	11.1825	0.1635	0.4824	0.0052	2539	40	2539	14	2538	23	100
FP-7-12	68	82	99	0.82	0.1684	0.0041	11.2059	0.1617	0.4827	0.0052	2542	40	2540	13	2539	22	100

FP-7-13	124	213	173	1.23	0.1668	0.0038	11.0225	0.1343	0.4793	0.0046	2526	38	2525	11	2524	20	100
FP-7-14	71	83	105	0.79	0.1697	0.0041	11.3482	0.1721	0.4852	0.0054	2554	40	2552	14	2550	23	100
FP-7-15	64	83	94	0.89	0.1660	0.0040	10.9292	0.1511	0.4777	0.0049	2517	39	2517	13	2517	22	100
FP-7-16	86	114	125	0.91	0.1676	0.0039	11.1107	0.1389	0.4808	0.0047	2534	38	2533	12	2531	20	100
FP-7-17	137	251	230	1.09	0.1637	0.0042	10.2380	0.1739	0.4537	0.0054	2494	42	2457	16	2412	24	97
FP-7-18	178	352	298	1.18	0.1634	0.0043	9.9607	0.1771	0.4422	0.0054	2491	43	2431	16	2361	24	94
FP-7-19	75	103	109	0.95	0.1678	0.0040	11.1468	0.1501	0.4818	0.0049	2536	39	2536	13	2535	21	100
FP-7-20	127	412	332	1.24	0.1662	0.0047	10.4179	0.2255	0.4546	0.0066	2520	47	2473	20	2416	29	96
FP-7-21	138	206	283	0.73	0.1638	0.0041	9.9558	0.1624	0.4408	0.0051	2496	42	2431	15	2354	23	94
FP-7-22	56	83	81	1.03	0.1658	0.0040	10.8583	0.1525	0.4752	0.0049	2515	40	2511	13	2506	22	100
FP-7-23	80	47	140	0.34	0.1636	0.0043	10.6376	0.1910	0.4716	0.0059	2494	43	2492	17	2490	26	100
FP-7-24	81	87	121	0.72	0.1689	0.0039	11.2519	0.1451	0.4833	0.0048	2546	39	2544	12	2542	21	100
FP-7-25	122	119	194	0.61	0.1684	0.0039	11.2032	0.1358	0.4825	0.0046	2542	38	2540	11	2538	20	100
FP-7-26	82	72	133	0.54	0.1677	0.0039	10.8103	0.1418	0.4676	0.0046	2535	39	2507	12	2473	20	97
FP-7-27	293	458	478	0.96	0.1645	0.0037	10.1652	0.1085	0.4481	0.0039	2503	37	2450	10	2387	17	95
FP-7-28	103	202	157	1.29	0.1722	0.0044	11.5370	0.2007	0.4859	0.0060	2580	42	2568	16	2553	26	99
FP-7-29	98	136	150	0.91	0.1704	0.0043	11.4347	0.1904	0.4868	0.0058	2562	42	2559	16	2557	25	100

FP-7-30	106	168	158	1.07	0.1642	0.0040	10.6849	0.1554	0.4721	0.0050	2499	40	2496	14	2493	22	100
FP-7-31	149	259	260	1.00	0.1688	0.0039	9.6075	0.1173	0.4128	0.0039	2546	38	2398	11	2228	18	86
FP-7-32	71	74	105	0.71	0.1669	0.0039	11.0294	0.1472	0.4793	0.0048	2527	39	2526	12	2524	21	100
FP-7-33	76	77	115	0.67	0.1687	0.0041	11.0418	0.1657	0.4748	0.0052	2545	40	2527	14	2505	23	98
FP-7-34	164	310	271	1.14	0.1664	0.0038	9.7333	0.1131	0.4243	0.0039	2522	38	2410	11	2280	18	89
FP-7-35	92	108	129	0.84	0.1683	0.0039	11.1721	0.1373	0.4815	0.0046	2541	38	2538	11	2534	20	100
FP-7-36	109	133	153	0.87	0.1735	0.0040	11.8314	0.1513	0.4947	0.0049	2591	38	2591	12	2591	21	100
FP-7-37	42	64	59	1.09	0.1667	0.0043	10.9888	0.1910	0.4783	0.0058	2524	43	2522	16	2520	25	100
FP-7-38	181	346	303	1.14	0.1676	0.0039	9.8660	0.1267	0.4270	0.0041	2534	39	2422	12	2292	19	89
FP-7-39	290	197	460	0.43	0.1727	0.0039	11.7291	0.1237	0.4927	0.0043	2584	37	2583	10	2583	18	100
FP-7-40	356	376	796	0.47	0.1592	0.0041	9.4758	0.1628	0.4318	0.0051	2447	43	2385	16	2314	23	94
FP-29-1																	
FP-29-1-01	46	29	83	0.35	0.1680	0.0043	10.4794	0.1806	0.4524	0.0055	2538	43	2478	16	2406	24	95
FP-29-1-02	135	96	243	0.40	0.1641	0.0038	10.3827	0.1306	0.4589	0.0045	2498	39	2470	12	2435	20	97
FP-29-1-04	82	46	144	0.32	0.1695	0.0046	10.8935	0.2097	0.4661	0.0062	2553	44	2514	18	2466	27	96
FP-29-1-06	98	64	173	0.37	0.1675	0.0042	10.9526	0.1776	0.4743	0.0055	2533	42	2519	15	2502	24	99
FP-29-1-08	102	81	172	0.47	0.1640	0.0039	10.6976	0.1514	0.4730	0.0050	2497	40	2497	13	2497	22	100

FP-29-1-09	166	152	310	0.49	0.1621	0.0041	10.1117	0.1692	0.4524	0.0053	2478	42	2445	15	2406	24	97
FP-29-1-11	89	55	160	0.35	0.1654	0.0044	10.7306	0.1991	0.4705	0.0060	2512	44	2500	17	2486	26	99
FP-29-1-12	214	160	412	0.39	0.1678	0.0039	10.7144	0.1392	0.4631	0.0046	2536	39	2499	12	2453	20	97
FP-29-1-13	52	38	88	0.43	0.1691	0.0044	11.1842	0.2037	0.4797	0.0061	2549	43	2539	17	2526	27	99
FP-29-1-14	118	75	196	0.38	0.1678	0.0038	11.1430	0.1308	0.4817	0.0045	2535	38	2535	11	2535	20	100
FP-29-1-15	189	156	329	0.47	0.1669	0.0038	10.9944	0.1259	0.4777	0.0044	2527	38	2523	11	2517	19	100
FP-29-1-16	86	56	143	0.39	0.1691	0.0039	11.1469	0.1403	0.4780	0.0047	2549	38	2536	12	2519	20	99
FP-29-1-18	88	52	144	0.36	0.1693	0.0039	11.2847	0.1425	0.4834	0.0048	2551	38	2547	12	2542	21	100
FP-29-1-20	85	46	141	0.33	0.1672	0.0039	11.0646	0.1406	0.4800	0.0047	2530	38	2529	12	2527	21	100
FP-29-1-21	72	45	118	0.38	0.1675	0.0039	11.0828	0.1460	0.4798	0.0048	2533	39	2530	12	2526	21	100
FP-29-1-22	170	111	276	0.40	0.1670	0.0038	11.0429	0.1259	0.4796	0.0044	2528	37	2527	11	2525	19	100
FP-29-1-23	185	172	349	0.49	0.1639	0.0039	10.4534	0.1507	0.4626	0.0049	2496	40	2476	13	2451	22	98
FP-29-1-24	135	73	224	0.32	0.1673	0.0038	11.0745	0.1282	0.4802	0.0045	2530	37	2529	11	2528	20	100
FP-29-1-25	71	45	116	0.39	0.1686	0.0039	11.2287	0.1492	0.4831	0.0049	2544	39	2542	12	2541	21	100
FP-29-1-26	87	20	163	0.12	0.1657	0.0042	10.8454	0.1816	0.4747	0.0056	2515	42	2510	16	2504	25	100
FP-29-1-27	166	132	276	0.48	0.1661	0.0038	10.9013	0.1280	0.4760	0.0045	2519	38	2515	11	2510	20	100
FP-29-1-28	107	66	184	0.36	0.1639	0.0038	10.6466	0.1335	0.4711	0.0046	2496	38	2493	12	2489	20	100

FP-29-1-29	137	136	218	0.62	0.1685	0.0038	11.1355	0.1355	0.4792	0.0046	2543	38	2535	11	2524	20	99
FP-29-1-30	111	61	184	0.33	0.1669	0.0038	11.0338	0.1346	0.4793	0.0046	2527	38	2526	11	2524	20	100

Table 3-7 LA-MC-ICP-MS Lu-Hf isotopic data.

Sample No.	Age (Ma)	$^{176}\text{Yb}/^{177}\text{Hf}$	$^{176}\text{Lu}/^{177}\text{Hf}$	$^{176}\text{Hf}/^{177}\text{Hf}$	2s	$^{176}\text{Hf}/^{177}\text{Hf}_i$	$\epsilon_{\text{Hf}}(0)$	$\epsilon_{\text{Hf}}(t)$	$T_{\text{DM}}(\text{Ma})$	$T_{\text{DM}}^{\text{C}}(\text{Ma})$	$f_{\text{Lu/Hf}}$
FP-7 TTG gneiss											
FP-7-04	2513	0.017799	0.000730	0.281221	0.000011	0.281186	-54.9	0.2	2813	2996	-0.98
FP-7-09	2513	0.044475	0.001469	0.281388	0.000012	0.281318	-48.9	4.9	2637	2709	-0.96
FP-7-11	2513	0.021876	0.000806	0.281215	0.000013	0.281176	-55.1	-0.1	2827	3017	-0.98
FP-7-18	2513	0.022935	0.000823	0.281267	0.000011	0.281228	-53.2	1.7	2757	2905	-0.98
FP-7-25	2513	0.016277	0.000655	0.281161	0.000010	0.281129	-57.0	-1.8	2888	3119	-0.98
FP-7-27	2513	0.024077	0.000889	0.281310	0.000012	0.281267	-51.7	3.1	2704	2820	-0.97
FP-7-33	2513	0.024173	0.000871	0.281258	0.000012	0.281216	-53.5	1.3	2773	2930	-0.97
FP-7-39	2513	0.038033	0.001237	0.281307	0.000013	0.281248	-51.8	2.4	2732	2861	-0.96
FP-29-1											
Pyroxene hornblende											
FP-29-1-01	2514	0.009589	0.000377	0.281362	0.000013	0.281343	-49.9	5.9	2599	2652	-0.99

FP-29-1-04	2514	0.008602	0.000345	0.281382	0.000014	0.281365	-49.2	6.7	2570	2604	-0.99
FP-29-1-07	2514	0.018615	0.000702	0.281322	0.000014	0.281288	-51.3	3.9	2675	2773	-0.98
FP-29-1-18	2514	0.009537	0.000395	0.281352	0.000013	0.281333	-50.2	5.5	2613	2674	-0.99
FP-29-1-19	2514	0.008998	0.000353	0.281340	0.000012	0.281323	-50.6	5.1	2627	2697	-0.99
FP-29-1-22	2514	0.014055	0.000593	0.281320	0.000012	0.281291	-51.4	4.0	2670	2766	-0.98
FP-29-1-25	2514	0.011042	0.000469	0.281274	0.000015	0.281252	-53.0	2.6	2723	2852	-0.99
FP-29-1-30	2514	0.010993	0.000484	0.281292	0.000015	0.281269	-52.3	3.2	2699	2814	-0.99

Table 3-8 Zircon oxygen isotopic data.

Sample No.	$^{16}\text{O}/^{18}\text{O}$	$\delta^{18}\text{O}$ (‰)	2s (‰)	Sample No.	$^{16}\text{O}/^{18}\text{O}$	$\delta^{18}\text{O}$ (‰)	2s (‰)
FP-7 TTG gneiss				FP-29-1 Pyroxene hornblendite			
FP-7@1	0.002017	6.7	0.3	FP-29-1@1	0.002015	6.4	0.2
FP-7@2	0.002017	6.4	0.3	FP-29-1@2	0.002017	6.9	0.2
FP-7@3	0.002017	6.6	0.2	FP-29-1@3	0.002015	6.2	0.2
FP-7@4	0.002016	6.3	0.3	FP-29-1@4	0.002015	6.3	0.2
FP-7@5	0.002017	6.3	0.2	FP-29-1@5	0.002015	6.0	0.2
FP-7@6	0.002017	6.6	0.2	FP-29-1@6	0.002016	6.7	0.1

FP-7@7	0.002016	5.8	0.3	FP-29-1@7	0.002016	6.4	0.4
FP-7@8	0.002016	6.0	0.3	FP-29-1@8	0.002015	6.2	0.3
FP-7@9	0.002012	4.1	0.3	FP-29-1@9	0.00201	3.8	0.3
FP-7@10	0.002017	6.4	0.3	FP-29-1@10	0.002017	7.0	0.2
FP-7@11	0.002016	6.0	0.3	FP-29-1@1	0.002015	6.4	0.2
FP-7@12	0.002017	6.5	0.3				

Table 4-1 Details of samples from the Fuping Complex used for this study

Sample No.	Location	Coordinate	Rock type	Mineral assemblage
FP-1-1	Hujiazui	N 38 °20'55"; E 114 °01'44"	Gneissic granite	Pl + Qtz + Kfs + Bt + Rt + Mag
FP-1-2	Hujiazui	N 38 °20'55"; E 114 °01'44"	Amphibolite	Hbl + Pl + Qtz + Spn
FP-2-1	Hanzhuang	N 38 °21'33"; E 114 °01'55"	Amphibolite	Hbl + Pl + Qtz + Spn
FP-2-2	Hanzhuang	N 38 °21'33"; E 114 °01'55"	Gneissic granite	Pl + Qtz + Kfs + Bt + Rt + Mag
FP-3	Lijiazhuang	N 38 °22'48"; E 114 °00'44"	Gneissic syenogranite	Kfs + Qtz + Pl + Bt + Mag
FP-6-2	Xiaozishi	N 38 °26'08"; E 113 °40'57"	Amphibolite	Hbl + Pl + Qtz + Spn
FP-8	Kuanhuiwan	N 38 °28'18"; E 113 °39'40"	Epidote biotite schist	Pl + Qtz + Bt + Ep + Ms
FP-9-2	Gudu	N 38 °31'20"; E 113 °41'01"	Amphibolite	Hbl + Pl + Qtz + Spn

FP-14-1	Nanping	N 38 °32'52"; E 113°55'06"	Amphibolite	Hbl + Pl + Qtz + Spn
FP-15	Liujiawan	N 38 °32'38"; E 113 °55'12"	Amphibolite	Hbl + Pl + Qtz + Spn
FP-16	Liumouyuan	N 38 °33'35"; E 113 °54'49"	Amphibolite	Hbl + Pl + Qtz + Spn
FP-17	Huoshaocheng	N 38 °34'27"; E 113 °54'55"	Amphibolite	Hbl + Pl + Qtz + Spn
FP-18	Xialiu	N 38 °25'09"; E 113 °49'47"	Mica-schist	Pl + Qtz + Bt + Ms
FP-23	Huangjiagou	N 38 °32'55"; E 113 °47'08"	Amphibolite	Hbl + Pl + Qtz + Spn
FP-30-1	Guyue	N 38 °16'58"; E 113 °53'36"	Amphibolite	Hbl + Pl + Qtz + Rt + Spn
FP-30-2	Guyue	N 38 °16'58"; E 113 °53'36"	Gneissic granite	Kfs + Pl + Qtz + Bt + Mag
FP-34-1	Fulinggou	N 38 °21'48"; E 113 °56'04"	Amphibolite	Hbl + Pl + Qtz + Rt + Spn
FP-34-2	Fulinggou	N 38 °21'48"; E 113 °56'04"	Gneissic granite	Kfs + Pl + Qtz + Bt + Mag

Mineral abbreviations: Hbl-hornblende; Pl-plagioclase; Kfs-K-feldspar; Qtz-quartz; Bt-biotite; Ms-muscovite; Mag-magnetite; Spn-sphene; Ep-epidote.

Table 4-2 Major, trace and rare earth element concentrations of the whole-rock samples from the Fuping Complex

Sample No.	FP-1	FP-2	FP-3	FP-30	FP-33	FP-1	FP-2	FP-6	FP-30	FP-33	FP-9	FP-23	FP-14	FP-15	FP-16	FP-17
	-1	-2		-2	-2	-2	-1	-2	-1	-1	-2		-1			
Rock type	Granite		Syeno- granite	Granite			Amphibolite									
Major elements (wt.%)																
SiO ₂	77.18	76.70	72.53	77.67	74.29	51.48	50.29	49.56	49.96	48.84	49.61	48.27	48.68	47.10	48.69	48.88
Al ₂ O ₃	11.81	12.60	12.71	11.08	11.72	15.37	14.17	13.52	13.41	13.83	13.12	15.31	15.06	15.90	16.35	13.52
CaO	0.28	0.30	0.82	0.36	0.15	8.48	8.86	9.60	8.83	6.57	9.58	9.02	9.50	9.80	10.58	10.72
Fe ₂ O ₃	1.03	0.25	2.10	1.44	2.08	3.45	3.75	4.90	4.02	8.94	3.42	2.47	3.57	3.11	2.93	2.64
FeO	0.32	0.43	1.26	0.56	0.74	6.29	8.98	8.15	9.50	6.77	10.53	8.68	6.88	7.13	6.05	5.48
K ₂ O	5.09	5.13	5.33	5.28	9.22	1.07	1.33	1.12	1.08	0.35	0.97	1.70	1.54	1.76	0.90	0.87
MgO	0.10	0.20	0.23	0.07	0.09	7.10	6.66	7.12	6.07	4.47	6.54	7.14	7.58	8.16	7.03	12.06
MnO	0.01	0.01	0.04	0.01	0.01	0.13	0.18	0.25	0.22	0.17	0.23	0.17	0.16	0.15	0.14	0.13
Na ₂ O	3.20	3.35	3.60	2.50	0.64	3.70	2.52	3.18	2.31	4.93	2.93	3.15	3.17	2.71	3.33	2.44
P ₂ O ₅	0.01	0.01	0.03	0.01	0.04	0.17	0.14	0.08	0.15	0.72	0.11	0.26	0.17	0.20	0.16	0.03
TiO ₂	0.15	0.07	0.28	0.24	0.36	0.85	0.97	0.95	1.21	2.32	1.00	1.15	0.90	0.90	0.79	0.50

CO ₂	0.17	0.58	0.17	0.17	0.26	0.17	0.17	0.33	1.11	0.17	0.33	0.26	0.69	0.26	0.26	0.69
H ₂ O+	0.52	0.64	0.38	0.36	0.18	1.10	1.30	0.58	1.64	0.52	0.96	1.12	1.02	1.68	1.64	1.02
LOI	0.38	0.63	0.43	0.39	0.32	0.91	1.16	0.43	1.57	0.58	0.59	1.20	0.86	1.54	1.78	1.42
Total	100.25	100.90	99.91	100.14	100.10	100.27	100.48	99.77	101.08	99.18	99.92	99.90	99.78	100.40	100.63	100.40
A/CNK	1.05	1.08	0.96	1.06	1.03											
Mg#	12.62	35.47	11.62	6.36	5.84	57.63	49.25	50.51	45.44	35.20	46.38	54.10	57.48	59.67	59.30	73.43
Trace elements (ppm)																
Rb	137	184	191	241	402	42.2	60.8	9.10	39.0	13.1	14.6	44.0	34.5	50.5	22.3	16.4
Sr	49.3	68.2	69.4	16.1	13.1	364	191	155	159	174	168	422	440	474	427	378
Mo	0.15	1.86	0.24	0.76	0.21	0.79	0.29	0.31	0.21	0.39	0.32	0.31	0.24	0.16	0.21	0.13
Cs	0.48	1.33	0.70	1.21	0.85	0.28	0.27	0.16	0.22	0.11	0.15	0.45	0.32	0.31	0.32	0.24
Ba	424	435	956	150	976	278	239	85.4	152	49.8	151	1620	364	397	256	183
Pb	6.64	12.3	18.2	18.2	8.10	3.18	6.52	5.38	3.12	20.8	4.59	3.31	9.62	4.17	3.41	4.51
Th	22.2	11.5	18.7	21.6	15.2	0.55	1.56	0.35	0.89	2.29	0.56	1.01	0.70	0.75	0.55	0.56
U	2.40	0.97	3.12	2.29	2.02	0.10	0.44	0.24	2.74	0.40	0.38	0.18	0.12	0.23	0.12	0.46
Nb	41.9	5.25	18.4	17.9	19.8	3.72	3.36	2.47	3.65	6.64	3.41	5.28	3.55	4.08	3.37	2.80
Ta	3.35	0.45	1.28	1.27	1.25	0.22	0.26	0.18	0.27	0.47	0.25	0.34	0.22	0.28	0.21	0.19

Zr	342	115	515	800	738	89.2	79.4	46.1	77.3	140	60.8	106	75.1	78.7	64.1	50.6
Hf	13.2	4.94	13.9	15.8	13.7	2.43	2.31	1.42	2.42	4.02	1.80	2.96	2.23	2.28	1.85	1.48
Sn	3.08	0.65	3.61	3.44	3.48	0.92	0.87	0.56	0.95	1.51	1.00	1.09	0.95	0.91	0.79	0.87
Ti	931	426	1745	963	2117	5301	6113	5892	6897	14231	6211	6607	5492	5381	4702	2911
V	3.88	4.92	2.77	3.73	12.5	223	243	277	474	486	293	369	364	314	305	192
La	56.2	16.9	84.2	45.2	42.2	10.4	9.84	5.21	13.1	19.9	8.19	23.3	15.2	17.2	13.2	8.99
Ce	112	43.0	170	240	167	27.0	21.3	10.6	25.8	58.0	16.7	54.6	36.2	42.7	32.2	22.4
Pr	13.1	3.98	20.5	10.2	10.7	4.00	3.09	1.71	3.86	7.26	2.61	7.05	4.71	5.39	4.20	2.87
Nd	52.1	14.2	78.9	11.5	21.0	19.2	14.4	8.6	16.5	33.8	12.6	30.7	20.4	23.3	18.7	12.0
Sm	12.2	2.34	13.20	5.82	7.30	4.22	3.53	2.58	3.81	7.68	3.28	6.73	4.35	4.77	3.84	2.54
Eu	0.50	0.36	1.68	0.25	0.66	1.31	1.12	0.93	1.12	2.52	1.14	1.75	1.28	1.36	1.21	0.75
Gd	13.3	1.63	10.30	4.23	5.19	4.07	4.07	3.17	4.57	8.12	4.31	5.35	4.23	4.19	3.57	2.12
Tb	2.45	0.23	1.57	0.90	1.05	0.59	0.67	0.56	0.80	1.32	0.72	0.85	0.69	0.69	0.58	0.36
Dy	15.8	1.13	9.11	5.05	5.47	3.45	4.21	3.65	4.83	7.12	4.64	4.56	3.84	3.57	3.16	1.91
Ho	3.39	0.21	1.87	1.02	1.07	0.71	0.92	0.80	0.97	1.42	1.05	0.85	0.72	0.68	0.57	0.37
Er	9.12	0.59	5.24	3.26	3.16	1.93	2.49	2.25	3.03	4.36	2.89	2.53	2.21	2.07	1.80	1.19
Tm	1.47	0.10	0.84	0.47	0.47	0.30	0.40	0.36	0.42	0.55	0.45	0.34	0.28	0.26	0.23	0.15

Yb	8.98	0.68	5.41	3.16	3.27	1.82	2.49	2.33	2.91	3.67	2.93	2.17	1.88	1.67	1.63	1.09
Lu	1.23	0.12	0.82	0.44	0.49	0.27	0.37	0.36	0.43	0.55	0.44	0.31	0.28	0.27	0.24	0.17
Sc	1.17	1.22	3.46	1.56	2.84	34.1	46.0	50.5	48.6	43.9	52.6	34.5	38.2	27.2	29.7	15.7
Y	69.2	4.8	43.1	25.8	27.8	16.9	21.2	19.4	27.9	39.9	24.5	24.4	21.0	19.3	17.2	10.9
(La/Yb) _N	4.90	15.09	11.00	11.01	9.23	4.13	2.85	1.55	3.27	3.88	1.99	8.06	5.82	6.83	5.89	5.67
δEu	0.12	0.53	0.42	0.15	0.31	0.95	0.90	0.99	0.82	0.97	0.93	0.86	0.90	0.91	0.98	0.96

Table 4-3 Zircon U-Pb analytical data.

Sample	Element concentration(ppm)				Isotope ratios($\pm 1\sigma$)						Age(Ma $\pm 1\sigma$)			Concordance (%)			
	Spots	Pb _T	Th	U	Th/U	²⁰⁷ Pb/ ²⁰⁶ Pb	²⁰⁷ Pb/ ²³⁵ U	²⁰⁶ Pb/ ²³⁸ U	²⁰⁷ Pb/ ²⁰⁶ Pb	²⁰⁷ Pb/ ²³⁵ U	²⁰⁶ Pb/ ²³⁸ U						
FP-1-1																	
FP-1-1-01	18	27	35	0.77	0.1254	0.0037	6.4140	0.1432	0.3713	0.0049	2034	51	2034	20	2035	23	100
FP-1-1-05	58	79	124	0.64	0.1259	0.0031	6.4271	0.0940	0.3704	0.0037	2041	42	2036	13	2031	17	100
FP-1-1-06	253	668	561	1.19	0.1261	0.0028	6.3481	0.0691	0.3652	0.0032	2045	39	2025	10	2007	15	98
FP-1-1-07	185	488	475	1.03	0.1253	0.0031	5.6048	0.0856	0.3246	0.0033	2033	43	1917	13	1812	16	88
FP-1-1-08	171	126	480	0.26	0.1133	0.0028	4.1899	0.0621	0.2683	0.0026	1853	44	1672	12	1532	13	79

FP-1-1-09	92	179	173	1.04	0.1274	0.0030	6.5166	0.0836	0.3712	0.0035	2062	41	2048	11	2035	16	99
FP-1-1-10	150	595	477	1.25	0.1290	0.0040	6.5197	0.1604	0.3667	0.0053	2084	53	2049	22	2014	25	97
FP-1-1-12	156	54	383	0.14	0.1142	0.0027	4.5439	0.0579	0.2887	0.0026	1867	42	1739	11	1635	13	86
FP-1-1-15	101	154	199	0.77	0.1271	0.0030	6.5723	0.0834	0.3749	0.0035	2059	41	2056	11	2053	16	100
FP-1-1-16	147	455	393	1.16	0.1267	0.0034	5.6384	0.1061	0.3226	0.0037	2053	47	1922	16	1803	18	86
FP-1-1-18	236	548	493	1.11	0.1273	0.0030	6.3840	0.0843	0.3638	0.0035	2060	41	2030	12	2000	16	97
FP-1-1-19	114	114	288	0.40	0.1182	0.0032	5.4233	0.1007	0.3326	0.0038	1930	47	1889	16	1851	18	96
FP-1-1-20	153	373	420	0.89	0.1268	0.0034	5.9303	0.1060	0.3391	0.0038	2054	46	1966	16	1882	18	91
FP-1-1-21	147	225	245	0.92	0.1263	0.0031	6.4794	0.0983	0.3721	0.0038	2047	43	2043	13	2039	18	100
FP-1-1-22	57	29	183	0.16	0.1181	0.0031	5.5367	0.0939	0.3401	0.0037	1927	46	1906	15	1887	18	98
FP-1-1-23	83	131	155	0.84	0.1287	0.0031	6.7429	0.0894	0.3800	0.0036	2080	41	2078	12	2077	17	100
FP-1-1-24	152	180	471	0.38	0.1261	0.0034	5.1666	0.0948	0.2971	0.0033	2044	47	1847	16	1677	17	78
FP-1-1-26	60	70	128	0.55	0.1259	0.0033	6.4648	0.1092	0.3723	0.0041	2041	45	2041	15	2040	19	100
FP-1-1-27	33	45	62	0.73	0.1269	0.0042	6.5742	0.1784	0.3754	0.0058	2056	57	2056	24	2055	27	100
FP-1-1-28	211	386	428	0.90	0.1242	0.0032	6.2631	0.1017	0.3656	0.0039	2017	44	2013	14	2009	18	100
FP-1-1-29	45	98	82	1.19	0.1258	0.0035	6.4577	0.1305	0.3720	0.0046	2040	49	2040	18	2039	21	100
FP-1-1-30	161	347	340	1.02	0.1262	0.0030	6.3361	0.0827	0.3638	0.0034	2046	41	2024	11	2000	16	98

FP-3

FP-3-01	107	161	210	0.77	0.1274	0.0031	6.5248	0.0909	0.3713	0.0036	2063	42	2049	12	2035	17	99
FP-3-02	51	80	102	0.78	0.1287	0.0034	6.5436	0.1141	0.3686	0.0041	2080	45	2052	15	2023	19	97
FP-3-03	53	85	101	0.84	0.1277	0.0032	6.6369	0.1059	0.3768	0.0039	2067	44	2064	14	2061	18	100
FP-3-04	47	75	95	0.79	0.1262	0.0034	6.3564	0.1149	0.3653	0.0041	2045	46	2026	16	2007	20	98
FP-3-05	36	41	78	0.53	0.1269	0.0034	6.0790	0.1152	0.3473	0.0040	2056	47	1987	17	1922	19	93
FP-3-06	138	90	327	0.27	0.1286	0.0030	6.1368	0.0715	0.3460	0.0030	2079	40	1996	10	1916	15	91
FP-3-07	56	86	110	0.79	0.1287	0.0038	6.6675	0.1496	0.3758	0.0050	2080	51	2068	20	2056	24	99
FP-3-08	54	83	108	0.77	0.1286	0.0034	6.5666	0.1134	0.3702	0.0041	2079	45	2055	15	2030	19	98
FP-3-09	40	59	80	0.74	0.1275	0.0033	6.4456	0.1119	0.3666	0.0040	2064	45	2039	15	2014	19	98
FP-3-10	36	38	74	0.51	0.1300	0.0034	6.8646	0.1223	0.3830	0.0043	2097	46	2094	16	2090	20	100
FP-3-11	33	42	65	0.65	0.1300	0.0035	6.8289	0.1252	0.3810	0.0044	2098	46	2090	16	2081	21	99
FP-3-12	33	38	70	0.55	0.1297	0.0035	6.4814	0.1206	0.3624	0.0042	2094	46	2043	16	1994	20	95
FP-3-13	38	48	81	0.60	0.1289	0.0035	6.5431	0.1237	0.3681	0.0043	2083	47	2052	17	2021	20	97
FP-3-14	33	41	68	0.60	0.1285	0.0035	6.7071	0.1260	0.3786	0.0044	2077	47	2074	17	2070	21	100
FP-3-15	87	88	212	0.41	0.1250	0.0032	6.0487	0.0979	0.3510	0.0037	2028	44	1983	14	1940	18	95
FP-3-16	42	52	84	0.61	0.1316	0.0040	7.0600	0.1654	0.3890	0.0055	2120	52	2119	21	2118	25	100

FP-3-17	39	53	79	0.66	0.1317	0.0034	6.6734	0.1164	0.3675	0.0041	2121	45	2069	15	2018	19	95
FP-3-18	50	91	124	0.73	0.1283	0.0032	5.3375	0.0798	0.3018	0.0030	2075	43	1875	13	1700	15	78
FP-3-19	43	46	95	0.49	0.1274	0.0033	6.2325	0.1079	0.3548	0.0039	2063	45	2009	15	1957	18	95
FP-3-20	44	72	86	0.83	0.1296	0.0034	6.7713	0.1226	0.3789	0.0043	2093	46	2082	16	2071	20	99
FP-3-21	49	75	126	0.60	0.1283	0.0035	6.4385	0.1252	0.3641	0.0044	2074	47	2038	17	2002	21	96
FP-3-22	45	70	85	0.82	0.1281	0.0035	6.6491	0.1282	0.3766	0.0045	2072	47	2066	17	2061	21	99
FP-3-23	42	62	85	0.73	0.1299	0.0036	6.8559	0.1334	0.3828	0.0046	2097	47	2093	17	2089	21	100
FP-3-24	33	43	66	0.65	0.1311	0.0035	7.0012	0.1310	0.3874	0.0045	2113	46	2112	17	2111	21	100
FP-3-25	43	52	88	0.58	0.1248	0.0032	6.3428	0.1073	0.3687	0.0040	2026	45	2024	15	2023	19	100
FP-3-26	44	65	90	0.72	0.1279	0.0034	6.4922	0.1174	0.3681	0.0042	2070	46	2045	16	2020	20	98
FP-3-27	40	52	80	0.65	0.1295	0.0035	6.6070	0.1259	0.3702	0.0044	2091	47	2060	17	2030	21	97
FP-3-28	38	49	77	0.64	0.1290	0.0033	6.6991	0.1112	0.3768	0.0040	2084	44	2073	15	2061	19	99
FP-3-29	53	73	109	0.66	0.1286	0.0034	6.6609	0.1184	0.3758	0.0042	2079	45	2068	16	2057	20	99
FP-3-30	37	48	76	0.63	0.1276	0.0035	6.5213	0.1302	0.3709	0.0045	2065	48	2049	18	2034	21	98
FP-8																	
FP-8-02	93	107	238	0.45	0.1199	0.0030	5.8291	0.0908	0.3526	0.0037	1955	44	1951	14	1947	17	100
FP-8-03	87	58	143	0.40	0.1664	0.0039	10.9389	0.1414	0.4769	0.0047	2521	39	2518	12	2514	21	100

FP-8-04	1042	105	265	0.40	0.1677	0.0043	9.0543	0.1520	0.3917	0.0046	2534	43	2344	15	2131	21	81
FP-8-05	169	140	444	0.32	0.1579	0.0044	9.7528	0.1963	0.4481	0.0060	2433	46	2412	19	2387	27	98
FP-8-06	164	182	498	0.37	0.1761	0.0049	11.4935	0.2389	0.4733	0.0067	2617	46	2564	19	2498	29	95
FP-8-07	165	156	411	0.38	0.1598	0.0040	8.3211	0.1336	0.3776	0.0042	2454	42	2267	15	2065	20	81
FP-8-08	144	56	293	0.19	0.1635	0.0039	9.7861	0.1358	0.4342	0.0045	2492	40	2415	13	2324	20	93
FP-8-09	204	149	707	0.21	0.1239	0.0029	4.5314	0.0546	0.2653	0.0024	2013	41	1737	10	1517	12	67
FP-8-10	209	161	834	0.19	0.1239	0.0028	3.5834	0.0394	0.2098	0.0018	2013	40	1546	9	1228	10	36
FP-8-11	258	154	383	0.40	0.1656	0.0039	9.9344	0.1275	0.4351	0.0043	2514	39	2429	12	2329	19	92
FP-8-12	163	512	338	1.52	0.1439	0.0033	5.9468	0.0680	0.2997	0.0027	2275	39	1968	10	1690	13	65
FP-8-13	201	289	301	0.96	0.1697	0.0043	10.3228	0.1740	0.4413	0.0052	2554	42	2464	16	2356	23	92
FP-8-14	162	138	504	0.27	0.1678	0.0040	8.6510	0.1214	0.3740	0.0039	2536	40	2302	13	2048	18	76
FP-8-15	62	93	94	0.99	0.1673	0.0041	11.0207	0.1633	0.4778	0.0052	2531	40	2525	14	2518	23	99
FP-8-17	204	139	470	0.30	0.1645	0.0041	10.7208	0.1669	0.4727	0.0053	2502	41	2499	14	2496	23	100
FP-8-18	99	200	134	1.50	0.1648	0.0039	10.7419	0.1422	0.4727	0.0048	2506	39	2501	12	2495	21	100
FP-8-20	95	143	183	0.78	0.1689	0.0045	11.1763	0.2179	0.4801	0.0065	2546	44	2538	18	2528	28	99
FP-8-21	70	58	163	0.35	0.1691	0.0043	10.7140	0.1793	0.4595	0.0055	2549	42	2499	16	2437	24	95
FP-8-22	111	199	224	0.89	0.1605	0.0043	10.0011	0.1935	0.4518	0.0059	2461	45	2435	18	2403	26	98

FP-8-24	275	140	544	0.26	0.1544	0.0035	9.4702	0.1073	0.4450	0.0041	2395	38	2385	10	2373	18	99
FP-8-25	36	29	63	0.46	0.1524	0.0040	9.3441	0.1665	0.4447	0.0054	2373	44	2372	16	2372	24	100
FP-8-26	229	680	630	1.08	0.1664	0.0041	8.1823	0.1279	0.3566	0.0039	2522	41	2251	14	1966	19	72
FP-8-27	325	731	1029	0.71	0.1267	0.0030	4.7889	0.0643	0.2742	0.0026	2052	41	1783	11	1562	13	69
FP-8-28	202	165	621	0.27	0.1494	0.0041	7.1090	0.1424	0.3452	0.0044	2339	46	2125	18	1912	21	78
FP-8-29	155	165	400	0.41	0.1499	0.0036	6.5814	0.0889	0.3184	0.0031	2345	40	2057	12	1782	15	68
FP-8-30	98	78	154	0.51	0.1680	0.0040	11.1655	0.1519	0.4822	0.0050	2537	39	2537	13	2537	22	100
FP-8-31	93	75	209	0.36	0.1591	0.0038	10.0706	0.1400	0.4590	0.0047	2447	39	2441	13	2435	21	100
FP-8-32	235	556	727	0.76	0.1262	0.0029	5.0801	0.0603	0.2919	0.0026	2046	40	1833	10	1651	13	76
FP-8-33	175	191	372	0.51	0.1582	0.0039	9.3730	0.1433	0.4297	0.0047	2437	41	2375	14	2304	21	94
FP-8-34	136	97	357	0.27	0.1592	0.0038	10.0963	0.1443	0.4601	0.0048	2447	40	2444	13	2440	21	100
FP-8-36	144	141	386	0.37	0.1373	0.0032	5.9433	0.0747	0.3139	0.0029	2194	40	1968	11	1760	14	75
FP-8-40	186	175	556	0.32	0.1385	0.0031	5.1341	0.0558	0.2688	0.0024	2209	38	1842	9	1535	12	56
FP-9-2																	
FP-9-2-01	200	7	57	0.12	0.1118	0.0027	4.4908	0.0656	0.2914	0.0028	1829	43	1729	12	1649	14	89
FP-9-2-02	159	205	287	0.72	0.1291	0.0039	5.4426	0.1262	0.3058	0.0041	2086	52	1892	20	1720	20	79
FP-9-2-03	8	88	127	0.69	0.1256	0.0042	6.3286	0.1748	0.3656	0.0056	2037	57	2022	24	2009	27	99

FP-9-2-04	125	102	389	0.26	0.1105	0.0030	4.9100	0.0975	0.3224	0.0038	1807	49	1804	17	1802	18	100
FP-9-2-08	82	224	138	1.62	0.1260	0.0030	6.3729	0.0854	0.3669	0.0035	2043	41	2029	12	2015	17	99
FP-9-2-09	256	385	610	0.63	0.1260	0.0028	5.7189	0.0645	0.3293	0.0029	2043	39	1934	10	1835	14	89
FP-9-2-11	25	8	70	0.12	0.1168	0.0037	5.1524	0.1324	0.3201	0.0045	1907	56	1845	22	1790	22	93
FP-9-2-12	104	300	170	1.77	0.1261	0.0035	6.0168	0.1245	0.3462	0.0043	2044	49	1978	18	1917	21	93
FP-9-2-13	67	177	116	1.52	0.1283	0.0033	6.4453	0.1101	0.3643	0.0040	2075	45	2039	15	2003	19	96
FP-9-2-15	99	87	213	0.41	0.1169	0.0030	5.3879	0.0896	0.3342	0.0036	1910	45	1883	14	1859	17	97
FP-9-2-16	119	174	191	0.91	0.1657	0.0038	10.6418	0.1297	0.4658	0.0044	2515	38	2492	11	2465	20	98
FP-9-2-17	87	40	217	0.18	0.1237	0.0032	6.2223	0.1107	0.3650	0.0041	2010	46	2008	16	2006	20	100
FP-9-2-18	105	279	165	1.69	0.1294	0.0036	6.5682	0.1349	0.3682	0.0047	2090	48	2055	18	2021	22	97
FP-9-2-19	38	24	103	0.23	0.1157	0.0032	5.2704	0.1028	0.3305	0.0039	1890	49	1864	17	1841	19	97
FP-9-2-21	66	2	21	0.09	0.1155	0.0030	5.1757	0.0871	0.3249	0.0035	1888	46	1849	14	1814	17	96
FP-9-2-23	56	39	106	0.37	0.1593	0.0039	9.5286	0.1473	0.4337	0.0048	2449	41	2390	14	2322	21	95
FP-9-2-26	121	268	224	1.19	0.1273	0.0030	6.5572	0.0832	0.3736	0.0035	2060	41	2054	11	2046	16	99
FP-9-2-27	69	60	111	0.54	0.1672	0.0040	10.9672	0.1466	0.4755	0.0048	2530	39	2520	12	2508	21	99
FP-9-2-29	291	229	684	0.34	0.1231	0.0028	5.9456	0.0622	0.3500	0.0030	2002	39	1968	9	1935	14	97
FP-9-2-30	49	105	80	1.31	0.1319	0.0033	7.0768	0.1104	0.3889	0.0041	2123	43	2121	14	2118	19	100

FP-17

FP-17-01	3	6	7	0.79	0.1245	0.0064	5.4562	0.2672	0.3180	0.0079	2021	89	1894	42	1780	39	86
FP-17-02	23	57	34	1.70	0.1294	0.0060	6.5726	0.2867	0.3686	0.0085	2089	80	2056	38	2023	40	97
FP-17-03	112	153	266	0.58	0.1255	0.0039	6.3458	0.1595	0.3668	0.0054	2035	54	2025	22	2015	25	99
FP-17-04	6	0	16	0.02	0.1176	0.0059	5.5761	0.2650	0.3440	0.0083	1919	87	1912	41	1906	40	99
FP-17-05	38	23	65	0.35	0.1119	0.0036	5.0644	0.1331	0.3281	0.0047	1831	57	1830	22	1829	23	100
FP-17-06	100	150	142	1.06	0.1627	0.0038	10.4810	0.1357	0.4671	0.0047	2484	39	2478	12	2471	20	99
FP-17-07	20	11	45	0.25	0.1258	0.0037	6.3929	0.1417	0.3685	0.0049	2040	50	2031	19	2022	23	99

FP-18

FP-18-01	119	90	178	0.50	0.1581	0.0036	9.9741	0.1185	0.4578	0.0044	2436	38	2432	11	2430	19	100
FP-18-02	167	220	572	0.38	0.1233	0.0029	3.8748	0.0527	0.2281	0.0022	2004	41	1608	11	1324	12	49
FP-18-03	126	132	267	0.49	0.1298	0.0032	5.4175	0.0823	0.3029	0.0032	2095	42	1888	13	1706	16	77
FP-18-04	137	341	386	0.88	0.1472	0.0041	6.6083	0.1361	0.3258	0.0042	2314	47	2061	18	1818	21	73
FP-18-05	227	172	590	0.29	0.1299	0.0029	5.1379	0.0584	0.2869	0.0026	2097	39	1842	10	1626	13	71
FP-18-06	170	147	310	0.47	0.1563	0.0035	8.5911	0.1025	0.3989	0.0038	2416	38	2296	11	2164	17	88
FP-18-07	259	214	719	0.30	0.1245	0.0028	4.5499	0.0533	0.2652	0.0024	2021	40	1740	10	1517	12	67
FP-18-08	120	190	228	0.84	0.1643	0.0040	8.2901	0.1292	0.3661	0.0041	2500	41	2263	14	2011	19	76

FP-18-10	324	222	545	0.41	0.1250	0.0029	6.3664	0.0782	0.3695	0.0035	2029	40	2028	11	2027	16	100
FP-18-11	256	64	833	0.08	0.1289	0.0029	4.3271	0.0455	0.2435	0.0021	2083	38	1699	9	1405	11	52
FP-18-12	414	63	413	0.15	0.1675	0.0045	9.7447	0.1873	0.4220	0.0055	2533	44	2411	18	2269	25	88
FP-18-13	150	31	464	0.07	0.1250	0.0029	4.4245	0.0521	0.2567	0.0023	2029	40	1717	10	1473	12	62
FP-18-14	588	480	1002	0.48	0.1697	0.0039	10.0897	0.1224	0.4314	0.0042	2554	38	2443	11	2312	19	90
FP-18-15	206	80	604	0.13	0.1266	0.0029	5.3125	0.0629	0.3044	0.0028	2051	40	1871	10	1713	14	80
FP-18-16	206	140	377	0.37	0.1612	0.0037	10.2851	0.1242	0.4627	0.0044	2469	38	2461	11	2451	20	99
FP-18-17	60	55	118	0.47	0.1690	0.0046	11.2615	0.2206	0.4833	0.0065	2548	44	2545	18	2541	28	100
FP-18-18	239	374	457	0.82	0.1647	0.0040	7.7823	0.1104	0.3426	0.0035	2505	40	2206	13	1899	17	68
FP-18-19	162	134	358	0.37	0.1608	0.0038	10.1932	0.1346	0.4598	0.0046	2464	39	2453	12	2439	20	99
FP-18-20	320	254	893	0.28	0.1293	0.0029	5.0381	0.0578	0.2827	0.0025	2088	39	1826	10	1605	13	70
FP-18-21	196	176	569	0.31	0.1264	0.0029	4.9299	0.0572	0.2828	0.0025	2049	40	1807	10	1606	13	72
FP-18-22	219	127	605	0.21	0.1281	0.0031	4.6988	0.0647	0.2661	0.0026	2071	42	1767	12	1521	13	64
FP-18-23	253	47	916	0.05	0.1119	0.0039	4.9837	0.1469	0.3231	0.0051	1830	62	1817	25	1805	25	99
FP-18-24	80	114	178	0.64	0.1654	0.0049	7.3622	0.1652	0.3228	0.0046	2512	49	2156	20	1803	22	61
FP-18-25	225	175	818	0.21	0.1285	0.0030	4.1948	0.0500	0.2367	0.0021	2078	40	1673	10	1369	11	48
FP-18-26	235	76	895	0.09	0.1127	0.0028	3.7617	0.0587	0.2420	0.0024	1844	45	1585	13	1397	13	68

FP-18-28	201	138	440	0.31	0.1503	0.0035	7.3843	0.0922	0.3562	0.0034	2350	39	2159	11	1964	16	80
FP-18-30	228	384	618	0.62	0.1297	0.0039	4.3370	0.0962	0.2425	0.0031	2093	51	1700	18	1400	16	50
FP-18-31	264	75	704	0.11	0.1406	0.0032	6.3268	0.0683	0.3262	0.0029	2235	39	2022	9	1820	14	77
FP-18-32	360	754	1013	0.74	0.1281	0.0043	6.5807	0.1866	0.3726	0.0060	2071	58	2057	25	2042	28	99
FP-18-33	169	359	305	1.17	0.1456	0.0035	6.5259	0.0882	0.3250	0.0032	2295	41	2049	12	1814	15	74
FP-18-34	242	361	459	0.79	0.1671	0.0039	7.4796	0.0890	0.3245	0.0030	2529	38	2171	11	1812	15	60
FP-18-35	62	64	92	0.69	0.1658	0.0041	10.9053	0.1644	0.4768	0.0052	2516	41	2515	14	2513	23	100
FP-18-36	153	156	247	0.63	0.1664	0.0040	10.7909	0.1444	0.4702	0.0047	2522	39	2505	12	2485	21	99
FP-18-37	218	162	435	0.37	0.1674	0.0039	10.9485	0.1350	0.4743	0.0045	2532	39	2519	11	2502	20	99
FP-18-38	280	329	479	0.69	0.1846	0.0043	10.2207	0.1250	0.4015	0.0038	2694	38	2455	11	2176	18	76
FP-18-39	331	158	535	0.30	0.1728	0.0041	7.7147	0.1029	0.3237	0.0032	2585	39	2198	12	1808	15	57

Table 4-4 Rare earth element concentrations for zircons of the rock samples from the Fuping Complex.

Sample No.	La	Ce	Pr	Nd	Sm	Eu	Gd	Tb	Dy	Ho	Er	Tm	Yb	Lu
FP-1-1														
FP-1-1-01	0.016	0.25	0.018	0.20	0.27	0.061	0.93	0.34	3.50	1.26	5.11	0.98	8.69	1.56
FP-1-1-05	0.034	0.81	0.022	0.20	0.27	0.033	1.04	0.41	4.65	1.77	7.54	1.52	13.81	2.52

FP-1-1-06	0.170	2.16	0.094	0.69	0.85	0.061	3.57	1.42	15.53	5.66	23.46	4.54	40.29	7.15
FP-1-1-07	2.020	8.63	0.640	3.28	1.40	0.063	4.06	1.56	16.77	6.01	24.40	4.63	39.32	6.65
FP-1-1-08	0.630	5.93	0.420	2.00	2.34	0.270	6.47	2.34	20.07	6.08	23.19	4.44	39.96	6.83
FP-1-1-09	0.039	1.27	0.032	0.32	0.40	0.038	1.53	0.60	6.71	2.43	10.29	2.00	17.66	3.20
FP-1-1-10	1.390	8.71	0.820	3.63	2.47	0.150	6.57	2.76	28.84	9.27	35.18	6.51	54.79	8.59
FP-1-1-12	0.530	4.86	0.300	1.51	1.46	0.120	4.68	1.75	17.13	5.58	21.68	4.18	36.50	6.23
FP-1-1-15	0.370	2.60	0.160	0.90	0.52	0.037	1.68	0.65	7.42	2.75	11.58	2.31	20.86	3.73
FP-1-1-16	0.920	8.54	0.590	2.95	4.07	0.330	10.79	4.35	37.91	10.52	36.46	6.29	50.27	7.49
FP-1-1-18	1.150	5.74	0.370	1.94	1.48	0.059	5.34	2.23	24.56	8.80	35.49	6.60	56.07	9.46
FP-1-1-19	0.270	1.96	0.130	0.71	0.50	0.047	1.52	0.61	6.91	2.59	11.40	2.33	22.01	4.19
FP-1-1-20	0.970	7.51	0.570	2.55	1.71	0.100	5.22	2.16	22.99	8.09	32.63	6.21	54.49	9.30
FP-1-1-21	0.240	1.93	0.110	0.85	0.90	0.051	3.73	1.53	16.66	6.05	24.13	4.49	38.51	6.57
FP-1-1-22	0.035	0.89	0.017	0.20	0.30	0.032	1.25	0.54	5.92	2.18	9.14	1.81	16.21	2.90
FP-1-1-23	0.032	1.83	0.043	0.36	0.47	0.044	1.91	0.82	9.18	3.30	13.75	2.72	24.47	4.35
FP-1-1-24	0.760	4.03	0.290	1.10	0.67	0.047	1.60	0.69	7.92	2.95	13.07	2.73	26.75	5.00
FP-1-1-26	0.036	1.14	0.026	0.20	0.29	0.028	1.19	0.53	6.20	2.36	10.15	2.06	18.95	3.38
FP-1-1-27	2.090	6.57	0.800	3.73	0.92	0.058	1.48	0.50	5.15	1.81	7.42	1.45	13.08	2.36

FP-1-1-28	3.130	10.72	0.840	3.66	1.88	0.100	4.45	1.80	19.31	6.78	27.75	5.48	49.81	9.00
FP-1-1-29	0.320	1.73	0.130	0.89	0.84	0.088	3.25	1.27	12.77	4.33	16.59	3.01	25.60	4.40
FP-1-1-30	0.094	3.23	0.045	0.41	0.83	0.050	3.65	1.63	17.30	5.95	23.81	4.53	39.46	6.68
FP-3														
FP-3-01	0.929	20.56	0.898	9.40	8.94	0.418	36.73	11.62	130.47	47.34	201.71	39.54	350.20	61.17
FP-3-02	0.108	12.53	0.483	8.00	10.50	0.635	43.10	12.89	138.41	48.55	201.69	39.28	353.96	59.61
FP-3-03	8.960	39.80	5.160	32.35	17.01	1.310	50.58	14.58	150.23	53.16	216.37	42.41	376.76	64.18
FP-3-04	0.104	11.65	0.457	7.51	10.30	0.588	41.42	12.01	133.26	47.68	198.63	39.22	351.98	60.45
FP-3-05	0.449	11.64	0.614	5.44	5.26	0.528	19.01	5.99	68.71	25.75	113.62	23.58	224.48	39.79
FP-3-06	1.400	20.84	0.908	6.29	4.62	0.653	15.68	5.19	66.34	26.36	124.77	27.45	270.77	47.38
FP-3-07	0.088	12.48	0.328	5.72	7.87	0.586	32.23	10.30	114.76	41.40	172.84	33.95	311.10	52.87
FP-3-08	29.600	89.89	9.960	49.25	15.63	0.680	39.98	11.61	123.24	43.44	183.73	35.95	325.41	54.60
FP-3-09	3.930	24.97	2.255	16.10	9.88	0.834	31.60	9.73	105.94	38.38	158.78	31.51	290.17	49.06
FP-3-10	0.029	9.89	0.058	0.87	1.63	0.110	8.72	2.97	36.91	14.42	65.48	13.75	132.22	23.16
FP-3-11	0.032	8.06	0.139	2.09	4.48	0.440	21.97	7.33	84.98	31.16	133.32	26.99	245.61	42.66
FP-3-12	0.196	16.53	0.243	2.37	2.79	0.274	12.13	4.24	51.41	19.40	87.44	18.35	176.91	31.01
FP-3-13	0.210	15.50	0.203	2.34	3.15	0.285	15.25	5.28	61.20	24.06	103.52	21.31	200.93	34.94

FP-3-14	0.040	8.95	0.103	1.52	2.65	0.154	13.55	4.65	56.23	21.25	93.89	19.57	189.95	33.62
FP-3-15	0.708	20.29	0.885	8.19	7.55	0.602	23.75	7.38	85.88	32.04	141.48	29.93	294.42	54.18
FP-3-16	24.910	49.10	5.590	20.80	6.14	0.447	19.13	5.98	66.47	24.13	104.12	21.25	199.60	34.83
FP-3-17	0.026	10.86	0.081	1.52	3.12	0.144	16.42	5.46	65.37	24.79	107.72	22.06	211.52	36.62
FP-3-18	1.717	18.79	1.299	12.10	15.32	2.840	64.28	24.58	283.76	94.44	368.33	68.47	588.82	93.23
FP-3-19	0.532	14.38	0.560	4.47	4.37	0.545	15.30	4.96	57.81	21.73	96.83	20.46	201.52	37.28
FP-3-20	0.064	11.25	0.451	6.60	9.32	0.535	37.24	11.70	128.40	45.07	184.13	36.41	328.38	55.73
FP-3-21	0.829	20.56	1.177	9.82	11.63	1.532	43.83	13.68	144.64	51.31	210.71	41.31	382.59	65.17
FP-3-22	0.050	11.25	0.488	8.03	9.32	0.581	37.39	11.76	125.74	44.37	180.15	35.84	324.40	54.16
FP-3-23	0.035	10.89	0.269	4.25	6.14	0.350	27.57	8.83	98.96	36.16	149.06	29.96	279.50	46.63
FP-3-24	0.245	9.54	0.139	2.13	3.13	0.218	15.04	5.35	60.94	23.19	100.86	20.79	198.40	33.87
FP-3-25	2.380	15.17	1.158	9.92	8.56	0.601	29.29	8.87	98.71	34.92	143.94	28.87	273.21	46.23
FP-3-26	0.071	10.58	0.338	4.55	7.09	0.508	30.95	9.66	106.45	38.94	159.97	31.74	294.98	49.89
FP-3-27	0.024	10.53	0.190	2.94	4.24	0.255	17.44	5.84	66.98	24.76	105.17	21.70	203.63	34.56
FP-3-28	0.021	10.39	0.078	1.15	2.75	0.189	15.16	5.33	63.82	24.05	103.70	21.59	204.70	35.42
FP-3-29	0.563	18.00	0.489	4.53	5.59	0.361	23.25	7.52	86.36	31.98	138.52	28.28	268.50	45.68
FP-3-30	0.037	10.37	0.097	1.84	3.25	0.215	15.81	5.18	61.92	23.39	101.68	21.48	204.71	34.57

FP-9-2

FP-9-2-01	6.900	52.98	1.943	18.89	22.71	7.290	107.49	39.02	462.85	174.29	778.14	164.59	1522.70	251.95
FP-9-2-02	1.003	34.10	0.602	4.21	4.74	1.772	19.82	6.18	68.99	26.13	117.32	25.31	263.67	51.53
FP-9-2-03	0.029	0.27	0.028	0.27	0.16	0.152	1.68	1.04	16.48	8.65	53.25	14.78	186.93	49.30
FP-9-2-04	2.690	22.86	1.332	10.07	6.97	2.220	21.59	6.95	80.95	31.74	149.83	33.47	341.32	63.84
FP-9-2-08	0.440	15.43	0.656	8.14	10.68	4.810	53.80	19.63	236.73	93.77	423.25	88.71	817.57	137.14
FP-9-2-09	1.206	77.95	3.000	38.11	50.27	16.100	214.39	67.90	695.30	216.49	778.61	135.25	1096.15	153.73
FP-9-2-11	0.032	1.09	0.034	0.15	0.21	0.164	1.73	0.71	11.94	5.62	33.92	9.10	118.54	28.42
FP-9-2-12	2.480	15.73	1.350	9.93	6.38	2.490	23.00	8.50	111.18	52.05	290.82	72.12	749.40	132.24
FP-9-2-13	0.235	13.99	0.411	5.22	6.41	4.780	33.39	11.72	151.61	65.03	330.07	78.95	841.04	149.84
FP-9-2-15	1.127	8.51	0.382	3.65	3.77	1.334	20.78	7.81	104.30	44.62	223.67	52.35	522.50	97.09
FP-9-2-16	0.688	35.53	0.516	3.83	3.83	1.268	12.15	3.73	41.29	15.43	71.66	16.71	181.39	38.04
FP-9-2-17	2.810	191.73	11.220	165.69	200.99	50.780	397.59	76.44	528.07	122.84	373.21	61.62	494.03	73.89
FP-9-2-18	0.237	19.32	0.688	9.85	15.69	3.710	85.46	32.01	392.20	153.82	702.35	147.91	1376.11	231.14
FP-9-2-19	0.682	8.62	0.549	4.65	2.44	8.480	9.07	3.03	37.94	15.95	80.47	19.65	218.31	45.89
FP-9-2-21	0.110	10.60	0.336	5.18	9.13	1.264	44.50	14.96	170.56	61.49	256.31	51.65	472.58	79.75
FP-9-2-23	0.033	15.38	0.046	0.77	1.64	0.463	7.64	2.78	30.81	10.70	45.34	9.45	95.13	17.89

FP-9-2-26	1.003	41.84	1.890	28.60	41.98	5.710	158.80	46.41	424.47	117.72	402.15	71.25	584.17	82.54
FP-9-2-27	0.067	10.70	0.401	6.64	10.23	1.170	42.49	12.66	132.09	44.89	182.85	36.08	325.49	56.81
FP-9-2-29	63.420	194.96	26.730	124.54	22.47	0.534	25.66	8.29	106.42	42.65	197.04	42.16	407.55	73.84
FP-9-2-30	1.015	13.42	0.925	6.35	8.63	1.680	44.13	16.31	203.01	76.81	343.10	71.99	660.20	111.66
FP-17														
FP-17-04	0.205	1.34	0.081	0.66	0.42	0.119	2.18	0.65	8.41	2.97	16.20	5.14	75.85	22.50
FP-17-07	2.900	28.40	1.891	12.62	6.41	1.379	12.94	3.42	33.35	11.92	60.36	17.18	239.88	64.56
FP-17-11	15.300	109.00	7.220	46.06	21.98	4.200	55.38	15.60	151.28	47.15	181.46	35.33	321.32	54.87
FP-17-14	0.035	0.19	0.029	0.21	0.16	0.090	0.39	0.05	1.37	1.28	13.70	6.71	136.13	46.31
FP-17-20	0.046	7.21	0.067	0.72	1.83	0.894	8.80	2.77	32.36	12.78	60.60	13.77	146.44	30.19
FP-17-23	0.077	32.80	0.365	5.63	8.43	1.721	35.16	10.57	113.55	40.43	175.42	36.87	354.90	65.22
FP-17-30	0.139	2.31	0.114	0.77	0.36	0.245	0.97	0.24	2.54	1.23	9.48	3.69	69.76	24.92
FP-8														
FP-8-02	1.333	19.92	0.830	8.91	10.48	0.285	37.66	12.27	132.82	47.85	202.48	40.49	369.20	66.61
FP-8-03	0.031	7.64	0.051	1.26	2.78	0.363	14.71	4.79	55.96	20.48	86.91	17.72	164.32	30.72
FP-8-04	2.690	25.92	1.433	10.45	6.98	6.840	22.38	6.67	73.20	25.78	110.92	22.33	214.32	41.06
FP-8-05	0.101	17.93	0.138	2.80	5.20	0.457	23.48	7.84	88.05	31.57	136.45	28.46	268.49	49.85

FP-8-06	0.596	27.78	0.981	9.93	7.81	3.570	21.97	5.83	60.46	20.38	87.82	18.41	176.63	32.50
FP-8-07	2.189	44.64	1.172	7.97	5.48	6.040	19.94	5.39	56.85	21.14	98.40	22.66	239.18	49.46
FP-8-08	0.310	14.84	0.375	2.78	2.17	0.682	9.11	2.89	31.18	11.52	52.26	11.58	118.17	25.49
FP-8-09	2.330	22.34	1.493	9.86	1.96	2.030	6.66	2.64	34.92	14.73	74.41	17.76	182.47	33.83
FP-8-10	1.046	14.60	0.587	4.08	2.29	3.000	9.02	3.21	38.65	16.22	76.86	17.66	179.12	34.91
FP-8-11	0.700	27.97	1.052	9.31	5.52	5.030	16.71	4.58	49.09	17.04	77.81	17.36	182.95	38.01
FP-8-12	2.750	165.19	3.550	38.03	38.56	12.340	110.98	29.72	275.81	80.76	298.09	56.13	483.63	80.68
FP-8-13	8.870	73.48	4.600	27.71	17.35	6.440	55.31	16.46	162.79	54.39	216.58	41.82	374.81	65.57
FP-8-14	1.820	64.26	3.720	32.38	8.93	7.240	16.72	3.80	38.62	14.29	66.09	14.30	148.44	30.99
FP-8-15	0.319	21.63	0.631	8.28	11.30	2.350	41.55	12.66	135.11	45.71	184.00	35.99	326.68	58.78
FP-8-17	0.299	19.09	0.144	1.45	2.15	1.404	9.35	2.93	30.95	11.23	52.89	11.59	120.82	25.84
FP-8-18	0.567	32.79	1.158	11.11	10.10	3.590	32.28	9.30	95.17	32.50	133.42	26.60	248.64	46.57
FP-8-20	0.676	19.41	0.726	6.80	8.40	1.495	36.74	11.57	124.77	43.65	176.71	34.55	313.08	55.36
FP-8-21	1.435	23.51	0.857	5.74	1.41	4.490	4.07	1.29	15.36	6.35	31.38	7.65	82.99	18.56
FP-8-22	0.646	46.49	0.993	11.44	9.87	5.920	24.11	5.44	53.58	17.88	79.81	18.28	193.17	36.54
FP-8-24	10.380	39.49	4.410	21.55	7.95	0.902	18.76	5.80	65.41	24.11	109.36	23.76	232.31	43.67
FP-8-25	1.906	23.03	0.999	6.57	4.43	2.640	16.36	5.08	54.03	18.67	81.02	16.22	154.42	28.85

FP-8-26	6.510	55.86	3.960	23.14	7.55	3.810	26.84	8.96	111.68	43.85	201.63	43.39	432.05	82.37
FP-8-27	2.210	66.37	2.880	25.83	13.52	6.930	26.57	5.75	54.92	18.48	79.92	16.92	168.44	30.91
FP-8-28	3.420	35.66	2.490	16.19	6.28	7.510	15.27	4.52	53.11	20.52	99.48	22.01	224.45	42.83
FP-8-29	1.833	34.27	1.285	9.42	4.39	10.730	12.34	3.57	43.06	17.30	82.80	19.48	207.54	42.19
FP-8-30	0.078	13.93	0.093	1.38	2.99	0.410	14.09	5.06	57.91	22.01	97.79	20.59	199.01	37.65
FP-8-31	0.455	12.09	0.604	7.82	10.71	2.530	40.18	11.61	119.92	40.29	161.05	30.37	274.63	49.27
FP-8-32	1.041	11.51	0.222	1.31	1.01	0.357	4.65	1.72	22.40	9.09	44.03	10.87	121.34	26.24
FP-8-33	0.147	20.93	0.181	1.93	2.32	0.665	11.47	3.99	50.07	19.74	94.50	21.88	230.61	46.54
FP-8-34	2.181	23.91	1.324	10.30	6.80	3.620	26.61	8.33	88.25	31.13	131.28	26.88	253.41	45.32
FP-8-36	1.302	29.19	1.112	8.85	6.68	7.620	19.70	5.75	61.59	22.19	99.12	21.23	210.73	40.77
FP-8-40	2.630	41.94	1.612	9.96	3.61	3.510	10.18	3.01	33.67	13.60	67.31	16.58	188.12	42.65
FP-18														
FP-18-01	-	32.13	-	24.73	-	11.410	501.62	-	117.30	-	126.90	532.16	225.31	113.03
FP-18-02	-	34.33	-	7.06	-	6.950	144.51	-	61.09	-	90.04	375.42	236.25	135.27
FP-18-03	-	48.49	-	30.32	-	9.780	313.98	-	97.98	2626.92	101.27	283.16	180.88	86.76
FP-18-04	-	175.88	-	119.81	-	28.020	435.60	-	144.42	1461.43	132.07	307.00	214.94	97.76
FP-18-05	6119	56.46	-	27.60	-	4.530	207.02	-	122.77	910.29	149.79	333.18	283.88	131.57

FP-18-06	527.270	92.88	-	85.99	ud	78.090	180.43	-	62.48	331.95	76.08	172.51	190.12	105.81
FP-18-07	242.860	44.16	-	18.87	499.14	22.730	125.00	-	88.63	308.38	102.76	167.32	194.46	80.88
FP-18-08	120.800	65.69	-	33.57	439.38	33.020	170.35	-	92.54	233.32	80.56	110.51	134.55	56.82
FP-18-10	144.480	70.95	-	32.45	100.35	2.460	98.90	-	92.32	232.60	128.99	176.64	277.35	119.58
FP-18-11	37.410	36.63	-	65.89	215.24	76.250	87.60	-	39.20	78.49	46.50	58.93	97.04	39.96
FP-18-12	2.520	21.02	-	1.60	13.76	2.440	25.59	-	30.25	67.66	46.69	62.11	121.31	55.13
FP-18-13	104.37	36.92	47.21	14.52	13.07	8.490	11.02	40.21	13.03	18.73	16.12	15.85	36.91	14.36
FP-18-14	274.75	285.04	319.450	197.33	265.76	234.83	212.88	372.52	204.95	275.00	266.55	245.53	579.68	222.74
FP-18-15	9.430	15.94	3.540	2.79	7.72	1.580	21.05	30.09	28.79	38.51	43.68	41.57	111.67	45.97
FP-18-16	14.640	33.01	14.940	19.68	57.86	1.650	131.35	168.67	174.44	211.68	206.05	150.05	340.95	119.73
FP-18-17	13.760	25.82	10.900	11.76	27.85	8.420	66.78	66.71	84.90	96.67	98.83	70.87	169.02	60.06
FP-18-18	8.630	45.78	12.130	32.80	112.75	6.070	247.00	204.76	277.92	289.65	300.51	200.94	499.30	168.70
FP-18-19	23.310	33.22	6.620	9.43	11.38	2.650	27.69	22.30	41.04	44.59	62.01	46.84	160.65	67.80
FP-18-20	9.450	31.69	4.750	6.99	9.81	2.200	24.63	18.37	43.65	46.91	67.80	49.98	168.57	59.66
FP-18-21	36.040	77.80	33.020	58.63	56.27	15.300	97.73	54.57	112.92	94.15	117.26	71.50	212.80	66.61
FP-18-22	90.150	73.99	26.570	34.13	28.66	4.500	52.02	33.86	84.66	76.96	104.58	65.30	209.26	68.31
FP-18-23	4.450	14.54	1.090	1.24	1.44	0.580	5.22	4.44	16.64	18.50	34.11	25.13	96.28	32.23

FP-18-24	21.050	37.88	5.080	8.74	13.36	3.040	37.01	22.13	63.97	55.84	86.40	51.91	186.33	65.18
FP-18-25	8.700	40.68	4.530	11.38	15.69	3.940	49.88	24.68	88.76	65.15	106.17	55.31	208.99	62.53
FP-18-26	5.030	16.90	2.360	5.53	3.58	0.870	6.30	3.69	16.77	15.08	33.02	20.44	95.29	30.98
FP-18-28	8.020	32.88	9.280	32.65	30.05	35.950	53.72	22.18	90.72	64.99	124.59	62.93	271.89	83.73
FP-18-30	34.690	45.54	5.080	14.92	22.50	1.670	79.07	37.12	174.29	118.38	227.35	96.91	389.43	107.43
FP-18-31	12.450	19.89	3.210	5.57	2.99	0.830	12.18	6.44	37.74	28.11	66.91	34.29	183.21	58.75
FP-18-32	28.330	91.35	11.440	28.89	26.77	8.980	87.73	40.46	207.49	131.70	270.61	113.14	515.76	136.96
FP-18-33	6.200	125.45	4.300	28.24	53.52	13.800	158.36	56.04	249.35	123.19	228.89	83.42	356.59	84.55
FP-18-34	39.810	106.64	13.520	27.96	14.41	6.690	37.45	14.70	75.12	45.64	102.86	44.36	239.20	73.03
FP-18-35	1.290	21.75	2.210	16.98	27.15	9.830	69.74	22.61	110.52	60.59	125.33	45.33	218.37	60.23
FP-18-36	2.140	43.27	1.730	6.07	8.62	6.210	26.81	10.43	59.62	36.33	91.33	39.48	225.97	66.29
FP-18-37	2.280	29.14	2.080	11.54	18.21	1.290	62.22	24.33	155.97	86.26	205.26	70.50	363.54	87.70
FP-18-38	4.250	63.65	2.270	10.06	12.56	5.150	39.02	13.79	85.07	44.95	115.37	44.00	257.27	68.85
FP-18-39	9.930	53.26	4.300	14.30	12.16	26.240	35.43	12.34	78.33	40.29	107.29	37.78	224.87	57.06

Table 4-5 LA-MC-ICP-MS Lu-Hf isotope data on zircons from the rock samples of the Fuping Complex.

No.	Age (Ma)	$^{176}\text{Yb}/^{177}\text{Hf}$	$^{176}\text{Lu}/^{177}\text{Hf}$	$^{176}\text{Hf}/^{177}\text{Hf}$	2s	$^{176}\text{Hf}/^{177}\text{Hf}_i$	$\varepsilon_{\text{Hf}}(0)$	$\varepsilon_{\text{Hf}}(t)$	T_{DM}	T_{DM}^{C}	$f_{\text{Lu/Hf}}$
FP-1-1 Gneissic granite											
FP-1-1-12	2050	0.109382	0.003804	0.281800	0.000016	0.281652	-34.4	6.2	2201	2273	-0.89
FP-1-1-18	2050	0.042362	0.001423	0.281634	0.000013	0.281578	-40.3	3.6	2294	2436	-0.96
FP-1-1-22	2050	0.017196	0.000614	0.281509	0.000017	0.281485	-44.7	0.3	2415	2639	-0.98
FP-1-1-27	2050	0.045838	0.001573	0.281654	0.000014	0.281592	-39.5	4.1	2275	2404	-0.95
FP-1-1-28	2050	0.121580	0.003952	0.281828	0.000018	0.281674	-33.4	6.9	2170	2226	-0.88
FP-1-1-29	2050	0.027367	0.000927	0.281619	0.000020	0.281583	-40.8	3.7	2284	2425	-0.97
FP-3 Gneissic syenogranite											
FP-3-01	2077	0.041735	0.001434	0.281581	0.000017	0.281524	-42.1	2.2	2368	2537	-0.96
FP-3-02	2077	0.014065	0.000566	0.281527	0.000013	0.281504	-44.0	1.6	2388	2580	-0.98
FP-3-04	2077	0.033008	0.001115	0.281522	0.000012	0.281478	-44.2	0.6	2429	2637	-0.97
FP-3-05	2077	0.029003	0.001040	0.281535	0.000015	0.281494	-43.7	1.2	2406	2603	-0.97
FP-3-08	2077	0.034619	0.001175	0.281591	0.000012	0.281545	-41.8	3.0	2338	2492	-0.96
FP-3-10	2077	0.017763	0.000624	0.281508	0.000012	0.281483	-44.7	0.8	2418	2627	-0.98
FP-3-13	2077	0.020136	0.000734	0.281529	0.000016	0.281501	-43.9	1.4	2395	2589	-0.98

FP-3-27	2077	0.027465	0.000940	0.281557	0.000013	0.281520	-43.0	2.1	2370	2546	-0.97
FP-8 Epidote biotite schist											
FP-8-02	1955	0.022321	0.000743	0.281366	0.000016	0.281339	-49.7	-7.1	2617	3021	-0.98
FP-8-05	2502	0.010109	0.000334	0.281424	0.000012	0.281408	-47.7	7.9	2513	2520	-0.99
FP-8-07	2502	0.019710	0.000729	0.281347	0.000011	0.281312	-50.4	4.5	2643	2729	-0.98
FP-8-10	2031	0.022334	0.000748	0.281446	0.000013	0.281417	-46.9	-2.6	2510	2801	-0.98
FP-8-15	2502	0.018533	0.000638	0.281427	0.000013	0.281396	-47.6	7.5	2528	2544	-0.98
FP-8-18	2502	0.019419	0.000648	0.281405	0.000013	0.281374	-48.3	6.7	2558	2593	-0.98
FP-8-20	2502	0.013642	0.000485	0.281297	0.000014	0.281274	-52.1	3.1	2693	2811	-0.99
FP-8-27	2031	0.007081	0.000256	0.281446	0.000013	0.281436	-46.9	-1.9	2477	2759	-0.99
FP-17 Amphibolite											
FP-17-02	2044	0.039295	0.001436	0.281778	0.000015	0.281722	-35.2	8.5	2094	2124	-0.96
FP-17-03	2044	0.047031	0.001402	0.281737	0.000017	0.281683	-36.6	7.1	2149	2210	-0.96
FP-17-04	1858	0.011057	0.000742	0.281607	0.000021	0.281581	-41.2	-0.7	2289	2552	-0.98
FP-17-05	1858	0.003153	0.000154	0.281495	0.000012	0.281490	-45.2	-4.0	2405	2753	-1.00
FP-17-06	2484	0.021308	0.000777	0.281372	0.000015	0.281335	-49.5	4.9	2612	2690	-0.98
FP-17-07	2044	0.005297	0.000331	0.281553	0.000015	0.281540	-43.1	2.1	2338	2522	-0.99

FP-18 Mica-schist

FP-18-03	2060	0.025981	0.000921	0.281486	0.000014	0.281450	-45.5	-0.8	2466	2710	-0.97
FP-18-11	2060	0.013411	0.000453	0.281441	0.000009	0.281424	-47.1	-1.7	2496	2768	-0.99
FP-18-12	2506	0.010923	0.000425	0.281391	0.000018	0.281371	-48.8	6.7	2563	2598	-0.99
FP-18-13	2060	0.013306	0.000463	0.281427	0.000011	0.281409	-47.6	-2.2	2516	2800	-0.99
FP-18-19	2506	0.013589	0.000568	0.281413	0.000012	0.281386	-48.1	7.2	2542	2564	-0.98
FP-18-20	2060	0.011940	0.000443	0.281449	0.000013	0.281432	-46.8	-1.4	2486	2750	-0.99
FP-18-35	2506	0.014944	0.000562	0.281422	0.000015	0.281395	-47.7	7.5	2530	2544	-0.98
FP-18-39	2506	0.015000	0.000621	0.281381	0.000010	0.281351	-49.2	6.0	2589	2640	-0.98

Table 4-6 Compilation of 2.1-2.0 Ga age data from the TNCO.

Complex	Sample No.	Rock	Method	Age (Ma)	Reference
Fuping	FP188-2	Monzogranitic gneiss	SHRIMP	2077 ± 13	Zhao et al., 2002
Fuping	FP-204	Granodioritic gneiss	SHRIMP	2024 ± 21	Zhao et al., 2002
Fuping	FP30	Granitic gneiss	SHRIMP	2045 ± 64	Guan et al., 2002
Fuping	FP-1-1	Gneissic granite	LA-ICP-MS	2050 ± 21	This study
Fuping	FP-3	Gneissic syenogranite	LA-ICP-MS	2077 ± 16	This study

Fuping	FP-9-2	Amphibolite	LA-ICP-MS	2054 ± 26	This study
Fuping	FP-17	Amphibolite	LA-ICP-MS	2044 ± 61	This study
Wutai	95-PC-50	Pink granite	SHRIMP	2117 ± 17	Wilde et al., 2005
Wutai	95-PC-51	Pink granite	SHRIMP	2116 ± 16	Wilde et al., 2005
Wutai	95-PC-60	Granite	SHRIMP	2084 ± 20	Wilde et al., 2005
Hengshan	09LYK06	Amphibole monzonite granite	SIMS	2084 ± 4	Zhao et al., 2011
Hengshan	09LYK06	Amphibole monzonite granite	LA-ICP-MS	2052 ± 17	Zhao et al., 2011
Hengshan	09LYK13	Biotite monzonitic granite	SIMS	2083 ± 15	Zhao et al., 2011
Hengshan	09LYK13	Biotite monzonitic granite	LA-ICP-MS	2060 ± 18	Zhao et al., 2011
Hengshan	980844	Anatectic granite	SHRIMP	2113 ± 8	Kroner et al., 2005b
Hengshan	02SX109	mafic dyke	SHRIMP	2035-2060	Peng et al., 2012b
Luliang	L9735	Monzonitic granite	TIMS	2031 ± 47	Geng et al., 2000
Luliang	LY1-15	Plagioclase amphibolite	TIMS	2051 ± 68	Yu et al., 1997
Luliang	LY1-10	Metarhyolite	TIMS	2099 ± 41	Yu et al., 1997
Luliang	LL401-1	Monzogranite	SHRIMP	2088 ± 18	Liu et al., 2009
Luliang	IL015-1	Monzogranite	SHRIMP	2050 ± 40	Liu et al., 2009
Luliang	LLC-11	Granodiorite	LA-ICP-MS	2070 ± 34	Santosh et al., 2015

Luliang	LLC-10A1	Gabbroic diorite	LA-ICP-MS	2053 ± 32	Santosh et al., 2015
Zanhuang	Z19-1	Granite	SHRIMP	2090 ± 10	Yang et al., 2011
Zanhuang	GT0403	Metabasalt	SHRIMP	2087 ± 16	Xie et al., 2012
Zanhuang	09FP28-1	Rhyolite	LA-ICP-MS	2088 ± 8	Liu et al., 2012
Huai'an	M28	Granitic gneiss	SHRIMP	2036 ± 16	Zhao et al., 2008
Huai'an	DJG08	Garnet-syenogranite	LA-ICP-MS	2003 ± 24	Zhang et al., 2011

Table 5-1 Details of samples from the Fuping Complex and Zanhuang Complex.

Sample No.	Rock type	Coordinate	Cal	Dol	Di	OI	Ms	Phl	Mt	Py
Fuping Complex										
15FP-07-2	Calc-silicate rock	E 113°49'19"; N 38°25'15"	+++	++	++		+	+		
15FP-08-1	Calc-silicate rock	E 113°49'10"; N 38°25'19"	+++	++	++		+	+		
15FP-08-2	Calc-silicate rock	E 113°49'10"; N 38°25'19"	+++	++	+		++	+		
15FP-09-1	Calc-silicate rock	E 113°50'41"; N 38°25'37"	+++	++	+	+	+	+		
15FP-09-2	Calc-silicate rock	E 113°50'41"; N 38°25'37"	+++	++	+		+	+	+	+
15FP-09-3	Dolomite-calcite marble	E 113°50'41"; N 38°25'37"	+++	++			+			
15FP-10-1	Dolomite-calcite marble	E 113°44'01"; N 38°26'34"	+++	+++			+			

15FP-11-1	Calc-silicate rock	E 113°43'55"; N 38°26'49"	+++	++	++			+	+		
15FP-11-3	Dolomite-calcite marble	E 113°43'55"; N 38°26'49"	+++	++	+						
15FP-12-1	Dolomite-calcite marble	E 113°43'43"; N 38°29'11"	+++	++				+			
15FP-12-2	Dolomite-calcite marble	E 113°43'43"; N 38°29'11"	+++	++				+			
15FP-13-1	Dolomite-calcite marble	E 113°41'57"; N 38°19'17"	+++	++				+			
15FP-13-2	Dolomite-calcite marble	E 113°41'57"; N 38°19'17"	+++	++				+			
15FP-13-3	Calc-silicate rock	E 113°41'57"; N 38°19'17"	+++	++	+	+		+	+	+	+
15FP-14-1	Dolomite-calcite marble	E 113°49'33"; N 38°30'05"	+++	++				+			
15FP-14-2	Calc-silicate rock	E 113°49'33"; N 38°30'05"	+++	++			++	+			+
15FP-14-3	Calc-silicate rock	E 113°49'33"; N 38°30'05"	+++	++			++	+			+
15FP-15	Dolomite-calcite marble	E 113°50'22"; N 38°31'09"	+++	++				+			
Zanhuang Complex											
ZH-9	Dolomite-calcite marble	E 114°14'45"; N 37°20'58"	+++	+++				+			
ZH-10	Dolomite-calcite marble	E 114°15'32"; N 37°20'13"	+++	+++				+			
ZH-15-1	Dolomite-calcite marble	E 114°17'27"; N 37°13'17"	+++	+++							
ZH-15-4	Dolomite-calcite marble	E 114°17'27"; N 37°13'17"	+++	+++							
ZH-15-5	Dolomite-calcite marble	E 114°17'27"; N 37°13'17"	+++	+++				+	+		

ZH-19-1	Dolomite marble	E 114°01'23"; N 37°08'27"	+++		+
ZH-19-2	Dolomite marble	E 114°01'23"; N 37°08'27"	+++	+	+

Mineral abbreviations: Cal, calcite; Dol, dolomite; Di, diopside; Ol, olivine; Ms, muscovite; Phl, phlogopite; Mt, magnetite; Py, pyrite.

+++ : abundant, ++ : moderate, + : rare.

Table 5-2 Major and trace element compositions for samples from the Fuping Complex and Zanhuang Complex

Sample No.	ZH-9	ZH-15 -1	ZH-19 -1	ZH-19 -2	15FP-07 -2	15FP-08 -2	15FP-09 -2	15FP-10 -1	15FP-12 -1	15FP-13 -1	15FP-13 -3	15FP-14 -1	15FP-15
Major elements (wt.%)													
SiO ₂	0.62	0.02	0.28	0.74	13.25	17.56	23.88	4.21	3.46	1.80	30.03	6.12	6.01
Al ₂ O ₃	0.27	0.07	0.21	0.32	2.87	3.49	4.26	0.10	0.21	0.23	5.17	1.30	1.03
CaO	30.11	30.26	0.34	0.44	26.77	32.69	29.41	29.62	29.57	30.10	23.37	28.53	28.35
Fe ₂ O ₃	0.04	0.03	0.04	0.04	0.18	0.29	0.76	0.03	0.01	0.02	0.38	0.21	0.12
FeO	0.36	0.20	1.25	1.55	0.80	0.83	1.33	0.40	0.39	0.25	1.21	0.27	0.27
K ₂ O	0.19	0.04	0.05	0.08	1.28	1.75	2.13	0.05	0.11	0.11	1.91	0.18	0.41
MgO	21.06	21.38	46.32	45.54	19.02	12.21	12.61	20.69	20.75	20.69	16.45	20.96	19.95
MnO	0.02	0.03	0.05	0.07	0.02	0.05	0.07	0.03	0.03	0.02	0.04	0.02	0.02

Na ₂ O	<0.01	<0.01	<0.01	<0.01	0.14	0.03	0.25	<0.01	<0.01	<0.01	0.85	0.11	0.17
P ₂ O ₅	0.01	0.03	0.03	0.04	0.13	0.09	0.12	0.04	0.02	0.04	0.14	0.04	0.06
CO ₂	45.12	46.67	49.54	49.26	32.77	27.72	21.61	42.88	43.30	44.84	17.12	39.65	41.26
H ₂ O+	1.30	1.10	1.44	1.24	2.00	2.48	2.48	1.30	1.28	1.46	1.78	1.66	1.42
LOI	46.14	47.41	51.37	50.86	34.49	29.84	23.49	43.68	44.06	45.73	18.53	41.00	42.33
Total	99.10	99.83	99.55	99.32	99.23	99.19	98.91	99.35	99.13	99.56	98.45	99.05	99.07

Trace elements (ppm)

Mn	125	228	287	455	148	350	499	229	212	123	267	118	105
Rb	1.78	0.35	0.38	0.90	36.5	55.4	55.6	0.71	1.94	2.25	61.7	7.22	6.65
Sr	50.8	25.7	2.25	2.74	80.2	201	154	59.9	58.2	51.0	154	64.8	46.7
Ba	6.84	4.19	0.81	1.35	718	1413	1678	8.93	12.4	19.2	2790	20.1	60.0
La	2.25	0.35	0.68	0.50	8.11	14.1	21.7	1.50	1.22	1.43	14.8	2.59	2.42
Ce	4.16	0.64	2.08	1.48	15.9	27.0	48.1	2.51	2.02	2.42	30.5	5.53	5.08
Pr	0.52	0.07	0.33	0.26	2.00	3.26	6.06	0.28	0.24	0.28	3.74	0.67	0.65
Nd	2.06	0.31	1.45	1.12	6.74	11.6	22.0	0.97	0.94	0.99	13.7	2.50	2.49
Sm	0.34	0.06	0.39	0.25	1.60	2.56	4.71	0.14	0.14	0.15	3.78	0.41	0.47
Eu	0.07	<0.05	0.06	0.07	0.34	0.63	1.10	0.05	0.05	<0.05	0.91	0.11	0.11

Gd	0.28	0.06	0.48	0.31	0.85	1.34	3.13	0.14	0.11	0.11	1.80	0.36	0.32
Tb	<0.05	<0.05	0.07	<0.05	0.13	0.19	0.46	<0.05	<0.05	<0.05	0.25	0.05	<0.05
Dy	0.26	0.06	0.36	0.23	0.61	0.98	2.38	0.09	0.09	0.09	1.27	0.27	0.29
Ho	<0.05	<0.05	0.07	0.05	0.11	0.18	0.45	<0.05	<0.05	<0.05	0.26	0.05	0.06
Er	0.13	0.05	0.18	0.13	0.35	0.51	1.21	<0.05	<0.05	<0.05	0.70	0.15	0.15
Tm	<0.05	<0.05	<0.05	<0.05	<0.05	0.08	0.19	<0.05	<0.05	<0.05	0.11	<0.05	<0.05
Yb	0.10	<0.05	0.13	0.10	0.30	0.51	1.17	<0.05	<0.05	<0.05	0.71	0.15	0.15
Lu	<0.05	<0.05	<0.05	<0.05	<0.05	0.08	0.17	<0.05	<0.05	<0.05	0.10	<0.05	<0.05
Y	1.68	0.68	2.56	1.93	3.13	5.12	12.5	0.59	0.51	0.59	6.90	1.67	2.18
Mn/Sr	2.46	8.87	128	166	1.85	1.74	3.24	3.82	3.64	2.41	1.73	1.82	2.25
Ca/Sr	4234	8410	1079	1147	2384	1161	1364	3532	3629	4216	1084	3145	4336
Fe/Sr	60.6	68.7	4445	4502	93.0	42.2	101.7	55.4	53.3	40.9	78.4	55.1	63.0
Mg/Ca	0.59	0.59	114.4	86.9	0.60	0.31	0.36	0.59	0.59	0.58	0.59	0.62	0.59

Table 5-3 Zircon U-Pb analytical data.

Sample Spot	Element (ppm)			Th/U	Isotope ratios						Age (Ma)				Concordance (%)		
	Pb*	Th	U		²⁰⁷ Pb/ ²³⁵ U	²⁰⁶ Pb/ ²³⁸ U	²⁰⁷ Pb/ ²⁰⁶ Pb	²⁰⁷ Pb/ ²³⁵ U	²⁰⁶ Pb/ ²³⁸ U	²⁰⁷ Pb/ ²⁰⁶ Pb	²⁰⁶ Pb/ ²³⁸ U	²⁰⁷ Pb/ ²⁰⁶ Pb	²⁰⁶ Pb/ ²⁰⁶ Pb				
15FP-07-2																	
15FP-07-2.03	203	348	365	0.95	9.0155	0.1148	0.4222	0.0041	0.1549	0.0017	2340	30	2270	22	2400	19	94
15FP-07-2.04	128	265	250	1.06	8.0528	0.1029	0.3936	0.0038	0.1484	0.0017	2237	29	2139	21	2328	19	91
15FP-07-2.05	122	133	222	0.60	9.6553	0.1258	0.4326	0.0042	0.1619	0.0018	2402	31	2317	23	2475	19	93
15FP-07-2.06	16	69	32	2.19	5.7350	0.0770	0.3310	0.0032	0.1257	0.0015	1937	26	1843	18	2038	21	89
15FP-07-2.07	60	76	137	0.55	6.1208	0.0781	0.3559	0.0035	0.1247	0.0014	1993	25	1962	19	2025	20	97
15FP-07-2.08	104	183	185	0.99	9.5769	0.1280	0.4288	0.0042	0.1620	0.0020	2395	32	2300	23	2477	20	92
15FP-07-2.10	67	47	113	0.42	10.8830	0.1474	0.4761	0.0050	0.1658	0.0019	2513	34	2510	26	2515	19	100
15FP-07-2.11	20	45	42	1.06	6.2848	0.0963	0.3507	0.0041	0.1300	0.0015	2016	31	1938	23	2097	20	92
15FP-07-2.13	17	55	40	1.38	5.7991	0.0959	0.3218	0.0038	0.1307	0.0016	1946	32	1799	21	2107	21	83
15FP-07-2.14	50	132	104	1.27	7.0585	0.0954	0.3523	0.0037	0.1453	0.0016	2119	29	1946	21	2291	19	82
15FP-07-2.15	20	51	42	1.21	6.8587	0.0897	0.3673	0.0035	0.1354	0.0016	2093	27	2017	19	2170	20	92
15FP-07-2.16	35	83	75	1.10	6.8832	0.0883	0.3508	0.0034	0.1423	0.0016	2096	27	1938	19	2256	20	84

15FP-07-2.17	98	74	233	0.32	7.1914	0.0932	0.3515	0.0035	0.1484	0.0017	2135	28	1942	19	2327	19	80
15FP-07-2.18	46	67	100	0.67	6.9761	0.0904	0.3684	0.0036	0.1373	0.0016	2108	27	2022	20	2194	20	91
15FP-07-2.19	152	301	263	1.15	8.9143	0.1141	0.4208	0.0041	0.1537	0.0017	2329	30	2264	22	2387	19	95
15FP-07-2.21	279	390	599	0.65	7.7912	0.1026	0.3650	0.0037	0.1548	0.0017	2207	29	2006	20	2400	19	80
15FP-07-2.22	69	99	141	0.71	7.7300	0.0990	0.3913	0.0038	0.1433	0.0016	2200	28	2129	21	2267	19	94
15FP-07-2.23	40	76	66	1.15	10.1491	0.1302	0.4454	0.0043	0.1653	0.0019	2448	31	2375	23	2510	19	94
15FP-07-2.24	104	142	170	0.84	10.4941	0.1343	0.4690	0.0045	0.1623	0.0018	2479	32	2479	24	2479	19	100
15FP-07-2.25	15	117	21	5.48	7.7174	0.1053	0.3735	0.0036	0.1498	0.0018	2199	30	2046	20	2344	21	85
15FP-07-2.26	14	73	24	3.03	7.7166	0.1092	0.3790	0.0037	0.1477	0.0018	2199	31	2072	20	2319	21	88
15FP-07-2.27	98	121	165	0.73	9.9741	0.1269	0.4556	0.0044	0.1588	0.0018	2432	31	2420	23	2443	19	99
15FP-07-2.28	324	307	578	0.53	9.8250	0.1253	0.4462	0.0043	0.1597	0.0018	2419	31	2378	23	2452	19	97
15FP-07-2.29	16	69	24	2.87	9.3003	0.1290	0.4429	0.0044	0.1523	0.0019	2368	33	2364	23	2372	21	100
15FP-07-2.30	62	183	160	1.14	4.8779	0.0650	0.3066	0.0031	0.1154	0.0013	1798	24	1724	17	1886	20	91
15FP-08-2																	
15FP-08-2.01	194	290	359	0.81	8.6398	0.1106	0.4265	0.0042	0.1469	0.0017	2301	29	2290	22	2311	19	99
15FP-08-2.03	161	731	426	1.72	5.1771	0.0669	0.2971	0.0029	0.1264	0.0014	1849	24	1677	17	2048	20	78
15FP-08-2.05	245	534	450	1.19	8.6442	0.1099	0.4108	0.0040	0.1526	0.0017	2301	29	2219	22	2375	19	93

15FP-08-2.06	171	362	401	0.90	6.5670	0.0847	0.3227	0.0032	0.1476	0.0016	2055	26	1803	18	2318	19	71
15FP-08-2.08	78	132	152	0.87	8.1639	0.1069	0.3954	0.0040	0.1497	0.0017	2249	29	2148	22	2343	19	91
15FP-08-2.11	114	68	267	0.25	7.1221	0.0916	0.3590	0.0035	0.1439	0.0016	2127	27	1977	19	2275	19	85
15FP-08-2.12	50	91	119	0.76	5.7041	0.0759	0.3442	0.0034	0.1202	0.0014	1932	26	1907	19	1959	20	97
15FP-08-2.13	79	122	198	0.62	5.6838	0.0729	0.3252	0.0032	0.1268	0.0014	1929	25	1815	18	2054	20	87
15FP-08-2.15	157	271	376	0.72	6.4080	0.0887	0.3320	0.0034	0.1400	0.0016	2033	28	1848	19	2227	20	79
15FP-08-2.16	220	275	481	0.57	7.2598	0.0942	0.3740	0.0036	0.1408	0.0016	2144	28	2048	20	2237	20	91
15FP-08-2.18	65	101	139	0.73	7.9297	0.1416	0.3430	0.0035	0.1677	0.0024	2223	40	1901	20	2535	24	67
15FP-08-2.19	186	210	488	0.43	6.0160	0.0785	0.3109	0.0030	0.1404	0.0016	1978	26	1745	17	2232	20	72
15FP-08-2.20	109	20	312	0.06	5.4378	0.0742	0.3076	0.0030	0.1282	0.0015	1891	26	1729	17	2073	21	80
15FP-08-2.21	153	123	325	0.38	7.8240	0.1011	0.3902	0.0038	0.1454	0.0016	2211	29	2124	21	2293	19	92
15FP-08-2.22	74	109	186	0.59	5.6462	0.0724	0.3293	0.0032	0.1244	0.0014	1923	25	1835	18	2020	20	90
15FP-08-2.23	141	158	366	0.43	5.5194	0.0716	0.3216	0.0031	0.1245	0.0014	1904	25	1797	18	2022	20	88
15FP-08-2.25	49	43	124	0.35	5.3346	0.0698	0.3342	0.0033	0.1158	0.0013	1874	25	1859	18	1892	21	98
15FP-08-2.26	251	326	408	0.80	10.2417	0.1323	0.4640	0.0046	0.1601	0.0018	2457	32	2457	24	2457	19	100
15FP-08-2.27	18	21	45	0.47	5.3361	0.0716	0.3370	0.0033	0.1148	0.0014	1875	25	1872	18	1877	22	100
15FP-08-2.28	160	192	433	0.44	5.3850	0.0689	0.3033	0.0030	0.1288	0.0014	1882	24	1707	17	2081	20	78

15FP-08-2.29	139	213	251	0.85	8.7809	0.1138	0.4108	0.0041	0.1550	0.0017	2316	30	2219	22	2402	19	92
15FP-08-2.30	88	122	215	0.57	5.7605	0.0752	0.3322	0.0032	0.1258	0.0015	1940	25	1849	18	2040	21	90
15FP-08-2.31	58	69	110	0.63	8.9203	0.1168	0.3893	0.0038	0.1662	0.0019	2330	31	2120	21	2519	20	81
15FP-08-2.32	24	19	49	0.40	7.3779	0.1003	0.3878	0.0038	0.1380	0.0016	2158	29	2112	21	2202	21	96
15FP-13-1																	
15FP-13-1.02	160	202	283	0.71	9.9583	0.1270	0.4480	0.0044	0.1612	0.0018	2431	31	2387	23	2468	19	97
15FP-13-1.06	84	155	128	1.22	11.2719	0.1465	0.4840	0.0049	0.1689	0.0019	2546	33	2545	26	2547	19	100
15FP-13-1.09	225	318	383	0.83	10.4912	0.1342	0.4571	0.0045	0.1665	0.0019	2479	32	2427	24	2522	19	96
15FP-13-1.11	86	133	140	0.95	10.4343	0.1402	0.4696	0.0049	0.1612	0.0018	2474	33	2482	26	2468	19	99
15FP-13-1.14	100	178	157	1.14	10.7591	0.1387	0.4740	0.0047	0.1646	0.0018	2503	32	2501	25	2504	19	100
15FP-13-1.15	316	444	786	0.57	5.8137	0.0918	0.3250	0.0040	0.1298	0.0015	1948	31	1814	23	2095	20	85
15FP-13-1.17	159	110	347	0.32	7.9454	0.1083	0.3813	0.0040	0.1511	0.0017	2225	30	2082	22	2359	19	87
15FP-13-1.18	97	384	205	1.87	7.6050	0.0985	0.3354	0.0034	0.1645	0.0018	2185	28	1864	19	2502	19	66
15FP-13-1.22	244	431	399	1.08	9.6626	0.1331	0.4514	0.0048	0.1553	0.0017	2403	33	2401	26	2405	19	100
15FP-13-1.23	173	252	287	0.88	10.2517	0.1312	0.4503	0.0045	0.1651	0.0018	2458	31	2397	24	2509	19	95
15FP-13-1.25	251	365	575	0.63	6.7791	0.0867	0.3408	0.0034	0.1443	0.0016	2083	27	1891	19	2279	19	79
15FP-13-1.26	145	437	301	1.45	8.1173	0.1096	0.3540	0.0038	0.1663	0.0019	2244	30	1954	21	2521	19	71

15FP-13-1.27	241	291	503	0.58	7.3298	0.0947	0.3808	0.0038	0.1396	0.0016	2152	28	2080	21	2222	19	93
15FP-13-1.28	94	182	187	0.98	8.7707	0.1205	0.3821	0.0043	0.1665	0.0019	2314	32	2086	23	2522	19	79
15FP-13-1.29	444	707	1017	0.69	7.0103	0.0967	0.3465	0.0038	0.1467	0.0016	2113	29	1918	21	2308	19	80
15FP-13-1.30	373	440	783	0.56	8.2664	0.1089	0.3598	0.0036	0.1666	0.0020	2261	30	1981	20	2524	20	73
ZH-9																	
ZH-9.02	959	426	2590	0.16	5.1021	0.0734	0.3258	0.0038	0.1136	0.0013	1836	26	1818	21	1857	20	98
ZH-9.04	544	205	1477	0.14	5.1850	0.0968	0.3241	0.0054	0.1160	0.0013	1850	35	1810	30	1896	20	95
ZH-9.05	235	177	583	0.30	5.9996	0.0833	0.3429	0.0037	0.1269	0.0014	1976	27	1900	20	2056	20	92
ZH-9.07	677	726	1266	0.57	8.7921	0.1126	0.4300	0.0043	0.1483	0.0017	2317	30	2306	23	2326	19	99
ZH-9.08	325	328	1001	0.33	4.4501	0.0586	0.2779	0.0028	0.1162	0.0013	1722	23	1581	16	1898	20	80
ZH-9.11	691	867	1928	0.45	4.8679	0.0624	0.3043	0.0030	0.1160	0.0013	1797	23	1712	17	1896	20	89
ZH-9.12	371	677	932	0.73	5.8510	0.0745	0.3271	0.0032	0.1297	0.0015	1954	25	1824	18	2094	20	85
ZH-9.13	459	268	1644	0.16	4.1646	0.0531	0.2411	0.0024	0.1253	0.0014	1667	21	1392	14	2033	20	54
ZH-9.18	245	309	513	0.60	7.2846	0.0933	0.3942	0.0039	0.1340	0.0015	2147	28	2142	21	2151	20	100
ZH-9.22	157	132	268	0.49	11.1962	0.1565	0.4739	0.0049	0.1714	0.0020	2540	36	2501	26	2571	19	97
ZH-9.24	515	878	1115	0.79	7.3583	0.0998	0.3821	0.0038	0.1397	0.0017	2156	29	2086	20	2223	21	93
ZH-9.26	141	265	364	0.73	6.1461	0.0855	0.3096	0.0033	0.1440	0.0017	1997	28	1739	18	2275	20	69

ZH-9.30 234 340 787 0.43 4.3468 0.0564 0.2461 0.0025 0.1281 0.0014 1702 22 1418 14 2072 20 54

Table 5-4 Carbon and Oxygen isotopic compositions for samples in this study.

Sample No.	$\delta^{13}\text{C}_{\text{VPDB}}$	error	$\delta^{18}\text{O}_{\text{VPDB}}$	error	Sample No.	$\delta^{13}\text{C}_{\text{VPDB}}$	error	$\delta^{18}\text{O}_{\text{VPDB}}$	error
ZH-9	-2.68	0.11	-7.76	0.24	15FP-10-1	3.65	0.17	-5.39	0.60
ZH-10	0.33	0.15	-11.77	0.41	15FP-11-1	3.30	0.16	-5.84	0.72
ZH-15-1	1.33	0.14	-10.85	0.23	15FP-11-3	2.89	0.16	-6.37	0.53
ZH-15-4	1.44	0.14	-11.12	0.36	15FP-12-1	3.55	0.16	-3.96	0.73
ZH-15-5	0.57	0.14	-8.17	0.40	15FP-12-2	2.86	0.15	-4.97	0.46
ZH-19-1	-3.31	0.09	-12.98	0.29	15FP-13-1	3.54	0.18	-2.96	0.42
ZH-19-2	-3.69	0.09	-13.59	0.27	15FP-13-2	3.27	0.16	-3.75	0.45
15FP-07-2	-0.65	0.13	-8.83	0.36	15FP-13-3	-1.28	0.12	-8.88	0.60
15FP-08-1	-0.31	0.12	-9.12	0.34	15FP-14-1	2.96	0.15	-7.25	0.51
15FP-08-2	-1.56	0.13	-12.89	0.29	15FP-14-2	1.99	0.14	-6.34	0.58
15FP-09-1	-0.98	0.12	-10.43	0.60	15FP-14-3	1.99	0.15	-6.47	0.45
15FP-09-2	-0.33	0.13	-7.93	0.43	15FP-15	3.27	0.21	-3.97	0.64
15FP-09-3	0.84	0.25	-5.77	0.45					

Table 6-1 Bulk rock compositions (wt.%) of mafic granulites from the Fuping Complex.

Sample No.	SiO ₂	Al ₂ O ₃	CaO	Fe ₂ O ₃	FeO	K ₂ O	MgO	MnO	Na ₂ O	P ₂ O ₅	TiO ₂	CO ₂	H ₂ O+	LOI	Total
15FP-02	53.23	12.13	4.30	9.22	11.25	2.70	3.05	0.18	1.31	0.20	0.50	0.42	1.24	0.64	100.37
15FP-03	48.88	12.68	8.15	4.48	11.88	2.57	5.21	0.26	1.38	0.25	1.95	0.30	1.20	0.72	99.91
15FP-06	48.48	14.09	11.17	3.07	9.28	0.82	7.39	0.18	2.39	0.06	0.90	0.30	1.28	1.09	100.50

Table 6-2. EPMA data of garnet.

No.	56	57	58	59	71	72	81	82	1	2	3	4	5	6	7	8
Sample No.	15FP-02															
Comment	core	core	rim	rim	core	rim	Grt	Grt	line 17	line 18	line 19	line 20	line 21	line 22	line 23	line 24
SiO ₂	38.04	38.18	37.85	38.17	38.15	37.66	37.46	38.17	38.21	38.35	37.54	37.46	37.96	37.91	36.08	38.33
Al ₂ O ₃	20.49	20.07	20.71	20.19	20.29	20.71	20.78	20.67	20.64	20.90	20.37	20.39	20.59	20.52	19.75	20.47
TiO ₂	-	0.02	-	-	0.02	-	-	0.01	0.02	-	-	0.03	-	0.01	-	0.06
Cr ₂ O ₃	0.03	0.02	0.10	0.01	0.03	0.01	0.02	0.01	0.03	0.03	0.04	-	0.01	0.04	0.02	0.05
FeO	29.61	29.98	29.38	29.74	29.12	29.52	29.68	30.10	29.58	29.55	28.64	27.95	29.13	28.67	29.27	29.01
MnO	0.66	0.61	0.97	1.07	0.74	1.24	1.42	1.45	1.18	1.18	0.91	0.77	0.71	0.79	1.03	0.83
NiO	0.03	0.05	0.03	-	0.03	-	-	0.07	0.04	-	-	-	0.03	0.05	-	-

MgO	3.75	3.78	3.82	3.88	3.63	3.77	3.74	3.81	3.57	3.74	4.01	3.89	4.15	4.04	4.00	4.29
CaO	7.26	7.46	7.06	7.10	8.38	6.97	6.42	6.70	6.95	7.35	7.38	7.39	7.44	7.75	6.85	7.59
Na ₂ O	-	-	0.07	0.02	0.04	0.03	-	-	-	0.08	0.07	0.12	-	0.03	0.04	-
Total	99.88	100.17	100.01	100.17	100.43	99.92	99.52	100.97	100.22	101.20	98.99	98.06	100.01	99.82	97.06	100.62
Si	3.02	3.03	3.00	3.03	3.02	3.00	2.99	3.01	3.03	3.01	3.01	3.02	3.01	3.01	2.97	3.02
Al	1.92	1.88	1.94	1.89	1.89	1.94	1.96	1.92	1.93	1.93	1.92	1.94	1.92	1.92	1.92	1.90
Fe ²⁺	1.97	1.99	1.95	1.97	1.93	1.96	1.98	1.98	1.96	1.94	1.92	1.88	1.93	1.90	2.01	1.91
Mn	0.04	0.04	0.07	0.07	0.05	0.08	0.10	0.10	0.08	0.08	0.06	0.05	0.05	0.05	0.07	0.06
Mg	0.44	0.45	0.45	0.46	0.43	0.45	0.45	0.45	0.42	0.44	0.48	0.47	0.49	0.48	0.49	0.50
Ca	0.62	0.63	0.60	0.60	0.71	0.59	0.55	0.57	0.59	0.62	0.63	0.64	0.63	0.66	0.60	0.64
Na	-	-	0.01	-	0.01	-	-	-	-	0.01	0.01	0.02	-	0.01	0.01	-
Total	8.02	8.03	8.03	8.03	8.04	8.03	8.03	8.03	8.01	8.03	8.04	8.02	8.03	8.03	8.07	8.03
Alm%	64	64	64	64	62	64	65	64	64	63	62	62	62	62	63	61
Pyr%	14	14	15	15	14	14	14	14	14	14	15	15	16	15	15	16
Grs%	20	20	20	19	23	19	18	18	19	20	20	21	20	21	19	21
Sps%	1	1	2	2	2	3	3	3	3	3	2	2	2	2	2	2

Table 6-2 continued

No.	9	10	11	12	13	14	15	16	18	19	20	21	22	23	24	25
Sample No.	15FP-02															
Comment	line 25	line 26	line 27	line 28	line 29	line 30	line 31	line 32	line 34	line 35	line 36	line 37	line 38	line 39	line 40	line 41
SiO ₂	37.80	37.93	37.35	37.40	38.27	38.04	37.86	37.25	37.65	37.68	37.46	38.03	37.86	37.11	38.33	37.48
Al ₂ O ₃	20.56	20.54	20.41	20.27	20.81	20.59	20.31	20.09	20.71	20.42	20.85	20.54	20.60	20.68	20.57	20.42
TiO ₂	0.04	0.01	-	-	-	-	0.08	0.07	0.05	0.01	-	-	0.01	-	0.02	0.01
Cr ₂ O ₃	-	0.04	0.03	-	0.02	-	0.01	0.05	0.03	-	0.08	-	-	0.05	0.08	-
FeO	28.33	28.90	28.96	28.63	28.94	29.18	29.65	29.99	29.17	29.07	29.06	29.23	29.86	29.09	29.55	29.19
MnO	0.74	0.82	0.78	0.84	0.98	0.90	1.05	0.92	0.86	0.87	0.86	0.94	0.92	1.01	1.07	0.94
MgO	4.30	4.05	4.37	4.10	3.94	3.93	3.65	3.90	4.13	3.93	4.13	4.06	4.05	4.08	3.84	4.02
CaO	7.47	7.38	7.32	7.13	7.54	7.44	7.31	7.33	6.51	7.09	6.91	6.87	6.73	6.87	7.40	6.94
Na ₂ O	-	0.06	0.02	0.14	0.04	0.06	0.01	0.03	0.02	0.03	0.06	0.03	0.02	0.04	0.04	0.03
Total	99.24	99.72	99.24	98.52	100.56	100.22	99.93	99.63	99.12	99.12	99.41	99.70	100.07	98.95	100.89	99.02
Si	3.01	3.01	2.99	3.01	3.01	3.01	3.01	2.99	3.01	3.01	2.99	3.02	3.01	2.98	3.02	3.00
Al	1.93	1.92	1.92	1.92	1.93	1.92	1.91	1.90	1.95	1.92	1.96	1.92	1.93	1.96	1.91	1.93
Fe ²⁺	1.89	1.92	1.94	1.93	1.91	1.93	1.97	2.01	1.95	1.94	1.94	1.94	1.98	1.95	1.94	1.96

Mn	0.05	0.06	0.05	0.06	0.07	0.06	0.07	0.06	0.06	0.06	0.06	0.06	0.06	0.07	0.07	0.06
Mg	0.51	0.48	0.52	0.49	0.46	0.46	0.43	0.47	0.49	0.47	0.49	0.48	0.48	0.49	0.45	0.48
Ca	0.64	0.63	0.63	0.61	0.64	0.63	0.62	0.63	0.56	0.61	0.59	0.58	0.57	0.59	0.62	0.60
Na	-	0.01	-	0.02	0.01	0.01	-	-	-	0.01	0.01	-	-	0.01	0.01	-
Total	8.02	8.03	8.05	8.04	8.02	8.04	8.03	8.06	8.02	8.03	8.04	8.02	8.03	8.05	8.03	8.03
Alm%	61	62	62	62	62	63	64	63	64	63	63	63	64	63	63	63
Pyr%	17	16	17	16	15	15	14	15	16	15	16	16	15	16	15	16
Grs%	21	20	20	20	21	20	20	20	18	20	19	19	18	19	20	19
Sps%	2	2	2	2	2	2	2	2	2	2	2	2	2	2	2	2

Table 6-2 continued

No.	26	27	29	30	29	30	44	45	46	47	48	49	58	59	27	28								
Sample No.	15FP-02				15FP-03																			
Comment			mantle		rim		rim		mantle		mantle		core		core		rim		rim		line 27		line 28	
SiO ₂	37.49	38.17	37.67	37.58	38.09	37.88	38.21	37.97	38.42	38.35	37.98	38.09	38.35	38.43	37.69	36.30								
Al ₂ O ₃	20.75	20.74	20.44	20.44	20.99	20.60	20.81	20.55	21.24	21.56	20.96	20.86	20.86	21.15	20.90	19.78								
TiO ₂	-	0.03	0.07	-	-	-	-	0.02	0.12	-	0.07	0.08	0.01	0.01	-	-								

Cr ₂ O ₃	0.01	0.05	0.01	0.02	-	0.05	0.03	0.01	0.03	-	0.01	0.07	0.04	-	-	0.04
FeO	29.31	29.35	29.23	29.32	28.26	27.92	27.33	26.54	26.09	26.43	26.72	26.83	26.08	26.50	28.28	27.08
MnO	1.01	0.98	1.05	1.23	3.52	3.68	2.28	2.30	1.67	1.69	2.05	2.03	1.46	1.41	2.45	2.09
MgO	4.13	3.90	4.08	4.02	3.05	2.99	3.60	3.41	3.00	3.04	2.94	2.91	3.47	3.33	3.44	3.52
CaO	6.84	7.01	7.30	6.93	7.01	7.04	8.99	9.49	11.00	10.44	10.14	9.83	10.07	9.99	7.16	8.70
Na ₂ O	0.03	0.06	0.04	0.04	-	0.01	-	0.04	0.02	-	-	0.01	-	0.04	-	-
Total	99.57	100.29	99.89	99.57	100.92	100.16	101.26	100.34	101.59	101.52	100.89	100.74	100.39	100.91	99.95	97.50
Si	2.99	3.02	3.00	3.00	3.01	3.02	3.00	3.00	2.99	2.99	2.99	3.00	3.01	3.01	3.00	2.97
Al	1.95	1.93	1.92	1.92	1.95	1.93	1.92	1.92	1.95	1.98	1.94	1.94	1.93	1.95	1.96	1.91
Fe ²⁺	1.95	1.94	1.94	1.96	1.87	1.86	1.79	1.75	1.70	1.72	1.76	1.77	1.71	1.73	1.88	1.85
Mn	0.07	0.07	0.07	0.08	0.24	0.25	0.15	0.15	0.11	0.11	0.14	0.14	0.10	0.09	0.16	0.14
Mg	0.49	0.46	0.48	0.48	0.36	0.36	0.42	0.40	0.35	0.35	0.34	0.34	0.41	0.39	0.41	0.43
Ca	0.58	0.59	0.62	0.59	0.59	0.60	0.75	0.80	0.92	0.87	0.85	0.83	0.85	0.84	0.61	0.76
Na	-	0.01	0.01	0.01	-	-	-	0.01	-	-	-	-	-	-	0.01	-
Total	8.04	8.02	8.04	8.04	8.02	8.02	8.04	8.04	8.03	8.02	8.03	8.02	8.02	8.02	8.02	8.07
Alm%	63	63	62	63	61	61	57	56	55	56	57	58	56	57	61	58
Pyr%	16	15	15	15	12	12	13	13	11	12	11	11	13	13	13	13

Grs%	19	19	20	19	19	20	24	26	30	29	28	27	28	27	20	24
Sps%	2	2	2	3	8	8	5	5	4	4	4	4	3	3	5	5

Table 6-2 continued

No.	29	30	31	32	33	37	38	39	40	41	42	43	44	45	46
Sample No.	15FP-03														
Comment	line 29	line 30	line 31	line 32	line 33	line 37	line 38	line 39	line 40	line 41	line 42	line 43	line 44	line 45	line 46
SiO ₂	37.03	37.98	37.64	37.68	37.07	37.51	37.85	37.26	37.23	37.62	37.74	37.71	37.77	37.79	37.70
Al ₂ O ₃	20.19	20.75	20.87	20.86	20.56	20.28	20.69	20.87	20.92	20.95	20.89	20.60	20.48	20.62	20.73
TiO ₂	0.05	0.05	0.07	0.02	0.10	0.05	0.10	0.04	0.06	0.03	-	0.05	0.07	-	0.11
Cr ₂ O ₃	0.08	-	0.03	0.10	0.04	0.06	0.01	0.02	-	0.04	0.05	-	-	0.01	0.04
FeO	25.12	26.11	25.06	25.08	24.97	24.54	25.01	24.54	24.88	24.73	25.89	26.75	26.82	27.31	26.74
MnO	1.72	1.74	1.50	1.24	1.48	1.74	1.62	1.48	1.44	1.49	1.71	1.80	1.78	1.68	1.84
NiO	0.04	-	0.02	0.02	-	-	0.02	-	0.01	-	-	-	0.07	-	-
MgO	3.35	3.18	2.90	2.73	2.65	2.61	2.74	2.79	2.70	3.21	3.36	3.56	3.49	3.78	3.70
CaO	9.83	10.05	11.20	12.05	11.79	11.81	11.75	11.70	11.33	11.05	9.74	8.76	8.86	8.12	8.50
Total	97.42	99.87	99.28	99.81	98.71	98.61	99.82	98.72	98.60	99.11	99.37	99.23	99.35	99.33	99.35

Si	3.00	3.01	2.99	2.99	2.98	3.01	3.00	2.98	2.98	2.99	3.00	3.01	3.01	3.01	3.00
Al	1.93	1.94	1.96	1.95	1.95	1.92	1.93	1.97	1.98	1.96	1.96	1.94	1.92	1.94	1.94
Fe ²⁺	1.70	1.73	1.67	1.66	1.68	1.65	1.66	1.64	1.67	1.64	1.72	1.78	1.79	1.82	1.78
Mn	0.12	0.12	0.10	0.08	0.10	0.12	0.11	0.10	0.10	0.10	0.11	0.12	0.12	0.11	0.12
Mg	0.40	0.37	0.34	0.32	0.32	0.31	0.32	0.33	0.32	0.38	0.40	0.42	0.41	0.45	0.44
Ca	0.85	0.85	0.95	1.02	1.01	1.01	1.00	1.00	0.97	0.94	0.83	0.75	0.76	0.69	0.72
Total	8.03	8.02	8.02	8.04	8.05	8.03	8.03	8.03	8.03	8.02	8.02	8.02	8.02	8.02	8.02
Alm%	55	56	54	54	54	53	54	53	54	54	56	58	58	59	58
Pyr%	13	12	11	10	10	10	10	11	11	12	13	14	13	15	14
Grs%	28	28	31	33	33	33	32	33	32	31	27	24	25	23	24
Sps%	4	4	3	3	3	4	4	3	3	3	4	4	4	4	4

Table 6-2 continued

No.	47	48	49	50	51	52	53	54	55	56	74	78	79	80	81	82
Sample	15FP-03										15FP-06					
Comment	line 47	line 48	line 49	line 50	line 51	line 52	line 53	line 54	line 55	line 56	line 74	line 78	line 79	line 80	line 81	line 82
SiO ₂	37.13	37.63	37.42	37.05	37.26	37.75	38.03	37.59	37.24	36.49	37.73	37.78	37.57	37.71	37.69	37.73

Al ₂ O ₃	20.47	20.37	20.95	20.45	20.70	20.63	20.59	20.69	20.74	20.01	20.42	20.47	20.60	20.72	20.45	20.46
TiO ₂	0.02	-	0.06	0.04	0.07	0.09	0.08	0.03	0.03	0.09	0.02	-	-	-	-	-
FeO	27.37	26.16	27.35	26.35	25.12	25.65	25.56	25.00	27.36	28.65	28.84	28.84	27.67	27.14	27.43	27.71
MnO	1.88	1.86	1.82	1.70	1.72	1.58	1.60	1.76	2.42	2.78	1.46	1.57	1.33	1.00	0.97	0.87
MgO	4.01	3.63	3.59	3.52	3.36	3.29	3.31	3.14	3.50	3.32	3.58	3.67	3.61	3.66	3.89	3.92
CaO	7.74	8.84	8.40	8.89	10.52	10.36	10.40	10.69	7.80	6.78	7.32	7.39	8.45	9.03	8.98	8.76
Na ₂ O	0.01	-	0.02	-	-	-	0.01	-	-	0.04	-	-	-	-	0.01	-
Total	98.69	98.55	99.64	98.01	98.73	99.38	99.57	98.92	99.15	98.20	99.46	99.76	99.25	99.25	99.42	99.48
Si	2.98	3.02	2.98	2.99	2.98	3.00	3.01	3.00	2.98	2.98	3.01	3.01	3.00	3.00	3.00	3.00
Al	1.94	1.92	1.97	1.95	1.95	1.93	1.92	1.95	1.96	1.92	1.92	1.92	1.94	1.94	1.92	1.92
Fe ²⁺	1.84	1.75	1.82	1.78	1.68	1.70	1.69	1.67	1.83	1.95	1.93	1.92	1.85	1.81	1.83	1.84
Mn	0.13	0.13	0.12	0.12	0.12	0.11	0.11	0.12	0.16	0.19	0.10	0.11	0.09	0.07	0.07	0.06
Mg	0.48	0.43	0.43	0.42	0.40	0.39	0.39	0.37	0.42	0.40	0.43	0.44	0.43	0.43	0.46	0.47
Ca	0.67	0.76	0.72	0.77	0.90	0.88	0.88	0.91	0.67	0.59	0.63	0.63	0.72	0.77	0.77	0.75
Total	8.05	8.02	8.04	8.03	8.04	8.03	8.02	8.02	8.03	8.06	8.02	8.03	8.03	8.02	8.04	8.04
Alm%	59	57	59	58	54	55	55	54	59	62	63	62	60	59	59	59
Pyr%	15	14	14	14	13	13	13	12	14	13	14	14	14	14	15	15

Grs%	21	25	23	25	29	29	29	30	22	19	20	20	23	25	25	24
Sps%	4	4	4	4	4	3	3	4	5	6	3	3	3	2	2	2

Table 6-2 continued

No.	83	84	85	86	87	88	89	90	91	92	93	94	95	96	97	98	99	100
Sample	15FP-06																	
SiO ₂	37.23	37.55	37.66	37.79	37.70	37.55	37.91	37.65	38.20	37.78	37.93	37.65	37.47	36.91	37.73	37.44	37.62	38.18
Al ₂ O ₃	20.32	20.22	20.53	20.43	20.07	20.11	20.13	20.19	20.46	20.34	20.35	20.03	20.24	19.97	20.53	20.54	20.47	20.62
TiO ₂	0.06	0.05	0.08	0.03	0.02	0.02	-	0.06	0.05	0.03	0.10	0.09	0.02	0.01	0.02	0.02	0.04	0.04
Cr ₂ O ₃	0.02	-	0.02	-	0.06	0.03	0.01	0.01	-	0.04	0.05	0.03	0.02	-	-	-	0.04	-
FeO	27.27	27.28	27.57	26.83	27.15	27.25	27.50	27.67	27.55	27.50	27.72	27.04	27.38	28.01	26.98	28.11	27.44	26.54
MnO	0.74	0.65	0.70	0.67	0.66	0.69	0.72	0.69	0.68	0.67	0.63	0.72	0.85	0.83	0.81	0.95	1.02	1.33
NiO	0.01	0.02	-	-	-	0.03	-	0.04	-	0.04	0.01	-	-	0.06	0.01	0.03	-	0.03
MgO	3.86	3.84	3.75	3.71	3.47	3.72	3.68	3.78	3.68	3.71	3.63	3.60	3.74	3.98	3.53	3.68	3.60	3.45
CaO	9.24	9.38	9.12	9.63	9.73	9.46	9.30	9.25	9.13	9.31	9.25	9.39	9.30	8.74	9.56	8.35	8.97	9.21
Na ₂ O	-	0.01	-	-	-	0.02	0.02	0.03	0.03	-	0.02	-	-	-	-	0.04	0.02	0.01
Total	98.75	99.00	99.43	99.09	98.86	98.88	99.27	99.36	99.78	99.42	99.68	98.56	99.01	98.50	99.17	99.16	99.22	99.40

Si	2.99	3.00	3.00	3.01	3.02	3.01	3.02	3.00	3.03	3.01	3.01	3.02	3.00	2.98	3.01	3.00	3.00	3.03
Al	1.92	1.91	1.93	1.92	1.89	1.90	1.89	1.90	1.91	1.91	1.90	1.89	1.91	1.90	1.93	1.94	1.93	1.93
Fe ²⁺	1.83	1.82	1.83	1.79	1.82	1.82	1.83	1.85	1.82	1.83	1.84	1.81	1.83	1.89	1.80	1.88	1.83	1.76
Mn	0.05	0.04	0.05	0.05	0.04	0.05	0.05	0.05	0.05	0.05	0.04	0.05	0.06	0.06	0.05	0.06	0.07	0.09
Mg	0.46	0.46	0.44	0.44	0.41	0.44	0.44	0.45	0.43	0.44	0.43	0.43	0.45	0.48	0.42	0.44	0.43	0.41
Ca	0.79	0.80	0.78	0.82	0.83	0.81	0.79	0.79	0.77	0.79	0.79	0.81	0.80	0.76	0.82	0.72	0.77	0.78
Total	8.05	8.04	8.03	8.03	8.03	8.04	8.03	8.04	8.02	8.03	8.03	8.02	8.04	8.07	8.03	8.04	8.03	8.00
Alm%	58	58	59	58	58	58	59	59	59	59	59	59	58	59	58	61	59	58
Pyr%	15	15	14	14	13	14	14	14	14	14	14	14	14	15	14	14	14	13
Grs%	25	26	25	27	27	26	26	25	25	26	25	26	25	24	26	23	25	26
Sps%	2	1	2	1	1	1	2	1	1	1	1	2	2	2	2	2	2	3

Table 6-3 EMPA data of amphibole.

No.	3	4	52	53	68	63	64	76	78	79	14	15	50	1	2	3
Sample												15FP-02	15FP-03	15FP-03	15FP-03	15FP-03
Comment	PG	PG	PG	PG	PG	RG	RG	RG	RG	RG	RG	RG	PG	PG	RG	RG
SiO ₂	40.09	40.48	41.46	42.11	42.41	40.66	40.41	41.09	41.15	41.65	40.73	40.57	41.40	41.57	40.88	40.97
Al ₂ O ₃	12.44	12.83	11.71	11.84	11.22	11.91	12.04	11.44	11.58	11.53	11.78	11.33	11.14	11.24	11.54	11.56
TiO ₂	0.60	0.56	1.12	1.12	0.96	1.04	1.02	1.15	0.94	0.92	0.93	0.87	2.06	2.11	2.17	2.12
FeO	18.61	18.40	20.27	20.07	19.52	20.85	20.76	20.92	21.01	20.96	20.60	20.30	20.73	20.42	20.37	20.37
MnO	0.06	0.07	0.03	0.05	0.08	0.11	0.09	0.09	0.12	0.13	0.12	0.11	0.21	0.24	0.24	0.24
MgO	9.24	8.95	8.02	8.09	7.86	7.46	7.51	7.62	8.00	8.10	7.80	8.05	7.89	7.75	7.64	7.72
CaO	11.24	11.22	11.41	11.41	10.91	11.22	11.25	11.22	11.24	11.46	11.20	11.05	11.22	11.32	11.30	11.33
Na ₂ O	1.44	1.37	1.33	1.17	1.15	1.40	1.43	1.41	1.34	1.39	1.25	1.33	1.41	1.49	1.53	1.49
K ₂ O	1.72	1.66	1.59	1.50	1.64	1.83	1.83	1.81	1.74	1.77	1.60	1.59	1.63	1.63	1.80	1.79
Total	95.44	95.60	96.95	97.39	95.89	96.53	96.42	96.87	97.11	97.99	96.04	95.25	97.78	97.78	97.56	97.61
Si	6.27	6.30	6.41	6.45	6.58	6.35	6.33	6.40	6.39	6.40	6.38	6.40	6.37	6.39	6.32	6.32
Al	2.29	2.35	2.13	2.14	2.05	2.19	2.22	2.10	2.12	2.09	2.17	2.11	2.02	2.04	2.10	2.10
Ti	0.07	0.07	0.13	0.13	0.11	0.12	0.12	0.13	0.11	0.11	0.11	0.10	0.24	0.24	0.25	0.25

Fe ²⁺	2.43	2.40	2.62	2.57	2.53	2.72	2.72	2.72	2.73	2.69	2.70	2.68	2.67	2.62	2.63	2.63
Mn	0.01	0.01	-	0.01	0.01	0.01	0.01	0.01	0.02	0.02	0.02	0.01	0.03	0.03	0.03	0.03
Mg	2.15	2.08	1.85	1.85	1.82	1.74	1.75	1.77	1.85	1.85	1.82	1.89	1.81	1.77	1.76	1.77
Ca	1.88	1.87	1.89	1.87	1.81	1.88	1.89	1.87	1.87	1.89	1.88	1.87	1.85	1.86	1.87	1.87
Na	0.44	0.41	0.40	0.35	0.35	0.42	0.43	0.42	0.40	0.41	0.38	0.41	0.42	0.45	0.46	0.44
K	0.34	0.33	0.31	0.29	0.32	0.36	0.36	0.36	0.34	0.35	0.32	0.32	0.32	0.32	0.36	0.35
Total	15.90	15.82	15.75	15.67	15.61	15.82	15.84	15.81	15.82	15.82	15.77	15.80	15.74	15.73	15.78	15.78

Table 6-3 continued

No.	4	5	40	41	52	53	60	70	71	67	68
Sample	15FP-03	15FP-03	15FP-03	15FP-03	15FP-03	15FP-03	15FP-06	15FP-06	15FP-06	15FP-06	15FP-06
Comment	RG	RG	RG	RG	RG	RG	PK	PK	PK	RG	RG
SiO ₂	41.16	41.45	41.43	41.70	42.18	41.17	42.17	41.58	41.94	54.44	52.99
Al ₂ O ₃	11.79	11.77	11.49	11.35	10.81	11.21	10.48	10.52	10.48	0.51	0.29
TiO ₂	2.26	2.34	2.04	1.96	1.99	1.98	1.84	2.28	2.18	0.01	0.05
FeO	20.21	20.31	20.12	20.28	20.34	20.80	19.29	19.01	19.23	19.12	21.69
MnO	0.17	0.26	0.21	0.25	0.22	0.21	0.14	0.18	0.16	0.08	0.17

NiO	0.05	0.01	0.02	-	0.10	-	0.02	0.02	-	0.05	-
MgO	7.75	7.72	7.99	7.98	8.25	7.97	8.85	8.61	8.62	11.71	9.99
CaO	11.22	11.32	11.33	11.38	11.44	11.33	10.98	11.00	11.05	10.61	11.86
Na ₂ O	1.41	1.48	1.55	1.43	1.34	1.44	1.57	1.77	1.67	0.13	0.08
K ₂ O	1.74	1.79	1.72	1.69	1.45	1.61	0.82	0.78	0.82	0.06	0.01
Total	97.84	98.43	97.96	98.01	98.14	97.71	96.20	95.76	96.17	96.72	97.11
Si	6.32	6.33	6.35	6.39	6.45	6.35	6.51	6.46	6.49	8.09	7.99
Al	2.13	2.12	2.08	2.05	1.95	2.04	1.91	1.93	1.91	0.09	0.05
Ti	0.26	0.27	0.24	0.23	0.23	0.23	0.21	0.27	0.25	-	0.01
Fe ²⁺	2.59	2.59	2.58	2.60	2.60	2.68	2.49	2.47	2.49	2.37	2.73
Mn	0.02	0.03	0.03	0.03	0.03	0.03	0.02	0.02	0.02	0.01	0.02
Mg	1.77	1.76	1.82	1.82	1.88	1.83	2.04	1.99	1.98	2.59	2.24
Ca	1.84	1.85	1.86	1.87	1.87	1.87	1.82	1.83	1.83	1.69	1.92
Na	0.42	0.44	0.46	0.43	0.40	0.43	0.47	0.53	0.50	0.04	0.02
K	0.34	0.35	0.34	0.33	0.28	0.32	0.16	0.16	0.16	0.01	-
Total	15.73	15.74	15.77	15.74	15.69	15.77	15.63	15.66	15.63	14.89	14.99

Table 6-4 EMPA data of plagioclase.

No.	54	55	69	5	6	77	13	16	17	20	21	22	11	12	20
Sample	15FP-02								15FP-03	15FP-03	15FP-03	15FP-03	15FP-03	15FP-03	
Comment	PG	PG	PK	PK	PK	RG	RG	RG	RG	PG	PG	PG	PK	PK	PK
SiO ₂	57.40	57.23	57.88	57.51	57.73	57.60	57.33	57.50	56.40	57.63	57.08	56.61	57.72	57.24	56.49
Al ₂ O ₃	26.26	26.74	26.50	26.20	26.09	26.01	26.19	26.44	26.00	27.11	26.99	27.32	26.80	26.78	26.75
FeO	0.18	0.20	0.20	0.05	0.16	0.14	0.26	0.19	0.18	0.50	0.51	0.41	0.16	0.12	0.22
MnO	-	-	-	-	-	-	0.03	0.01	-	0.03	0.05	0.07	0.01	0.03	-
MgO	0.03	-	-	-	-	-	-	-	-	-	0.02	0.01	-	0.02	-
CaO	9.13	9.30	8.88	8.35	8.53	8.51	8.61	8.59	8.50	9.47	9.15	9.40	9.21	9.26	9.22
Na ₂ O	6.17	6.36	6.43	6.56	6.65	6.70	6.61	6.64	6.50	6.33	6.22	6.12	6.50	6.43	5.95
K ₂ O	0.20	0.18	0.25	0.37	0.35	0.32	0.14	0.15	0.15	0.19	0.18	0.18	0.16	0.17	0.15
Total	99.41	100.01	100.19	99.07	99.50	99.27	99.19	99.59	97.74	101.30	100.20	100.13	100.64	100.06	98.88
Si	2.59	2.57	2.59	2.60	2.60	2.60	2.59	2.59	2.59	2.56	2.56	2.54	2.58	2.57	2.56
Al	1.40	1.41	1.40	1.40	1.39	1.38	1.40	1.40	1.41	1.42	1.43	1.45	1.41	1.42	1.43
Fe ²⁺	0.01	0.01	0.01	-	0.01	0.01	0.01	0.01	0.01	0.02	0.02	0.02	0.01	-	0.01
Ca	0.44	0.45	0.43	0.40	0.41	0.41	0.42	0.41	0.42	0.45	0.44	0.45	0.44	0.45	0.45

Na	0.54	0.55	0.56	0.57	0.58	0.59	0.58	0.58	0.58	0.54	0.54	0.53	0.56	0.56	0.52
K	0.01	0.01	0.01	0.02	0.02	0.02	0.01	0.01	0.01	0.01	0.01	0.01	0.01	0.01	0.01
Total	4.99	5.00	5.00	5.00	5.01	5.01	5.00	5.00	5.00	5.01	5.00	5.00	5.00	5.01	4.99
An%	44	44	43	40	41	41	42	41	42	45	44	45	44	44	46
Ab%	54	55	56	57	57	58	58	58	58	54	55	54	56	55	53
Or%	1	1	1	2	2	2	1	1	1	1	1	1	1	1	1

Table 6-4 continued

No.	26	27	38	39	13	14	42	43	28	72	65	66	106	107
Sample	15FP-03								15FP-06	15FP-06	15FP-06	15FP-06	15FP-06	15FP-06
Comment	RG	RG	RG	RG	RG	RG	RG	RG	PK	PK	RG	RG	RG	RG
SiO ₂	56.46	57.98	57.64	57.34	56.77	57.00	57.43	57.13	57.99	58.15	55.67	55.24	54.71	55.45
Al ₂ O ₃	26.63	27.08	26.66	26.90	27.37	26.85	26.80	27.07	27.15	25.50	27.77	27.91	27.37	27.45
TiO ₂	0.03	-	-	-	-	-	-	-	-	0.01	-	0.04	0.03	-
Cr ₂ O ₃	0.05	0.06	-	0.06	0.03	0.01	0.05	0.02	-	0.01	-	0.05	0.06	0.04
FeO	0.10	0.05	0.10	0.09	0.19	0.17	0.10	0.14	0.13	0.29	0.26	0.24	0.13	0.13
MgO	0.01	0.02	0.01	-	0.01	0.02	0.02	0.01	0.02	0.01	0.01	-	0.02	0.03

CaO	9.20	9.08	9.23	9.34	9.60	9.60	9.19	9.23	8.96	7.60	10.22	10.17	9.90	9.81
Na ₂ O	6.24	6.50	6.23	6.21	6.19	6.08	6.31	6.42	6.35	7.19	5.57	5.47	5.71	5.75
K ₂ O	0.29	0.23	0.28	0.28	0.23	0.21	0.25	0.24	0.26	0.18	0.16	0.13	0.15	0.20
Total	99.03	101.00	100.14	100.29	100.43	99.95	100.16	100.28	100.88	98.94	99.77	99.27	98.09	98.86
Si	2.56	2.58	2.58	2.57	2.54	2.56	2.57	2.56	2.58	2.63	2.51	2.51	2.51	2.52
Al	1.42	1.42	1.41	1.42	1.44	1.42	1.42	1.43	1.42	1.36	1.48	1.49	1.48	1.47
Fe ²⁺	-	-	-	-	0.01	0.01	-	0.01	-	0.01	0.01	0.01	0.01	-
Ca	0.45	0.43	0.44	0.45	0.46	0.46	0.44	0.44	0.43	0.37	0.49	0.49	0.49	0.48
Na	0.55	0.56	0.54	0.54	0.54	0.53	0.55	0.56	0.55	0.63	0.49	0.48	0.51	0.51
K	0.02	0.01	0.02	0.02	0.01	0.01	0.01	0.01	0.01	0.01	0.01	0.01	0.01	0.01
Total	5.01	5.00	4.99	5.00	5.01	5.00	5.00	5.01	4.99	5.01	5.00	4.99	5.01	5.00
An%	44	43	44	45	46	46	44	44	43	37	50	50	48	48
Ab%	54	56	54	54	53	53	55	55	55	62	49	49	51	51
Or%	2	1	2	2	1	1	1	1	2	1	1	1	1	1

Table 6-5 EMPA data of clinopyroxene.

No.	18	19	56	57	54	55	24	25	36	37	58	59	62	63	64	104	105
Sample	15FP-02		15FP-03								15FP-06						
Comment	PK	PK	PG	PG	PK	PK	RG	RG	RG	RG	PK	PK	PK	RG	RG	RG	RG
SiO ₂	51.62	51.64	52.13	51.51	52.24	52.06	51.55	51.58	51.57	51.78	50.37	50.25	50.91	50.83	50.28	51.01	50.39
Al ₂ O ₃	1.85	1.91	1.95	1.83	1.06	1.46	1.69	1.61	1.61	1.66	1.88	1.92	1.82	1.60	1.66	1.70	1.84
TiO ₂	0.16	0.08	0.16	0.10	0.02	0.11	0.15	0.05	0.07	0.15	0.13	0.19	0.24	0.09	0.17	0.16	0.18
FeO	13.62	13.59	13.57	13.67	13.61	13.58	13.52	14.04	13.62	13.79	13.10	13.47	13.02	13.62	15.77	13.41	13.54
MnO	0.37	0.29	0.32	0.37	0.40	0.46	0.52	0.60	0.56	0.55	0.24	0.33	0.27	0.23	0.36	0.43	0.40
NiO	-	0.06	0.04	-	0.07	0.04	-	-	0.01	0.02	0.01	-	-	0.04	0.03	-	-
MgO	11.38	11.32	11.25	11.11	10.40	10.74	10.67	11.04	10.80	10.90	10.80	10.73	10.79	10.99	10.93	10.94	10.54
CaO	21.45	21.40	21.50	21.58	22.28	21.66	21.54	21.45	21.15	21.21	21.19	21.30	21.23	21.25	19.69	20.72	20.90
Na ₂ O	0.33	0.41	0.32	0.38	0.49	0.43	0.41	0.32	0.38	0.36	0.42	0.39	0.39	0.36	0.36	0.34	0.35
Total	100.78	100.70	101.27	100.55	100.62	100.58	100.06	100.76	99.76	100.45	98.15	98.67	98.74	99.04	99.27	98.71	98.14
Si	1.95	1.95	1.96	1.95	1.98	1.97	1.96	1.96	1.97	1.97	1.95	1.95	1.96	1.96	1.95	1.97	1.96
Al	0.08	0.09	0.09	0.08	0.05	0.07	0.08	0.07	0.07	0.07	0.09	0.09	0.08	0.07	0.08	0.08	0.08
Fe ²⁺	0.43	0.43	0.43	0.43	0.43	0.43	0.43	0.45	0.43	0.44	0.43	0.44	0.42	0.44	0.51	0.43	0.44

Mn	0.01	0.01	0.01	0.01	0.01	0.01	0.02	0.02	0.02	0.02	0.01	0.01	0.01	0.01	0.01	0.01	0.01
Mg	0.64	0.64	0.63	0.63	0.59	0.61	0.61	0.62	0.61	0.62	0.62	0.62	0.62	0.63	0.63	0.63	0.61
Ca	0.87	0.87	0.86	0.88	0.91	0.88	0.88	0.87	0.87	0.86	0.88	0.88	0.88	0.88	0.82	0.86	0.87
Na	0.02	0.03	0.02	0.03	0.04	0.03	0.03	0.02	0.03	0.03	0.03	0.03	0.03	0.03	0.03	0.03	0.03
Total	4.01	4.02	4.01	4.02	4.01	4.01	4.01	4.02	4.01	4.01	4.01	4.02	4.01	4.02	4.02	4.00	4.01

Table 6-5 EMPA data of orthopyroxene.

No.	74	75	86	87	61	62	67	102	103	109
Sample	15FP-02						15FP-06	15FP-06	15FP-06	
Comment	PK	PK	PK	PK	RG	RG	RG	RG	RG	RG
SiO ₂	49.76	47.13	50.20	50.10	49.93	50.27	49.58	49.46	49.34	49.26
Al ₂ O ₃	0.91	1.02	0.90	0.88	0.89	0.87	0.89	0.91	0.77	0.83
TiO ₂	-	0.01	0.04	-	0.03	0.01	-	-	0.05	0.03
Cr ₂ O ₃	0.07	0.16	0.05	0.03	-	0.04	0.02	0.05	0.01	0.01
FeO	34.12	32.69	33.43	34.12	33.13	32.60	33.13	32.11	31.76	31.06
MnO	0.46	0.44	0.56	0.66	0.51	0.48	0.51	0.85	0.90	0.75
NiO	-	-	0.01	-	0.01	-	0.06	0.01	-	0.02

MgO	13.95	12.85	13.66	13.67	14.24	14.11	14.64	14.45	14.46	15.26
CaO	0.59	0.62	0.74	0.75	0.64	0.62	0.62	0.61	0.59	0.49
Na ₂ O	0.00	0.23	0.07	0.02	0.00	0.05	0.02	0.02	0.02	0.03
K ₂ O	0.01	0.13	0.01	0.01	0.01	0.05	0.02	-	-	-
Total	99.85	95.27	99.67	100.24	99.39	99.10	99.49	98.47	97.90	97.74
Si	1.97	1.96	1.98	1.98	1.98	1.99	1.96	1.97	1.98	1.97
Al	0.04	0.05	0.04	0.04	0.04	0.04	0.04	0.04	0.04	0.04
Fe ²⁺	1.13	1.14	1.11	1.13	1.10	1.08	1.10	1.07	1.06	1.04
Mn	0.02	0.02	0.02	0.02	0.02	0.02	0.02	0.03	0.03	0.03
Mg	0.82	0.80	0.80	0.80	0.84	0.83	0.86	0.86	0.86	0.91
Ca	0.02	0.03	0.03	0.03	0.03	0.03	0.03	0.03	0.03	0.02
Total	4.01	3.99	3.99	4.00	4.00	3.99	4.02	4.01	4.00	4.01

Table 6-6 EMPA data of ilmenite and magnetite.

No.	21	25	1	33	61	108	7	70	12	73	83	22	23	26	32	73
Sample No.	15FP-02	15FP-02	15FP-03	15FP-03	15FP-06	15FP-06	15FP-02	15FP-02	15FP-02	15FP-02	15FP-02	15FP-03	15FP-03	15FP-03	15FP-03	15FP-06
Mineral	Ilm	Ilm	Ilm	Ilm	Ilm	Ilm	Mgt	Mgt	Mgt	Mgt	Mgt	Mgt	Mgt	Mgt	Mgt	Mgt
Stage	PG	PG	PG	PK	PK	PK	PG	PG	PK	PK	RG	PG	PG	PG	RG	PG
SiO ₂	0.02	6.56	0.02	0.06	0.02	-	0.05	0.03	0.06	0.03	0.09	0.09	0.04	0.10	0.09	0.03
Al ₂ O ₃	0.02	0.34	-	-	0.04	-	0.20	0.12	0.16	0.15	0.22	1.85	0.16	0.00	0.12	0.05
TiO ₂	49.58	50.57	47.85	50.84	48.86	50.79	0.13	0.11	0.16	0.03	0.07	4.66	0.34	0.14	0.01	0.11
Cr ₂ O ₃	-	0.01	0.05	0.02	0.02	-	0.07	0.10	0.08	0.06	0.08	0.12	0.03	0.11	0.06	0.05
FeO	46.23	33.40	50.03	46.90	48.86	46.29	90.68	91.88	90.87	91.87	93.17	86.58	91.48	91.79	92.60	91.31
MnO	2.14	2.02	0.93	1.79	0.91	2.01	0.03	-	0.05	0.06	0.01	0.24	0.02	0.05	0.03	0.04
NiO	-	0.05	-	-	-	-	0.05	0.04	0.04	0.02	-	-	-	-	-	-
MgO	0.02	0.05	0.08	0.03	0.05	0.06	-	-	-	0.03	-	0.07	0.01	-	0.01	0.01
CaO	0.01	5.53	-	-	-	-	-	-	-	-	-	0.16	-	-	-	0.01
Na ₂ O	0.03	0.02	-	-	-	-	0.02	-	-	0.03	0.09	-	0.02	-	0.05	0.05
K ₂ O	-	-	0.02	0.02	-	-	-	-	-	-	0.03	0.01	-	-	-	0.02

Total	98.05	98.55	98.97	99.65	98.75	99.15	91.24	92.28	91.42	92.29	93.75	93.79	92.09	92.19	92.97	91.68
Si	-	0.16	-	-	-	-	-	-	-	-	-	-	-	-	-	-
Al	-	0.01	-	-	-	-	0.01	0.01	0.01	0.01	0.01	0.08	0.01	-	0.01	-
Ti	0.97	0.91	0.94	0.98	0.96	0.98	-	-	-	-	-	0.13	0.01	-	-	-
Fe ²⁺	1.01	0.67	1.09	1.00	1.06	0.99	2.97	2.98	2.97	2.98	2.97	2.60	2.96	2.98	2.98	2.98
Mn	0.05	0.04	0.02	0.04	0.02	0.04	-	-	-	-	-	0.01	-	-	-	-
Ca	-	0.14	-	-	-	-	-	-	-	-	-	0.01	-	-	-	-
Total	2.03	1.93	2.06	2.02	2.04	2.02	2.99	2.99	2.99	2.99	2.99	2.83	2.99	2.99	2.99	3.00

Table 6-7 EMPA data of K-feldspar and biotite.

No.	65	66	84	85	6	9	10	1	2	10	11	88	89	34	35
Sample	15FP-0	15FP-0	15FP-0	15FP-0	15FP-0	15FP-0	15FP-0	15FP-0	15FP-0	15FP-0	15FP-0	15FP-0	15FP-0	15FP-0	15FP-0
No.	2	2	2	2	3	3	3	2	2	2	2	2	2	3	3
Mineral	Kfs	Kfs	Kfs	Kfs	Kfs	Kfs	Kfs	Bt	Bt	Bt	Bt	Bt	Bt	Bt	Bt
Stage	PK	PK	PK	PK	PK	PK	PK	PG	PG	PK	PK	PK	PK	PK	PK
SiO ₂	64.77	64.52	64.54	66.56	64.56	65.16	64.49	35.29	36.57	32.76	35.59	36.58	34.96	35.71	36.30
Al ₂ O ₃	18.44	18.08	18.58	18.64	18.66	18.48	18.46	13.75	13.77	13.51	14.78	13.91	13.51	15.04	15.28

TiO ₂	-	-	-	0.03	0.01	0.02	-	2.69	2.68	2.52	2.85	4.41	4.70	4.55	4.44
Cr ₂ O ₃	0.01	0.02	0.07	-	-	0.02	0.02	0.04	-	0.05	0.08	0.07	0.05	-	0.03
FeO	0.10	0.02	-	0.06	0.06	0.10	0.04	19.40	18.94	23.48	21.55	23.35	23.09	19.80	19.96
MgO	0.02	-	-	-	-	0.01	-	11.22	11.21	8.46	9.28	9.03	9.07	9.58	9.37
CaO	0.08	0.08	0.09	0.17	0.05	0.04	0.05	0.03	0.01	0.12	0.09	0.03	0.07	0.01	0.02
Na ₂ O	1.21	1.35	0.95	2.79	0.97	1.20	0.88	0.33	0.26	0.07	0.17	0.09	0.13	0.13	0.13
K ₂ O	14.99	14.72	15.20	12.13	15.21	14.91	15.48	8.75	8.87	8.02	8.97	9.33	9.31	9.44	9.42
Total	99.61	98.81	99.44	100.48	99.55	99.98	99.44	91.54	92.33	89.13	93.41	96.82	94.95	94.40	95.06
Si	2.99	3.00	2.99	3.01	2.99	3.00	2.99	2.82	2.87	2.75	2.81	2.80	2.75	2.77	2.79
Al	1.00	0.99	1.01	0.99	1.02	1.00	1.01	1.29	1.27	1.34	1.37	1.26	1.25	1.37	1.38
Ti	-	-	-	-	-	-	-	0.16	0.16	0.16	0.17	0.25	0.28	0.26	0.26
Fe ²⁺	-	-	-	-	-	-	-	1.29	1.24	1.65	1.42	1.50	1.52	1.28	1.28
Mg	-	-	-	-	-	-	-	1.33	1.31	1.06	1.09	1.03	1.06	1.11	1.07
Ca	-	-	-	0.01	-	-	-	-	-	0.01	0.01	-	0.01	-	-
Na	0.11	0.12	0.09	0.24	0.09	0.11	0.08	0.05	0.04	0.01	0.03	0.01	0.02	0.02	0.02
K	0.88	0.87	0.90	0.70	0.90	0.87	0.92	0.89	0.89	0.86	0.90	0.91	0.93	0.93	0.92
Total	5.00	5.00	4.99	4.96	5.00	4.99	5.00	7.85	7.79	7.85	7.80	7.77	7.82	7.76	7.73

Table 6-8 Calculated P–T conditions for the peak mineral assemblage.

Method	Reference	15FP-02		15FP-03		15FP-06	
		T (°C)	P (kbar)	T (°C)	P (kbar)	T (°C)	P (kbar)
g–opx geothermometer	Lee and Ganguly (1988)	845–865					
(calculated at 9 kbar)	Aranovich and Berman (1997)	772–854					
g–opx–pl–q geobarometer	Moecher et al. (1988)		8.2–10.2				
(calculated at 850 °C)	Perkins and Chipera (1985)		9.5–10.2				
g–cpx geothermometer	Ellis and Green (1979)			789–793		783–796	
(calculated at 10 kbar)	Dahl (1980)			859–886		829–859	
g–cpx–pl–q geobarometer	Eckert et al. (1991)				8.9–9.1		9.1–9.3
(calculated at 850 °C)	Moecher et al. (1988)				9.9–12.3		9.2–11.3
hb–pl geothermometer	Holland and Blundy (1994)	750–765		780–795		800–810	

g, garnet; opx, orthopyroxene; cpx, clinopyroxene; hb, hornblende; pl, plagioclase; q, quartz.

Table 6-9 Zircon U-Pb analytical data.

Sample Spot	Element (ppm)			Th/U	Isotope ratios						Age (Ma)				Concordance (%)		
	Pb*	Th	U		$\frac{^{207}\text{Pb}}{^{235}\text{U}}$	$\frac{^{206}\text{Pb}}{^{238}\text{U}}$	$\frac{^{207}\text{Pb}}{^{206}\text{Pb}}$	$\frac{^{207}\text{Pb}}{^{235}\text{U}}$	$\frac{^{206}\text{Pb}}{^{238}\text{U}}$	$\frac{^{207}\text{Pb}}{^{206}\text{Pb}}$							
15FP-02																	
15FP-02.01	554.6	13.9	1468.3	0.01	5.2070	0.0674	0.3392	0.0034	0.1113	0.0012	1854	24	1883	19	1822	20	97
15FP-02.02	184.2	5.3	494.0	0.01	5.1938	0.1204	0.3335	0.0040	0.1130	0.0016	1852	43	1855	22	1848	26	100
15FP-02.03	397.2	122.7	1087.6	0.11	5.0467	0.0643	0.3222	0.0032	0.1136	0.0013	1827	23	1801	18	1858	20	97
15FP-02.04	330.5	8.1	906.6	0.01	5.0345	0.0646	0.3274	0.0032	0.1115	0.0012	1825	23	1826	18	1824	20	100
15FP-02.05	227.9	7.6	625.9	0.01	4.9687	0.0633	0.3272	0.0032	0.1101	0.0012	1814	23	1825	18	1802	20	99
15FP-02.07	202.8	32.5	533.3	0.06	5.2524	0.0681	0.3374	0.0033	0.1129	0.0013	1861	24	1874	19	1846	20	99
15FP-02.08	350.7	47.7	948.9	0.05	5.1712	0.0683	0.3264	0.0033	0.1149	0.0013	1848	24	1821	19	1878	20	97
15FP-02.09	431.7	153.1	869.5	0.18	8.7073	0.1133	0.4204	0.0042	0.1502	0.0017	2308	30	2262	22	2348	19	96
15FP-02.10	226.6	14.1	626.6	0.02	4.9517	0.0642	0.3243	0.0032	0.1107	0.0012	1811	23	1811	18	1812	20	100
15FP-02.11	206.8	7.3	572.1	0.01	4.9597	0.0632	0.3247	0.0031	0.1108	0.0012	1812	23	1812	18	1813	20	100
15FP-02.12	249.4	7.7	687.1	0.01	5.0058	0.0639	0.3261	0.0032	0.1113	0.0012	1820	23	1819	18	1821	20	100
15FP-02.13	94.9	2.7	263.0	0.01	4.9483	0.0634	0.3231	0.0031	0.1111	0.0012	1811	23	1805	17	1817	20	99

15FP-02.14	143.8	48.6	280.5	0.17	8.7023	0.1114	0.4346	0.0042	0.1452	0.0016	2307	30	2326	22	2290	19	98
15FP-02.15	233.9	170.5	437.2	0.39	8.8817	0.1139	0.4389	0.0042	0.1468	0.0017	2326	30	2346	23	2308	19	98
15FP-02.17	179.3	140.2	442.4	0.32	5.2520	0.0687	0.3345	0.0034	0.1139	0.0013	1861	24	1860	19	1862	20	100
15FP-02.18	405.0	26.5	797.2	0.03	9.1083	0.1162	0.4385	0.0043	0.1506	0.0017	2349	30	2344	23	2353	19	100
15FP-02.19	245.3	20.2	672.2	0.03	5.0156	0.0640	0.3262	0.0032	0.1115	0.0012	1822	23	1820	18	1824	20	100
15FP-02.21	207.9	13.1	548.8	0.02	5.2597	0.0667	0.3381	0.0032	0.1128	0.0013	1862	24	1877	18	1846	20	98
15FP-02.22	231.7	208.7	462.1	0.45	7.9773	0.1016	0.4090	0.0039	0.1414	0.0016	2228	28	2211	21	2245	19	98
15FP-02.23	237.0	8.6	652.9	0.01	5.0036	0.0645	0.3256	0.0032	0.1115	0.0012	1820	23	1817	18	1823	20	100
15FP-02.24	173.4	2.3	475.7	0.00	5.0282	0.0643	0.3271	0.0032	0.1115	0.0013	1824	23	1824	18	1824	20	100
15FP-02.25	622.4	15.2	1707.9	0.01	5.0337	0.0644	0.3270	0.0032	0.1116	0.0013	1825	23	1824	18	1826	20	100
15FP-02.26	233.2	158.7	446.1	0.36	8.8654	0.2016	0.4272	0.0049	0.1505	0.0038	2324	53	2293	26	2352	43	97
15FP-02.27	68.8	5.4	184.3	0.03	5.2128	0.1030	0.3300	0.0046	0.1146	0.0015	1855	37	1838	26	1873	23	98
15FP-03																	
15FP-03.01	62.2	1.0	169.6	0.01	5.0677	0.0671	0.3297	0.0035	0.1115	0.0013	1831	24	1837	19	1824	20	99
15FP-03.02	56.3	4.8	151.0	0.03	5.1875	0.0672	0.3323	0.0034	0.1132	0.0013	1851	24	1850	19	1851	20	100
15FP-03.03	39.0	1.2	106.5	0.01	5.0568	0.0682	0.3288	0.0035	0.1115	0.0013	1829	25	1833	19	1825	21	100
15FP-03.04	24.5	1.8	64.3	0.03	5.2930	0.0706	0.3403	0.0035	0.1128	0.0013	1868	25	1888	19	1845	21	98

15FP-03.05	51.9	4.0	138.2	0.03	5.1524	0.0670	0.3353	0.0034	0.1115	0.0013	1845	24	1864	19	1823	20	98
15FP-03.06	29.9	2.1	81.7	0.03	5.0500	0.0659	0.3269	0.0033	0.1120	0.0013	1828	24	1823	19	1833	21	99
15FP-03.07	14.0	1.3	38.2	0.03	5.0867	0.0698	0.3289	0.0034	0.1122	0.0014	1834	25	1833	19	1835	22	100
15FP-03.08	24.0	8.0	63.6	0.13	5.1717	0.0687	0.3318	0.0034	0.1131	0.0013	1848	25	1847	19	1849	21	100
15FP-03.09	27.2	16.4	66.1	0.25	5.7097	0.0987	0.3487	0.0049	0.1187	0.0014	1933	33	1929	27	1937	21	100
15FP-03.10	31.7	0.6	86.7	0.01	5.0608	0.0677	0.3279	0.0034	0.1119	0.0013	1830	24	1828	19	1831	21	100
15FP-03.11	19.8	1.6	49.8	0.03	5.6903	0.0810	0.3508	0.0037	0.1177	0.0014	1930	27	1938	20	1921	21	99
15FP-03.12	27.5	1.9	74.9	0.03	5.0898	0.0678	0.3291	0.0035	0.1122	0.0013	1834	24	1834	19	1835	21	100
15FP-03.13	15.7	3.6	42.6	0.08	5.0803	0.0702	0.3263	0.0034	0.1129	0.0013	1833	25	1820	19	1847	21	99
15FP-03.14	30.8	3.9	84.7	0.05	4.9388	0.0655	0.3234	0.0033	0.1108	0.0013	1809	24	1806	19	1812	21	100
15FP-03.15	71.4	0.8	198.3	0.00	4.9492	0.0634	0.3240	0.0032	0.1108	0.0012	1811	23	1809	18	1812	20	100
15FP-03.16	45.8	0.8	127.2	0.01	4.9410	0.0652	0.3231	0.0034	0.1109	0.0013	1809	24	1805	19	1814	21	99
15FP-03.17	38.1	31.3	98.9	0.32	5.0825	0.0669	0.3294	0.0033	0.1119	0.0013	1833	24	1835	19	1831	21	100
15FP-03.18	54.5	1.2	151.2	0.01	4.9112	0.0632	0.3242	0.0032	0.1099	0.0012	1804	23	1810	18	1797	20	99
15FP-03.19	41.9	3.9	115.5	0.03	5.0082	0.0834	0.3238	0.0035	0.1122	0.0015	1821	30	1808	19	1835	24	99
15FP-03.20	59.1	10.4	166.2	0.06	4.7897	0.0619	0.3134	0.0031	0.1108	0.0013	1783	23	1758	17	1813	21	97
15FP-03.21	50.4	5.6	136.1	0.04	5.0168	0.0642	0.3302	0.0033	0.1102	0.0012	1822	23	1839	18	1802	21	98

15FP-03.22	63.1	13.6	170.7	0.08	5.0466	0.0650	0.3281	0.0033	0.1116	0.0013	1827	24	1829	18	1825	20	100
15FP-03.23	69.7	1.0	194.3	0.01	4.9539	0.0639	0.3223	0.0033	0.1115	0.0013	1811	23	1801	18	1824	20	99
15FP-03.24	20.2	4.4	53.2	0.08	5.2612	0.0802	0.3337	0.0033	0.1143	0.0015	1863	28	1856	19	1869	24	99
15FP-03.25	29.4	2.4	81.0	0.03	5.0268	0.0698	0.3236	0.0033	0.1127	0.0013	1824	25	1807	19	1843	21	98
15FP-03.26	14.5	5.0	36.3	0.14	5.6459	0.0836	0.3483	0.0037	0.1176	0.0015	1923	28	1927	20	1919	22	100
15FP-03.27	21.4	5.7	53.4	0.11	5.6614	0.0763	0.3494	0.0035	0.1175	0.0014	1926	26	1931	19	1919	21	99
15FP-03.28	40.5	2.9	107.1	0.03	5.3302	0.0985	0.3353	0.0039	0.1153	0.0015	1874	35	1864	22	1885	23	99
15FP-03.29	36.0	2.6	97.2	0.03	5.0741	0.0741	0.3301	0.0036	0.1115	0.0013	1832	27	1839	20	1824	21	99
15FP-03.30	23.7	7.2	63.3	0.11	4.9167	0.0737	0.3280	0.0036	0.1087	0.0014	1805	27	1828	20	1778	24	97
15FP-06																	
15FP-06.01	9.3	2.7	25.6	0.10	5.0256	0.0688	0.3231	0.0032	0.1128	0.0014	1824	25	1805	18	1845	22	98
15FP-06.02	1.8	0.3	4.7	0.07	5.2386	0.1468	0.3340	0.0034	0.1138	0.0030	1859	52	1858	19	1860	48	100
15FP-06.03	3.1	2.5	7.8	0.32	5.2359	0.0982	0.3342	0.0033	0.1136	0.0020	1858	35	1859	18	1858	32	100
15FP-06.04	6.2	0.7	16.9	0.04	5.1170	0.0725	0.3265	0.0032	0.1137	0.0014	1839	26	1822	18	1859	23	98
15FP-06.05	2.9	2.9	7.8	0.37	4.8955	0.1004	0.3219	0.0032	0.1103	0.0021	1801	37	1799	18	1804	35	100
15FP-06.06	6.4	2.0	17.2	0.12	5.1491	0.0788	0.3273	0.0032	0.1141	0.0016	1844	28	1825	18	1866	25	98
15FP-06.07	1.0	0.2	2.6	0.10	5.6609	0.0951	0.3453	0.0034	0.1189	0.0028	1925	32	1912	19	1940	42	99

15FP-06.08	1.8	0.1	4.7	0.02	5.1803	0.1651	0.3324	0.0035	0.1130	0.0035	1849	59	1850	19	1849	55	100
15FP-06.09	2.4	1.5	6.2	0.23	5.2774	0.1654	0.3355	0.0034	0.1141	0.0035	1865	58	1865	19	1865	56	100
15FP-06.15	4.1	8.8	9.6	0.92	5.2226	0.1226	0.3323	0.0034	0.1140	0.0026	1856	44	1850	19	1864	41	99
15FP-06.16	6.5	1.7	17.3	0.10	5.1674	0.0814	0.3315	0.0033	0.1130	0.0016	1847	29	1846	18	1849	26	100
15FP-06.18	0.4	0.0	1.1	0.01	5.7132	0.0982	0.3449	0.0041	0.1202	0.0027	1933	33	1910	23	1959	40	97
15FP-06.19	1.3	0.1	3.5	0.03	5.2554	0.2013	0.3341	0.0037	0.1141	0.0043	1862	71	1858	20	1865	68	100
15FP-06.20	9.2	1.5	24.1	0.06	5.3644	0.0733	0.3376	0.0033	0.1152	0.0014	1879	26	1875	18	1884	22	100
15FP-06.21	1.8	0.8	4.5	0.17	5.5497	0.1165	0.3448	0.0036	0.1167	0.0025	1908	40	1910	20	1907	39	100
15FP-06.23	16.0	3.6	40.8	0.09	5.5917	0.0774	0.3441	0.0033	0.1178	0.0014	1915	27	1907	19	1924	22	99
15FP-06.25	5.1	1.3	13.3	0.09	5.4420	0.0838	0.3356	0.0033	0.1176	0.0017	1892	29	1865	18	1920	25	97
15FP-06.26	2.3	0.5	6.0	0.08	5.6184	0.0829	0.3435	0.0037	0.1186	0.0016	1919	28	1904	21	1936	23	98
15FP-06.28	0.9	0.9	2.3	0.39	5.2390	0.2736	0.3347	0.0042	0.1135	0.0060	1859	97	1861	24	1857	95	100
15FP-06.29	23.3	1.7	60.1	0.03	5.5445	0.0760	0.3450	0.0033	0.1166	0.0014	1908	26	1911	18	1904	22	100
15FP-06.30	3.6	0.4	9.3	0.04	5.6273	0.1377	0.3478	0.0042	0.1174	0.0025	1920	47	1924	23	1916	37	100

Table 7-1 Compilation of age data from representative GGBs of the NCC.

Granite-green stone belt	Sample No.	Rock type	Formation age (Ma)	Metamorphic age (Ma)	Method	Reference
	SY0336	Gneissic trondhjemite	2711±10		SHRIMP	Wan et al., 2011
	S0503	Tonalitic gneiss	2714±13		SHRIMP	Wan et al., 2011
	S0741	Granodiorite	2712±7		SHRIMP	Wan et al., 2011
	S0732	Gneissic trondhjemite	2707±9		SHRIMP	Wan et al., 2011
	SY0311	Quartz diorite	2740±6		SHRIMP	Wan et al., 2011
	GY001TM1	Gneissic tonalite	2735±19	2607±13	SHRIMP	Ren et al., 2016
Yanlingguan	S1141	Gneissic trondhjemite		2613±19	SHRIMP	Ren et al., 2016
GGB	S1314	Gneissic trondhjemite	2641±12	2630±5	SHRIMP	Ren et al., 2016
	TS09109	Gneissic trondhjemite	2642±7	2622±11	SHRIMP	Ren et al., 2016
	TS09111	Quartz diorite	2645±9	2597±12	SHRIMP	Ren et al., 2016
	S0761	Gneissic tonalite	2602±12	2590±7	SHRIMP	Ren et al., 2016
	S1455	Gneissic trondhjemite		2606±9	SHRIMP	Ren et al., 2016
	S1457	Gneissic tonalite	2744±16	2616±11	SHRIMP	Ren et al., 2016
	ZFY-1, 9	BIF	2750-2710		LA-ICP-MS	Liu and Yang, 2015

	313ZX84-3	Amphibolite (BIF)	2711±31	LA-ICP-MS	Yang et al., 2014
Western Shandong GGB	08YS-98	Plagioclase amphibolite	2532±15	SHRIMP	Penget al., 2013a
	08YS-112	Granite	2543±16	LA-ICP-MS	Penget al., 2013b
	08YS-105	Granite	2520±12	LA-ICP-MS	Penget al., 2013b
	YS9656	Granite	2538±6	SHRIMP	Shen et al., 2007
	YS9573	Enderbite	2532±9	SHRIMP	Shen et al., 2007
	06TK-1	Sanukitoid	2542±16	LA-ICP-MS	Wang et al., 2009
	05SD-90	Sanukitoid	2536±22	LA-ICP-MS	Wang et al., 2009
	S0844-2	Meta-felsic volcanic rock (BIF)	2561±24	SHRIMP	Wang et al., 2010c
Wutai GGB	H1228	Garnet amphibolite	2528±19	LA-ICP-MS	Qian and Wei, 2016
	95-PC-34	Granite	2566±13	SHRIMP	Wilde et al., 1997
	95-19	Granite	2555±6	SHRIMP	Wilde et al., 1997
	95-PC-94	Granite	2553±8	SHRIMP	Wilde et al., 1997
	95-PC-96	Granite	2537±10	SHRIMP	Wilde et al., 1997
	WC7	Tonalite	2552±11	SHRIMP	Wilde et al., 2005
	95-PC-6B	Tonalite	2551±5	SHRIMP	Wilde et al., 2005
	WC6	Granodiorite	2546±6	SHRIMP	Wilde et al., 2005

	WC5	Granodiorite	2538 \pm 6		SHRIMP	Wilde et al., 2005
	95-PC-98	Monzogranite	2531 \pm 4		SHRIMP	Wilde et al., 2005
	95-PC-76	Granodiorite	2531 \pm 5		SHRIMP	Wilde et al., 2005
	95-PC-62	Granodiorite	2520 \pm 9		SHRIMP	Wilde et al., 2005
	95-PC-63	Granodiorite	2517 \pm 12		SHRIMP	Wilde et al., 2005
	96PC153	Tonalitic gneiss	2513 \pm 15		SHRIMP	Wilde et al., 2005
	96PC154	Quartz dioritic gneiss	2499 \pm 4		SHRIMP	Wilde et al., 2005
	WJZ2-1	Amphibolite (BIF)	2543 \pm 4		SIMS	Wang et al., 2014a
	09DF-18	Amphibolite	2540 \pm 7		LA-ICP-MS	Diwu et al., 2011
	14DF27-01	Basaltic amphibolite		2507 \pm 26	LA-ICP-MS	Deng et al., 2016
	14DF05-05	Diorites	2518 \pm 36		LA-ICP-MS	Deng et al., 2016
	14DF03-01	TTG gneiss	2514 \pm 26		LA-ICP-MS	Deng et al., 2016
Dengfeng	14DF15A-01	Granite dyke	2486 \pm 20		LA-ICP-MS	Deng et al., 2016
GGB	09DF-19	Meta-diorite	2525 \pm 9		LA-ICP-MS	Diwu et al., 2011
	DF07-08	Trondhjemitic gneiss	2511 \pm 10		LA-ICP-MS	Diwu et al., 2011
	DF07-15	Tonalitic gneiss	2547 \pm 17		LA-ICP-MS	Diwu et al., 2011
	DF07-24	Tonalitic gneiss	2542 \pm 6		LA-ICP-MS	Diwu et al., 2011

	DF07-10	Trondhjemitic gneiss	2510±20		LA-ICP-MS	Diwu et al., 2011
Zunhua GGB	11JD07-4	Mafic granulite	2518±15	2470±15	LA-ICP-MS	Guo et al., 2013
	TP3	Amphibolite	2539±9		LA-ICP-MS	Yang et al., 2016
	TP4/1	Amphibolite	2529±8		LA-ICP-MS	Yang et al., 2016
	TP1/1	Charnockite	2578±7		LA-ICP-MS	Yang et al., 2016
	TP2/1	Charnockite	2568±9		LA-ICP-MS	Yang et al., 2016
	Q337-6	Gneiss (BIF)	2503±15		SHRIMP	Han et al., 2014
	Q325-1	Amphibole gneiss (BIF)	2536±8		SHRIMP	Han et al., 2014
	Q327-2	Gneiss (BIF)	2510±6		SHRIMP	Han et al., 2014
	Q302-1	Gneiss (BIF)	2517±7		SHRIMP	Han et al., 2014
	Q321-1	Mica quartz schist (BIF)	2605±9		SHRIMP	Han et al., 2014
	SC-4	Plagioclase hornblende gneiss (BIF)	2547±7	2513±4	SIMS	Zhang et al., 2011
	SRG-1	Plagiogneiss (BIF)	2541±21	2512±13	SIMS	Zhang et al., 2011
	SRG-2	Amphibolite (BIF)	2553±31	2510±21	SIMS	Zhang et al., 2011
Dongwufenzi	GYM-24	Amphibolite (BIF)	2569±78		SIMS	Liu et al., 2014c
GGB	GYM-28	Tonalite (BIF)	2555±56		SIMS	Liu et al., 2014c

	08XM40	Charnockite	2533±15	2490±11	SIMS	Ma et al., 2013a
	08XM36	Charnockite	2524±4	2498±3	SIMS	Ma et al., 2013a
	08XM20	Granite	2523±15		SIMS	Ma et al., 2013b
	08XM04	Granite	2480±20		SIMS	Ma et al., 2013b
	10GY26	Amphibolite (BIF)	2538±9	2452±7	LA-ICP-MS	Ma et al., 2014
	08XM20	Sanukitoid	2523±13		LA-ICP-MS	Ma et al., 2014
	SHM-2	Amphibolite (BIF)	2562±14		SIMS	Liu et al., 2012c
	ZH01	Trondhjemite	2502±6		LA-ICP-MS	Jian et al., 2012
	XWLBL02	Mafic granulite		2503±12	LA-ICP-MS	Jian et al., 2012
	XWLBL01	Garnetiferous gneiss		2515±8	LA-ICP-MS	Jian et al., 2012
	GY51-2	Pegmatite	2508±17			Jian et al., 2012
Hongtoushan- Qingyuan-Hel ong GGB	14JN11-2	Amphibolite	2558±13	2510±32, 2482±33	LA-ICP-MS	Guo et al., 2016
	13JN16-2	Amphibolite	2557±10		LA-ICP-MS	Guo et al., 2016
	P10NC5	Amphibolite		2480±9	SIMS	Penget al., 2015
	P10BHG5	TTG	2520±12		SIMS	Penget al., 2015
	P10PJW1	TTG	2526±11		SIMS	Penget al., 2015

	P10YJD3	Quartz monzodiorite	2512±10		SIMS	Penget al., 2015
	13JN01-5	Trondhjemitic gneiss	2551±19	2502±15	LA-ICP-MS	Guo et al., 2015
	13JN08-2	Trondhjemitic gneiss	2551±9	2508±14	LA-ICP-MS	Guo et al., 2015
	13JN09-4	Trondhjemitic gneiss	2532±4	2500±8	LA-ICP-MS	Guo et al., 2015
	WTS-11	Amphibolite (BIF)	2533±11		SIMS	Dai et al., 2012
	CTG-7	Quartz schist (BIF)	2551±10		LA-ICP-MS	Dai et al., 2013
	HTS3/4	Massive sulfide ore	2507±4		SIMS	Zhu et al., 2015
	HTS3/9	Banded sulfide ore	2508±4		SIMS	Zhu et al., 2015
	12FX25-6	Amphibolite	2546±19		LA-ICP-MS	Wang et al., 2015
	12FX26-3	Palimpsest basalt	2522±25		LA-ICP-MS	Wang et al., 2015
	12FX28-3	Amphibolite	2540±17	2470±14	LA-ICP-MS	Wang et al., 2015
Yixian-Fuxin	YX011-2	Hornblende plagioclase gneiss	2567±7	2493±7	LA-ICP-MS	Wang et al., 2011
GGB	FX009-1	Hornblende plagioclase gneiss	2536±16	2498±12	LA-ICP-MS	Wang et al., 2011
	FX013-2	Hornblende plagioclase gneiss	2589±16	2502±13	LA-ICP-MS	Wang et al., 2011
	12FX18-2	Garnet plagioclase gneiss		2521±14	LA-ICP-MS	Wang et al., 2015
	FX09-1	Hornblende plagioclase gneiss	2534±6	2482±5	LA-ICP-MS	Wang et al., 2015

Appendix III: Curriculum Vitae

Name: Li TANG

Gender: Male

Date of Birth: 24/05/1990

Nationality: Chinese

Place of Birth: Sichuan, China

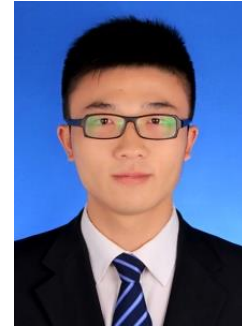
Address: China University of Geosciences (Beijing)

School of Earth Sciences and Resources

No. 29, Xueyuan Road, Haidian District, Beijing 100083, China

E-mail: tangli199005@126.com; ltang@cugb.edu.cn

Tel: (+86) 15600762296



Education Background

- September 2008—June 2012
Bachelor of Science in Geology (Resource Prospecting and Engineering)
Chengdu University of Technology, China
 - September 2012—June 2014
Master of Science in Geology (Mineral Resource Prospecting and Exploration)
China University of Geosciences Beijing, China
 - September 2014—June 2017
Ph.D. in Geology (Mineralogy, Petrology and Mineral Deposit Geology)
China University of Geosciences Beijing, China
 - October 2015—September 2017
Ph.D. in Geology (Petrology)
University of Tsukuba, Japan
-

Publications in SCI Journals

1. **Tang, L.**, Santosh, M., Tsunogae, T., Koizumi, T., Hu, X.K., Teng, X.M., 2016. Petrology, phase equilibria modelling and zircon U-Pb geochronology of Paleoproterozoic mafic granulites from the Fuping Complex, North China Craton. *Journal of Metamorphic Geology*, doi:10.1111/jmg.12243.
2. **Tang, L.**, Santosh, M., Tsunogae, T., Teng, X.M., 2016. Late Neoproterozoic arc magmatism and crustal growth associated with microblock amalgamation in the North China Craton: Evidence from the Fuping Complex. *Lithos* 248-251, 324-338.
3. **Tang, L.**, Santosh, M., Teng, X.M., 2015. Paleoproterozoic (ca. 2.1-2.0 Ga) arc magmatism in the Fuping Complex: implications for the tectonic evolution of the Trans-North China Orogen. *Precambrian Research* 268, 16-32.
4. **Tang, L.**, Santosh, M., Tsunogae, T., Teruyuki, M., 2016. Paleoproterozoic meta-carbonates from the central segment of the Trans-North China Orogen: Zircon U-Pb geochronology, geochemistry, and carbon and oxygen isotopes. *Precambrian Research* 284, 14-29.
5. **Tang, L.**, Santosh, M., 2017. Neoproterozoic granite-greenstone belts and related ore mineralization in the North China Craton: An overview. *Geoscience Frontiers*, <https://doi.org/10.1016/j.gsf.2017.04.002>.
6. **Tang, L.**, Santosh, M., Dong, Y.P., Tsunogae, T., Zhang, S.T., Cao, H.W., 2016. Early Paleozoic tectonic evolution of the North Qinling orogenic belt: Evidence from geochemistry, phase equilibrium modelling and geochronology of metamorphosed mafic rocks from the Songshugou ophiolite. *Gondwana Research* 30, 48-64.
7. **Tang, L.**, Santosh, M., Dong, Y.P., 2015. Tectonic evolution of a complex orogenic system: evidence from the northern Qinling belt, central China. *Journal of Asian Earth Sciences* 113, 544-559.
8. **Tang, L.**, Rajesh, S., Santosh, M., Tsunogae, T., Pradeepkumar, A.P., Tsutsumi, Y., Takamura, Y., 2017. Metamorphic phase equilibria modelling and zircon U-Pb

- geochronology of ultrahigh-temperature cordierite granulites from the Madurai Block, India: implications for hot Gondwana crust. *International Geology Review*, <http://dx.doi.org/10.1080/00206814.2017.1313711>.
9. Santosh, M., Tsunogae, T., Malaviarachchi, S.P.K., Zhang, Z.M., Ding, H.X., **Tang, L.**, Dharmapriya, P.L., 2014. Neoproterozoic crustal evolution in Sri Lanka: Insights from petrologic, geochemical and zircon U–Pb and Lu–Hf isotopic data and implications for Gondwana assembly. *Precambrian Research* 255, 1-29.
 10. Santosh, M., Yang, Q.Y., Teng, X.M., **Tang, L.**, 2015. Paleoproterozoic crustal growth in the North China Craton: Evidence from the Lüliang Complex. *Precambrian Research* 263, 197-231.
 11. Cao, H.W., Zhang, S.T., Santosh, M., Zheng, L., **Tang, L.**, Li, D., Zhang, X.H., Zhang, Y.H., 2015. The Luanchuan Mo–W–Pb–Zn–Ag magmatic–hydrothermal system in the East Qinling metallogenic belt, China: Constrains on metallogenesis from C–H–O–S–Pb isotope compositions and Rb–Sr isochron ages. *Journal of Asian Earth Sciences* 111, 751-780.
 12. Dharmapriya, P.L., Malaviarachchi, S.P., Santosh, M., **Tang, L.**, Sajeev, K., 2015. Late-Neoproterozoic ultrahigh-temperature metamorphism in the Highland Complex, Sri Lanka. *Precambrian Research* 271, 311-333.
 13. Santosh, M., Teng, X.M., He, X.F., **Tang, L.**, Yang, Q.Y., 2016. Discovery of Neoproterozoic suprasubduction zone ophiolite suite from Yishui Complex in the North China Craton. *Gondwana Research* 38, 1-27.
 14. Renjith, M.L., Santosh, M., **Tang, L.**, Satyanarayanan, M., Korakoppa, M.M., Tsunogae, T., Rao, D.V.S., Krishna, A.K., Charan, S.N., 2016. Zircon U–Pb age, Lu–Hf isotope, mineral chemistry and geochemistry of Sundamalai peralkaline pluton from the Salem Block, southern India: Implications for Cryogenian adakite-like magmatism in an aborted-rift. *Journal of Asian Earth Sciences* 115, 321-344.
 15. Cao, H.W., Zou, H., Zhang, Y.H., Zhang, S.T., Zheng, L., Zhang, L.K., **Tang, L.**, Pei, Q.M., 2016. Late Cretaceous magmatism and related metallogeny in the Tengchong area: Evidence from geochronological, isotopic and geochemical data

- from the Xiaolonghe Sn deposit, western Yunnan, China. *Ore Geology Reviews* 78, 196-212.
16. Manikyamba, C., Santosh, M., Kumar, B.C., Rambabu, S., **Tang, L.**, Saha, A., Khelen, A.C., Ganguly, S., Singh, T.D., Rao, D.V.S., 2016. Zircon U-Pb geochronology, Lu-Hf isotope systematics, and geochemistry of bimodal volcanic rocks and associated granitoids from Kotri Belt, Central India: implications for Neoproterozoic-Paleoproterozoic crustal growth. *Gondwana Research* 38, 313-333.
 17. Renjith, M.L., Santosh, M., Satyanarayana, M., Rao, D.S., **Tang, L.**, 2016. Multiple rifting and alkaline magmatism in southern India during Paleoproterozoic and Neoproterozoic. *Tectonophysics* 680, 233-253.
 18. Teng, X.M., Santosh, M., Tsunogae, T., **Tang, L.**, 2016. Magma chamber processes in Early Cretaceous Shangzhuang layered mafic intrusion from the North China Craton. *Geological Journal*, DOI: 10.1002/gj.2856.
 19. Cao, H.W., Zhang, Y.H., Pei, Q.M., Zhang, R.Q., **Tang, L.**, Lin, B., Cai, G.J., 2017. U-Pb dating of zircon and cassiterite from the Early Cretaceous Jiaojiguan iron-tin polymetallic deposit, implications for magmatism and metallogeny of the Tengchong area, western Yunnan, China. *International Geology Review* 59, 234-258.
 20. Yang, F., Wang, G.W., Cao, H.W., Li, R., **Tang, L.**, Huang, Y., Zhang, H., Xue, F., Guo, N., 2017. Timing of formation of the Hongdonggou Pb-Zn polymetallic ore deposit, Henan Province, China: Evidence from Rb-Sr isotopic dating of sphalerites. *Geoscience Frontiers* 8, 605-616.
 21. Cao, H.W., Pei, Q.M., Zhang, S.T., Zhang, L.K., **Tang, L.**, Lin, J.Z., Zheng, L., 2017. Geology, geochemistry and genesis of the Eocene Lailishan Sn deposit in the Sanjiang region, SW China. *Journal of Asian Earth Sciences* 137, 220-240.
 22. Yang, F., Santosh, M., Tsunogae, T., **Tang, L.**, Teng, X.M., 2017. Multiple magmatism in an evolving suprasubduction zone mantle wedge: The case of the composite mafic-ultramafic complex of Gaositai, North China Craton. *Lithos* 284-285, 525-544.
 23. Teng, X.M., Santosh, M., **Tang, L.**, 2017. The Early Cretaceous Shangzhuang

layered mafic intrusion and its bearing on decratonization of the North China Craton. *Geological Magazine*, DOI: 10.1017/S0016756817000371.

Publications in Chinese Journals

1. **Tang, L.**, Zhang, S.T., Cao, H.W., Tian, H.H., Zhang, X.H., Zhang, Y.F., Chen, H.J., Zhang, W., 2014. Geochemical features of ore-forming fluids of the Sandaogou Pb-Zn-Ag deposit in Luanchuan County, Henan Province. *Geoscience* 02, 359-368. (in Chinese with English abstract).
2. **Tang, L.**, Zhang, S.T., Cao, H.W., Li, D., Zhang, X.H., Zhang, Y.H., Tian, H.H., Zhang, H., 2014. Metallogenic system and evolutionary characteristics of Mo-W-Pb-Zn-Ag polymetallic metallogenic concentration area in Luanchuan, Henan, China. *Journal of Chengdu University of Technology* 03, 356-368. (in Chinese with English abstract).
3. Zou, H., Zhang, S.T., Fang, Y., Chen, A.Q., Gao, F., **Tang, L.**, Deng, M.Z., 2014. The radioactive elements content of natural fluorite and its influence. *Geophysical and Geochemical Exploration* 03, 478-484. (in Chinese with English abstract).
4. Zhang, W., Zhang, S.T., Cao, H.W., Wu, J.D., Xiao, C.X., Chen, H.J., **Tang, L.**, 2014. Characteristics of chlorite minerals from Xiaolonghe tin deposit in West Yunnan, China and their geological implications. *Journal of Chengdu University of Technology* 03, 318-328. (in Chinese with English abstract).
5. Pei, Q.M., Zhang, S.T., Cao, H.W., **Tang, L.**, Xu, T., Li, J.J., Zhang, X.H., Guo, N.N., 2015. Trace element geochemistry of the Luotuoshan sulfur-zinc polymetallic deposit in Luanchuan, western Henan, and its geological implications. *Acta Petrologica ET Mineralogica* 05, 741-754. (in Chinese with English abstract).
6. Tang, C.H., Zhang, S.T., Zhang, Y.H., Cao, H.W., **Tang, L.**, Chen, H.J., Xu, T., Wu, Z.L., 2015. Compositional characteristics of biotites from Nannihu and Shangfanggou granites in the Luanchuan ore belt, Henan Province, and its significance for petrogenesis and metallogeny. *Bulletin of Mineralogy, Petrology and Geochemistry* 32, 539-545. (in Chinese with English abstract).

7. Chen, H.J., Zhang, S.T., Cao, H.W., Wang, X.F., Nie, X.L., Zhang, W., **Tang, L.**, 2015. Compositional characteristics, petrogenesis and metallogenic significance of biotite from granite in the Guyong region of Western Yunnan Province, China. *Acta Mineralogica Sinica* 02, 267-275. (in Chinese with English abstract).
 8. Cao, H.W., Pei, Q.M., Zhang, S.T., Xiang, H., Zhang, L.K., **Tang, L.**, 2016. Geochemistry and Sm-Nd age of calcites from the Sandaogou Pb-Zn-Ag deposit in Luanchuan, western Henan Province. *Geochimica* 45, 144-154. (in Chinese with English abstract).
-

Conference Presentations

- November 2016: International Association for Gondwana Research (IAGR) 2016 Annual Convention and 13th International symposium on GONDWANA TO ASIA, Trivandrum, India
Oral presentation: **Tang, L.**, Santosh, M., Tsunogae, T., Petrology, phase equilibria modeling and zircon U-Pb geochronology of Paleoproterozoic mafic granulites from the Fuping Complex, North China Craton
- October 2015: International Association for Gondwana Research (IAGR) 2015 Annual Convention and 12th International symposium on GONDWANA TO ASIA, Tsukuba, Japan
Poster presentation: **Tang, L.**, Santosh, M., Teng, X.M., Arc magmatism in the Fuping Complex and its bearing on Paleoproterozoic tectonics of the North China Craton
- September 2014: International Association for Gondwana Research (IAGR) 2014 Annual Convention and 11th International symposium on GONDWANA TO ASIA, Beijing, China
Poster presentation: **Tang, L.**, Santosh, M., Dong, Y.P., Precambrian tectonothermal history of a complex orogen: The Qinling belt, central China
- April 2014: International Conference on Continental Dynamics, Xi'an, China
Poster presentation: New constraints on the petrology and zircon U-Pb

geochronology of the Songshugou ophiolite: implications for Paleozoic tectonic evolution of the Qinling orogenic belt

Poster presentation: **Tang, L.**, Santosh, M., Dong, Y.P., Tsunogae, T., New constraints on the petrology and zircon U-Pb geochronology of the Songshugou ophiolite: implications for Paleozoic tectonic evolution of the Qinling orogenic belt

Google Scholar page:

<https://scholar.google.com/citations?hl=zh-CN&user=kActjZIAAAAJ>

Research Gate page:

https://www.researchgate.net/profile/Li_Tang22